

Progress Report
Grant No. N00014-91-J-4164
September 15, 1995 - September 15, 1996

**MECHANISMS FOR THE HYDROGEN ENVIRONMENT
EMBRITTLEMENT RESISTANCE OF HIGH STRENGTH ALLOYS**

Submitted to:

Office of Naval Research
800 N. Quincy Street
Arlington, VA 22217-5660

Attention:

Dr. A. John Sedriks
Materials Division, Code 1131M

Submitted by:

R. P. Gangloff
Professor

J. R. Scully
Associate Professor

R. G. Kelly
Assistant Professor

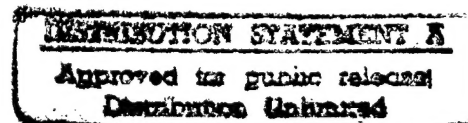
Report No. UVA/525461/MSE97/104
January 1997

DEPARTMENT OF MATERIALS SCIENCE AND ENGINEERING

19970214 056

SCHOOL OF
ENGINEERING 
& APPLIED SCIENCE

University of Virginia
Thornton Hall
Charlottesville, VA 22903



UNIVERSITY OF VIRGINIA
School of Engineering and Applied Science

The University of Virginia's School of Engineering and Applied Science has an undergraduate enrollment of approximately 1,500 students with a graduate enrollment of approximately 600. There are 160 faculty members, a majority of whom conduct research in addition to teaching.

Research is a vital part of the educational program and interests parallel academic specialties. These range from the classical engineering disciplines of Chemical, Civil, Electrical, and Mechanical and Aerospace to newer, more specialized fields of Applied Mechanics, Biomedical Engineering, Systems Engineering, Materials Science, Nuclear Engineering and Engineering Physics, Applied Mathematics and Computer Science. Within these disciplines there are well equipped laboratories for conducting highly specialized research. All departments offer the doctorate; Biomedical and Materials Science grant only graduate degrees. In addition, courses in the humanities are offered within the School.

The University of Virginia (which includes approximately 2,000 faculty and a total of full-time student enrollment of about 17,000), also offers professional degrees under the schools of Architecture, Law, Medicine, Nursing, Commerce, Business Administration, and Education. In addition, the College of Arts and Sciences houses departments of Mathematics, Physics, Chemistry and others relevant to the engineering research program. The School of Engineering and Applied Science is an integral part of this University community which provides opportunities for interdisciplinary work in pursuit of the basic goals of education, research, and public service.

REPORT DOCUMENTATION PAGEForm Approved
OMB No. 0704-0188

Public reporting burden for the collection of information is estimated to average 1 hour per response, including the time for reviewing instructions, searching existing data sources, gathering and maintaining the data needed, and completing and reviewing the collection of information. Send comments regarding this burden estimate or any other aspect of this collection of information, including suggestions for reducing this burden to Washington Headquarters Services, Directorate for Information Operations and Reports, 1215 Jefferson Davis Highway, Suite 1294, Arlington, VA 22202-4302, and to the Office of Management and Budget, Paperwork Reduction Project (0704-0188), Washington, DC 20503.

1. AGENCY USE ONLY (Leave Blank)

2. REPORT DATE
January 19973. REPORT TYPE AND DATES COVERED
Progress 09/15/95-09/15/96

4. TITLE AND SUBTITLE

Mechanisms for the Hydrogen Environment Embrittlement Resistance of High Strength Alloys

5. FUNDING NUMBERS

N00014-91-J-4164

6. AUTHOR(S)

R. P. Gangloff
J. R. Scully and R. G. Kelly

7. PERFORMING ORGANIZATION NAME(S) AND ADDRESS(ES)

Department of Materials Science and Engineering
School of Engineering and Applied Science
University of Virginia
Thornton Hall
Charlottesville, VA 22903-24428. PERFORMING ORGANIZATION
REPORT NUMBER

UVA/525461/MSE97/104

9. SPONSORING MONITORING AGENCY NAME(S) AND ADDRESS(ES)

Office of Naval Research
800 North Quincy Street
Arlington, VA 22217-566010. SPONSORING/MONITORING
AGENCY REPORT NUMBER

11. SUPPLEMENTARY NOTES

12a. DISTRIBUTION/AVAILABILITY STATEMENT

12b. DISTRIBUTION CODE

13. ABSTRACT (Maximum 200 words)

See Attached Pages

14. SUBJECT TERMS

Titanium alloys, hydrogen embrittlement, stress corrosion cracking, mechanical properties, intergranular cracking, microstructures, hydrides, passive film, beta titanium alloys, fracture threshold, fracture mechanics, repassivation, hydrogen trapping

15. NUMBER OF PAGES
10

16. PRICE CODE

17. SECURITY CLASSIFICATION
OF REPORT

Unclassified

18. SECURITY CLASSIFICATION
OF THIS PAGE

Unclassified

19. SECURITY CLASSIFICATION
OF ABSTRACT

Unclassified

20. LIMITATION OF ABSTRACT

Unlimited

Standard Form 298 (Rev 2-89)

Table of Contents

		Page
I.	Research Goals	1
II.	Summary of Results	1
III.	Appendices	

J.A. Lillard, R.G. Kelly and R.P. Gangloff, "Effect of Electrode Potential on Stress Corrosion Cracking and Crack Chemistry of a Nickel-Base Superalloy", Corrosion '97, NACE, Houston, TX, in press (1996).

B.P. Somerday and R.P. Gangloff, "Effects of Yield Strength and Microstructure on Environment-Assisted Cracking of Ti-3Al-8V-6Cr-4Mo-4Zr in Aqueous NaCl", Metallurgical and Materials Transactions A, in preparation (1996).

B.P. Somerday and R.P. Gangloff, "The Effect of Crack Tip Strain Rate on Aqueous Environmental Cracking Resistant Ti-3Al-8V-6Cr-4Mo-4Zr", Corrosion, in preparation (1996).

B.P. Somerday and R.P. Gangloff, "Measurement of Crack Opening Displacement and Crack Tip Strain for Transgranular and Intergranular Cracks in Aged β -Ti", Scripta Metallurgica et Materialia, in preparation (1996).

R.P. Gangloff, B.P. Somerday and D.L. Cooke, "Understanding Crack Tip Strain Rate Effects in Hydrogen Embrittlement for Improved Fitness-for-Service Modeling", in Life Prediction of Structures Subject to Environmental Degradation, R.N. Parkins and P.L. Andresen, eds., NACE, Houston, TX, in press (1996).

M.A. Gaudett and J.R. Scully, "Effect of Pre-dissolved Hydrogen on Fracture Initiation in Metastable Beta Ti-3Al-8V-6Cr-4Mo-4Zr", Scripta Metallurgica et Materialia, Vol. 31 (1996).

S.Y. Yu and J.R. Scully, "Enhanced Resistance to Steady State Active Dissolution and Passivity of Ti Alloyed with Nb and Zr", in the Passivity Conference Proceedings of the 190th Meeting of the Electrochemical Society, San Antonio, TX (1996).

D.G. Kolman and J.R. Scully, "Understanding the pH and Potential Dependency of β -Titanium Alloy Environmental Crack Initiation in 0.6 M NaCl through Investigation of Crack Tip Electrode Kinetics", Metallurgical and Materials Transactions A, in review (1996).

D.G. Kolman and J.R. Scully, "On the Repassivation Behavior of High-Purity Titanium and Selected α , β and $\beta + \alpha$ Titanium Alloys in Aqueous Chloride Solutions", Journal of the Electrochemical Society, Vol. 143, pp. 1847-1866 (1996).

D.G. Kolman and J.R. Scully, "On the Requirements for a Sharp Notch or Precrack to Cause Environmentally Assisted Crack Initiation of β -Titanium Alloys Exposed to Aqueous Chloride Environments", in Effects of the Environment on the Initiation of Crack Growth, ASTM STP 1298, W.A. Van der Sluys, R.S. Piascik, and R. Zawierucha, ASTM, Philadelphia, PA, in press (1996).

I. SCIENTIFIC RESEARCH GOALS

The objectives of this research are to: (1) identify conditions under which high strength β -titanium alloys and Fe-Ni-based superalloys resist environment assisted cracking (EAC) in marine environments, (2) characterize EAC initiation and propagation versus metallurgical, chemical and mechanical variables that may destabilize the crack tip passive film to promote both dissolution and hydrogen uptake, (3) test the hydrogen embrittlement mechanism, and (4) model EAC by integrating crack chemistry, surface repassivation kinetics, hydrogen uptake to trap sites, and crack tip process zone damage.

This report summarizes the results obtained for FY 96 and includes papers published or prepared during the period from September, 1995 to September 1996.¹ Two faculty members, Professors Richard Gangloff and John Scully, as well as three PhD graduate students; Messrs Jennifer Lillard, Michelle Gaudett and Brian Somerday; conducted this research.

II. RESULTS

II.a. Significant Results for FY 96 (*Brian P. Somerday, Jennifer A. Lillard, and Richard P. Gangloff*) The following conclusions were established in FY 96 based on fracture mechanics

¹ Mr. Somerday coauthored the following papers during FY96, but this work is not represented in this report because it is apart from the central theme of marine environmental cracking of high strength alloys.

Michael J. Haynes, Brian P. Somerday, Cynthia L. Lach and Richard P. Gangloff, "Micromechanical Modeling of Temperature-Dependent Initiation Fracture Toughness in Advanced Aluminum Alloys", in Elevated Temperature Effects on Fatigue and Fracture, ASTM STP 1297, eds., R.S. Piascik, R.P. Gangloff and A. Saxena, ASTM, Philadelphia, PA, pp. 165-190 (1996).

B.P. Somerday, Yang Leng and R.P. Gangloff, "Elevated Temperature Fracture Toughness of a Particulate Reinforced Aluminum Alloy Composite--Part II: Micromechanical Modeling", Fatigue and Fracture of Engineering Materials and Structures, Vol. 18, pp. 1031-1050 (1995).

B.P. Somerday, Yang Leng and R.P. Gangloff, "Elevated Temperature Fracture Toughness of a Particulate Reinforced Aluminum Alloy Composite--Part I: Fracture Toughness", Fatigue and Fracture of Engineering Materials and Structures, Vol. 18, pp. 565-582 (1995).

experiments with a high strength β -titanium alloy, Beta-C (Ti-8V-4Mo-6Cr-4Zr-3Al; RMI), and a precipitation hardened nickel-based superalloy, Inconel 718 (Ni-18.5Fe-18.5Cr-5Nb-3Mo-1Ti-0.5Al), stressed in aqueous solutions. The paper associated with each conclusion is presented in the Appendix to this progress report.

Both δ -subsolvus and δ -supersolvus heat treated microstructures of precipitation-strengthened IN718 are embrittled by stressed exposure in acidic chloride solutions at 25°C. Precracked specimens stressed under rising displacement exhibit slow, subcritical crack growth along transgranular slip band and grain boundary paths. The threshold stress intensity for this cracking is low, equaling about 50% of the plane strain fracture toughness; but crack growth rates are slow, on the order of 1 to 20 nm/s. EAC continues under constant displacement loading, but at greatly reduced rates. This behavior is analogous to gaseous hydrogen embrittlement of high strength superalloys. (J.A. Lillard, R.G. Kelly and R.P. Gangloff, "Effect of Electrode Potential on Stress Corrosion Cracking and Crack Chemistry of a Nickel-Base Superalloy", Corrosion '97, NACE, Houston, TX, in press (1996).)

Electrode potential affects the threshold stress intensity, growth kinetics and crack path for EAC in IN718, with the dependence differing with alloy microstructure. For the δ -subsolvus heat treatment, mixed transgranular-intergranular EAC is maximized at potentials somewhat cathodic to the free corrosion condition. In contrast δ -supersolvus IN718 is most severely embrittled at high levels of cathodic polarization; cracking in this larger grain size microstructure is predominantly intergranular at cathodic potentials. (J.A. Lillard, R.G. Kelly and R.P. Gangloff, "Effect of Electrode Potential on Stress Corrosion Cracking and Crack Chemistry of a Nickel-Base Superalloy", Corrosion '97, NACE, Houston, TX, in press (1996).)

The occluded crack solution, extracted from IN718 stressed in acidic solutions, contains the major alloying elements as well as one or two anions. Frozen crack solution was analyzed successfully for ionic content by capillary electrophoresis. Fe, Ni and Cr cations were present in proportions typical of the composition of IN718, indicating dissolution of metal at the crack tip, for each potential examined. These analyses demonstrated that nitrate is present in the crack solution, but have not established the presence of anions such as sulfide that could indicate the microstructural and mechanistic origins of EAC. (J.A. Lillard, R.G. Kelly and R.P. Gangloff, "Effect of Electrode Potential on Stress Corrosion Cracking and Crack Chemistry of a Nickel-Base Superalloy", Corrosion '97, NACE, Houston, TX, in press (1996).)

Intergranular EAC of solution treated and aged (ST/A) Beta-C in neutral NaCl solution is not governed uniquely by high yield strength, intense slip localization, or grain boundary α

precipitates. The immunity of solution treated and cold worked (ST/CW) Beta-C, compared to the susceptibility of aged (ST/A) Beta-C at similar strength, establishes that σ_{YS} alone does not promote severe EAC. Neither grain boundary α precipitates nor intragranular planar slip bands are present in sufficient number and uniformity to explain the fully IG crack path and severe EAC in ST/A Beta-C. Low σ_{YS} , limited microstructural sites for stress concentration, and contained crack tip yielding preclude extensive slip localization in aged Beta-C. High-magnification back-scattered SEM images, and TEM, show that α -film and α -precipitates form only occasionally in grain boundary planes for ST/A Beta-C. Grain boundary decohesion, promoted by localized hydrogen uptake at the crack tip-electrolyte interface and perhaps solute segregation during aging, appears to govern EAC. (B.P. Somerday and R.P. Gangloff, "Effects of Yield Strength and Microstructure on Environment-Assisted Cracking of Ti-3Al-8V-6Cr-4Mo-4Zr in Aqueous NaCl", Metallurgical and Materials Transactions A, in preparation (1996).)

Solution treated and cold worked Beta-C is immune intrinsically to EAC over a range of loading rates, but this high strength alloy suffers from low fracture toughness. Experiments in FY95 demonstrated the immunity of ST/CW Beta-C to EAC at a crack tip strain rate which caused intergranular cracking of aged Beta-C in aqueous NaCl. Experiments in FY96, spanning three orders of magnitude change in loading rate, established high EAC resistance for the cold worked single phase microstructure. The low fracture toughness of cold worked Beta-C hinders applications, as well as the use of cold work to unambiguously eliminate yield strength as the factor governing the susceptibility of aged Beta C to intergranular EAC. (B.P. Somerday and R.P. Gangloff, "The Effect of Crack Tip Strain Rate on Aqueous Environmental Cracking Resistant Ti-3Al-8V-6Cr-4Mo-4Zr", Corrosion, in preparation (1996).)

In situ SEM measurements of crack tip opening displacement and strain can guide modeling of crack ohmic voltage drop and the role of time-dependent crack tip deformation in EAC, but results to date are not fully informative. SEM-stereoimaging measurements showed that crack openings and crack tip strains are reduced substantially for an intergranular environmental crack in ST/A Beta-C compared to a transgranular fatigue crack, except for the special case of strain concentration at a grain boundary triple point. Crack tip strain does not change with time at constant K and 25°C; both transgranular and intergranular cracks in high strength ST/A Beta-C exhibited a similar lack of creep. Decaying crack tip creep strain rate at the continuum level does not account for the EAC immunity of ST/A Beta-C, prestained in air for 24 h and subsequently exposed to aqueous NaCl. The effect of prior strain on EAC may be caused by creep deformation at the microstructural level, not resolved by stereoimaging. (B.P. Somerday and R.P. Gangloff, "Measurement of Crack Opening Displacement and Crack Tip Strain for Transgranular and Intergranular Cracks in Aged β -Ti", Scripta Metallurgica et Materialia, in preparation (1996).)

Active crack tip strain rate promotes severe intergranular and transgranular hydrogen embrittlement in low strength steels, and in titanium alloys that form a passive crack tip film during environmental exposure. Fitness-for-service, Ratio Analysis Diagram, and remaining-life models are accordingly complicated. A rising load fracture mechanics experiment provides important data for hydrogen-resistant alloy development and quantitative component performance predictions. Loading rate effects are explained qualitatively by crack tip strain rate and active plasticity that enhance hydrogen production and uptake, and that promote process zone hydrogen transport and microscopic damage. Mechanism-based models of the hydrogen cracking threshold and stable crack growth rate parameters do not exist, and systematic laboratory studies to define the pertinent variables are limited. (R.P. Gangloff, B.P. Somerday and D.L. Cooke, "Understanding Crack Tip Strain Rate Effects in Hydrogen Embrittlement for Improved Fitness-for-Service Modeling", in Life Prediction of Structures Subject to Environmental Degradation, R.N. Parkins and P.L. Andresen, eds., NACE, Houston, TX, in press (1996).)

II.b. Significant Results for FY 96 (*David G. Kolman, Michelle A. Gaudett, Steven Y. Yu and John R. Scully*). The following conclusions were established in FY 96 based on passivity, electrochemistry, hydrogen embrittlement and hydrogen trapping experiments. Hydrogen embrittlement studies were conducted using hydrogen pre-charged notched tensile specimens to decouple hydrogen embrittlement from aqueous dissolution. A finite element solution of notch stress and strain fields was utilized to analyze fracture initiation data. Hydrogen partitioning and trapping studies were conducted using thermal desorption spectroscopy and x-ray diffraction. Studies of high strength titanium alloys were continued in FY 96 to examine the relationships between alloy microstructure, composition, applied potential, crack depth/shape and resulting crack chemistries, electrochemical dissolution kinetics, hydrogen reaction rates and likely hydrogen absorption scenarios. All studies were conducted using high strength β -titanium or near β -titanium alloys, Beta-21S (Ti-15Mo-3Nb-3Al, by wt pct; TIMET), 15-3 (Ti-15V-3Cr-3Al-3Sn, by wt. pct; TIMET), Beta-C (Ti-8V-4Mo-6Cr-4Zr-3Al; RMI) and near β Ti-13Zr-13Nb (Smith and Nephew Orthopedics). Results are sufficient to develop understandings of the potential dependency of high strength titanium alloy EAC susceptibility, and guide future mechanistic studies of the influence of crack or flaw geometry and solution flow rate on EAC susceptibility.

Results continue to indicate that pre-dissolved hydrogen embrittles Beta-C Ti at levels above the as-received level (100 wt. ppm.), but below those required to cause massive hydriding and/or cleavage of the beta phase. Finite element analysis of circumferentially notched tensile samples electrochemically pre-charged with hydrogen show a decrease in the fracture initiation stress of the ST/A condition ($\sigma_{YS} = 1260$ MPa) coincident with the introduction of an intergranular fracture mode

at approximately 1200 wt. ppm. hydrogen. The ST condition ($\sigma_{YS} = 865$ MPa) shows some hydrogen-affected ductile fracture modes, but the fracture initiation stress is not affected until approximately 2500 wt. ppm. where cleavage fracture is observed. Additional stroke rates, solution treatments, and aging conditions are currently being examined to explain the difference in hydrogen embrittlement resistance between the STA and ST conditions. (M.A. Gaudett and J.R. Scully, "Effect of Pre-dissolved Hydrogen on Fracture Initiation in Metastable Beta Ti-3Al-8V-6Cr-4Mo-4Zr", Scripta Metallurgica et Materialia, Vol. 31 (1996).)

Testing conducted on ST Beta-C cold-rolled to a similar yield strength as the ST/A condition ($\sigma_{YS} = 1110$ MPa) indicates that yield strength alone does not control hydrogen-induced intergranular crack initiation, rather a governing microstructural feature or condition brought about by the aging heat treatment to produce $\beta + \alpha$ microstructures is implicated. The fracture initiation stress of cold-rolled Beta-C as a function of pre-dissolved hydrogen content was compared to the ST and ST/A conditions. Intergranular fracture initiation was not observed in the cold-rolled condition and a decrease in the fracture initiation stress was not observed until cleavage fracture was introduced at 5000 wt. ppm. hydrogen. The governing microstructural feature or condition promoting intergranular EAC in STA $\beta + \alpha$ titanium remains elusive, but is not believed to be uniquely associated with either yield strength, grain boundary α films or colonies, or deformation mode. Instead, results suggest the role for a grain boundary segregant. (M.A. Gaudett and J.R. Scully, "Effect of Pre-dissolved Hydrogen on Fracture Initiation in Metastable Beta Ti-3Al-8V-6Cr-4Mo-4Zr", Scripta Metallurgica et Materialia, Vol. 31 (1996).)

Alloying of Ti with Nb and Zr results in improved resistance to active dissolution in reducing acids, improved steady state passivity, and repassivation in comparison to pure Ti. However, highly segregated Al concentrations may exert a negative influence on passivity and repassivation. The improved resistance to dissolution and enhanced passivity of Ti-Nb-Zr alloys was attributed to the enrichment of surface Nb and Zr. Two mechanisms for enrichment were identified; preferential electrochemical dissolution of Ti, and preferential chemical dissolution of TiO_2 . (S.Y. Yu and J.R. Scully, "Enhanced Resistance to Steady State Active Dissolution and Passivity of Ti Alloyed with Nb and Zr", in the Passivity Conference Proceedings of the 190th Meeting of the Electrochemical Society, San Antonio, TX (1996).)

EAC susceptibility in high strength Ti alloys does not appear to be controlled by differences in the repassivation behavior of α precipitates compared to the β matrix. Moreover, anodic bare surface current and charge densities were found to be similar for various Beta-Ti alloys in solutions of widely varying pH over a broad range of potentials between bare and oxide-covered open circuit potentials. Despite such repassivation behavior, crack initiation in fatigue pre-cracked compact tension specimens in aqueous solutions is strongly dependent on bulk solution

pH (e.g. cracking is observed in acidic solutions but can be suppressed in strongly alkaline solutions) and applied potential (e.g. cracking is observed at anodic potentials where hydrolytic acidification occurs and is suppressed at cathodic potentials where alkaline crack chemistries form). These results, coupled with the finding that film rupture rate or intensity is independent of solution pH on dynamically strained STA β -titanium tensile bars, suggest that *slip-film rupture-dissolution* models of SCC alone do not control observed pH and potential dependent environment-assisted crack initiation in NaCl solutions. Further, bare surface anodic kinetics, repassivation kinetics and film rupture rate were found to be within experimental error on both EAC-susceptible and immune alloys, again indicating that dissolution alone does govern alloy-specific EAC initiation in high strength β -titanium alloys. However, it is speculated that the rapid dissolution and slow repassivation of Ti-Al grain boundaries containing a high Al content or some other unidentified grain boundary segregant may promote intergranular cracking. (D.G. Kolman and J.R. Scully, "On the Repassivation Behavior of High-Purity Titanium and Selected α , β and $\beta + \alpha$ Titanium Alloys in Aqueous Chloride Solutions", Journal of the Electrochemical Society, Vol. 143, pp. 1847-1866 (1996).)

Anodic and cathodic inhibition of hydrogen-controlled EAC of high strength β -Ti alloys in room temperature, near-neutral NaCl solutions has been explained using experimental crack tip electrode kinetics and modeling of resulting crack tip potentials for given applied potentials. Anodic inhibition occurs due to anodic polarization of crack tips above the reversible hydrogen potential and β -titanium's excellent resistance to pitting in room temperature NaCl. Cathodic inhibition occurs due to decreases in crack tip hydrogen production and absorption rates when crack tip solutions become very alkaline at cathodic potentials. Unlike high strength steels, there is minimal bulk hydrogen charging through the surface oxides of high strength β -Ti. Moreover, high strength β -titanium alloys resist hydriding of a large volume fraction of the beta phase. (D.G. Kolman and J.R. Scully, "Understanding the pH and Potential Dependency of β -Titanium Alloy Environmental Crack Initiation in 0.6 M NaCl through Investigation of Crack Tip Electrode Kinetics", Metallurgical and Materials Transactions A, in review (1996).)

A hydrogen-based mechanism best explains EAC of pre-cracked high strength β -titanium alloys in 0.6 M NaCl and is consistent with the potential and pH dependencies of EAC in high strength titanium alloys. The following scenario for hydrogen embrittlement-controlled EAC was proposed and supported by experimental observations and calculations with input from experimental data: (1) crack tip film rupture occurring principally during plastic straining, (2) rapid dissolution of titanium, (3) crack tip acidification due to hydrolysis of titanium ions (except when exposed to high pH solutions or strong cathodic polarization), (4) significant excursions of crack tip potentials towards bare-metal open circuit potentials during film rupture due to loss of potentiostatic control at the crack tip caused by ohmic voltage drop in the crack tip solution, (5)

crack tip proton or water reduction concurrent with titanium dissolution, and (6) hydrogen uptake into the metal almost exclusively on the bare crack tip surface following proton or water reduction. Conditions for uptake are more favorable in acidic crack solutions typical of anodically polarized cracks. The proposed EAC scenario is consistent with the strong dependencies of crack initiation and growth on: (i) solution pH, (ii) applied potential and (iii) strain rate in high strength β -titanium alloys. (D.G. Kolman and J.R. Scully, "Understanding the pH and Potential Dependency of β -Titanium Alloy Environmental Crack Initiation in 0.6 M NaCl through Investigation of Crack Tip Electrode Kinetics", Metallurgical and Material Transactions A, in review (1996).)

The proposed framework for hydrogen embrittlement controlled EAC of high strength β -Ti alloys provides an explanation for the commonly observed EAC resistance or immunity of smooth or blunt notched compared to fatigue precracked high strength β -titanium specimens. The absence of a sharp crack delocalizes plastic strain, delocalizes film rupture, and minimizes occluded cell solution development and ohmic voltage drops to enable hydrogen production and entry. Long sharp cracks enable all of these phenomena and render the same ST/A β -Ti alloys susceptible to EAC. The scenario explains the observed propensity for cracking in fatigue-precracked ST/A β -titanium alloys as compared to EAC-resistant smooth or blunt notch specimens machined from the same heat. (D.G. Kolman and J.R. Scully, "On the Requirements for a Sharp Notch or Precrack to Cause Environmentally Assisted Crack Initiation of β -Titanium Alloys Exposed to Aqueous Chloride Environments", in Effects of the Environment on the Initiation of Crack Growth, ASTM STP 1298, W.A. Van der Sluys, R.S. Piascik, and R. Zawierucha, ASTM, Philadelphia, PA, in press (1996).)

**Effect of Electrode Potential on Stress Corrosion Cracking and Crack
Chemistry of a Nickel-Base Superalloy**

J. A. Lillard, R. G. Kelly and R. P. Gangloff

To be presented at CORROSION / 97, March 10, 1997, in New Orleans, LA

EFFECT OF ELECTRODE POTENTIAL ON STRESS CORROSION CRACKING AND CRACK CHEMISTRY OF A NICKEL-BASE SUPERALLOY

J. A. Lillard, R. G. Kelly, and R. P. Gangloff
Department of Materials Science and Engineering
University of Virginia
Charlottesville, Virginia 22903

ABSTRACT

The aqueous environment assisted cracking (EAC) resistance of a superalloy, Alloy 718 (Ni-19Fe-18Cr-5Nb-1Ti-0.6Al; Inconel 718⁽¹⁾), was characterized by a rising displacement fracture mechanics method. This precipitation-strengthened alloy was susceptible to room-temperature EAC in acidified sodium chloride at cathodic and anodic potentials. The threshold for stable crack growth in chloride (K_{TH}) was as low as 47 MPa√m, reduced from the laboratory air crack initiation toughness (K_{ICi}) of 81-85 MPa√m. The fracture morphology changed from ductile microvoids in air to a mixture of voids, transgranular facets, and intergranular facets in acidic chloride. Subcritical crack growth rates were on the order of 5×10^{-9} m/s for rising displacement at a stress intensity of 70 MPa√m and were an order of magnitude slower for constant displacement conditions. The degree of reduction in K_{TH} from K_{ICi} , the amount and type of fracture surface features, and the crack growth rate depended on the applied electrode potential. Microstructure produced by sub- or super- δ solvus heat treatment affected these dependencies. Ion analysis indicated that alloy dissolution occurred at the crack tip even at cathodic polarizations.

Keywords: crack chemistry, crack growth rate, electrode potential, fracture mechanics, hydrogen embrittlement, ion analysis, intergranular cracking, stress corrosion cracking, superalloys, transgranular cracking

INTRODUCTION

Applications in military systems as well as in the chemical, petrochemical, pulp and paper, and electric power industries often require a material with high strength and resistance to aqueous environmental embrittlement. Alloy 718, a precipitation-hardened, austenitic alloy, is a candidate material. While this alloy is susceptible to gaseous hydrogen embrittlement, aqueous cracking data are limited.

Embrittlement of Alloy 718 due to gaseous hydrogen was first observed in the late 1960's. Laboratory experiments revealed that the threshold stress intensity for crack extension (K_{TH}) was reduced to as low as 15% of the plane strain fracture toughness (K_{IC}).¹ Since that time, considerable work has been performed on the H₂ embrittlement of Alloy 718²⁻⁶ and on a similar, iron-based superalloy, Alloy 903 (41.4Fe-37.8Ni-15.3Co-1.3Ti-0.07Al-3.1Nb-0.15Mn-0.7Si-0.1Mo-0.04C, wt.%)⁷⁻¹². Figure 1 shows data from the literature where gaseous embrittlement was characterized by a reduced threshold stress intensity for subcritical crack growth with increasing hydrogen pressure. The fracture mode changed with increasing hydrogen gas pressure and hydrogen concentration

⁽¹⁾ Inconel is a trademark of Inco Alloys International, Incorporated.

in the crack tip process zone, as noted on the figure. Moody *et al.* reported that carbides were initiation sites for hydrogen-enhanced, transgranular slip band fracture^{7,8,10,13} and that γ' precipitates promoted coplanar slip, which increased the susceptibility to slip band cracking.¹⁰ The segregation of impurities, namely S and P, and atomic hydrogen trapped at austenite grain boundaries have been reported to promote intergranular fracture.¹⁴⁻¹⁹

Limited data exist on the aqueous environment embrittlement of Alloy 718 under cathodic charging conditions. Kane observed no failure in age-hardened, Alloy 718 C-ring samples coupled to steel and stressed statically to 100% of the transverse yield strength (σ_{YS}) in room temperature NACE solution (5% sodium chloride, 0.5% acetic acid, saturated with H_2S)²⁰. However, samples failed if they were cold rolled or aged for long times at moderate temperatures and then stressed to $\geq 90\%$ of σ_{YS} . Severe cathodic charging of large-grained Alloy 718 at room temperature caused intergranular embrittlement in slow strain rate ($10^{-6} s^{-1}$) deformation of tensile specimens.²¹ Fine-grained material exhibited transgranular and intergranular surface cracking under cathodic charging in constant extension rate tests of notched specimens.^{6,22} Embrittlement occurred in high temperature, pressurized water reactor environments, with crack growth rates depending on the concentration of Laves phases, carbides, and nitrides as well as grain size and hardness.²³ Work to date has not coupled active loading and an existing crack, and it has not compared aqueous EAC to the gaseous hydrogen data in Figure 1.

The objective of this research was to establish the effect of applied electrode potential, loading rate (crack tip strain rate), and microstructure on the kinetics of aqueous EAC in Alloy 718. EAC testing employed precracked specimens and a fracture mechanics approach. A slow, active loading rate was chosen to exacerbate embrittlement. Susceptibility to EAC was characterized by the stress intensity coincident with the onset of crack growth (K_{TH}), subcritical crack growth rate (da/dt), the fracture surface morphology as compared to that of laboratory air, and the presence and concentration of ions in the near crack tip solution.

EXPERIMENTAL PROCEDURE

Material

A wrought bar (2.5-cm diameter) of Alloy 718 with the composition shown in Table 1 was studied. Two heat treatments were employed, a super- δ and γ'' solvus solution treated and aged condition, and a sub- δ solvus solution treated and aged condition. These two conditions were designated "STA" and "Sub-STA," respectively. For STA, the material was solutionized for 1h at 1066°C in vacuum, argon quenched, aged at 718°C in air for 8 h, and air cooled to room temperature. For Sub-STA, the material was solutionized for 1h at 954°C in a vacuum, argon quenched, aged at 718°C in air for 8 h, and air cooled to room temperature. According to TTT diagrams, the STA microstructure should consist of intragranular and grain boundary carbides and nitrides; strengthening precipitates, γ'' (Ni_3Nb , bct) and γ' (Ni_3Al , cubic); and possibly intragranular, orthorhombic Ni_3Nb (δ).^{24, 25} The Sub-STA microstructure should consist of grain boundary δ , intragranular and grain boundary carbides and nitrides, as well as strengthening precipitates (γ'' and γ'). In both microstructures S and P, present as impurities, may segregate to grain boundaries or carbide/matrix interfaces due to thermal processing.¹⁵ The grain size of the STA microstructure should be larger than that of the Sub-STA microstructure, given the dissolution of grain boundary δ at temperatures above the solvus.

Fracture Test Methods

Test Configuration. EAC tests were performed on small, single-edge notch (SEN) specimens in the L-R orientation. Stress was applied in the longitudinal direction, and the crack grew in the radial direction of the round bar. The SEN specimens were machined to a thickness of 2.5 mm and a width of 11.4 mm, with a 0.89 mm deep notch (Figure 2). Threaded ends of the SEN specimen were attached to pinned grips, allowing free rotation.

Specimens were precracked in laboratory air at 23°C prior to EAC testing. Precracking was typically performed at a load-frequency of 5 Hz with a terminating K_{MAX} of 10 MPa \sqrt{m} , $R = 0.1$ and a final $a/W = 0.2$ (or $a = 2.3$ mm).

EAC tests were conducted under slow, monotonically rising grip displacement using a servohydraulic mechanical test system. The grip displacement rate was constant at 4×10^{-6} mm/s and corresponded to a dK/dt of approximately $1 \text{ MPa}\sqrt{\text{m/hr}}$ prior to the onset of cracking. To determine if crack growth occurred at constant stress intensity, the grip position was fixed at various K levels for a period of time ranging from hours to days.

Crack tip process zone damage initiation and subsequent crack growth were measured using the direct current potential difference (dcpd) technique. A constant current between 1 and 2 A was applied to the specimen, and the voltage across the crack plane was monitored (Figure 2). The direction of the current was switched every 15 minutes to account for extraneous thermal voltages. Switching the dcpd current or turning the current off had no effect on the measured electrochemical current, and the electrochemical current density was similar to that obtained in dc polarization experiments. Presumably, the dcpd current only passed through the low resistivity metal and did not enter the more resistive current path associated with the electrolyte in the crack. It has been shown that the dcpd current does not affect aqueous environment fatigue crack growth rates for aluminum^{26, 27} and steel in chloride solutions.²⁸

The dcpd method relies on the fact that the potential distribution in the vicinity of a crack changes with crack growth. The change is detected with suitable instrumentation, and a calibration curve is used to determine crack lengths.^{26, 29, 30} Under the experimental conditions, the noise in the dcpd signal was less than $0.5 \text{ } \mu\text{V}$, which corresponds to an average change in crack length of about $2 \text{ } \mu\text{m}$.

Environmental control was maintained using a poly(methyl methacrylate) (PMMA) cell, which contained 1.25 l of solution, ports for gas purging, a saturated calomel reference electrode, and a platinum counter electrode (Figure 2). Solution was not circulated during an experiment. EAC experiments employed two types of acidic chloride solutions: (a) 0.6 to 1.0 M NaCl plus 0.1 to 1.0 M HCl and sometimes 10 ppm Na_2S (pH 1.3 and 0, respectively) and (b) 1.0 M NaCl plus 0.4 to 0.5 M H_2SO_4 (pH 0.3 and 0.1, respectively). Gaseous nitrogen was bubbled through the solution for several hours before filling the cell, and nitrogen deaeration was continued throughout the test. The saturated calomel reference electrode was isolated from the bulk solution by a glass frit, and the frit was located approximately 5 cm from the notch. Electrode potential was maintained constant using a potentiostat with the working electrode grounded.

Data Analysis. Elastic K was calculated using Equation 1 for the SEN specimen with rotating ends.³¹ The equation has an accuracy better than 0.5% for any a/W , where a is crack length and W is specimen width.

$$K = \frac{P}{BW} \sqrt{\pi a} F(a/W) \quad (1)$$

$$\text{where } P = \text{applied load, } B = \text{SEN thickness, and } F(a/W) = \sqrt{\frac{2W}{\pi a} \tan \frac{\pi a}{2W}} \frac{[0.752 + 2.02 \frac{a}{W} + 0.37(1 - \sin \frac{\pi a}{2W})^3]}{\cos \frac{\pi a}{2W}}$$

The maximum stress intensity for a valid elastic analysis, calculated using the SEN limit load solution, was $100 \text{ MPa}\sqrt{\text{m}}$ for a precrack crack length of 2.3 mm. A conservative estimate suggests that the plane strain K limit is about $32 \text{ MPa}\sqrt{\text{m}}$;³² however, some through-thickness constraint should be maintained to higher K levels and will be judged based on crack appearance.

The initiation of crack growth was determined as the point where the dcpd-grip displacement trace became nonlinear (Figure 3). The monotonic increase in dcpd before initiation was attributed to plasticity-increased material resistivity. Because the dcpd signal was more sensitive to crack tip damage than load versus grip displacement, the load trace appeared linear in the region of initiation, as shown in the upper expansion in Figure 3.

Considering the maximum variability in the dcpd signal ($\pm 0.5 \mu\text{V}$), the accuracy in determining K_{TH} was estimated as $\pm 1.5 \text{ MPa}\sqrt{\text{m}}$.

Crack lengths were determined using Johnson's calibration for an SEN specimen.^{29, 33} The dcpd voltage (V), specimen width (W), probe spacing (y), initial crack length (a_0), and dcpd voltage at a_0 (V_0) were input for the equation:

$$a = \frac{2W}{\pi} \cos^{-1} \frac{\cosh(\pi y / 2W)}{\cosh\{(V / V_0) \cosh^{-1}[\cosh(\pi y / 2W) / \cos(\pi a_0 / 2W)]\}} \quad (2)$$

For fatigue precracking, a_0 was equal to the notch depth (0.89 mm), and for the EAC tests, a_0 equaled the fatigue precrack length (usually about 2.3 mm).

A typical plot of crack length as a function of time is presented in Figure 4 for continuous displacement and fixed displacement loading of Sub-STA 718 in an acidic solution. Equation 2 is an exact closed form solution and is thus valid for a/W up to 1. To check accuracy, the final crack length was measured using an optical microscope and compared to dcpd-calculated values in Figure 5. The difference between the predicted and measured final crack lengths was less than 3% for all of the specimens examined. The measured length for a fatigue precrack started from a notch (open squares in Figure 5) was consistently higher than the calculated length because Equation 2 is only accurate for crack length measurement after the crack has grown a finite distance from the notch³³.

Crack growth rates were calculated using a curve fit to the crack length versus time data. Either a polynomial or an exponential function was fit to the data (Figure 4). The time derivative of the function was determined and da/dt was calculated.

Crack Chemistry Methods

After completion of the EAC test, the specimen was removed from the cell, immersed in liquid nitrogen for several minutes, and fractured into two halves using the mechanical test system.

Solution Sampling. The two frozen halves were transferred to a glove bag where sampling was performed (Figure 6). The glove bag was previously filled with dry nitrogen gas. Each specimen half was placed under a stereoscope (30x magnification) and the half with the majority of the frozen crack solution was used for sampling. Strips of filter paper, 1-2 mm wide and 1 cm long, were pressed onto the region of the environmental crack just as the crack solution began to melt. The filter paper was then soaked in a plastic vial containing 20 μl of 10 mM mannitol ($\text{HOCH}_2(\text{CHOH})_4\text{CH}_2\text{OH}$) for several minutes. A mannitol solution was chosen because it is an oxygen scavenger and delays oxidation of sulfur species. After the filter paper was removed from the vial, the diluted sample was analyzed for ions.

Ion Analysis. Samples were analyzed for anions and cations using capillary electrophoresis. In this method, ions are injected into a small-diameter capillary filled with a carrier electrolyte and subjected to an applied potential. Separation of species occurs due to differences in ionic mobility. Details of the technique are given by Jandik and Bonn³⁴. Hollow fused-silica capillaries of 75 μm inner diameter and 60 cm length were used. Detection by ultraviolet absorbance occurred 52 cm from the end of the capillary where a portion of the polyimide coating was burned off. Weekly capillary conditioning consisted of purging for several minutes with 0.1 M LiOH, followed by a 10 minute purge with deionized water, and then a 15 minute purge with electrolyte. Capillaries were filled with deionized water for storage between experiments.

The carrier electrolyte was different for analysis of cations and anions. The cation electrolyte consisted of 5.0 mM 4-methylbenzylamine and 6.5 mM α -hydroxyisobutyric acid (pH 4.4). The anion electrolyte consisted of

5.0 mM sodium sulfate and 0.5 mM tetradecyltrimethylammonium bromide (TTAB) converted to the hydroxide form (pH 10.5) or a similar electrolyte which consisted of 25 mM sodium chloride and 1.5 mM TTAB converted to the hydroxide form (pH 11.0). Capillaries were electrolyte specific.

Samples were hydrostatically injected into the capillary using a sampling time of 30 s and a height difference of 10 cm. The capillary was purged with electrolyte for 2 min before each injection. All analyses were carried out at room temperature using a power supply at +15 kV for cations and -15 kV for anions. Ionic species were identified using known standards for comparison.

RESULTS

Air Mechanical Properties

Table 2 shows laboratory air tensile properties, fracture toughness, and average grain diameter for the two microstructures of Alloy 718 studied. The Sub-STA material exhibited an 18% higher yield strength and a 14% higher ultimate strength than the STA material. Reduction in area for the Sub-STA condition was slightly lower. Figure 7 shows optical micrographs of the grain structure for the two heat treatments. The grains contained matrix and grain boundary carbides and probably nitrides as well as annealing twins. The grain diameter was determined by measuring the average number of grains intercepted by a random line through the cross section. The super- δ solvus heat treatment resulted in substantial grain growth as expected given dissolution of the δ phase.

The yield strengths differed significantly for Sub-STA and STA Alloy 718 (Table 2) and were lower than values reported in the literature for a typical, commercial aging process (solution treat below the δ solvus plus double age; Sub-STD).^{2, 25, 35-39} These strength differences are traced to solution treatment and aging conditions. In contrast to aging at a single temperature, double aging produces similar high strengths for Alloy 718 regardless of whether solutionization is sub- or super-solvus.³⁵ For Alloy 718 aged for 8 h at 718°C, the Sub-STA condition is harder due to smaller grain size and a faster time to peak aging. The time-temperature precipitation relationships can be shifted to longer or shorter times depending on the grain size, degree of retained forging deformation, and solution heat treatment temperature.²⁵

Air fracture toughness tests did not meet the criteria for plane-strain fracture toughness (K_{IC}).³² Specifically, the sample thickness was less than that required by the empirical formula for plane strain. However, SEM examination of an air toughness specimen, which was fatigued after initiation to mark the air crack growth, showed a thumbnail-shaped, flat fracture surface. At the specimen side surface, the crack length was only a few μm as compared to about 150 μm at the centerline, and shear walls were present. This suggests that plane strain constraint was sufficient near crack initiation, and the critical K approximated K_{IC} . This measured toughness is designated K_{ICi} .⁴⁰ This result also supports the accuracy of the dcpd indication of the onset of cracking (Figure 3).

The air fracture toughness value for the Sub-STA condition was consistent with plane strain values reported in the literature.^{4, 38, 41} Air fracture toughness of the STA material was more than 25 $\text{MPa}\sqrt{\text{m}}$ lower than reported values.^{4, 41} In each case, fracture progressed by microvoid processes, as discussed in an ensuing section. The reason for the relatively low toughness of the STA microstructure is not known.

Threshold for Subcritical Crack Growth

Sub-STA EAC threshold results for Sub-STA Alloy 718 tested in two environments and at various electrochemical potentials are shown in Figure 8. Environmental cracking was observed at each potential examined. The laboratory air fracture toughness (K_{ICi}) of this microstructure was 81 $\text{MPa}\sqrt{\text{m}}$, and K_{TH} was reduced by 18 to 32% compared to K_{ICi} , depending on electrode potential. There was an apparent minimum of 52 $\text{MPa}\sqrt{\text{m}}$ in K_{TH} at moderate cathodic potentials (-0.6 V_{SCE}). K_{TH} was slightly higher at the corrosion potential and increased to 63 $\text{MPa}\sqrt{\text{m}}$ at a potential 0.13 V anodic to the corrosion potential. At a highly cathodic potential (-1.0 V_{SCE}), K_{TH} was higher than observed at the corrosion potential.

Reproducibility of test results was good. Three tests were performed at $-0.6 V_{SCE}$ in the $0.4 M H_2SO_4 + 1.0 M NaCl$ solution. The average K_{TH} was $52.6 MPa\sqrt{m}$ with a maximum of $53.9 MPa\sqrt{m}$ and a minimum of $50.5 MPa\sqrt{m}$.

Solution pH over the range of 0.3 to 1.3 did not significantly affect embrittlement in terms of K_{TH} . Both at the corrosion potential and at $-1.0 V_{SCE}$, the values for the less acidic solution, which also contained Na_2S , agreed with a second-order polynomial fit of the data. At the corrosion potential, K_{TH} for the less acidic solution was slightly below the trend line, and at $-1.0 V_{SCE}$ it was above the trend line.

STA EAC threshold results for STA Alloy 718 tested in two environments and at various electrochemical potentials are shown in Figure 9. The laboratory air fracture toughness (K_{IC}) of this microstructure was $85 MPa\sqrt{m}$. K_{TH} was reduced by 20 to 50% compared to K_{IC} , depending on electrode potential. Unlike the Sub-STA microstructure, the STA material exhibited decreasing K_{TH} at large cathodic polarizations, without a minimum at $-0.6 V_{SCE}$. At $-1.0 V_{SCE}$, K_{TH} was $47 MPa\sqrt{m}$ which is 25% lower than that of the Sub-STA material at the same potential. Between -0.8 and $-0.6 V_{SCE}$, K_{TH} rose considerably, and then slowly between $-0.6 V_{SCE}$ and the E_{CORR} .

Reproducibility of K_{TH} for this microstructure was also good. At $-0.6 V_{SCE}$ in the $1.0 M HCl + 1.0 M NaCl$ solution, K_{TH} varied from 60.0 to $62.6 MPa\sqrt{m}$. At $-0.8 V_{SCE}$ in the $0.5 M H_2SO_4 + 1.0 M NaCl$ solution, K_{TH} varied from 45.1 to $46.6 MPa\sqrt{m}$.

The two aqueous solutions used in testing the STA material were similar with regard to chloride concentration and pH but had different acid anions. In one case the acid anion was chloride and in the other it was sulfate. For the tests where chloride was the acid anion, K_{TH} was slightly lower (e.g., at $-0.8 V_{SCE}$, $3 MPa\sqrt{m}$ lower), but the difference was greater than the typical experimental variation in K_{TH} .

While different acidified chloride solutions were employed, it is likely that heat treatment and microstructure caused the different electrode potential dependencies of K_{TH} shown in Figures 8 and 9. This conclusion is supported by the data for acidic, sulfate-chloride solutions where only pH varied from 0.3 for Sub-STA to 0.1 for STA. Effects of pH, between 0 and 1.3, as well as the Na_2S addition and acid anion, appear to be secondary. Nonetheless, low pH-high cathodic potential EAC data should be obtained for Sub-STA Alloy 718 in the HCl-NaCl solution. Additionally, experiments should be conducted with the STA microstructure in the very low pH, HCl-NaCl solution at the corrosion potential.

Subcritical Crack Growth Rate

Da/dt for Rising versus Constant Grip Displacement. Figure 10 shows da/dt as a function of K for three replicate experiments on Sub-STA Alloy 718 deformed under rising displacement in the pH 0.3 sulfate-chloride solution at $-0.6 V_{SCE}$. Subcritical EAC rate increased with a power law slope of 4.7, and plateau, K -independent cracking was not observed for the actively-rising displacement case. When the grip displacement was held constant, the crack growth rate was considerably reduced; da/dt decreased exponentially by an order of magnitude within about ten minutes of halting active loading. Furthermore, upon restarting active loading, da/dt typically increased to a value that was lower than that of the previous active loading rate (not shown in the figure). The behavior illustrated in Figure 10 was observed generally for both microstructures of Alloy 718 although the power law slope was typically about 2 for the STA microstructure.

Sub-STA Crack growth rates, at a stress intensity of $70 MPa\sqrt{m}$ and as a function of applied potential, are shown in Figure 11 for the Sub-STA microstructure. The rates were determined for increasing displacement conditions and varied between 1 and $16 nm/s$ over the range of applied potentials examined. The highest da/dt was observed at $-0.6 V_{SCE}$, where the average for three tests was $12.6 nm/s$. Da/dt decreased at higher and lower applied potentials and was typically less than $5 nm/s$. One notable exception occurred at $-1.0 V_{SCE}$, where da/dt in the more acidic solution was several times faster than in the less acidic solution. The potential dependence of da/dt mirrors that of K_{TH} (Figure 8).

STA The crack growth rates for the STA material, shown in Figure 12, varied less with applied potential than for the Sub-STA microstructure. Between the corrosion potential and $-0.4 V_{SCE}$, da/dt was 3 nm/s. The average da/dt increased slightly to 4.4 nm/s at a polarization of $-0.6 V_{SCE}$. The largest value of da/dt for the STA microstructure was 9 nm/s at an electrode potential of $-0.8 V_{SCE}$ in the 0.5 M H_2SO_4 + 1.0 M NaCl. For the same polarization in the 1.0 M HCl + 1.0 M NaCl solution, da/dt was 30% slower. Crack growth rate continued to increase with polarization to $-1.0 V_{SCE}$, but data are limited.

Fracture Surface Morphology

Sub-STA Scanning electron fractographs of Sub-STA fracture surfaces are shown in Figure 13 for each test environment. The air crack surface (13 a) consisted mainly of voids surrounding carbides. The diameter of the carbides was generally less than 5 μm , and the diameter of the voids was typically about 10 μm . Regions between the main dimples contained smaller voids, possibly nucleated at δ particles. It was reported that large carbide inclusions failed and nucleated primary microvoids; growth of the voids was interrupted by the formation of a secondary dimple network initiated by coarse δ particles.⁴¹ The EAC fracture surfaces for various electrode potentials are shown in Figures 13b-13d. At the highest and lowest polarizations (13b and 13d), the fracture surface contained mostly transgranular facets and microvoids. The voids contained carbides (some cracked) and were generally smaller in diameter than those observed for the air case. At high magnification, steps were observable on the transgranular facets. At the intermediate potential of $-0.6 V_{SCE}$ (13c), the surface consisted of intergranular facets, transgranular facets, and a very few dimples. At high magnification, particles a few μm in diameter protruded from some intergranular facets. On other intergranular facets, indentations were observed. Secondary cracking, perpendicular to the plane of fracture, was observed in all cases except for the air test.

STA Figure 14 shows micrographs of fracture surfaces from the second microstructure studied. The air crack surface (14a) consisted mainly of dimples surrounding carbides, similar to the air crack surface for the Sub-STA microstructure. A series of smaller dimples (less than 2 μm) connected the regions of large dimples, which may be due to nucleation of voids at δ particle remnants.⁴¹ The EAC fracture surfaces, produced at various electrode potentials, are shown in Figures 14b-14d. For an applied potential of $-0.4 V_{SCE}$ (14b), the surface exhibited transgranular facets intermixed with dimples and was similar to the Sub-STA crack surface at E_{CORR} (13b) and $-1.0 V_{SCE}$ (13d). Similar features were observed for STA cracking at $-0.6 V_{SCE}$ (not shown). At $-0.8 V_{SCE}$, the STA crack surface was mostly intergranular with a small amount of transgranular fracture (14c and 14d). The intergranular surfaces contained small particles and shallow, intersecting ridges. The fracture surface morphology at $-0.8 V_{SCE}$ was similar for both the chloride and sulfate acid anion solutions. In all cases, except for air, there were numerous secondary cracks

Crack Solution Ion Identification

Cations. Cations of the major alloying elements of Alloy 718 (Ni^+ , Fe^{2+} , and Cr^{3+}) were typically detected in the crack solution as illustrated in Figure 15. The absorbance and migration time of the crack sample was compared with that of known standards, and the cations were identified as Fe^{2+} , Cr^{3+} , and Ni^+ . The electrolyte used for ion analysis allows detection of most transition metals; the method does not allow detection of cations of aluminum, titanium, or niobium. Standards were also used to quantify the concentration of ions in a sample. Because the crack sample was diluted an unknown amount while removing it from the crack surface, the exact concentration of ions could not be determined. However, relative concentrations may be compared. For simplicity, Alloy 718 is 60% by weight Ni, 20% Fe, and 20% Cr. Samples taken from the near crack tip differed from this percentage. A summary of the relative Ni-Fe-Cr concentrations by weight in the solution analyzed is presented in Table 3. The relative concentration of Na found in the crack solution to that of the major alloying elements is also compared in Table 3. The presence of a large concentration of alloy ions in the crack solution suggests that the potential at the crack tip was at or above that of the E_{CORR} of the bare nickel in the crack tip solution. IR drop down the crack causes the crack tip potential to shift to a value between the applied potential and E_{CORR} . This issue will be discussed in a later section.

Anions. Anion species that could be detected using the chloride electrolyte include thiosulfate, sulfite, sulfide, nitrite, nitrate, and molybdate. Recent work has identified the presence of nitrate in an STA sample cracked at E_{CORR} in 1M H_2SO_4 + 1M NaCl (Figure 16). Although the standard and second sample peak are shifted slightly, spiking the sample with nitrate confirmed the identity of the peak. The first peak is a system peak due to the large amount of chloride in the sample. For other samples analyzed, a peak was observed with a similar migration time to that of nitrate. This peak was not confirmed to be nitrate because the small volume of the sample prevented re-analysis and the migration times varied somewhat depending on the room temperature. A second peak was sometimes detected in Sub-STA samples, but it has not yet been unambiguously identified.

DISCUSSION

Overview

Alloy 718 results show that the degree of aqueous EAC in acidified solutions depends on applied polarization, microstructure, and active crack tip strain. These observations are consistent with previous work on aqueous embrittlement of Alloy 718 and similar superalloys, where cathodic polarization, strain rate, and the size and type of precipitates controlled the degree of embrittlement.^{21-23, 42, 43} Environment produced transgranular and intergranular cracking modes that were unique compared to the microvoid fracture observed in air.

EAC results for Alloy 718 can be qualitatively understood based on hydrogen embrittlement as a controlling factor. Crack tip reactions are of prime importance. Hydrogen can be produced, after crack tip film rupture, by H^+ or water reduction concurrent with alloy dissolution, and then absorbed into the metal at the crack tip. Hydrogen can then be transported by dislocations or diffuse to critical microstructural features that act as trap sites (e.g., grain boundaries). Hydrogen uptake through a passive film on a boldly exposed specimen surface is unlikely,⁴⁴ as is bulk hydrogen diffusion over a mm-scale distance, based on the low hydrogen diffusion coefficient ($2 \times 10^{-11} \text{ cm}^2/\text{s}$ at 25°C ⁴⁵) and test time to EAC initiation. The following discusses the roles of electrode potential, microstructure, dK/dt , and near-crack tip solution chemistry on embrittlement.

Applied Polarization

K_{TH} , da/dt , and the fracture morphology depended on the electrode potential, and this dependence was different for the Sub-STA and STA microstructures of Alloy 718. Figures 17 and 18 summarize K_{TH} , da/dt , and fracture morphology for the two microstructures. Embrittlement was not as severe at potentials near E_{CORR} , particularly compared to cathodic polarization. Specifically, at E_{CORR} K_{TH} was higher than the minimum, da/dt was lower than the maximum, and the fracture surface had transgranular, not intergranular, facets. At cathodic polarizations, embrittlement was the most severe. K_{TH} was minimum, da/dt was maximum, and intergranular facets were observed on the fracture surface. For the Sub-STA microstructure, embrittlement was less severe at large, cathodic polarizations. For the STA microstructure, the degree of intergranular embrittlement was not reduced at large cathodic polarizations, in contrast to the Sub-STA case.

K_{TH} . The $K_{\text{TH}} - E$ curve (Figure 9) has similar features to the $K_{\text{TH}} - \text{H}_2$ pressure curve for STDA Alloy 718 in Figure 1. K_{TH} for electrode potentials of $-0.4 \text{ V}_{\text{SCE}}$, $-0.6 \text{ V}_{\text{SCE}}$, and E_{CORR} is about the same as K_{TH} for 10 MPa H_2 , and for electrode potentials of $-0.8 \text{ V}_{\text{SCE}}$ and $-1.0 \text{ V}_{\text{SCE}}$, K_{TH} is about equal to K_{TH} in 25 MPa H_2 . Figure 1 suggests that K_{TH} is a unique function of hydrogen concentration (c_{H}), and, speculatively, that c_{H} was about the same for E_{CORR} to $-0.6 \text{ V}_{\text{SCE}}$ as well as for $-0.8 \text{ V}_{\text{SCE}}$ and $-1.0 \text{ V}_{\text{SCE}}$. c_{H} can be determined by permeation techniques, but relevant data are not available. For gaseous environments, c_{H} depends on hydrogen pressure and environment temperature. For aqueous environments, c_{H} depends on the solution chemistry, applied polarization, and temperature. The crack tip potential and solution chemistry differ from that of the bulk conditions. Therefore, c_{H} cannot be readily determined.

The observed minimum in K_{TH} has not been reported in the literature for Alloy 718. Dull and Raymond reported a decreasing time-to-failure (TTF) with increasing overpotential from open circuit to below $-1.2 \text{ V}_{\text{SCE}}$ for notched tensile specimens loaded to 90% of the notch tensile strength in acidic chloride⁴². They also observed

surface cracking at high cathodic polarizations²². Precracked specimens can develop an occluded crack tip solution, whereas notched tensile specimens do not.

In other alloy systems, where EAC experiments employed an occluded precrack geometry, a minimum in K_{TH} was observed. In particular, precracked β and $\alpha + \beta$ titanium alloys exhibited EAC susceptibility at potentials between -0.3 and $-0.8 V_{SCE}$, but were immune to EAC at $-1.0 V_{SCE}$ in neutral chloride solutions.⁴⁶⁻⁴⁸ These alloys were susceptible to EAC at $-1.0 V_{SCE}$ in highly acidic solutions.⁴⁸ To understand the minimum in K_{TH} , the crack tip potential and pH must be examined.

The potential at the crack tip is determined by the amount of ohmic loss (IR) due to the restricted geometry and solution resistance of the crack. As a simplistic analysis, the outer surface of the crack is considered to be polarized at the applied potential, E_{app} , and will have a current, I_{app} . At the crack tip, the potential (E_{tip}) will equal ($E_{app} - I_{app}R_{crack}$). If the current is negative (cathodic), E_{tip} will be anodic to E_{app} ; if the current is positive, E_{tip} will be cathodic to E_{app} . The amount of IR is increasingly negative as cathodic polarization increases, as long as the current does not become limited. In the limit, potentiostatic control of the crack tip is lost and E_{tip} equals E_{corr} of the bare metal in the crack tip solution.

The pH of the crack solution can be a function of cathodic polarization. During a cathodic reaction, OH^- is produced by water or proton reduction. Large cathodic polarization can produce sufficient OH^- within the crack to cause solution at the occluded crack surface to become alkaline. After one EAC test on the Sub-STA material at $-1.0 V_{SCE}$, pH paper was pressed onto the frozen crack surface. Most of the surface solution was acidic, but there were random, small spots of alkalinity. These spots may correspond to high regions of the crack surface where the actual solution-metal surface pH was measured. The lower regions would have acted as pools containing solution from both the surface cathodic reaction and the more acidic, bulk solution.

An alkaline region at the crack tip, produced by cathodic polarization, could explain the minimum K_{TH} as a function of potential. If IR in the crack is large, potentiostatic control is compromised and the crack tip potential moves toward E_{CORR} for bare nickel in the crack tip solution. Kolman and Scully measured E_{CORR} of bare titanium in chloride as a function of pH in a buffered solution of 0.6 M NaCl.⁴⁹ The overpotential for hydrogen production ($E_{HER} - E_{CORR}$, where E_{HER} is the reversible potential for hydrogen production) decreased with increasing pH. They concluded that either strong cathodic polarization or high pH bulk solution promotes immunity as a result of an alkaline crack tip chemistry.

Da/dt. Crack growth rate, as a function of applied potential for aqueous embrittlement of Alloy 718, has not been reported in the literature. Figure 19 compares aqueous crack growth rate data with gaseous hydrogen da/dt results for Alloy 718 at an applied K of $70 \text{ MPa}\sqrt{\text{m}}$.⁴ These growth rates are plotted as a function of K_{TH} for each Alloy 718-environment condition. The gaseous hydrogen crack growth rates are plotted from data that exhibited Stage I behavior up to the fastest crack growth rates measured ($2 \times 10^{-7} \text{ m/s}$), and the da/dt values for the two highest hydrogen pressures were extrapolated from those data. These extrapolations are not accurate if rate-limited Stage II crack growth intervened at a K level below $70 \text{ MPa}\sqrt{\text{m}}$. In Stage I crack growth, da/dt is mechanically limited. Therefore, for the gaseous data it appears that neither hydrogen absorption at the crack tip (c_H) nor diffusion limited da/dt up to $2 \times 10^{-7} \text{ m/s}$. Da/dt for the aqueous case (Figure 10) were in the Stage II region where the crack growth rate was slightly dependent on K and was limited by reaction rates and/or mass transport. Since diffusion of hydrogen did not limit da/dt in the gaseous case, it should not limit the slower da/dt in the aqueous case. A speculative explanation of Figure 19 is that cracking occurs when a critical adsorbed hydrogen concentration (c_H) and K level are reached. It is likely that K_{TH} depends on c_H raised to a power between -0.25 and -0.75 .⁵⁰ A linear regression to the gaseous hydrogen data in Figure 1 shows K_{TH} proportional to $P_{H_2}^{-0.25}$. According to Sievert's Law, c_H is proportional to $P_{H_2}^{0.5}$, so K_{TH} is proportional to $c_H^{-0.5}$. Once crack growth begins, however, c_H in the aqueous system may be kinetically limited by hydrogen production or adsorption rates (e.g., by hydrogen recombination over adsorption). That is, c_H may be time dependent in the aqueous system but not in the gaseous system. The following analysis is based on the notion that da/dt depends directly on the concentration of adsorbed atomic hydrogen at the crack tip-solution interface. Assuming da/dt is proportional to c_H , suggests that da/dt is proportional

to K_{TH}^{-2} . The slope of a linear regression of the aqueous data in Figure 19 was -1.8 suggesting that c_H may dominate Stage II da/dt . Further work is necessary in order to verify these speculations.

Another issue under consideration for the aqueous da/dt data is constraint in the thin samples. Moody and Gerberich reported that for hydrogen-enhanced cleavage in an $\alpha+\beta$ titanium alloy, crack growth rates at K above K_{TH} depended on stress state and were exacerbated by plane strain constraint.⁵¹ At the same stress intensities, da/dt was up to several orders of magnitude lower in thinner samples due to the plane stress regions at sample surfaces restraining plane strain crack advance in the interior plane strain region. Figure 20 shows the full thickness of an SEN specimen. The ends of the air fatigue precrack and EAC region are noted with arrows. Examination of the edges shows the beginning of shear lip formation after 0.065 mm of crack growth. This corresponds to a K of 63 MPa \sqrt{m} . The loss in plane strain constraint was small ($< 1\%$). However, 5-mm thick $\alpha+\beta$ titanium samples ($\sigma_{YS} = 1010$ MPa, $K_{TH} = 35$ MPa \sqrt{m}) exhibited hydrogen-induced crack growth at rates orders of magnitude less than 10- or 20-mm thick samples.⁵¹ The effect of stress state on EAC, and particularly da/dt , in the SEN specimens of Alloy 718 should be further examined.

Fracture morphology. The environment-embrittled fracture surface exhibited transgranular and/or intergranular facets, and the area fraction of each depended on polarization and microstructure. This observation is similar to that previously reported for gaseous hydrogen embrittlement. Walter and Chandler observed transgranular and intergranular cracking of Alloy 718 in hydrogen gas, and the STDA condition was more likely to exhibit intergranular cracking compared to Sub-STDA.^{4, 5} Moody *et al.* reported that the fracture morphology changed from: (a) microvoids formed in air, to (b) microvoids and transgranular facets at low hydrogen pressures, to (c) intergranular facets at high hydrogen pressures for a similar, γ' -strengthened superalloy (Figure 1).⁹ They noted that the transgranular facets were due to mixed mode I-II cracking along the plane of an intense slip band, formed due to a hydrogen-dislocation interaction.

Figure 21 shows a high magnification SEM micrograph that is typical of the transgranular facets observed for Sub-STDA and STA 718. Intersecting slip bands and dimples along the slip bands were visible on the facets. Cracked carbides were also observed. The transgranular cracking is postulated to be slip band cracking. Moody and Greulich observed slip band cracking of a hydrogen-charged Fe-Ni-Co superalloy, initiated by microvoid formation at slip band intersections. These microvoids formed in highly deformed regions ahead of microcracks formed by fractured matrix carbides.⁷ Moody *et al.* also noted that slip band facets exhibited more local plasticity at low hydrogen concentrations.⁵²

The size of the transgranular facets on the Sub-STDA and STA EAC fracture surfaces differed (Figures 13 b,d and 14 b). The facets on the larger-grained STA material were larger, but the slip band spacing appeared to be the same in all cases. It is necessary to conclusively determine if the slip band spacings are the same and to determine if there is a correlation between K_{TH} and the degree of local plasticity on the facets.

For the cases where intergranular fracture occurred, the Sub-STDA and STA microstructures showed quite different behavior (Figures 13c and 14 b, d). The Sub-STDA microstructure showed small regions of intergranular cracking connected by regions of slip band fracture. The STA microstructure showed large regions of intergranular facets connected by small regions of slip band cracking. This suggests that the intergranular fracture strength of the large-grained material (STA) was less than that of the small-grained material (Sub-STDA) in the presence of hydrogen.

Microstructure

The two obvious microstructural differences between the Sub-STDA and STA microstructures were grain size and formation of δ during the solutionizing process. The STA material was solutionized at a temperature above

the δ solvus and had a grain size three times that of the Sub-STA material. The differences in microstructure can provide insight into the observed differences in embrittlement.⁽²⁾

Austenite grain size and δ phase can affect EAC. Walter *et al.* proposed that for Sub-STA 718 the fracture path followed the matrix (γ) / δ interface;⁵ however, this fracture morphology did not appear in the Sub-STA fracture surfaces in Figure 13. Both the present study and the Walter-Chandler work show that intergranular cracking is more prominent in the large-grained STA microstructure.^{4, 5} Moody *et al.* measured the intergranular fracture strength of a hydrogen-charged Fe-Ni-Co superalloy and found that as grain size increased, fracture strength decreased.⁵² This fracture strength is affected by at least three factors: (1) boundary impurity concentration, (2) boundary-trapped hydrogen concentration, and (3) intensity of slip band-grain boundary interactions. Impurities can segregate during the 718°C aging. As grain size increases, grain boundary area decreases and the concentration of segregants at the grain boundary may increase. Impurity segregation to grain boundaries, sulfur in particular, was proposed to cause intergranular fracture in nickel-base alloys.¹⁵⁻¹⁸ The role of each of these factors in reducing grain boundary fracture strength needs to be further examined.

dK/dt

Cessation of active loading during an EAC test considerably slowed da/dt but did not completely arrest brittle crack growth (Figure 10). Constant grip displacement tests were performed at a K level well above threshold, and the dK/dt effect is relevant to plane stress conditions. Similar results were found in the literature. Jewett *et al.* reported failure of Alloy 718 hydrogen gas storage tanks only after several years of service.¹ Kane reported no failures of STA 718 C-ring specimens stressed to 100% of the transverse yield strength and exposed for over 100 days to an acidic chloride environment with cathodic polarization.²⁰ Each of these cases involved essentially static loading.

Figure 22 shows da/dt as a function of electrode potential under constant displacement at a K level near 70 MPa \sqrt{m} . The crack growth rate under conditions of constant displacement was K-independent, unlike the rate for active loading in Figure 10. The static-K da/dt versus potential curve for the Sub-STA microstructure had a similar shape to that for active loading (Figure 11) although the maximum and minimum rates varied by over an order of magnitude for the static-K case. The STA microstructure rates also varied by over an order of magnitude between the maximum and minimum, but the data had a large scatter. The magnitude of the rates under constant displacement was typically an order of magnitude lower than the corresponding rates for rising K. An exception occurred at the potentials for the most severe embrittlement; these da/dt were about one-third of the corresponding da/dt for rising K. These results suggest that active displacement increases embrittlement, either by causing rupture of the oxide at the crack tip to allow hydrogen entry or by increasing hydrogen concentration by dislocation transport of hydrogen through the matrix. Additional analysis is required to relate da/dt in Figures 11, 12, and 22 to the governing variable of crack tip strain rate which depends on both dK/dt and da/dt.

Near Crack Tip Solution

Cations. The amount and ratio of alloying element cations within a crack provide insight into processes occurring at and near the crack tip. The presence of all of the major alloying elements in the Sub-STA near crack solution supports dissolution of the alloy at the crack tip even at cathodic potentials (Table 3). Due to changes in crack chemistry and ohmic drop down the crack, dissolution can occur at the crack tip for applied potentials that are below the reversible potential for the dissolution reaction of the boldly exposed surface. Although the data in Table 3 imply that dissolution may be more rapid at an applied potential of $-0.6 V_{SCE}$ than at $-0.2 V_{SCE}$, additional testing is required. The lack of stoichiometry in the near crack tip solution relative to the alloy composition is most likely due to the relative diffusivities of the major alloying elements.⁵³ Nickel cations are thought to diffuse faster than other

⁽²⁾ While aging temperature and time were constant, the STA microstructure was lower strength compared to the Sub-STA case. This difference may complicate interpretation of K_{TH} and da/dt data due to the importance of yield strength in hydrogen embrittlement. Since the lower strength STA case was more prone to intergranular hydrogen cracking, and since strength effects on transgranular slip band cracking are uncertain, the microstructural factors discussed here are important.

metal ions in occluded site solutions. This effect would lower the amount of Ni^{2+} relative to Fe^{2+} and Cr^{3+} in the near crack tip solution.

Anions. The nature and concentration of anions present within a crack can strongly affect the electrochemical processes occurring at and near the crack tip. These concepts are important because near the crack tip, the geometry becomes like that of an occluded cell (e.g., a crevice) where IR drop can cause a loss of potentiostatic control. In crevice geometries, high chloride content can lead to breakdown of the passive film⁵⁴⁻⁵⁵ and an increase in the activity coefficient for H^+ , thereby decreasing the pH at a given hydrogen ion concentration. Hydrogen ion concentration can also be increased at the crack tip by hydrolysis of cations (e.g., Cr^{3+}) after passive film rupture and alloy dissolution. Other species control the uptake of hydrogen produced by the reduction of protons and water, and thereby can affect the hydrogen embrittlement process.⁵⁶⁻⁶² Sulfur species, such as hydrogen sulfide, increase the efficiency with which atomic hydrogen enters a material from solution.⁶³⁻⁶⁵ For example, Iyer *et al.* found that hydrogen flux on iron was greatly increased in the presence of H_2S .⁶⁵ The addition of H_2S increased hydrogen surface coverage and the transfer coefficient and decreased the recombination constant.

In the present work, anion peaks were detected in the electropherographic analysis of solutions extracted from near the crack tip, but positive identification was accomplished only for chloride and recently for nitrate. In older samples, a peak was observed that migrated close to that of nitrate. This has not been confirmed because the small volume of the sample prevented re-analysis and the migration times differed from day to day due to experimental variables. However, the nature of the analysis allows several characteristics of species to be determined and compared with those of sulfur species. The unidentified species absorb strongly at 214 nm and have mobilities between nitrate and molybdate. These characteristics are consistent with sulfide and phosphate. No microstructural dependence of the unknown species has been established.

Segregation of sulfur and phosphorus, as well as other impurities, has been reported in Alloy 718,¹⁵ other nickel-base alloys^{16, 59, 60, 66}, and nickel.^{18, 19, 67-69} In Alloy 718-type alloys, segregation occurred for aging temperatures similar to those used in this work ($\sim 700^\circ\text{C}$).¹⁵ Thompson *et al.* reported that sulfur and phosphorus segregated to grain boundary surfaces when present as intentional additives.¹⁵ They also found that, when the sulfur level was low ($<0.01\%$), sulfur only segregated to carbide and Laves phase interfaces. MgS inclusions were found in Alloy 718 which contained 0.003% Mg and 0.003% S.⁷⁰ Dissolution of MnS inclusions in a low alloy steel containing 0.013% S was found to increase crack growth rate.⁷¹ In austenitic stainless steels, sulfide inclusions dissolve to form sulfide in occluded environments in chloride solutions, and alloy sulfur contents as low as 0.008 wt.% can lead to crevice corrosion due to the formation of sulfide.⁵⁵ The presence of sulfides or sulfur segregation has not been confirmed for Alloy 718 used in this study (0.002% S).

CONCLUSIONS

1. Sub-solvus solutionized and aged (Sub-STA) Alloy 718 is embrittled in acidic chloride solutions at all anodic and cathodic electrode potentials examined ($-0.2 V_{\text{SCE}}$ to $-1.0 V_{\text{SCE}}$). The precrack threshold stress intensity for EAC ($K_{\text{TH}} = 51$ to $63 \text{ MPa}\sqrt{\text{m}}$) is reduced from the fracture toughness, subcritical crack growth occurs albeit at slow rates (1-16 nm/s), and environment affects unique transgranular slip band cracks and intergranular facets rather than microvoiding.
2. Solutionized and aged (STA) Alloy 718 is embrittled in acidic chloride solutions at all electrode potentials examined ($-0.26 V_{\text{SCE}}$ to $-1.0 V_{\text{SCE}}$). The precrack threshold stress intensity for EAC ($K_{\text{TH}} = 47$ to $65 \text{ MPa}\sqrt{\text{m}}$) is reduced from K_{IC} , subcritical crack growth is slow (3-9 nm/s), and transgranular plus considerable intergranular cracking occurs.
3. STA Alloy 718 is more susceptible to embrittlement than the Sub-STA Alloy 718. The STA condition exhibits a lower K_{TH} and larger area fraction of intergranular cracking, but the Sub-STA condition has a faster maximum crack growth rate. The Sub-STA condition exhibits a maximum in EAC susceptibility at $-0.6 V_{\text{SCE}}$, while EAC

for STA Alloy 718 is most severe at $-0.8 V_{SCE}$ and $-1.0 V_{SCE}$. Impurity segregation, grain size, δ phase, or yield strength may play a role in the differences in susceptibility.

4. Aqueous embrittlement is consistent with H_2 embrittlement of Alloy 718 in terms of plane strain K_{TH} and fracture morphology. Crack growth rates are reduced from that reported in the literature, possibly due to hydrogen production kinetics or to loss of plane strain constraint in the small SEN specimen. Increased EAC resistance at $-1.0 V_{SCE}$ is speculatively traced to reduced hydrogen production at the crack tip due to alkalinity.
5. Ion analysis of the occluded crack solution supports dissolution of the alloy at the crack tip during active loading, even at cathodic potentials.
6. Crack growth in acidified chloride environments is enhanced by active crack-opening displacement loading and is reduced for static load. The beneficial effect may be due to increased crack tip passive film stability or reduced dislocation transport of hydrogen.

ACKNOWLEDGEMENTS

This research was supported by the Office of Naval Research (Grant N00014-91-J-4164), with A. John Sedriks as Scientific Monitor, a National Science Foundation Graduate Research Fellowship, and fellowship support from the University of Virginia. Equipment was generously provided by Waters Corporation (Jim Krol).

REFERENCES

1. R.P. Jewett, R.J. Walter, W.T. Chandler, R.P. Frohberg, "Hydrogen Environment Embrittlement of Metals," NASA, CR-2163, March 1973.
2. R.J. Walter, W.T. Chandler. *Mater. Sci. Eng.* 8 (1971): p. 90.
3. R.J. Walter, W.T. Chandler in Hydrogen in Metals, eds. I.M. Bernstein, A.W. Thompson (Metals Park, OH: ASM, 1974), pp. 515.
4. R.J. Walter, W.T. Chandler in Environmental Degradation of Engineering Materials, eds. M.R. Louthan, R.P. McNitt (Blacksburg, VA: VPI Press, 1977), pp. 513.
5. R.J. Walter, J.D. Frandsen, R.P. Jewett in Hydrogen Effects in Metals, eds. I.M. Bernstein, A.W. Thompson (Warrendale, PA: TMS/AIME, 1981), pp. 819.
6. P.D. Hicks, C.J. Altstetter in Superalloys 718, 625, and Various Derivatives, ed. E.A. Loria (Warrendale, PA: TMS/AIME, 1991), pp. 635.
7. N.R. Moody, F.A. Greulich, *Scripta Met.* 19 (1985): p. 1107.
8. N.R. Moody, R.E. Stoltz, M.W. Perra, *Metall. Trans. A*, 18A (1987): p. 1469.
9. N.R. Moody, M.W. Perra, S.L. Robinson, *Scripta Met.*, 22 (1988): p. 1261.
10. N.R. Moody, S.L. Robinson, J. W. M. Garrison, *Res. Mech.*, 30, 2 (1990): p. 143.
11. N.R. Moody, S.L. Robinson, M.W. Perra, *Engr. Fract. Mech.*, 39, 6 (1991): p. 941.
12. N.R. Moody, S.L. Robinson, M.W. Perra, "Internal Hydrogen Effects on Thresholds for Crack Growth in the Iron-based Superalloy IN903," Sandia Report, 90-8466, October 1991.
13. W.M. Garrison, N.R. Moody, *J. Phys. Chem. Solids*, 48, 11 (1987): p. 1035.
14. A.J. Sedriks, *Intl. Met. J.*, 101 (1973): p. 225.
15. R.G. Thompson, M.C. Koopman, B.H. King in Superalloys 718, 625 and Various Derivatives, ed. E.A. Loria (Warrendale, PA: TMS/AIME, 1991), p. 53.
16. G.A. Was, *Corr.*, 46, 4 (1990): p. 319.
17. R.M. Latanision, M. Kurkela, F. Lee in Hydrogen Effects in Metals, eds. I.M. Bernstein, A.W. Thompson (Warrendale, PA: TMS/AIME, 1981), p. 379.
18. R.H. Jones, S.M. Bruemmer, M.T. Thomas, D.R. Baer in Hydrogen Effects in Metals, eds. I.M. Bernstein, A.W. Thompson (Warrendale, PA: TMS/AIME, 1981), p. 369.

19. J. Eastman, T. Matsumoto, N. Narita, F. Heubaum, H.K. Birnbaum in Hydrogen Effects in Metals, eds. I.M. Bernstein, A.W. Thompson (Warrendale, PA: TMS/AIME, 1981), p. 397.
20. R.D. Kane, *Corr.*, 34, 12 (1978): p. 442.
21. C.-P. Wang, G.-P. Yu, J.H. Huang, "The Effects of Heat Treatment and Hydrogen on the SCC Behavior of Superalloy 718," *Corrosion / 96* (NACE, Houston, TX, 1996).
22. D. L. Dull, L. Raymond, *Metall. Trans.*, 4 (1973): p. 1635.
23. N.K. Sheth, B.C. Hendrix, H. Ide, J.M. Sanchez, M.T. Miglin in Microstructures and Mechanical Properties of Aging Material, eds. P.K. Liaw, R. Viswanathan, K.L. Murty, E.P. Simonen, D. Frear (Warrendale, PA: TMS, 1993), p. 493.
24. A. Oradei-Basile, J.F. Radavich in Superalloys 718, 625 and Various Derivatives, ed. E.A. Loria (Warrendale, PA: TMS/AIME, 1991), p. 325.
25. C.T. Sims, N.S. Stoloff, W.C. Hagel, Superalloys II (New York, NY: John Wiley & Sons, 1987), p. 615.
26. R.P. Gangloff, D.C. Slavik, R.S. Piascik, R.H. Van Stone in Small-Crack Test Methods, ASTM STP 1149, eds. J.M. Larsen, J.E. Allison (Philadelphia, PA: American Society for Testing and Materials, 1992), p. 116.
27. R.S. Piascik, "Mechanisms of Intrinsic Damage Localization During Corrosion Fatigue: Al-Li-Cu System," Ph.D. Dissertation, Department of Materials Science and Engineering, University of Virginia, Charlottesville, VA, 1989).
28. R.P. Gangloff, *Met. Trans. A*, 16A (1985): p. 953.
29. J.K. Donald, J. Ruschau in Fatigue Crack Measurement: Techniques and Applications, eds. K.J. Marsh, R.A. Smith, R.O. Ritchie (London: Chameleon Press Ltd., 1991), p. 11.
30. ASTM Standard E647-88a in 1989 Annual Book of ASTM Standards (Philadelphia, PA: American Society for Testing and Materials, 1989), p. 646.
31. H. Tada, P. Paris, G.I. Irwin in The Stress Analysis of Cracks Handbook, (St. Louis, MO: Del Research Corp., 1987), p. 210.
32. ASTM Standard E399-90 in Annual Book of ASTM Standards (Philadelphia, PA: ASTM, 1990), p. 506.
33. H.H. Johnson, *Matl. Res. and Std.*, 5, 9 (1965): p. 442.
34. P. Jandik, G. Bonn, Capillary Electrophoresis of Small Molecules and Ions (New York, NY: VCH Publishers, Inc., 1993), p. 298.
35. D.D. Krueger, "Effects of Grain Size and Precipitate Size on the Fatigue Crack Growth Behavior of Alloy 718 at 427C," Master's Thesis, Department of Metallurgical Engineering, University of Cincinnati, Cincinnati, OH, 1984).
36. C. Loier, M.C. Ottmann, C. Leymonie, *Mat. Sci. Eng.*, 63 (1984): p. 91.
37. K. Sadananda, P. Shaninian, "Effect of Heat Treatment on High Temperature Crack Growth Under Static Load in Alloy 718," Naval Research Laboratory, Report #3727, 1978.
38. M.G. Stout, W.W. Gerberich, *Metall. Trans. A*, 9A (1978): p. 649.
39. D. Fournier, A. Pineau, *Metall. Trans. A*, 8A (1977): p. 1095.
40. M.J. Haynes, R.P. Gangloff, *Metall. Trans. A*, submitted for publication, 1996.
41. W.J. Mills, L.D. Blackburn, "Fracture Toughness Variations in Alloy 718," Hanford Eng. Dev. Lab., Report #HEDL-TME 82-28, April 1983.
42. D.L. Dull, L. Raymond in Hydrogen Embrittlement Testing, ASTM STP 543 (Philadelphia, PA: ASTM, 1974), p. 20.
43. P.W. Rice, *Mat. Performance*, 17, 11 (1978): p. 16.
44. D.G. Kolman, "Passivity and Bare Surface Electrode Kinetics on Beta-Titanium Alloys in Aqueous Chloride Solutions and Their Relevancy to EAC," Ph.D. Dissertation, Department of Materials Science and Engineering, University of Virginia, Charlottesville, VA, 1996).
45. W.M. Robertson, *Metall. Trans. A*, 8A (1977): p. 1709.
46. B.P. Somerday, J.A. Grandle, R.P. Gangloff in Tri-Service Conference on Corrosion (Materials Laboratory, Wright Patterson Air Force Base, OH, 1994): p. 375.
47. L.M. Young, G.A. Young, J.R. Scully, R.P. Gangloff, *Met. and Mat. Trans. A*, 26A (1995): p. 1257.
48. M.J. Blackburn, J.A. Feeney, T.R. Beck in Advances in Corrosion Science and Technology eds. M.G. Fontana, R.W. Staehle (New York, NY: Plenum Press, 1972): p. 67.
49. D.G. Kolman, J.R. Scully, *J. Electrochem. Soc.*, 143 (1996): p. 1847.
50. R.P. Gangloff in Corrosion Prevention and Control, eds. M. Levy, S. Isserow (Watertown, MA: U.S. Army Materials Technology Laboratory, 1986): p. 64.

51. N.R. Moody, W.W. Gerberich, *Metall. Trans. A*, 13A (1982): p. 1055.
52. N.R. Moody, R.E. Stoltz, M.W. Perra in Corrosion Cracking ed. V.S. Goel (Metals Park, OH: ASM Int'l., 1986): p. 43.
53. H.S. Isaacs, J.-H. Cho, *J. Electrochem. Soc.*, 142 (1995): p. 1111.
54. N.D. Greene, G. Judd, *Corr.*, 21 (1965): p. 15.
55. C.S. Brossia, R.G. Kelly in Critical Factors in Localized Corrosion II (Pennington, NJ: Electrochemical Society, Inc., 1996): p. 201.
56. G.E. Kerns, R.W. Staehle, *Scripta Met.*, 6 (1972): p. 631.
57. E.P. Whelan in Hydrogen Effects in Metals, eds. I.M. Bernstein, A.W. Thompson (Warrendale, PA: TMS/AIME, 1981): p. 979.
58. R.D. Kane, *Intl. Met. Rev.*, 30, 6 (1985): p. 291.
59. R.H. Jones, S.M. Brummer in Environment-Induced Cracking of Metals, eds. R.P. Gangloff, M.B. Ives (Houston, TX: NACE, 1990): p. 287.
60. J. Kolts, N.Sridhar in Corrosion of Nickel-Base Alloys, ed. R.C. Scarberry (Metals Park, OH: ASM Int'l., 1985): p. 199.
61. J. Kolts, C.C. Burnette, M.W. Joosten in Environment-Induced Cracking of Metals, eds. R.P. Gangloff, M.B. Ives (Houston, TX: NACE, 1990): p. 401.
62. S.L. Robinson, N.R. Moody, S.M. Myers, J.C. Farmer, F.A. Greulich, *J. Electrochem. Soc.*, 137, 5 (1990): p. 1391.
63. R.D. McCright in Stress Corrosion Cracking and Hydrogen Embrittlement of Iron, eds. R.W. Staehle, J. Hochman, R.D. McCright, J.E. Slater (Houston, TX: NACE, 1977): p. 306.
64. M. Smialowski, Hydrogen in Steel (Reading, MA: Pergamon Press, 1962).
65. R.N. Iyer, I. Takeuchi, M. Zamanzadeh, H.W. Pickering, *Corr.*, 46, 6 (1990): p. 460.
66. G.P. Airey in Environment-Sensitive Fracture of Engineering Materials, ed. Z.A. Foroulis (Warrendale, PA: TMS/AIME, 1979): p. 205.
67. R.M. Latanision, J. H. Oppenhausser in Hydrogen in Metals, eds. I.M. Bernstein, A.W. Thompson (Metals Park, OH: ASM, 1974): p. 539.
68. R.M. Latanision, J. H. Oppenhausser, *Metall. Trans.*, 5 (1974): p. 483.
69. T.S.F. Lee, R.M. Latanision, *Metall. Trans. A*, 18A (1987): p. 1653.
70. S.L. Cockcroft, T. Degawa, A. Mitchell, D.W. Tripp, A. Schmalz in Superalloys 1992, eds. D.L. Anton, T. Khan, R.D. Kissinger, D.L. Klarstrom (Warrendale, PA: TMS, 1992): p. 577.
71. P.L. Andresen, L.M. Young, *Corr.*, 51, 3 (1995): p. 223.

Table 1. Composition of Alloy 718 used in EAC studies (weight %)

UNS N07718	Ni	Cr	Fe	Mo	Nb	Ti	Al	C	P	S
wt%	53.9	18.3	18.1	3.0	5.1	1.0	0.5	0.1	0.006	<.002

Table 2. Air Tensile and Fracture Properties of Alloy 718

UNS 07718	$\sigma_{YS, 0.2\%}$ (MPa)	σ_{UTS} (MPa)	% R.A.	No. Tests	K_{IC} (MPa \sqrt{m})	Grain Diameter (μm)
Sub-STA	988	1319	50	2	81	20
STA	840	1152	56	2	85	60

Table 3. Relative Concentrations of Crack Solution Samples for Sub-STA Alloy 718 in 0.4 M H₂SO₄ + 1 M NaCl

	Potential	Ni	Fe	Cr	Na, (Ni+Fe+Cr)
Alloy 718	--	60%	20%	20%	--
Sub-STA*	-0.6 & -1.0 V _{SCE}	51%	38%	11%	39%, 61%
Sub-STA*	-0.6 & -0.2 V _{SCE}	51%	34%	15%	20%, 80%
Sub-STA	-0.2 V _{SCE}	53%	34%	13%	92%, 8%

*The EAC crack was grown at two electrode potentials prior to solution sampling; however, most of the crack growth occurred at -0.6 V_{SCE}.

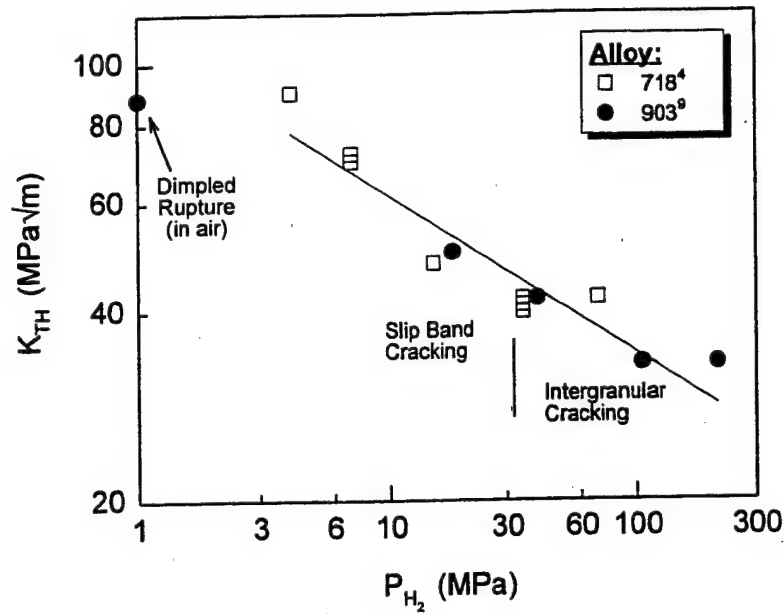


Figure 1. Literature data show that K_{TH} for the hydrogen embrittlement of two precipitation-hardened superalloys decreases with increasing H_2 pressure.^{4,9}

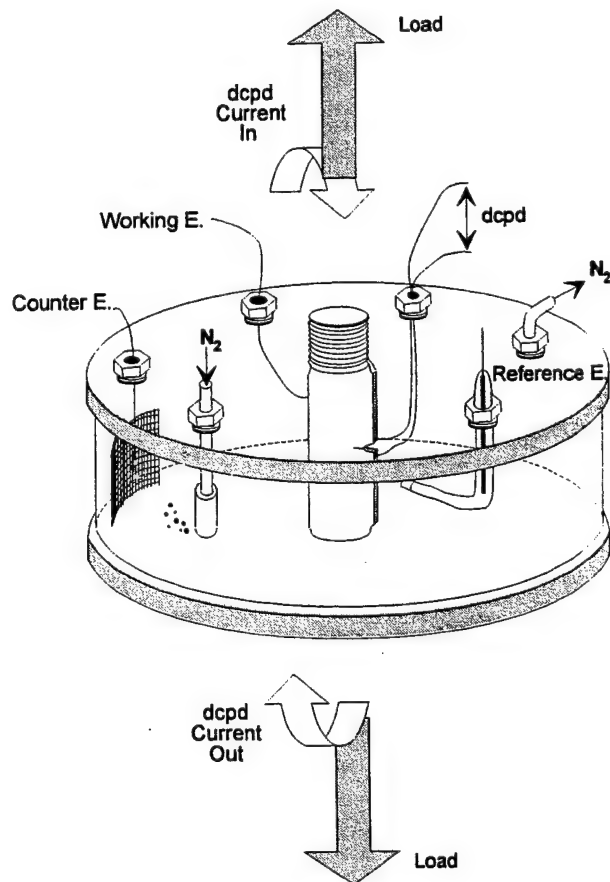


Figure 2. Schematic of the SEN specimen and cell used for aqueous EAC testing.

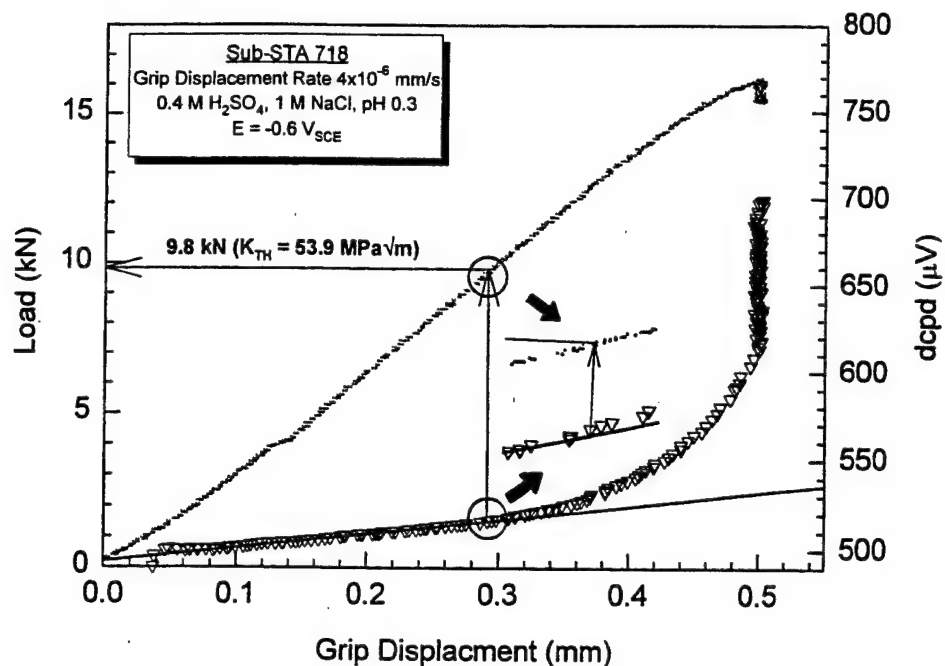


Figure 3. Typical graph of load and dcpd signal as a function of grip displacement. The method for defining K_{TH} is illustrated.

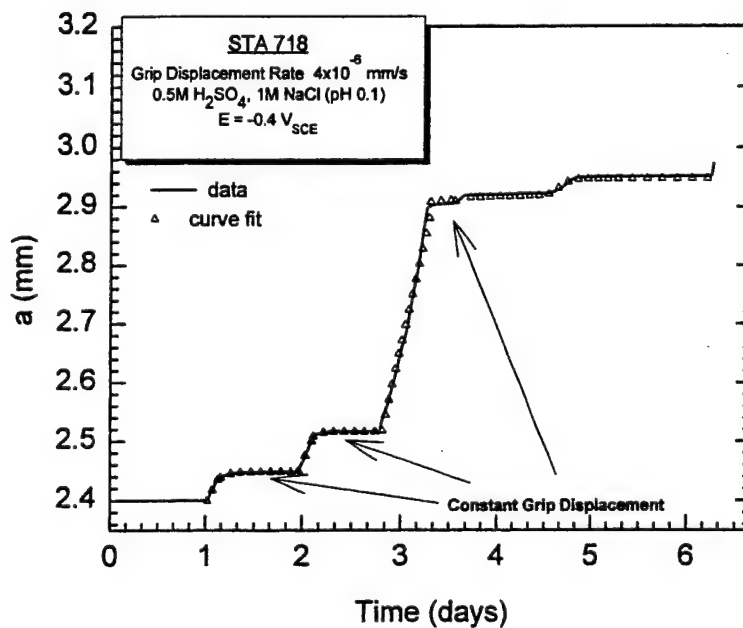


Figure 4. Typical plot of crack length as a function of time for an EAC test with the curve fit superimposed. Note that EAC was produced for both rising and fixed grip displacement conditions.

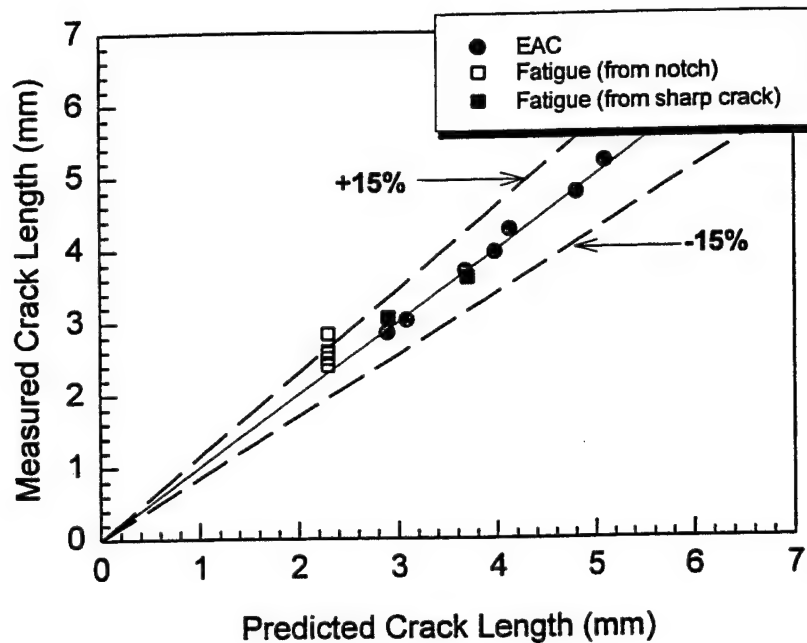


Figure 5. Comparison of optically-measured and dcpd-predicted crack lengths for EAC and fatigue tests. The solid line represents the condition where calculated and measured crack lengths are equal, and dashed lines show a +/- 15% error.

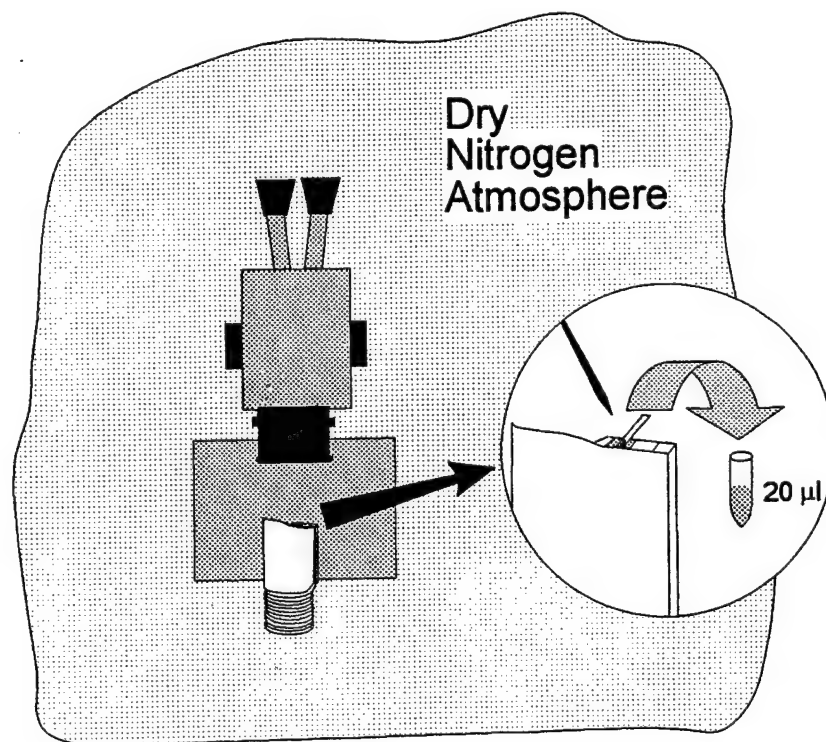


Figure 6. A nitrogen-filled glove bag and stereo-microscope were used to sample the solution from the environmental crack surface.

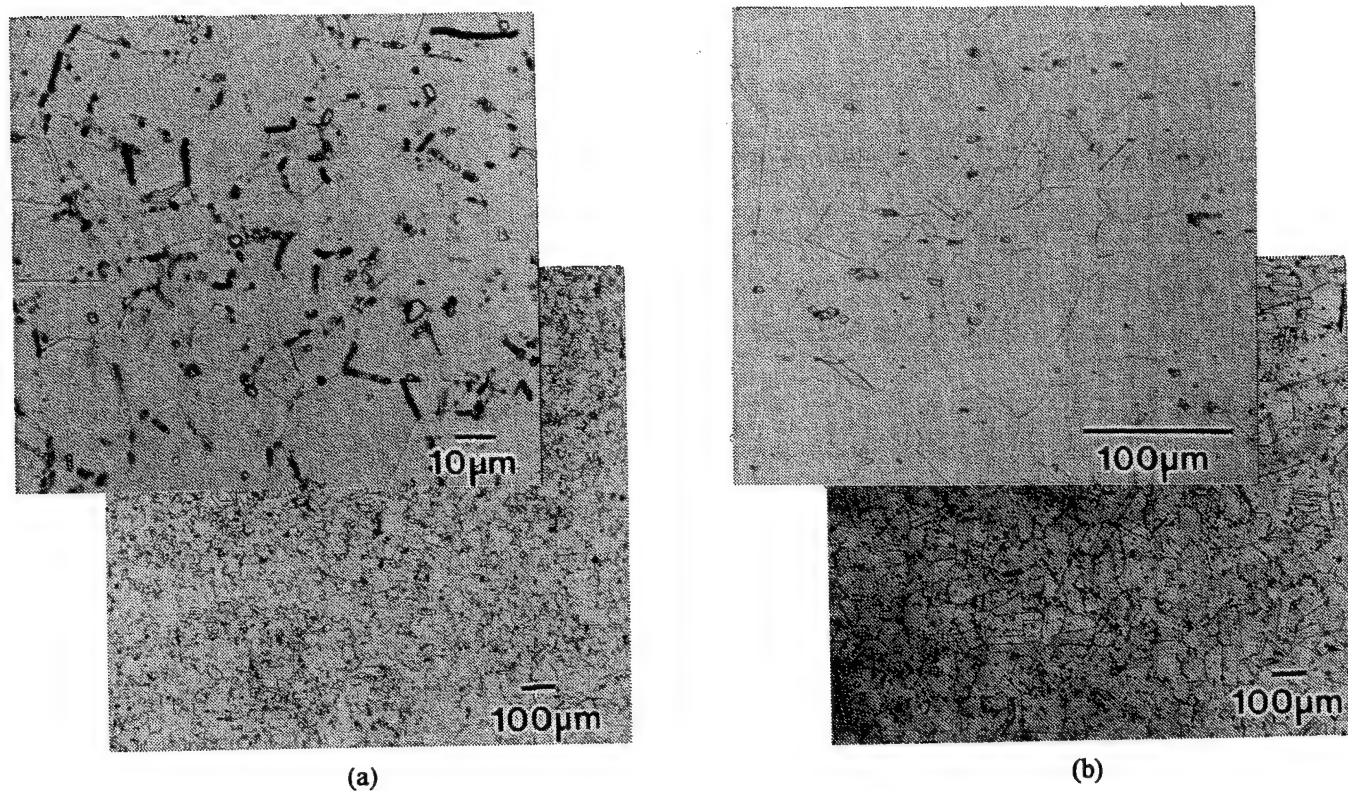


Figure 7. Optical micrographs of (a) Sub-STA and (b) STA grain microstructures. Etchant: 90 ml HCl, 5 ml H₂SO₄, 3 ml HNO₃.

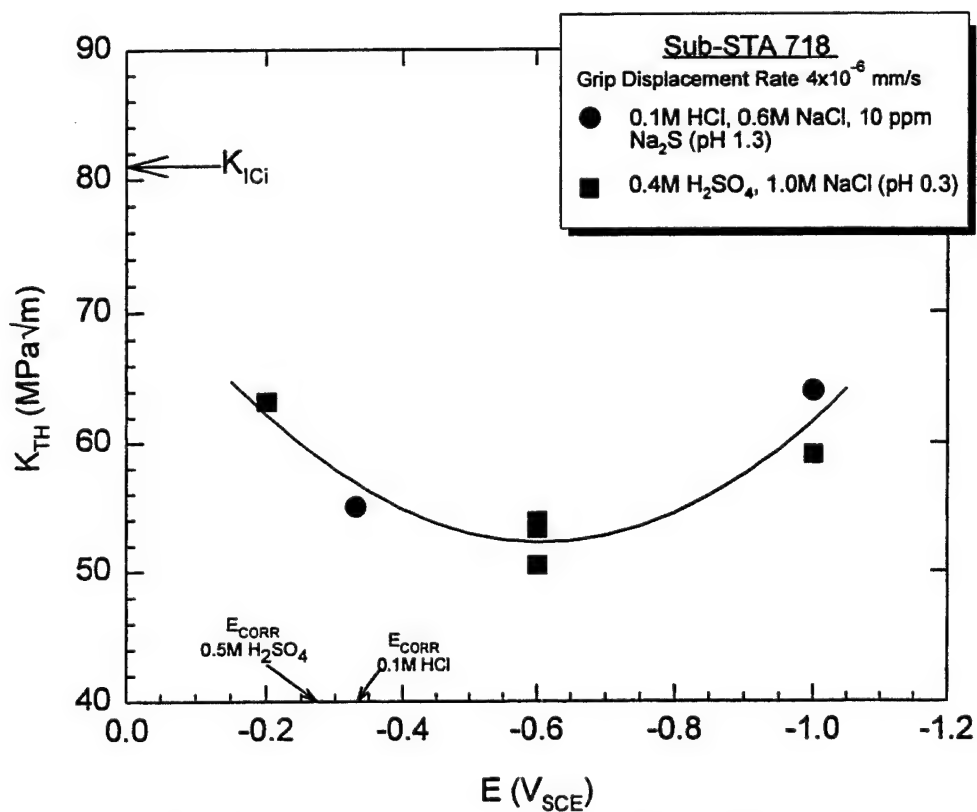


Figure 8. K_{TH} as a function of applied polarization for the Sub-STA condition of Alloy 718 in two acidified chloride solutions.

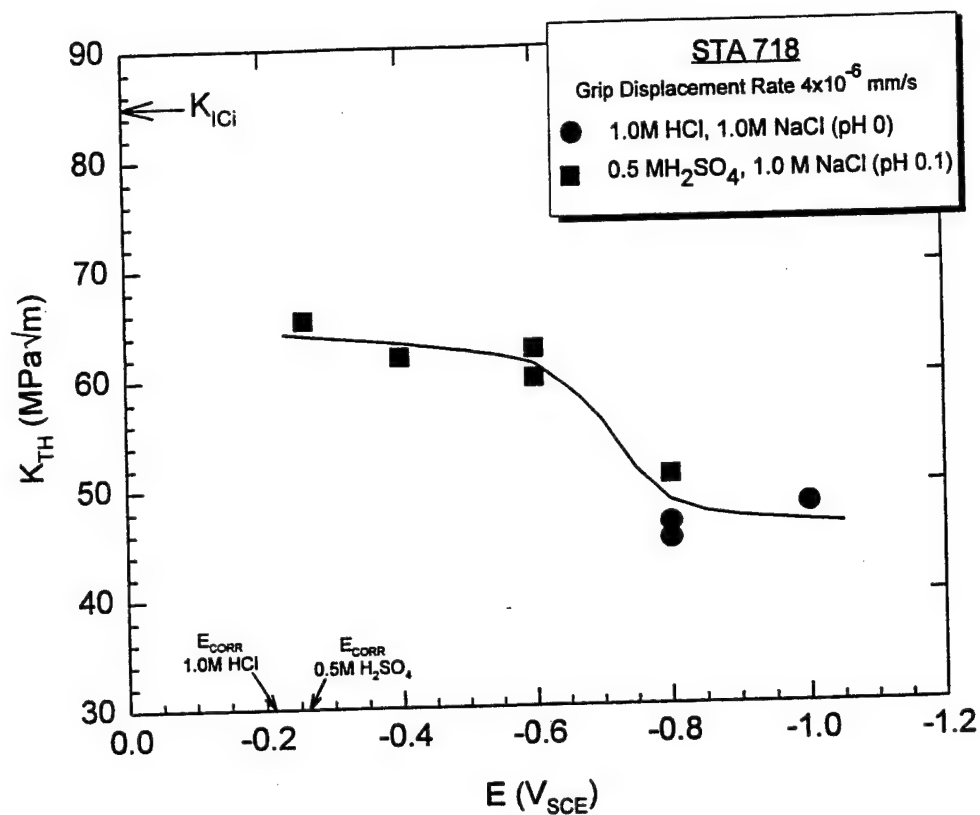


Figure 9. K_{TH} as a function of applied polarization for the STA condition of Alloy 718 in two acidified chloride solutions.

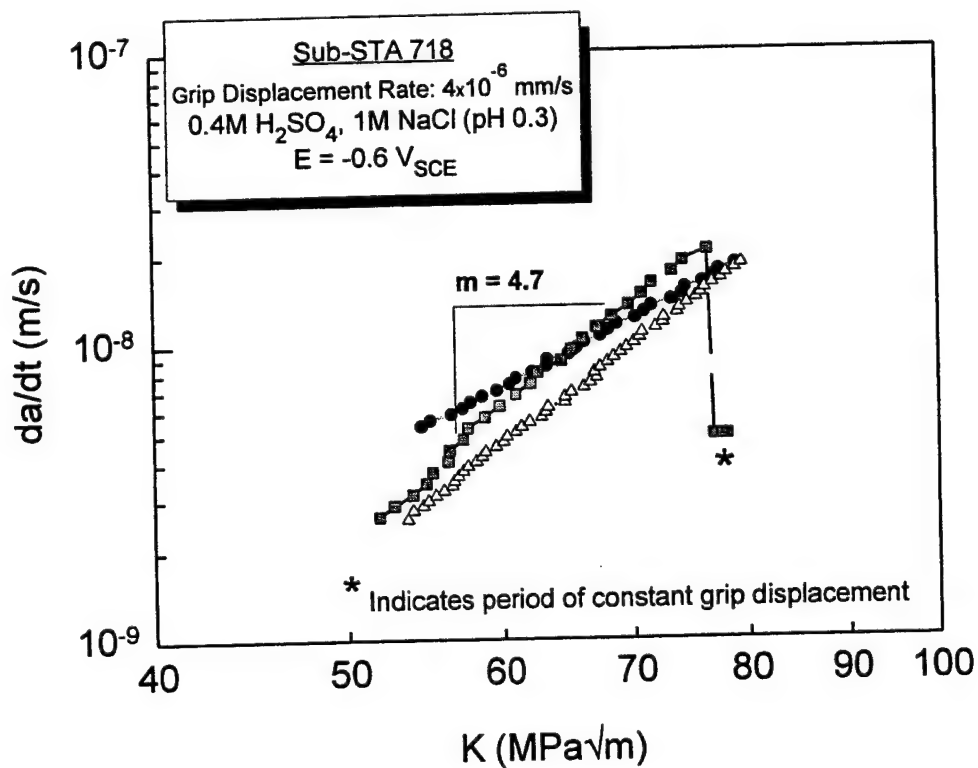


Figure 10. Da/dt as a function of K for three replicate EAC tests of the Sub-STA condition of Alloy 718 stressed in an acidified sulfate-chloride solution.

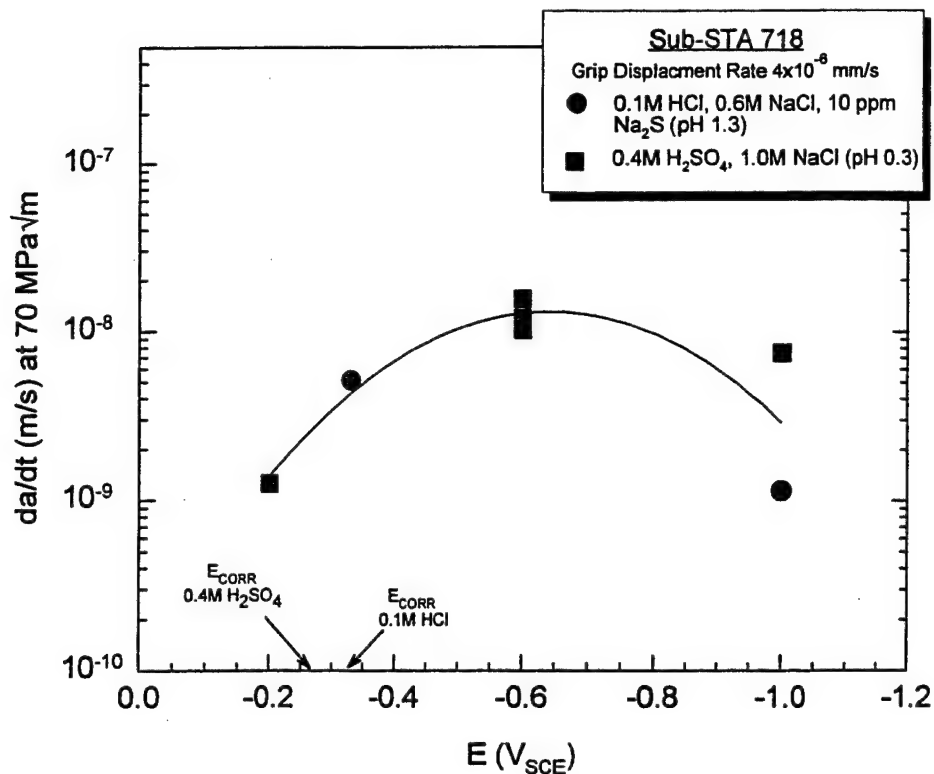


Figure 11. Da/dt at a K level of $70 \text{ MPa}\sqrt{\text{m}}$ as a function of applied polarization for the Sub-STA condition of Alloy 718 subjected to actively rising displacement in two acidified chloride solutions.

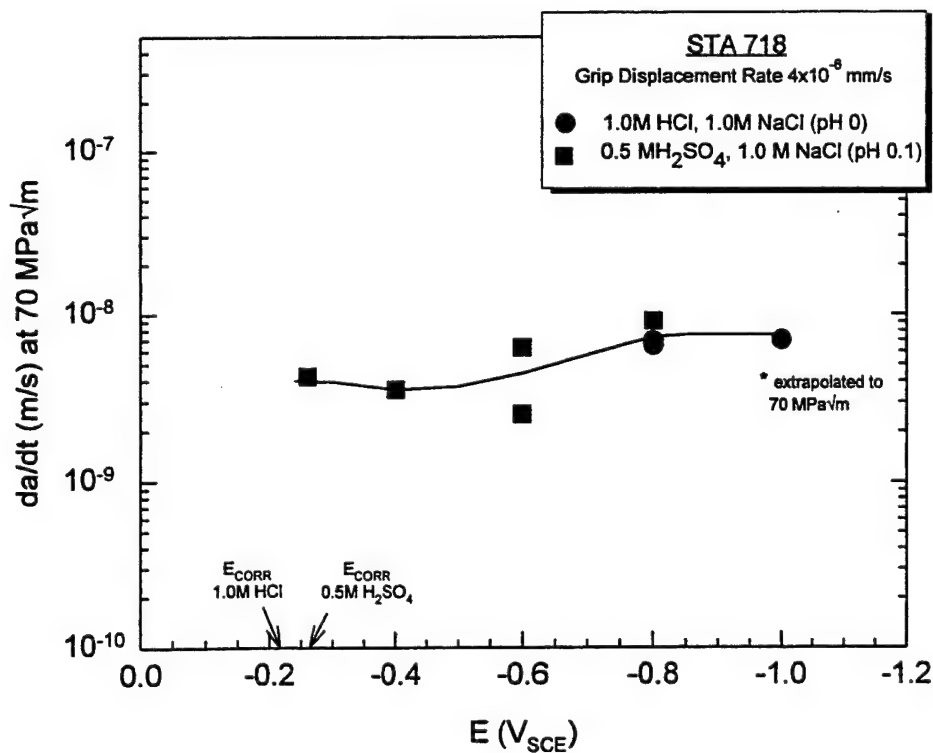
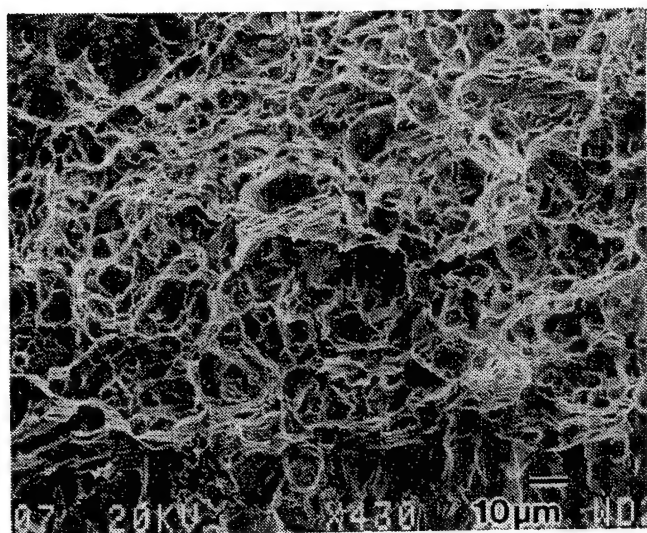
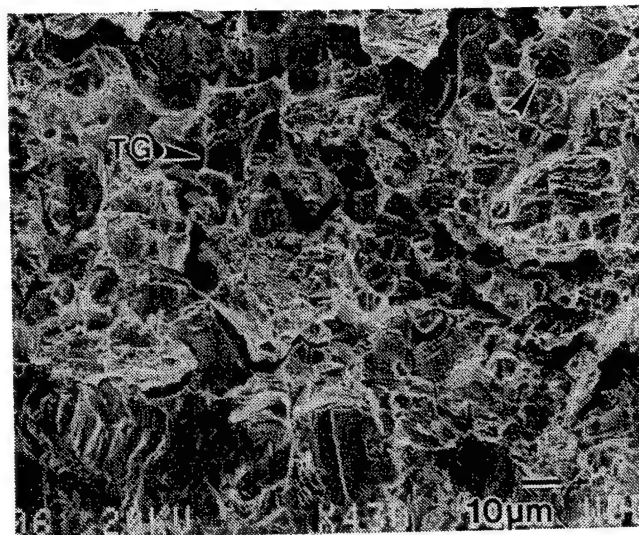


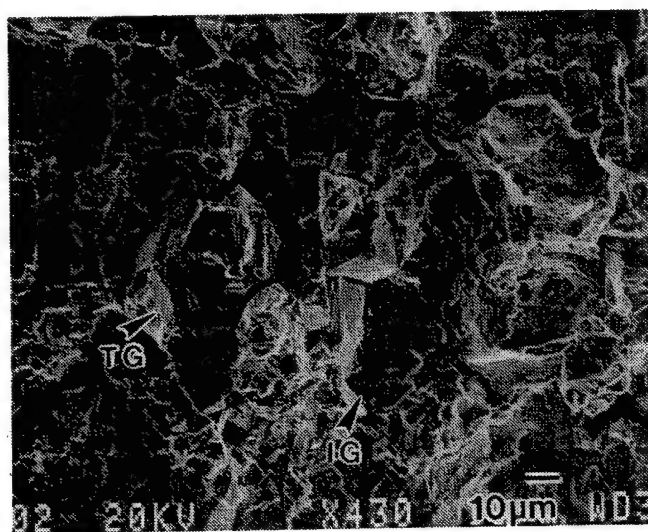
Figure 12. Da/dt at a K level of $70 \text{ MPa}\sqrt{\text{m}}$ as a function of applied polarization for the STA condition subjected to actively rising displacement in two acidified chloride solutions.



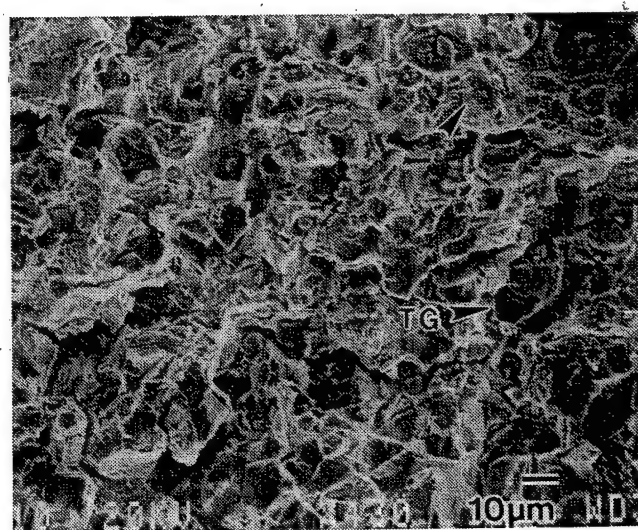
a) Air



b) E_{CORR} ($-0.33 V_{SCE}$; 0.1 M HCl+0.6 M NaCl+10 ppm Na_2S)

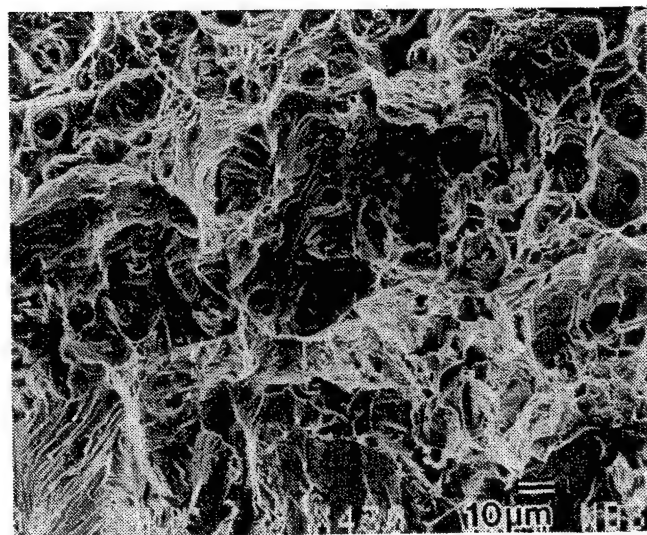


c) $-0.6 V_{SCE}$ (0.4 M H_2SO_4 + 1.0 M NaCl)

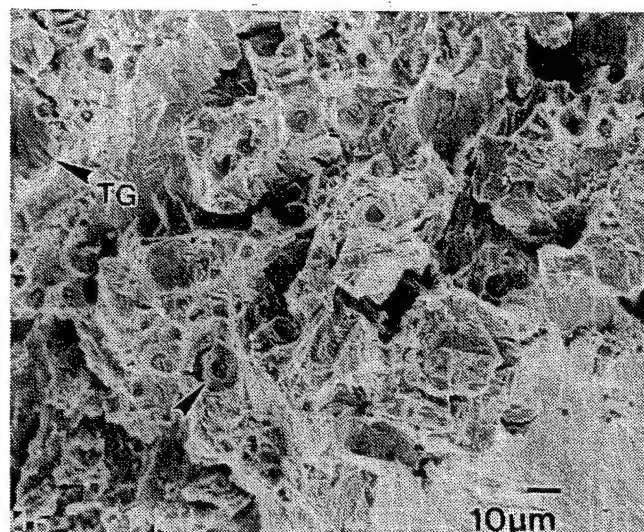


d) $-1.0 V_{SCE}$ (0.1 M HCl + 0.6 M NaCl + 10 ppm Na_2S)

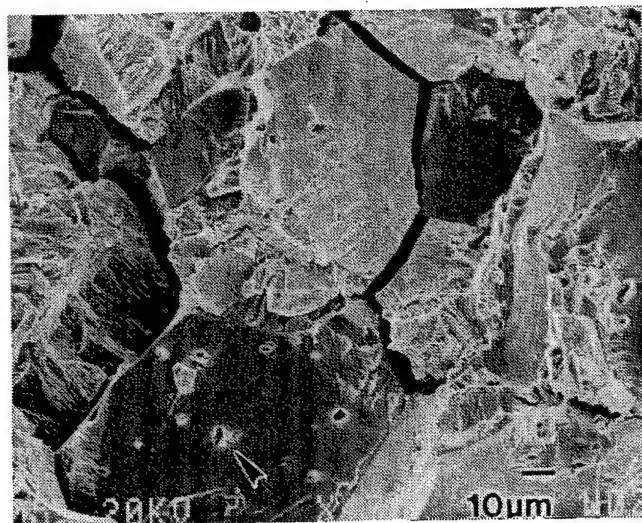
Figure 13. Scanning electron fractographs of the fracture surface of Sub-STA Alloy 718 in various environments. The crack grew from the bottom to the top of the page. The arrows show carbides and transgranular and intergranular facets.



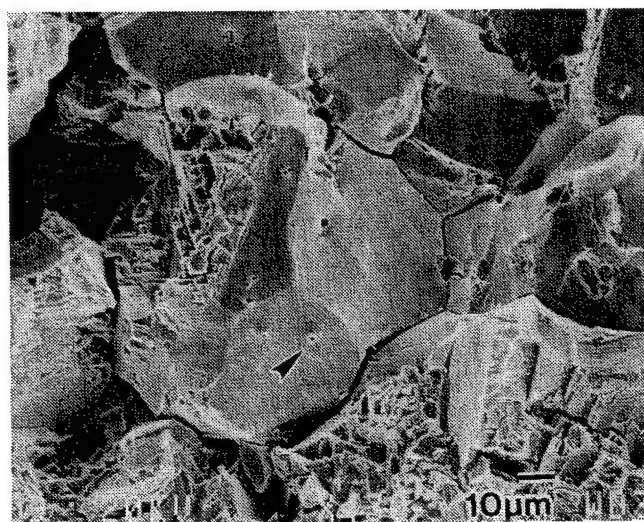
a) Air



b) $-0.4 V_{SCE}$ (0.5 M H_2SO_4 + 1.0 M NaCl)



c) $-0.8 V_{SCE}$ (0.5 M H_2SO_4 + 1.0 M NaCl)



d) $-0.8 V_{SCE}$ (1.0 M HCl + 1.0 M NaCl)

Figure 14. Scanning electron fractographs of the fracture surface of STA Alloy 718 in various environments. The crack grew from the bottom to the top of the page. The arrows show carbides and transgranular facets as well as small particles and dimples on intergranular facets.

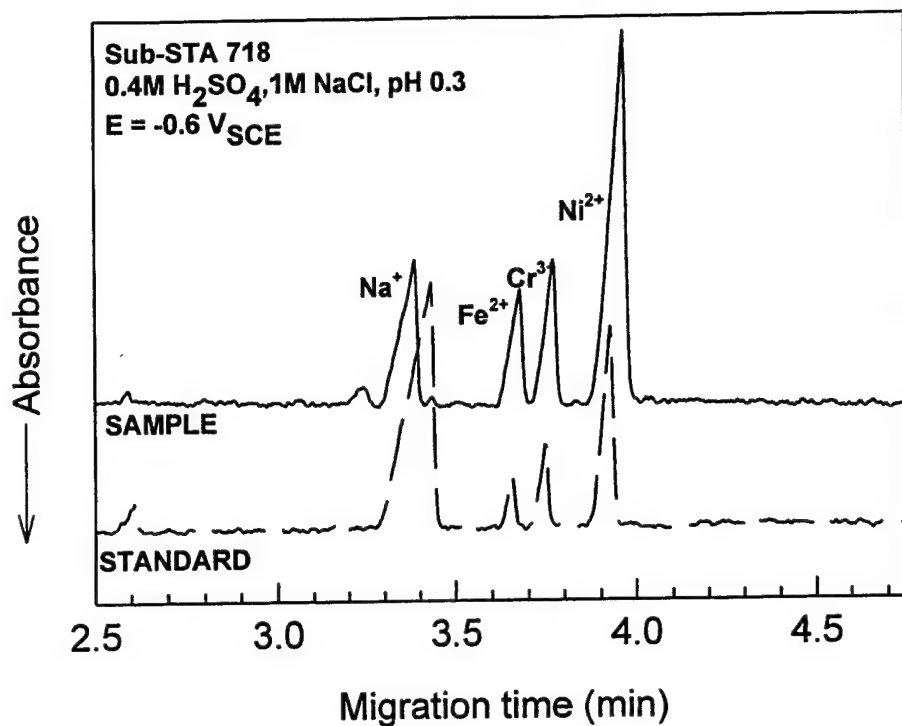


Figure 15. Electropherogram of cation species in the crack sample from Sub-STA Alloy 718 in acidified sulfate-chloride solution compared to a known standard.

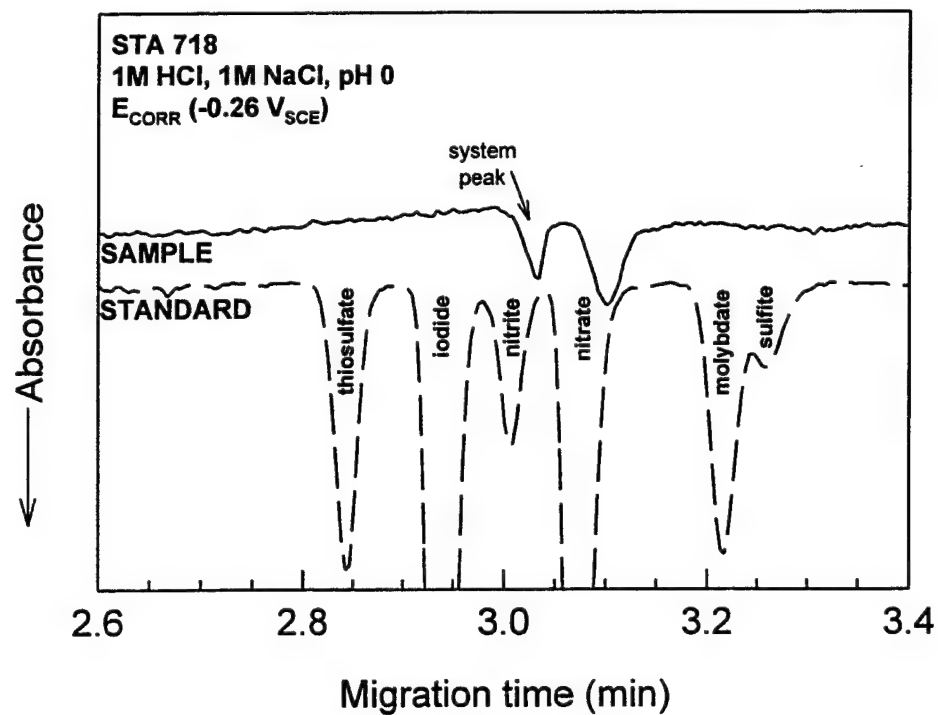


Figure 16. Electropherogram of anion species in the crack sample from STA Alloy 718 in acidified sulfate-chloride solution compared to a known standard.

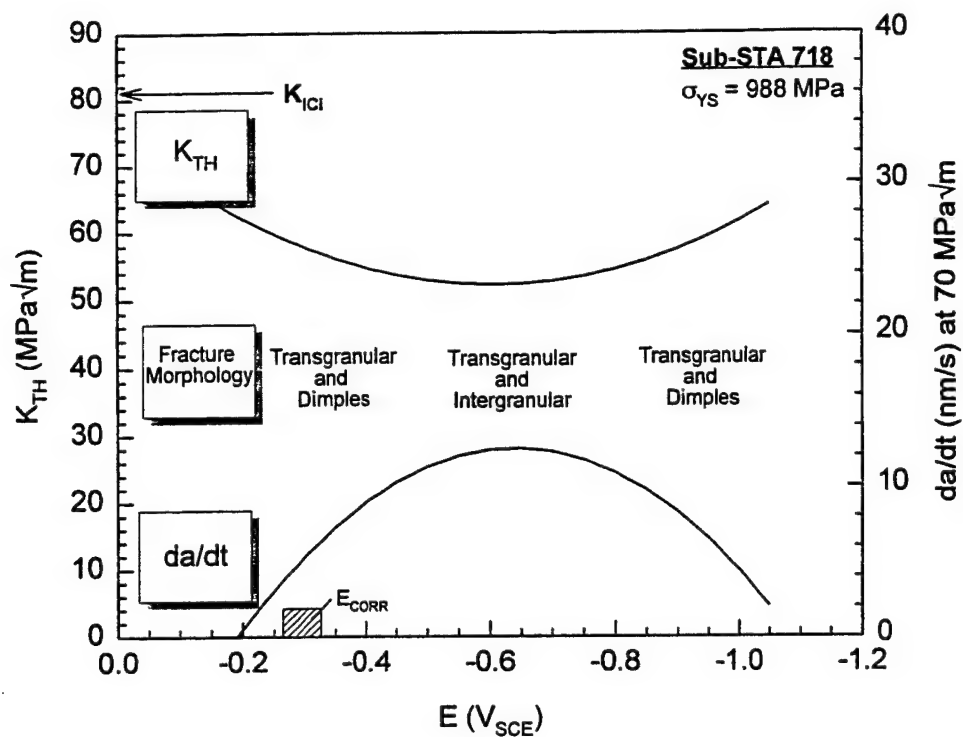


Figure 17. Summary of EAC behavior as a function of applied polarization for the Sub-STA condition of Alloy 718 loaded actively in acidified solution.

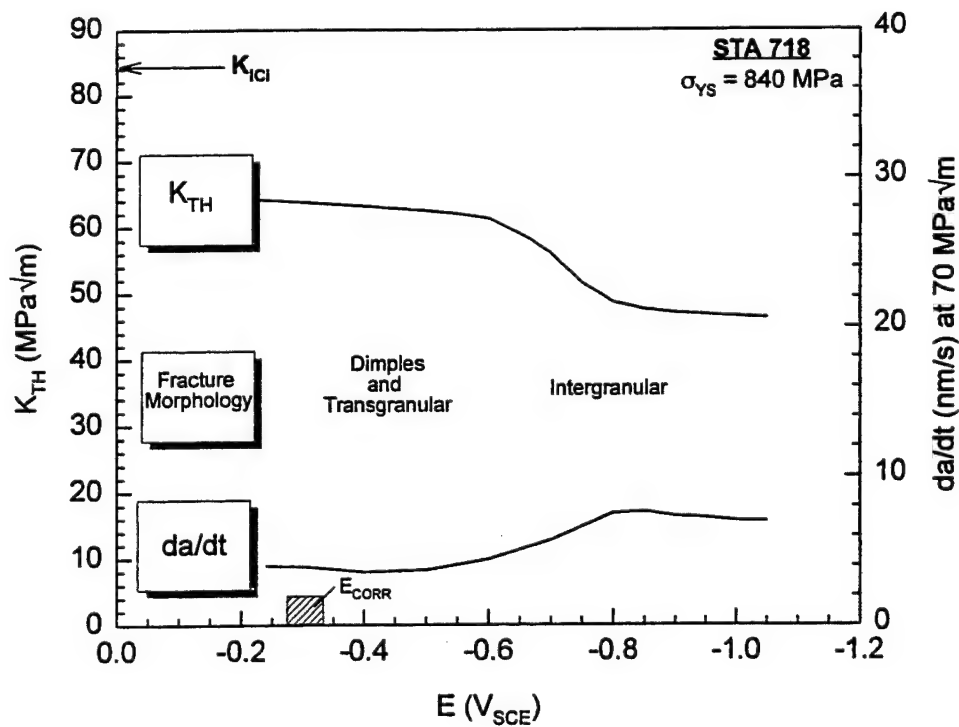


Figure 18. Summary of EAC behavior as a function of applied polarization for the STA condition of Alloy 718 loaded actively in acidified solution.

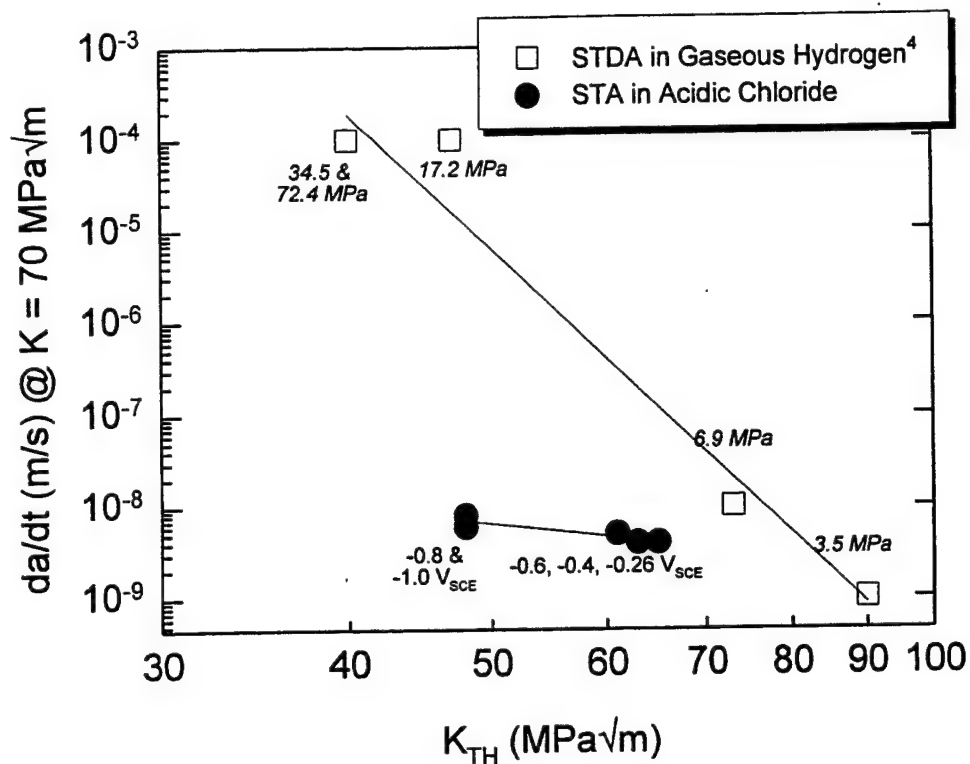


Figure 19. Comparison of Alloy 718 crack growth rate in acidified chloride solution and gaseous hydrogen⁴ subjected to actively rising displacement at 70 MPa√m. The yield strengths of these heat treatments are STDA = 1300 MPa and STA = 840 MPa.

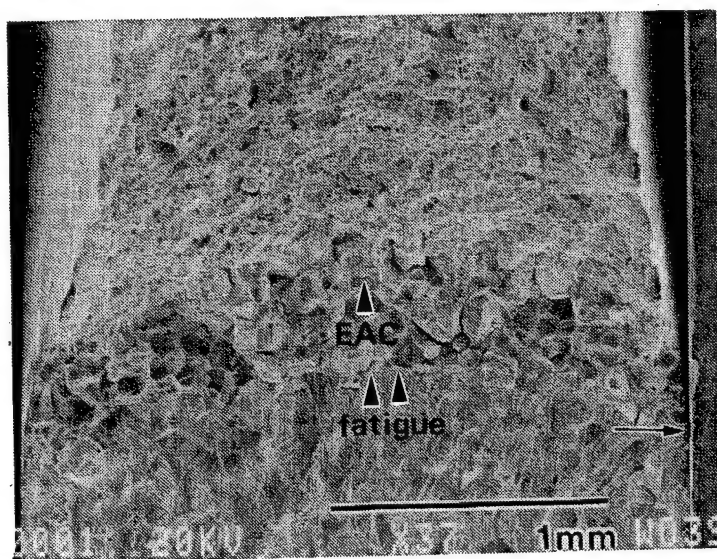


Figure 20. Scanning electron micrograph of an STA 718 fracture surface. The fatigue, EAC, and ductile regions are visible. A horizontal arrow indicates the beginning of shear wall formation.

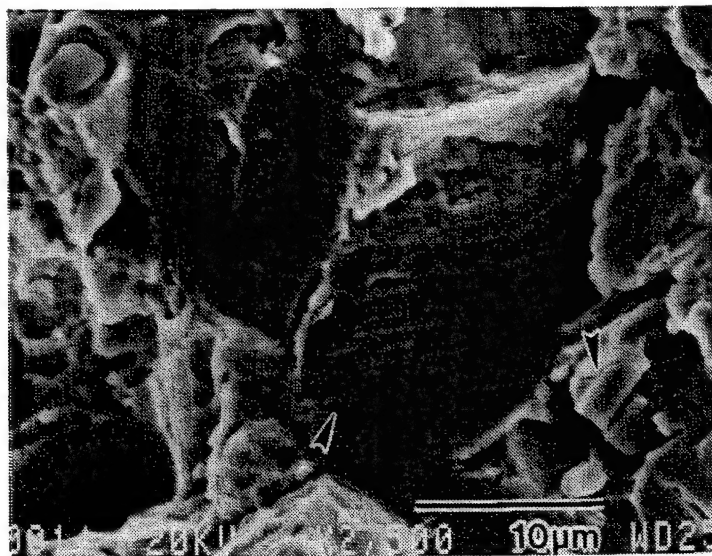
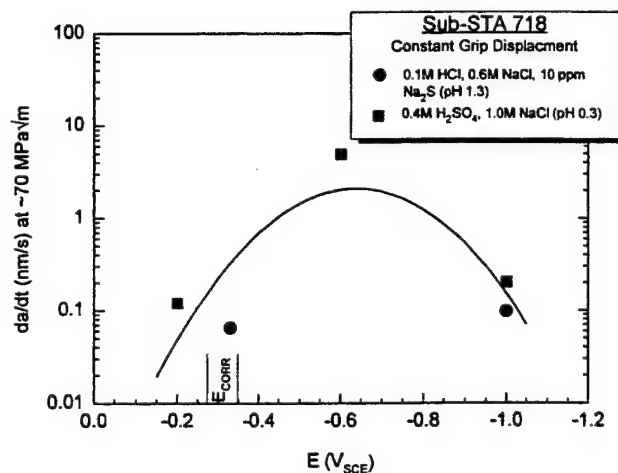
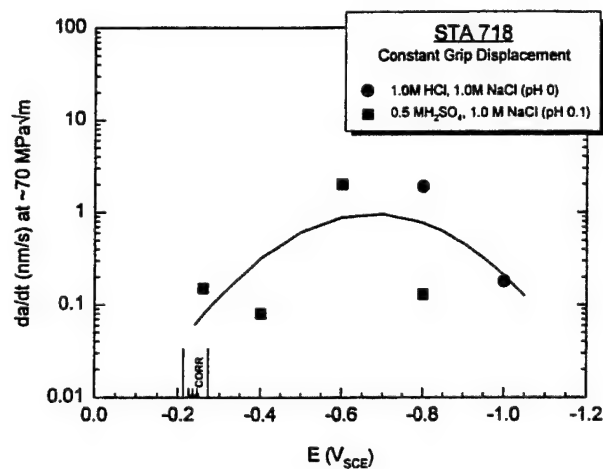


Figure 21. Scanning electron micrograph of a transgranular facet in Sub-STA Alloy 718 loaded actively in 0.1 M HCl + 0.6 M NaCl + 10 ppm Na_2S at E_{CORR} ($-0.33 \text{ V}_{\text{SCE}}$).



(a)



(b)

Figure 22. Da/dt at a K level near $70 \text{ MPa}\sqrt{\text{m}}$ as a function of applied polarization for the (a) Sub-STA and (b) STA condition of Alloy 718 subjected to constant grip displacement in two acidified chloride solutions.

**Effects of Yield Strength and Microstructure on Environment-Assisted
Cracking of Ti-3Al-8V-6Cr-4Mo-4Zr in Aqueous NaCl**

B. P. Somerday and R. P. Gangloff

Effects of Yield Strength and Microstructure on Environment-Assisted Cracking of Ti-3Al-8V-6Cr-4Mo-4Zr in Aqueous NaCl

B.P. Somerday and R.P. Gangloff

ABSTRACT

The objective of this research is to isolate the effects of σ_{YS} and α -precipitate microstructure on the EAC susceptibility of a high-strength β -Ti alloy, Ti-3Al-8V-6Cr-4Mo-4Zr (Beta-C), in aqueous NaCl at fixed electrode potential under active loading. Aging renders immune solution-treated Beta-C susceptible to severe EAC. The threshold for EAC is 40% of K_{ICi} , subcritical crack growth rates approach 100 $\mu\text{m/s}$, and the crack path is fully intergranular in microstructures aged longer than 7 h. Short-term-aged microstructures of Beta-C crack by IG separation in aqueous NaCl, but only under increased crack tip strain rate. The σ_{YS} increase due to α precipitation does not promote EAC susceptibility. Solution treated and cold worked Beta-C retains immunity to EAC for high σ_{YS} . For several levels of cold work, fracture of ST/CW Beta-C is by TG microvoid processes, with K_{TH} equaling K_{ICi} . Cold work reduces the air fracture toughness of ST Beta-C below levels for ST/A microstructures at similar σ_{YS} . Two explanations for the deleterious effect of aging on IG EAC susceptibility are eliminated. Neither grain boundary α precipitates nor intragranular planar slip bands are present in sufficient number to explain the fully IG crack path and severe EAC in ST/A Beta-C. Fractography features are consistent with decohesion due to H and elemental segregation stimulated by aging.

INTRODUCTION

Beta-titanium alloys, age hardened by α precipitation, are susceptible to severe intergranular (IG) environment-assisted cracking (EAC) in aqueous halide solutions at 25°C [1,2,3,4,5]. Hydrogen embrittlement (HE) is implicated as the cracking mechanism [2,6]. The intrinsic mechanical and metallurgical properties of high-strength β -Ti alloys that promote IG EAC have not been determined; however, the following variables may be important:

Yield strength (σ_{YS}). Increased σ_{YS} promotes EAC of steels and Ni-based superalloys, particularly for cases of HE [7]. Results suggest a similar deleterious effect of increased σ_{YS} for EAC of β -Ti alloys [3,4,8], but experiments are limited.

Alpha phase. Solution treated (ST) Ti-3Al-8V-6Cr-4Mo-4Zr (Beta-C), Ti-11.5Mo-6Zr-4.5Sn (Beta III) and Ti-8Mo-8V-3Al-2Fe (Ti-8-8-3-2) with a single-phase β microstructure are immune to EAC in aqueous NaCl, but become susceptible upon aging to precipitate the α phase [1,3]. The effect of aging time and α precipitation on EAC resistance has not been established.

Composition. The solution treated and aged (ST/A) alloys Ti-15V-3Cr-3Al-3Sn (Ti-15-3) and Ti-11.6Mo with a β/α microstructure are immune to EAC in aqueous halide solutions, and have different compositions compared to susceptible alloys such as Beta-C [1,2,5,9,10].

Deformation Mode. Heterogeneous planar slip is suggested to control the EAC susceptibility of ST/A Ti-15Mo-3Nb-3Al (Beta-21S), compared to immune ST/A Ti-15-3 which exhibits homogeneous wavy slip [2,11].

It is difficult to establish the factors that govern EAC by comparing immune and susceptible alloys because multiple properties are different. For example, comparing the EAC-immune ST and susceptible ST/A conditions is not informative because the latter condition has both increased σ_{YS} and precipitated α compared to the former [1].

The yield strength effect on EAC can be isolated because σ_{YS} for the immune ST alloy is increased readily by strain hardening. This procedure retains the single-phase β microstructure without precipitation of α , and does not vary composition. Although strain hardening may affect deformation mode, it is unlikely that this property alone promotes EAC; ω -strengthened β -Ti alloys

exhibit intense planar slip [12,13], but are immune to EAC in aqueous halides [3,5]. The effect of cold work on the EAC resistance of ST β -Ti alloys has not been investigated. Apart from EAC-mechanistic considerations, this dependence is important for applications involving localized or extensive cold-worked microstructures.

Determination of metallurgical effects is further complicated by the large number of variables that influence IG EAC in aqueous halide solutions. Previous studies demonstrate important effects of electrode potential [1-4], crack/stress state configuration [3,14], and loading rate [3,5,9,10,15,16] on EAC susceptibility of β/α and α/β Ti alloys. The windows of these extrinsic variables which promote EAC may depend on the specific alloy condition. Interpretation of EAC experiments designed to probe metallurgical variables must recognize this complication.

The objective of this work is to isolate the effects of σ_{YS} and metallurgical variables on the EAC susceptibility of ST/A β -Ti alloys in aqueous NaCl. The ST alloy Beta-C is cold worked to produce a range of σ_{YS} without precipitating α , and alternately subjected to isothermal heat treatment for increasing times to produce α and a wide range of σ_{YS} levels similar to the cold-worked case. Precracked specimens are tested in aqueous NaCl at fixed electrode potential under a constant rising displacement rate. The effect of crack tip strain rate on the governing metallurgical factors is considered elsewhere [17].

EXPERIMENTAL PROCEDURES

Material

The alloy studied was Beta-C with a composition of Ti-3.4 Al-8.3 V-5.9 Cr-4.1 Mo-4.4 Zr (wt pct), as specified by the manufacturer, RMI Titanium Company. The product form was hot-rolled 41-mm-diameter round bar that was solution heat treated at 815°C for 1 h and air cooled to room temperature (ST condition). The resulting microstructure consisted of single-phase β grains, equiaxed and 80 μm in size [18].

The yield strength of ST Beta-C was increased by two different means. First, ST Beta-C was cold worked to reductions between 20% and 65% (ST/CW condition). Two parallel surfaces were machined along 75 mm to 150 mm lengths of the round bar to produce a cross section that was 15

mm thick by 41 mm wide along the midplane. These pieces were cold rolled parallel to the longitudinal direction of the bar with reduction in the 15-mm dimension and without intermediate annealing. The resulting microstructure consisted only of β grains, which were 40 μm by 90 μm in cross-section and 130 μm in length for ST/CW 65% Beta-C [18]. X-ray diffraction of ST/CW 65% Beta-C confirmed that no other phases were formed during cold rolling [19]. Second, 40 mm to 75 mm lengths of the round bar of ST Beta-C were heat treated at 500°C for times between 1 h and 24 h to precipitate the α phase, which formed as fine plate-like particles (less than 1 μm in length) within β grains [18,20,21] and possibly as thin layers on β -grain boundaries [2,19]. This is the solution treated plus aged (ST/A) condition. A third condition (ST/CW/A) was produced by aging ST/CW 20% Beta-C for 24 h at 500°C.

Rockwell C (R_C) hardness was measured for each condition of Beta-C; each hardness value in Table 1 represents the average of 10 measurements. Uniaxial tensile properties were measured for the ST and ST/A 24 h conditions [10]. Measured σ_{YS} and elastic modulus (E) are shown in Table 1. Values of σ_{YS} for the remaining conditions were estimated from hardness, assuming a linear hardness vs σ_{YS} relationship given by the values for the ST and ST/A 24 h conditions. These σ_{YS} estimates are equivalent to a hardness vs σ_{YS} correlation reported for ST/A Beta-21S and ST/A Ti-15-3 [2].

Microscopy

Fractographic and high-magnification metallographic analyses were conducted in the scanning electron microscope (SEM). Secondary electron imaging was used to examine fracture surfaces of Beta-C. Back-scattered electron imaging of electropolished specimens was used to characterize the β/α microstructure of ST/A Beta-C. The operating conditions for back-scattered imaging included a working distance of 8 mm, a probe current of 1×10^{-10} amperes, and a LaB_6 filament. The specimens were polished at 25 V for 60 s with a solution of 60% methanol, 35% ethylene glycol, and 5% perchloric acid.

EAC-Fracture Mechanics

Sidegrooved compact-tension (CT) specimens were used for air fracture toughness as well

as EAC measurements of crack propagation threshold and growth rates. For the ST and ST/A specimens, the crack plane was perpendicular to the longitudinal axis of the round bar with crack growth in the radial direction. The ST/CW and ST/CW/A specimens were in the TL orientation; viz, with the crack plane perpendicular to the rolling plane and with crack growth parallel to the cold rolling direction (the original longitudinal axis). Additional specimens of ST/CW 65% Beta-C were in the LT orientation (crack growth perpendicular to the rolling direction). All specimens except ST/CW 65% Beta-C had a gross thickness (B) of 6.3 mm, net thickness (B_n) of 5.1 mm and width (W) of 30 mm. The ST/CW 65% specimens had reduced thickness, with B = 5.1 mm and B_n = 3.8 mm. The CT specimens were fatigue precracked in moist air, terminating with a K_{max} of 15 MPa \sqrt{m} and a crack length-to-width ratio of approximately 0.53.

Each fracture mechanics experiment was conducted under monotonically rising crack mouth

Table 1 *Hardness, yield strength, and elastic modulus for Beta-C*

Condition	R _C Hardness	σ_{YS} (MPa)	E (GPa)
ST	27.6	875	87.5
ST/CW 20%	30.0	900*	-
ST/CW 36%	32.4	985*	-
ST/CW 51%	35.1	1045*	-
ST/CW 58%	36.1	1070*	-
ST/CW 65%	37.4	1095*	-
ST/A 1 h	30.0	900*	97**
ST/A 2 h	31.1	950*	97**
ST/A 3 h	31.7	970*	97**
ST/A 4 h	32.3	985*	97**
ST/A 5.5 h	34.1	1025*	97**
ST/A 7 h	35.9	1065*	105**
ST/A 12 h	37.9	1110*	105**
ST/A 24 h	40.6	1170	105
ST/CW/A	45.6	1280*	105**

*Estimated from hardness

**Estimated from relationship between crack length and CT specimen compliance [22]

opening displacement (δ_m) at a fixed rate ($\dot{\delta}_m$) using a servohydraulic mechanical test system operated in δ_m -feedback control. A $\dot{\delta}_m$ equal to 30 nm/s was selected because this loading rate produced severe IG EAC in both ST/A 24 h Beta-C and ST/A Beta-21S [1,2]. The direct-current potential difference (DCPD) method was used to resolve crack tip process zone damage initiation and measure subsequent crack extension. Details of this technique are given elsewhere [10,23,24].

The fracture mechanics were characterized using the elastic-plastic J-integral [23]. The "plastic" component of the total J was small so that elastic analysis (stress-intensity factor, K) was sufficient for the ST/A, ST/CW, and ST/CW/A conditions of Beta-C. For ST/CW 20% and ST Beta-C, plasticity was significant and K levels were calculated from total J using the well-known relationship for small-scale yielding [25]. All experiments satisfied an approximate criterion for plane strain constraint [26]. All fracture surfaces were flat macroscopically, without shear walls, and were normal to the crack opening direction without macroscopic branching or deflection.

The onset of crack extension was evaluated by three different criteria using both load (P) vs δ_m and DCPD vs δ_m data. For ST/A Beta-C aged 7 h to 24 h, as well as ST/CW/A Beta-C, loaded in aqueous NaCl, initial crack extension was indicated by an abrupt increase in potential above the initial baseline DCPD vs δ_m trend. This point was always coincident with the first increase in specimen compliance from the initial linear P vs δ_m behavior [1,10]. For all conditions in air, as well as ST/A 1 h to 4 h and ST/CW Beta-C in aqueous NaCl, the DCPD vs δ_m data did not exhibit an abrupt increase in potential. Initial crack extension for these experiments was defined at the first increase in slope of the baseline DCPD vs δ_m trend [23], which was either linear with a positive slope or a constant potential, and was coincident generally with the first compliance increase from the initial linear P vs δ_m data. The third procedure for ST Beta-C is described elsewhere [1]. The K level associated with initial crack extension in aqueous NaCl under rising δ_m is defined as a lower-bound threshold (K_{TH}), equivalent to K_{TH} in Ref. 10. The K levels corresponding to initial crack extension in air (K_{ICi}) are lower bounds of the standardized values of fracture toughness [23].

Crack growth rates (da/dt) were calculated from DCPD-based crack length (a) vs time (t) data using two different methods. The method selected depended on the number of a-t data pairs, the crack growth rate, and data variability. The first method used secants between successive a-t data

points [22]. The applied K was evaluated at the mean crack length for each pair of data points. This method was used for measuring most environment-assisted rapid crack growth rates. The second method involved linear regression to measure da/dt over successive intervals of constant crack length. The applied K was calculated at the mean crack length in the interval evaluated. This method was used to measure all slow crack growth rates.

Environment

Experiments were conducted at 25°C in either moist air or flowing neutral 0.6 M (3.5 wt pct) aqueous NaCl (pH = 5 to 6) at a fixed electrode potential of -150 mV (vs the saturated calomel electrode). This electrode potential produced severe IG EAC in both ST/A 24 h Beta-C and ST/A Beta-21S [1,16]. Details are provided in Refs. 1 and 10.

RESULTS

Initial Crack Extension

Aged Beta-C in Air The hardness and σ_{YS} of Beta-C increase monotonically with increasing isothermal aging time; Table 1. The effect of aging condition on the plane strain fracture toughness, K_{ICi} , for Beta-C in air is shown in Fig. 1. The data (\diamond) are presented as K_{ICi} vs σ_{YS} , and the aging time for each σ_{YS} value is indicated. Figure 1 shows that σ_{YS} of ST Beta-C increases and K_{ICi} decreases with increasing aging time. The K_{ICi} decreases sharply after only 1 h aging time, and a small strength increase, and is essentially constant thereafter for increasing aging time or σ_{YS} ; K_{ICi} varies around a mean of 56 MPa \sqrt{m} with limits of 50 MPa \sqrt{m} and 63 MPa \sqrt{m} . The abrupt decrease in K_{ICi} from the value for the ST condition is consistent with tensile elongation vs aging time data reported for Beta-C aged near 500°C [21,27,28]. A similar mild effect of aging time on fracture toughness is reported for both Beta-C aged at 500°C [29] and Beta III aged at 620°C [5].

Figure 1 includes the K_{ICi} measurement for ST/CW/A Beta-C. This condition exhibits the highest σ_{YS} and the toughness value is below the K_{ICi} vs σ_{YS} trend line for ST/A Beta-C extrapolated to this strength level. Tensile elongations of ST/A and ST/CW/A Beta-C are nearly equal for aging times greater than 2 h at 538°C [27].

Aged Beta-C in NaCl Values of K_{TH} decrease upon aging ST Beta-C, however, the aging-time or σ_{YS} dependence for K_{TH} differs from that for K_{ICi} . Figure 1 shows that while K_{TH} (●) equals K_{ICi} for aging times less than 3 h (σ_{YS} less than 970 MPa), K_{TH} decreases below K_{ICi} for longer aging times or higher σ_{YS} . Data variability (K_{TH} from 24 MPa \sqrt{m} to 31 MPa \sqrt{m}) is shown for a σ_{YS} of 1170 MPa (24 h aging time). The EAC threshold for ST/CW/A Beta-C included in Fig. 1 is consistent with the ST/A values, and is less than K_{ICi} for this high-strength microstructure.

ST/CW and ST Beta-C in Air Similar to the effect of aging, increasing cold-work reductions between 20% and 65% increase σ_{YS} (Table 1) and lower K_{ICi} of ST Beta-C (Fig. 2). Figure 2 shows K_{ICi} vs σ_{YS} (◇) for ST/CW Beta-C fractured in air and includes the dashed trend line for ST/A Beta-C from Fig. 1. The K_{ICi} values for ST/CW Beta-C decrease with increasing σ_{YS} , however, data are insufficient to determine if the initial strong σ_{YS} dependence of K_{ICi} differs between the ST/CW and ST/A conditions. For σ_{YS} above about 1050 MPa, K_{ICi} for ST/CW Beta-C is significantly less than that of the ST/A microstructure. For ST/CW 65% Beta-C, K_{ICi} depends only mildly on specimen orientation; crack growth normal to the rolling direction (LT) initiates at slightly higher K (Δ).

The decrease in K_{ICi} with increasing cold work is consistent with tensile elongation data reported for cold-rolled and cold-drawn Beta-C [27,28]. Other data show, however, that the tensile reduction-of-area for cold-drawn Beta-C is independent of reductions up to 60%, decreases to a minimum at 75% reduction, then increases with additional cold work [28]. Values of K_{ICi} should correlate with reduction-of-area rather than elongation.

ST/CW and ST Beta-C in NaCl Figure 2 shows that K_{TH} for EAC of ST and ST/CW Beta-C in aqueous NaCl (●) equals K_{ICi} . This apparent immunity to EAC contrasts to the susceptibility of ST/A Beta-C at higher σ_{YS} , where K_{TH} is less than K_{ICi} . The K_{TH} of ST/CW Beta-C increases mildly in the LT orientation (■) at 65% reduction, similar to K_{ICi} .

Crack Propagation

Aged Beta-C in Air Cracks grow stably in air for ST/A and ST/CW/A Beta-C under constant δ_m loading and plane strain conditions, but the increment of stable cracking depends on the aging condition. A set of a vs t and K vs t data is plotted in Fig. 3 for ST/A 7 h Beta-C, and is representative of stable crack growth throughout each experiment for ST/A Beta-C aged 3 h and

longer, as well as ST/CW/A Beta-C. These results are typical of plane strain crack growth resistance (R) curve behavior [30]. The applied K increases during crack growth immediately following K_{ICi} , then is nearly constant or decreases mildly for all aging conditions. For increments of crack growth (Δa) on the order of 0.25 mm to 2 mm, crack length increases regularly with time and crack growth rates show two distinct regimes, i.e., periods of slow and rapid da/dt . On a finer scale, crack growth rates vary widely independent of whether the average da/dt is slow or fast.

Figure 4 shows da/dt as a function of K (O) from the data in Fig. 3 for ST/A 7 h Beta-C in air. Each da/dt data point represents a measurement from linear regression over Δa of about 0.25 mm. Most slow da/dt rates are near 5×10^{-4} mm/s and rapid da/dt can reach 10^2 mm/s. The da/dt data are clustered near K equaling $62 \text{ MPa}\sqrt{\text{m}}$, as K is nearly constant for crack lengths greater than 18 mm (Fig. 3). Similar behavior is observed for ST/A Beta-C aged longer than 3 h.

For ST/A Beta-C aged for 1 h and 2 h, stable crack growth characterized by slow da/dt and increasing K is interrupted by fracture instability, i.e., the crack advances instantaneously through nearly the entire remaining specimen ligament and da/dt cannot be measured. The increment of stable crack growth is larger for ST/A 2 h Beta-C (2.5 mm) compared to that for the ST/A 1 h condition (0.5 mm).

Aged Beta-C in NaCl The effect of aqueous NaCl on crack growth under constant $\dot{\delta}_m$ loading depends strongly on aging condition for Beta-C. For ST/A Beta-C aged 1 h and 2 h, the crack growth behavior in air (Figs. 3 and 4) is not altered by aqueous NaCl. In contrast novel environment-enhanced crack growth kinetics are observed for aqueous NaCl experiments with ST/A Beta-C aged 3 h and longer, as summarized in Figs. 5(a) and 5(b).

While the ratios of K_{TH} to K_{ICi} differ (Fig. 1), the a vs t and K vs t behaviors for ST/A Beta-C aged 3 h and 4 h are similar; data for the latter condition are shown in Fig. 5(a). The first 2.5 mm and 1 mm of crack extension in ST/A Beta-C aged 3 h and 4 h, respectively, resemble slow da/dt in air, as shown in Fig. 4 (▲, ■ compared to O). (The da/dt data were measured from linear regression over Δa intervals of 0.1 mm.) For the 3 h case, slow da/dt occurs under rising K exceeding K_{TH} , which equals K_{ICi} for air. For the 4 h case, K likewise increases above K_{TH} as slow crack growth progresses, and K_{ICi} is exceeded after some extension. For both conditions, da/dt accelerated occasionally to $10 \mu\text{m/s}$ and over a small Δa during otherwise slow crack extension. After this slow

da/dt sequence, the slope of the a vs t curve increases dramatically and K decreases (Fig. 5(a)). This rapid da/dt behavior is not plotted in Fig. 4 and differs from the fracture instability observed in both air and aqueous NaCl for ST/A Beta-C aged 1 h and 2 h, as well as the rapid bursts noted for the longer-aged conditions in air (Fig. 3); viz, crack length increases regularly between successive data points and da/dt is finite. Rapid da/dt commences at K levels of $90 \text{ MPa}\sqrt{\text{m}}$ and $72 \text{ MPa}\sqrt{\text{m}}$ (well above K_{ICI} , Fig. 1), and arrests after 9.5 mm ($K = 77 \text{ MPa}\sqrt{\text{m}}$) and 8.5 mm ($K = 42 \text{ MPa}\sqrt{\text{m}}$) of crack extension, for ST/A Beta-C aged 3 h and 4 h (Fig. 5(a)), respectively.

The a vs t and K vs t behaviors for ST/A Beta-C aged 7 h, 12 h and 24 h, as well as ST/CW/A Beta-C, in aqueous NaCl are similar as represented by data for the 7 h case in Fig. 5(b). Crack growth following initiation at K_{TH} is slow and regular with respect to time, i.e., da/dt never increases abruptly above the baseline levels, under increasing K . The da/dt levels (+, ∇ , \square , in Fig. 4) are similar to the lower rates for air fracture as well as for ST/A Beta-C aged 3 h and 4 h in aqueous NaCl, but the K levels are less than K_{ICI} (Fig. 1). A rapid da/dt sequence (with falling K), similar to those at high K in Fig. 5(a) and not plotted in Fig. 4, commences after a small crack growth increment. The K levels at the onset of rapid da/dt are less than those for ST/A Beta-C aged 3 h and 4 h; viz, equalling $41 \text{ MPa}\sqrt{\text{m}}$, $46 \text{ MPa}\sqrt{\text{m}}$ and $42 \text{ MPa}\sqrt{\text{m}}$ for aging times of 7 h, 12 h and 24 h, respectively, and $24 \text{ MPa}\sqrt{\text{m}}$ for ST/CW/A Beta-C; and are below K_{ICI} . The crack growth increment (from 1 mm to 5 mm) during each rapid da/dt sequence is smaller than those for ST/A Beta-C aged 3 h and 4 h. As such, several rapid da/dt sequences are observed during each experiment, separated by periods of slower da/dt. This alternating slow-rapid da/dt is reported for α/β Ti-6V-4Al and ST/A 24 h Beta-C under rising displacement in aqueous NaCl [1,9,10]. The alternating slow-rapid da/dt in Fig. 5(b) appears similar to the crack advance observed in air (Fig. 3), however, crack length increases regularly between successive data points and da/dt is environment-enhanced in aqueous NaCl. Imposing a fixed δ_m during rapid da/dt immediately arrests crack advance in air, but not in aqueous NaCl [10].

The 5.5 h-age case shows aspects of crack growth behavior that resemble those for both shorter and longer aging times. Although the ratio of K_{TH} to K_{ICI} is similar to those for ST/A Beta-C aged 3 h and 4 h (Fig. 1), crack growth following initiation at K_{TH} is slow and regular with respect to time, similar to the behavior for ST/A Beta-C aged 7 h and longer (\diamond compared to +, ∇ , \square , in Fig.

4). The occasional abrupt increase in slow da/dt above the baseline level, shown in Fig. 4 for the 3 h and 4 h cases ($\blacktriangle, \blacksquare$), is not resolved for ST/A 5.5 h Beta-C. The rapid da/dt behavior for the 5.5 h case resembles those for ST/A Beta-C aged 3 h and 4 h, as the K level at the onset of rapid da/dt is high ($78 \text{ MPa}\sqrt{\text{m}}$) and the Δa increment is large (6 mm).

The da/dt vs K relationships, measured for segments of rapid crack growth in ST/A Beta-C (aged 3 h and longer) exposed to aqueous NaCl, are presented in Fig. 6. The data in Fig. 6 represent the initial rapid da/dt sequence for ST/A Beta-C aged 12 h and 24 h, the first two such events for ST/A 7 h Beta-C and ST/CW/A Beta-C, and the final rapid-growth segments for the 3 h, 4 h, and 5.5 h cases. In each case EAC occurs under decreasing K during constant $\dot{\epsilon}_m$ loading. The da/dt levels for rapid crack growth range from $10 \text{ }\mu\text{m/s}$ to $100 \text{ }\mu\text{m/s}$, and do not vary systematically as a function of aging time. Crack growth rates are high for each aging condition; maximum da/dt levels equal one-third to one grain diameter per second.

ST/CW and ST Beta-C in Air Crack growth behavior for ST/CW Beta-C in air depends on specimen orientation. For TL-oriented ST/CW Beta-C, cracks grow unstably immediately upon initial extension at K equalling K_{IC} . For LT-oriented ST/CW Beta-C, cracks grow similarly to ST/A Beta-C aged 1 h and 2 h, viz, stable crack growth is interrupted by fracture instability after a modest Δa . Cracks grow stably and regularly in ST Beta-C under steeply rising K during the entire experiment [1].

ST/CW and ST Beta-C in NaCl Aqueous NaCl does not alter the air crack growth behavior for ST/CW Beta-C and ST Beta-C, at any K level.

Fractography

Aged Beta-C in Air

Low Magnification Microscopic plasticity dominates the fracture surfaces produced in air for ST/A and ST/CW/A Beta-C, however, the detailed morphologies are complex and vary with microstructure. Figures 7(a) through 7(d) show the similarities and differences in air fracture surface morphologies for ST/A Beta-C aged between 1 h and 24 h, as well as ST/CW/A Beta-C. The fatigue precrack from which fracture progresses is evident at the bottom of each scanning electron fractograph. Each fractograph represents the fracture mode for all crack lengths.

For ST/A Beta-C aged 1 h and 2 h (Fig. 7(a)), facet-like features are prominent on the fracture surfaces. The facets can be larger than the grain size, consist of only one face which can have steps, do not have sharply defined edges, and are covered by fine, uniform dimples when viewed at high magnification. These characteristics suggest that such facets result from shear instability rather than cleavage or IG separation. Areas of inhomogeneous deformation are likely for these short-time-aged microstructures, as some grains are devoid of α and thus strain localization may be promoted in these soft regions. The facet-like features in Fig. 7(a) resemble those in Ref. 21 for tensile fracture of Beta-C aged from 0.5 h to 24 h at 500°C. The facets in Fig. 7(a) are surrounded by dimple-like features typical of transgranular (TG) microvoid nucleation, growth and coalescence (MVC). Dimple shapes and sizes vary widely, characteristic of void nucleation at the interface of plate-like α of varying orientation in ST/A microstructures [12].

Fractographs for ST/A Beta-C aged for 3 h and 24 h in Figs. 7(b) and 7(c) show that as aging time is increased above 2 h, the facet-like features in Fig. 7(a) are produced infrequently while the TG dimple-like features dominate the air fracture surfaces. Two additional features evolve as the aging time increases to 24 h (Fig. 7(c)). First, distinct regions of the fracture surface consist only of finer dimples. Second, a small area fraction of facets is produced, but these features differ from those in Fig. 7(a). The facets in Fig. 7(c) are more typical of IG separation, as reported for higher-strength β/α alloys in air [12]. The facet planes in Fig. 7(c) are nearly parallel to the macroscopic fracture surface which suggests that the grain boundaries which separate are oriented favorably with respect to the maximum crack tip tensile stress. The fracture mode in Fig. 7(c) is consistent with that reported for fracture toughness specimens of Beta-C aged at 500°C for 8 h [29].

The air fracture surface of ST/CW/A Beta-C (Fig. 7(d)) shows evidence of ductile rupture, but the crack is extremely planar and most features are finer than those observed for ST/A Beta-C (Figs. 7(a) through 7(c)). In addition regions of these ductile features do not resemble dimples. The difference between these features and those from ST/A Beta-C fracture surfaces is likely due to the finer distribution of α which results from increased precipitation at dislocations introduced by the cold work.

High Magnification The detail on IG facets from air fracture surfaces of longer-term-aged ST/A Beta-C (i.e., Fig. 7(c)) are shown in Figs. 8(a) and 8(b). These fractographs are included in order

to compare air facets to those produced in aqueous NaCl. The fractographs in Figs. 8(a) and 8(b) are matching pairs from opposite fracture surfaces.

The primary feature on these facets is a homogeneous population of fine dimples characteristic of microscopic plasticity. Note the occasional protrusions which match with cavities on the opposite fracture surface (A, B, C, D, E in Figs. 8(a) and 8(b)). Some of these protrusions are identified as Ti-Zr silicides [20,] from energy-dispersive spectroscopy (EDS), but others yield compositions that are similar to that of the ST β phase. It is uncertain whether these latter results reflect the composition of the feature or matrix material in the EDS penetration volume.

Aged Beta-C in NaCl

Low Magnification Aqueous NaCl produces a pronounced transition from the air fracture mode for ST/A Beta-C aged 3 h and longer as well as ST/CW/A Beta-C, but not for ST/A Beta-C aged for 1 h and 2 h. Figure 9(a) represents aqueous NaCl fracture for the 1 h and 2 h cases, and shows that the morphology is nearly identical to that produced in air (Fig. 7(a)). (This fractograph shows an area 0.5 mm from the fatigue precrack.) Shear-facets and regions of dimpled rupture are observed, but there is evidence of additional cracking transverse to the macroscopic fracture surface.

For ST/A Beta-C aged for 7 h, 12 h and 24 h, as well as ST/CW/A Beta-C, aqueous NaCl crack extension from the fatigue precrack is solely by IG separation. Figures 9(b) (ST/A 12 h) and 9(c) (ST/CW/A) show that IG facets cover the entire fracture surface. The facets in Fig. 9(c) are elongated compared to those in Fig. 9(b) because of the grain shapes of ST/CW/A and ST/A Beta-C. These fractographs are typical for all crack lengths and every position along the crack front up to the specimen surfaces. Figures 9(b) and 9(c) show no evidence of a transition region between the fatigue precrack and EAC fracture mode, as the IG facets abut the precrack at the bottom of each fractograph. The extent and homogeneity of IG cracking in aqueous NaCl is striking for these longer-aged cases.

For ST/A Beta-C aged between 3 h and 5.5 h, the fracture mode in aqueous NaCl changes with crack extension during a single experiment, as shown by the fractographs in Figs. 10(a) through 10(c) for the 3 h case. The fracture surface morphology near the precrack (Fig. 10(a)) resembles that produced in air (Fig. 7(b)), but after some crack extension IG separation contributes to the fracture mode, as shown in Fig. 10(b) for Δa equalling 3.5 mm. The transition fracture morphology in Fig.

10(b) is not, however, a simple mixed mode of air fracture (Fig. 7(b)) and fully IG fracture (Fig. 9(b)). Rather, the fracture mode is better described as a transition from ductile TG fracture to IG cracking involving ductile fracture, as the IG facets exhibit significant microscopic plasticity. Evidence for IG cracking is noted after less crack extension for ST/A Beta-C aged 4 h and 5.5 h compared to ST/A 3 h Beta-C. In fact almost no TG cracking is observed for ST/A 5.5 h Beta-C near the fatigue precrack; this initial fracture surface morphology resembles the transition mode represented in Fig. 10(b). The fracture mode changes ultimately to IG cracking, consisting almost solely of smooth facets for all cases, as shown by the fractograph in Fig. 10(c) taken from near the end of crack extension ($\Delta a = 12$ mm). These facets resemble those in Fig. 9(b) for ST/A Beta-C aged 7 h and longer. The onset of rapid da/dt for ST/A Beta-C aged between 3 h and 5.5 h (Fig. 5(a)) occurs while the fracture mode is in the transition region (Fig. 10(b)).

High Magnification Figure 11 shows high-magnification fractographs of matching surfaces of IG facets produced in aqueous NaCl. Figures 11(c) and 11(d) are higher-magnification fractographs of the area in Figs. 11(a) and 11(b). The fractographs in Fig. 11 are from ST/A 4 h Beta-C but display features that are observed for every ST/A microstructure.

The detailed morphology of each EAC facet is distinct, but three general types of characteristics are noted. First, matching protrusion/cavity pairs on opposite fracture surfaces cover a portion of the facet area. These features range in shape from elongated to circular and are resolved at both magnifications in Fig. 11 (i.e., A,B,C,D,E,F, in Figs. 11(a) and 11(b); D,E,F,G,H,I in Figs. 11(c) and 11(d)). A small number of the circular protrusions are Ti-Zr silicides. Second, matched pairs of protruding thin ridges on opposite fracture surfaces cover an additional portion of the facet area. Many of these ridges form circular shapes, but others do not close on themselves to form a shape. These features are observed mostly at higher magnification (i.e., A,B,C in Figs. 11(c) and 11(d)). The flat areas surrounding the former two features constitute the third characteristic, and are notable because they are devoid of detail. The significance of this third feature is best demonstrated by comparing the facets in Fig. 11 with the air facets in Fig. 8. The matching air facets in Figs. 8(a) and 8(b) are covered entirely by the two prominent features, i.e., fine dimples and protrusion/cavity pairs.

A possible limitation to high-magnification fractography is loss of detail due to dissolution

during crack extension in aqueous NaCl. The features observed at high magnification near the precrack, where exposure is longest, are similar to those near the end of crack extension. In addition fine details match on opposite facets, i.e., "H" and "I" in Figs. 11(c) and 11(d). These observations suggest that dissolution does not affect resolution of detail on EAC facets.

ST/CW and ST Beta-C in Air Crack propagation in ST/CW and ST Beta-C is solely by MVC; the fracture surfaces produced in air are covered completely by dimples (Figs. 12(a) and 12(b)), but the morphologies differ. The dimples on fracture surfaces of ST/CW Beta-C (Fig. 12(a); ST/CW 58% Beta-C) are larger and more well-formed compared to those for the ST condition (Fig. 12(b)), and in some regions the dimples for ST/CW Beta-C appear to be aligned in rows. The only void-nucleating particles for the ST and ST/CW conditions are Ti-Zr silicides [20,31], which form during solution heat treating in the β phase field. Although these particles may align in rows during cold rolling, it is unlikely that they account for the frequency and regularity of the dimples in Fig. 12(a). Shear facets typical for fracture of Beta-C aged 1 h and 2 h are not observed for the ST and ST/CW cases.

ST/CW and ST Beta-C in NaCl In contrast to the aged microstructures of Beta-C, aqueous NaCl does not produce a transition in fracture mode for ST/CW and ST Beta-C. The fracture surfaces produced in aqueous NaCl exactly resemble those typical of air cracking (Figs. 12(a) and 12(b)).

DISCUSSION

Results show that the IG EAC susceptibility of Beta-C in aqueous NaCl depends strongly on aging treatment. The challenge is to elucidate the roles of σ_{YS} , α -microstructure and associated factors such as deformation mode in promoting EAC.

The present results are interpreted based on an EAC scenario proposed for β -Ti alloys in aqueous NaCl [2,6]. Environment-assisted crack extension is by hydrogen embrittlement (HE) where atomic hydrogen (H) is produced by cathodic electrochemical reaction on the crack tip surface. Crack tip strain enhances the production and uptake of H by rupturing the thermodynamically stable passive film, and exposing the electrochemically active and diffusion-barrier-free base alloy. Atomic hydrogen is transported from the crack tip surface to trap sites within the process zone. The exact trap sites, the location of cracking, and the mechanism by which H

lowers the IG fracture resistance of β -Ti have not been identified.

The EAC susceptibility is a function of the amount of H in the process zone, the level of crack tip stress which can be sustained to drive HE, and the intrinsic "strength" of the grain boundary region [32]. The amount of H in the crack tip process zone is governed by both electrochemical activity and trap sites in the microstructure. The former is enhanced by increased crack tip strain rate. Traps may be either preexisting microstructural features such as α/β interfaces, or plastic strain-generated during crack tip deformation. The maximum in the crack tip stress distribution is affected by σ_{YS} and work hardening, while the extent of the high-stress region ahead of the crack tip is a function of K [33]. Grain boundary strength is likely controlled by local alloy chemistry, the presence of a thin layer of α , and by slip-grain boundary interactions.

EAC of ST/CW Beta-C: Role of σ_{YS}

Previous experiments demonstrate a dramatic difference in the IG EAC resistance of ST Beta-C, which is immune, compared to that of high-strength ST/A Beta-C, which is susceptible [1]. The present results show that ST Beta-C cold worked between 20% and 65% is similarly immune to IG EAC in aqueous NaCl under rising δ_m , as evidenced by equal K_{ICi} and K_{TH} (Fig. 2), MVC fracture modes in both air and aqueous NaCl (Fig. 12(a)), and the lack of enhanced da/dt even at K levels above K_{ICi} . Such results are of practical importance to fastener applications of ST/CW β -Ti alloys in marine environments. For example, localized regions of cold work at thread or cap regions should not be susceptible to IG EAC.

The behavior of ST/CW Beta-C indicates that the increased σ_{YS} accompanying aging does not solely render the ST/A condition susceptible to EAC. Cold-work reductions between 36% and 65% do not alter the single-phase β microstructure or composition of ST Beta-C, but increase σ_{YS} to levels (975 MPa to 1100 MPa in Fig. 2) comparable to those of EAC-susceptible ST/A Beta-C aged 3 h and longer (975 MPa to 1275 MPa in Fig. 1). Thus for constant β microstructure and composition, as well as loading rate and environment, increased σ_{YS} does not promote EAC of Beta-C.

The fracture mode for ST/CW Beta-C in aqueous NaCl is fully TG MVC (Fig. 12(a)). It is expected that some IG separation should occur if the grain boundaries are inherently susceptible to

HE. Previous experiments show that ST Beta-C is immune to EAC in aqueous NaCl solutions containing sulfide ions to promote H uptake [1]. Based on these results, it is reasonable to speculate that the single-phase β ST and ST/CW microstructures of Beta-C are immune intrinsically to EAC.

Caution is required before eliminating an important role of alloy σ_{YS} in promoting EAC of ST/A Beta-C compared to the ST condition. The elongated grain shape of ST/CW Beta-C differs from the equiaxed grains in ST and ST/A Beta-C. The TL orientation used for experiments on ST/CW Beta-C provides the most likely opportunity for IG EAC, but none occurred. The ST/CW 65% Beta-C results include both the TL and LT orientations (Fig. 2), in which different amounts of grain boundary area are exposed to the propagating crack, but an environmental effect is not observed for either case.

More importantly, K_{ICi} for ST/CW Beta-C in air is unexpectedly low compared to values for ST/A Beta-C (Fig. 2).¹ For σ_{YS} above 1050 MPa, IG EAC is produced at K_{TH} levels for ST/A Beta-C that are nearly equal to K_{ICi} for ST/CW Beta-C at similar σ_{YS} . These K_{ICi} values for ST/CW Beta-C represent the maximum K levels sustained since no stable cracking is observed. The ST/CW microstructures may be susceptible to EAC at higher applied K.

The immunity of ST/CW Beta-C to EAC is demonstrated only for a single loading rate, and rapid unstable crack growth rate. The importance of $\dot{\epsilon}_{CT}$ in EAC is discussed in an ensuing section. It is possible that the $\dot{\epsilon}_{CT}$ dependence of K_{TH} is affected by cold work, and that reduced K_{TH} [10] occurs at values of $\dot{\epsilon}_m$ and da/dt that are not probed by the current experiments. For example, the grain boundary H concentration may be reduced in ST/CW Beta-C compared to the ST condition due to increased trapping at intragranular dislocations. The EAC of ST/CW Beta-C may be produced at alternate loading rates that allow for more H to accumulate at grain boundaries. Additional experiments which address $\dot{\epsilon}_{CT}$ effects are required to assess the importance of σ_{YS} in IG EAC of single-phase β -Ti alloys [17].

¹ Since the morphology of ST/CW Beta-C fracture surfaces is microvoid-based (Fig. 12(a)), it is possible that low K_{ICi} can be traced to reduced work hardening with increasing cold work. Reduced work hardening may accelerate the growth and coalescence stages of microvoid fracture and thus reduce K_{ICi} [34,35]. In addition cold work can increase the dislocation density around features which promote strain incompatibility and thus enhance void nucleation.

EAC of ST/A Beta-C: Role of σ_{ys}

The ST/A Beta-C aged for 7 h to 24 h, as well as ST/CW/A Beta-C, are susceptible similarly to EAC in aqueous NaCl under rising δ_m . This conclusion is based on results showing reduced K_{TH} below K_{ICi} (Fig. 1), a transition in fracture mode from ductile rupture in air (Figs. 7(c) and 7(d)) to fully IG cracking in aqueous NaCl at all K levels above K_{TH} (Figs. 9(b) and 9(c)), and high crack growth rates during rapid da/dt (Figs. 5(b) and 6). These results further demonstrate the susceptibility of high-strength aged β -Ti alloys to IG EAC, where K_{TH} can be less than 50% of K_{ICi} and subcritical da/dt approaches 100 $\mu\text{m/s}$, or about one grain diameter per second. Similar observations are reported for ST/A Beta III and ST/A Beta-21S under rising displacement in aqueous halide solutions [2,10,5].

The ST/A Beta-C, aged for short times between 1 h and 5.5 h, exhibits EAC behavior in aqueous NaCl that represents a complex transition between the immune ST case and highly susceptible ST/A microstructure. For ST/A Beta-C aged between 3 h and 5.5 h, K_{TH} essentially equals K_{ICi} (Fig. 1) and initial crack extension from the fatigue precrack involves TG MVC for both air (Fig. 7(b)) and aqueous NaCl exposures (Fig. 10(a)). Aqueous NaCl EAC occurs, however, for the 3 h, 4 h, and 5.5 h cases as the crack extends and K increases above K_{TH} . The EAC is indicated by evolving IG fracture (Figs. 10(b) and 10(c)), and accelerating da/dt to rapid rates (Figs. 5(a) and 6), albeit for higher K. These microstructures of ST/A Beta-C are susceptible inherently to EAC in aqueous NaCl. An $\dot{\epsilon}_{CT}$ -based explanation for the K and Δa dependencies of IG EAC is presented in an ensuing section.

The ST/A Beta-C aged 1 h and 2 h exhibits only a small effect of aqueous NaCl. Faceted features and TG dimples dominate the entire fracture surface for each environment (Fig. 7(a) compared to Fig. 9(a)), but aqueous NaCl exposure promotes some cracking transverse to the macroscopic crack (Fig. 9(a)). This mild alteration in the fracture mode is not manifested by either reduced K_{TH} below K_{ICi} (Fig. 1), or a change in the crack growth behavior. It is possible that these microstructures are also inherently susceptible to EAC, and that higher K levels or alternate δ_m may promote IG cracking similar to ST/A Beta-C aged between 3 h and 5.5 h.

The EAC results for ST/A and ST/CW/A Beta-C (Fig. 1) show that K_{TH} declines modestly with increasing aging time above 5.5 h, where crack extension at fixed δ_m is fully intergranular for

all crack lengths (Figs. 9(b) and 9(c)). While increasing σ_{YS} is not solely responsible for the EAC susceptibility of ST/A Beta-C compared to the ST case, strength may cause such a dependence of K_{TH} on aging time. The HE models identify crack tip tensile stress, proportional to σ_{YS} and work hardening [33], as the local driving force for crack extension [32]. Perhaps as an aspect of the aged microstructure renders the alloy susceptible to EAC, the threshold for IG crack growth is reduced by increased σ_{YS} and crack tip tensile stress.

The similar rapid IG crack growth rates in aqueous NaCl, illustrated in Fig. 6 for ST/A Beta-C aged 3 h and longer, as well as ST/CW/A Beta-C, indicate that da/dt is not a function of changes in either σ_{YS} or aged microstructure. The different effect of σ_{YS} or aging time on da/dt compared to K_{TH} is not understood because there is no model of EAC for this alloy-environment system. Higher $\dot{\epsilon}_{CT}$ is associated with the rapidly propagating environmental crack [10], and H production may be enhanced. Crack growth may be insensitive to the changes in crack tip stress and aged microstructure represented in Fig. 6.

EAC of β -Ti: Role of Metallurgical Variables

Experiments with ST, ST/CW and ST/A Beta-C show that IG EAC in aqueous NaCl is promoted primarily by a metallurgical property associated with aging and not by increasing σ_{YS} . Metallurgical variables may have two roles in IG EAC; viz, localizing H production and uptake at β grain boundaries, as well as enabling hydrogen cracking of grain boundaries at relatively low crack tip tensile stress. Fractographic results for ST/A Beta-C and ST/A Beta-21S containing precharged H distributed throughout the microstructure support the notion that H production and uptake are localized uniquely for EAC in aqueous NaCl [11,18]. An array of fracture modes is observed corresponding to different precharged H concentrations, whereas fracture is solely intergranular for ST/A 24 h Beta-C and ST/A Beta-21S in aqueous NaCl over a range of applied electrode potentials and crack tip strain rates [1,2,10]. The EAC mechanism operates similarly at every grain boundary in ST/A Beta-C, as the fracture surfaces are 100% intergranular for all crack extensions (Fig. 9(b)). Since aqueous NaCl produces TG EAC in moderate-strength α/β Ti alloys such as Ti-6Al-4V [3,9], the mechanism for IG cracking in alloys such as Beta-C must be unique to the β/α microstructure.

Candidate metallurgical variables and accompanying explanations for their roles in EAC are

considered. Grain boundary α precipitates and intragranular deformation mode are demonstrated to not explain EAC. Results are, however, insufficient to establish the governing metallurgical factor from variables such as near-grain boundary composition.

α Phase One salient difference between ST/A Beta-C and the ST condition is the presence of α in the former microstructure. Isothermal transformation kinetics suggest that the α and metastable β' phases² are present in β after aging for 1 h at 500°C [20,21]. For aging times from 2 h to 24 h, the β' phase dissolves leaving a microstructure consisting solely of α precipitates in a β matrix. The volume fraction of α increases with continued aging from 2 h and solute (Mo, V, Cr) partitions to the β phase. Optical microscopy corroborates these results for the present heat of Beta-C; α is observed for aging times greater than 1 h [18].

The site of α -precipitate nucleation may be important. Results for ST/A Beta III show that a recrystallized microstructure with an α layer in the plane of β grain boundaries is susceptible to EAC in aqueous NaCl, whereas an unrecrystallized microstructure with intragranular α is immune [36]. Results for unrecrystallized ST/A Ti-8-8-3-2 indicate similar EAC resistance [3].

Roles in Localizing H and Embrittlement Speculatively, α localizes the production and uptake of H at β grain boundaries. The α phase often precipitates in the plane of β grain boundaries, as observed for ST/A Ti-15-3 and ST/A Beta-21S [2,11], and projected for all solute-rich β -Ti alloys aged at temperatures above about 500°C[19]. Slip initiates in grain boundary α during deformation because these regions are softer than the interiors of α -precipitate and solid solution-hardened β grains [12,37-39]. High strains in grain boundary α may cause the associated crack tip passive film to rupture locally. The H will be produced near these grain boundaries and transported into the process zone along the least-resistive diffusion path.

Two embrittlement mechanisms involving α on or near β grain boundaries are reasonable. The first is consistent with results for α/β Ti alloys embrittled in hydrogen gas; α in the plane of the grain boundary forms a brittle hydride phase that permits separation of the boundary at relatively low crack tip tensile stress [40-42]. Second, experiments on ST/A Beta-21S and ST/A Ti-15-3 [2]

² Headley and Rack [20] report that the phase identified as β' in β -Ti alloys is present in Beta-C, but dispute the notion that it is derived from a phase separation reaction. These authors refer to this phase as "zones". The zones cluster into plate-like colonies.

suggest that relatively large colonies of plate-like α , formed preferentially near β grain boundaries as the result of reduced intragranular nucleation sites, trap H at α/β interfaces [43] or β matrix dislocations near α/β interfaces [44]. The H reduces the local stress or strain required to separate the interface.

Evidence Against Role of α in EAC Several results refute the hypothesis that α is a requisite for IG EAC. First, transmission electron microscopy (TEM) results show relatively thin grain boundary α layers in ST/A Ti-15-3, but this alloy is immune to EAC in aqueous NaCl [2]. Second, precipitation of α along β grain boundaries should be less prevalent in ST/CW/A Beta-C due to the increased number of intragranular nucleation sites produced by cold work, but this microstructure is susceptible to IG EAC (Figs. 1 and 9(c)).

Since aqueous NaCl cracking in ST/A Beta-C is 100% intergranular, each grain boundary plane should contain an α layer. However, high-magnification back-scattered SEM images of electropolished specimens of ST/A Beta-C do not reveal extensive precipitation of grain boundary α . Specific results are presented in Fig. 13. In these micrographs the dark features are α precipitates and the bright areas are β matrix. This contrast arises since the solute elements in β are of higher atomic weight compared to those in α . A continuous or semi-continuous layer of α covers some grain boundaries (Fig. 13(c)), but this is a minority feature. Most boundaries are devoid of any such precipitation (Figs. 13(a) and 13 (b)). The electropolish/SEM technique is selected for this analysis because it samples numerous grain boundaries. Because the imaging resolution of the SEM technique is limited to about 0.1 μm at this magnification, TEM is needed to corroborate the results in Fig. 13.

Other results for ST/A Beta-C show that the proposed embrittlement mechanisms involving α at or near β grain boundaries are not feasible. For example, the solution treatment and aging conditions employed do not produce copious α -colony trap sites at β grain boundaries [18] but EAC is observed. In addition the IG facets in Fig. 11 do not display "striation" markings typical of discontinuous crack advance involving hydrided α . Such discontinuous crack advance is often found for EAC by a hydride mechanism [40-42].

Slip Mode Intragranular slip mode can depend on ST alloy composition and ST/A aging condition for β -Ti alloys. Damage associated with locally intense slip interactions are oft-cited as key in EAC

and HE [45]. For example, heterogeneous planar slip in ST/A Beta-21S may promote EAC and HE compared to homogeneous wavy slip in ST/A Ti-15-3 [2,11].

Roles in Localizing H and Embrittlement Slip mode may be critical in IG EAC by either aiding H accumulation or promoting embrittlement at β grain boundaries. Heterogeneous planar slip may enable more efficient transport of H from the crack tip surface to grain boundary trap sites by the dislocation sweeping mechanism [11,46], or concentrated slip interactions with boundaries may produce strong H trap sites and elevate local tensile stress to enable HE cracking. Aging to precipitate intragranular α may localize slip in ST/A Beta-C compared to the ST condition since the α and β phases have common slip systems and similar Burgers vectors [12,21,47,48].

Evidence Against Role of Slip Mode in EAC Fractographic results for ST/A Beta-C as well as deformation studies on β/α and α/β Ti alloys suggest that slip mode does not govern the EAC susceptibility of ST/A β -Ti alloys. The deformation behavior of individual lamellar α/β colonies in Ti-8Al-1Mo-1V (Ti-8-1-1) indicates that the Burgers orientation relationship between α and β is not sufficient to ensure planar slip through the two phases [37]. Rather, the local intensity of planar slip (large slip line spacings and shear offsets across α/β interfaces) is a function of the crystallographic orientation of α as well as the orientation of the colony with respect to the stress axis [37]. Cooperative transfer of slip from α to β depends on the ability of a slip system in α to generate sufficient stress to yield the harder β . The intensity of deformation by planar slip may vary in each grain of ST/A Beta-C, since the grains are randomly oriented and contain multiple crystallographic variants of plate-like α [21,47].

Deformation and air fracture studies of polycrystalline Ti-10V-2Fe-3Al (Ti-10-2-3) reveal additional considerations for localized intragranular slip in β alloys hardened by plate-like α precipitates [12,48]. The deformable α precipitates strain harden more rapidly than the β matrix, and the resulting stress gradient between the two phases enables cooperative transfer of slip from β to α and localized deformation. A decrease in the size or increase in the volume fraction of α allows the α/β interfacial stress gradient to develop at lower strains and increases the intensity of localized slip. While the size and volume fraction of α precipitates which promote severe strain localization is not quantified, changes in these microstructural parameters are gauged by σ_{YS} ; localized strain develops in β/α Ti-10-2-3 for σ_{YS} greater than about 1250 MPa [48]. Fractography from fracture

mechanics specimens of Ti-10-2-3 exhibiting localized deformation shows that cracks propagate by shear instability, with microscopic crack advance over short distances (10 μm to 20 μm) alternately angled above or below the macroscopic crack plane ("zig-zag" pattern) and resulting in closely spaced parallel ridges on the fracture surface [48].

Despite the observation of strain localization in similar β/α microstructures, it is unlikely that IG EAC in ST/A Beta-C is promoted by intense planar slip. The distribution and size of α are coarser for both Ti-8-1-1 [37] and Ti-10-2-3 [12,48] compared to Beta-C (Fig. 13) at similar σ_{YS} , which allow longer slip lengths and higher stress concentration at α/β interfaces for the former two alloys. The ST/A 3 h Beta-C microstructure is susceptible inherently to IG EAC (Fig. 10(c)), yet has a σ_{YS} (970 MPa) well below the minimum strength level (1250 MPa) for heterogeneous localized slip in Ti-10-2-3 [48]. The air and aqueous NaCl fractographs for EAC-susceptible microstructures of ST/A Beta-C (Figs. 7(b), 7(c), 9(b) and 11) show no evidence for localized slip, as the air fracture mode is predominantly MVC and not all IG EAC facets display linear offsets typical of slip band-grain boundary intersections [13]. In addition the increments of crack advance by shear instability in Ti-10-2-3 are only 10 μm to 20 μm , a distance less than the grain size for this alloy as well as Beta-C. The EAC mechanism involving deformation mode suggests that planar slip extends from the crack tip surface to the grain boundary. The notion that only a limited region ahead of the crack tip may deform by localized slip is supported by calculations of plastic zone size for ST/A Beta-C. At K_{TH} for ST/A 24 h Beta-C, the plastic zone size (approximated by $K^2/6\pi\sigma_{YS}^2$) is 25 μm , a distance less than the grain size of about 80 μm . Finally, the localized slip bands observed in Ti-10-2-3 for lower σ_{YS} are not intensely planar. For σ_{YS} near 1200 MPa, the intersection of slip bands with α precipitates does not produce offsets across α/β interfaces, but rather uniformly deforms α to a bent shape [12]. It is expected that a deformation mode-based EAC mechanism involves intense planar slip. Other results support the notion that deformation is not intensely planar within each grain for ST/A Beta-C [38,44].

Although intragranular slip mode is unlikely to promote 100% IG EAC in ST/A Beta-C, the ST/CW/A microstructure may exhibit intense localized deformation. This is suggested by the high strength level (1280 MPa) and severe reduction in air fracture toughness below the ST/A values (Fig. 1).

Composition Of the remaining possibilities, compositional differences that occur during aging may govern EAC. The susceptibility of high-strength ST/A microstructures of Beta-C and Beta-21S to IG EAC, compared to the apparent immunity of Ti-15-3 and Ti-11.6 Mo, suggests that alloy composition is important [1,2,5,9,10]. Impurities and alloy elements which segregate to grain boundaries are well-known to exacerbate IG EAC and HE in ferrous and nickel-based alloy systems [49].

Roles in Localizing H and Embrittlement The near-grain boundary composition of β -Ti alloys may affect the H uptake and embrittlement elements of EAC. First, the repassivation kinetics may be reduced in the grain boundary regions of ST/A microstructures by either thermally activated elemental segregation or solute partitioning accompanying α precipitation, leading to enhanced dissolution and associated H production. For example, Al is believed to hinder repassivation of α -Ti in highly acidic crack solution [50]. Second, elements concentrated near grain boundaries may either enhance adsorption of H [51] or retard H recombination to H_2 [52], and thus increase the crack tip surface coverage of H in these regions. Finally, boundary segregants may act with trapped H in the process zone to promote IG decohesion analogous to the mechanism proposed for steels and nickel [49].

Evidence For Role of Composition in EAC There is no direct evidence for either differences in grain boundary composition that occur upon aging, or that any of the composition effects on EAC operate in β -Ti alloys. For example, Cr and Ti segregate to β grain boundaries, and V and Mo are depleted in these regions, during air cooling from the solution treatment temperature in Beta-C [29]. These changes are apparently not relevant to EAC, since the ST microstructure is immune to IG cracking. The compositions of β and α change during aging to equilibrium [53], and elemental segregation should be possible during heating at 500°C, but compositional changes specific to grain boundaries of the sort shown in Fig. 13 have not been measured.

If composition is important in EAC, one role of this variable is likely enabling H production and uptake at grain boundaries, since the fracture mode of susceptible ST/A alloys is always intergranular in aqueous NaCl, but not with precharged H. In addition fractographic evidence may support a composition effect on grain boundary cohesion. If H plus a second segregant promote grain boundary decohesion, then the IG facet morphology should reflect the grain boundary

microstructure; consisting of plate-like α precipitates, β matrix, and occasional silicide particles (Fig. 13). The SEM analysis shows that some silicide particle/cavity pairs are found on matching EAC IG facets. The flat, featureless areas on EAC facets (Figs. 11(c) and 11(d)) are consistent with separation of a boundary formed by β matrix on both sides. Some of the fine detail observed at high magnification may result from separation of α precipitates from β matrix on opposite sides of the grain boundary. For example, the matching protrusion/cavity pair marked "G" in Figs. 11(c) and 11(d) resembles the size and shape of plate-like α oriented with its long dimension in the boundary, and the pairs marked "H" and "I" may result from the ends of plate-like α intersecting the boundary. The remaining fractographic features in Fig. 11, which do not reflect the β/α microstructure, likely form from ligaments surrounding the decohered regions of the boundary. These ligaments may rupture to form the matching ridge-like protrusion pairs (A,B,C in Figs. 11(c) and 11(d)), or pull out from one side of the boundary to form the matching protrusion/cavity pairs (A,B,C,D,E,F in Figs. 11(a) and 11(b); and D,E,F in Figs. 11(c) and 11(d)).

Although the fractography in Fig. 11 may support IG EAC by decohesion, other embrittlement mechanisms should be considered. For example, Lynch has proposed an adsorption-induced localized slip mechanism for a variety of alloys (fcc, bcc, hcp) which exhibit high subcritical EAC kinetics [51], similar to those for ST/A Beta-C in aqueous NaCl (Fig. 6). A dimpled IG or TG fracture surface morphology, characteristic of MVC, results from this EAC mechanism. Voids nucleate at precipitates, slip band intersections, and dislocation cell boundaries very near the crack tip. Areas of the fracture surface which appear smooth and featureless at low magnification are covered with extremely fine dimples. Lynch argues that these dimples may not be resolved even with high-magnification TEM imaging of fracture surface replicas.

An adsorption-induced localized slip EAC mechanism cannot be disregarded for ST/A Beta-C. Plastic strain-driven separation of grain boundaries in ST/A Beta-C is demonstrated by the dimples produced on IG air facets (Fig. 8). The flat, featureless regions on EAC IG facets in Fig. 11 were examined by SEM at magnifications up to 20,000X without resolving a population of fine dimples, but fracture surface replicas were not imaged in the TEM. While dimples formed from voids at plate-like α precipitates should be resolvable below 20,000X, the spacing of other void-nucleation sites such as slip bands and dislocation cell boundaries is not known. Pairs of matching

ridge-like protrusions which close on themselves resemble dimples and may result from localized slip (A,B,C in Figs. 11(c) and 11(d)), but the matching protrusion/cavity pairs are difficult to reconcile with this mechanism. Lynch shows, however, that dimples do not entirely cover the EAC IG facets of Al alloys and steels [51]; other features termed “tear ridges” are present.

While the current results effectively eliminate governing roles of α microstructure and deformation mode in EAC of ST/A β -Ti alloys, data are insufficient to establish the metallurgical factor that promotes IG cracking. At present it is only possible to conclude that the results of the current study do not rule out a role of composition.

Effect of Crack Tip Strain Rate

Environmental cracking of ST/A β -Ti alloys may be governed interactively by threshold values of two crack tip parameters [1,10]. Crack tip strain rate, $\dot{\epsilon}_{CT}$, reasonably controls the passive film-rupture frequency and associated amount of crack tip dissolution and H uptake per unit time in aqueous NaCl, and K governs the size of the crack tip process zone that is subjected to high tensile stress [33,54]. Continuum-mechanics solutions of crack tip strain rate for stationary and propagating cracks show that $\dot{\epsilon}_{CT}$ is a complex function of alloy deformation properties and position between the crack tip surface and outer boundary of the plastic zone, as well as K, dK/dt and da/dt [16,30,55,56]. The aqueous NaCl EAC results for ST/A Beta-C aged 3 h and 4 h under constant $\dot{\delta}_m$ loading suggest two possible effects of $\dot{\epsilon}_{CT}$ that must be considered to establish intrinsic metallurgical factors.

If a threshold $\dot{\epsilon}_{CT}$ is needed to produce a critical level of process zone H given sufficient crack tip stress (K) to drive IG cracking, then the $\dot{\epsilon}_{CT}$ dependence on aging time (through changes in E and σ_{YS}) must first be considered. Values of $\dot{\epsilon}_{CT}$ are compared for ST/A Beta-C, aged 3 h or 24 h, at the K level which produces IG cracking from the stationary fatigue precrack for the latter. Although solutions of $\dot{\epsilon}_{CT}$ for stationary cracks exist [16], the crack tip opening displacement rate ($\dot{\delta}_{CT}$) is calculated so that relative deformation rates for stationary and propagating cracks can be compared. The parameters in solutions of crack tip strain rate for propagating cracks are uncertain, but $\dot{\delta}_{CT}$ should be proportional to $\dot{\epsilon}_{CT}$ [30,55,56]. For a stationary crack [16,55,57]:

$$\dot{\delta}_{CT} = 2\alpha \frac{dK}{dt} \frac{K(1-\nu^2)}{\sigma_{YS} E} \quad (1)$$

The parameter, α , is a constant equal to 0.65 for low strain hardening [2,16] and ν is Poisson's ratio, assumed to equal 0.33. Values of σ_{YS} and E for ST/A Beta-C aged 3 h and 24 h are given in Table 1. The dK/dt rates are 3.1×10^{-3} MPa $\sqrt{m/s}$ for the 3 h-age CT specimen and 3.5×10^{-3} MPa $\sqrt{m/s}$ for the 24 h-age CT specimen. At a K level of 25 MPa \sqrt{m} , calculated $\dot{\delta}_{CT}$ equals 1 nm/s and 0.8 nm/s for ST/A Beta-C aged 3 h and 24 h, respectively.

The crack tip deformation rates are essentially equal for ST/A Beta-C aged 3 h and 24 h at a K level which produces fully IG EAC for the latter condition but not for the former. Similar film rupture frequencies and crack tip tensile stress distributions result in different EAC behaviors. Accordingly, ST/A 3 h Beta-C is more resistant intrinsically to EAC compared to the higher-strength ST/A condition.

The 3 h- and 4 h-aged microstructures of Beta-C are not, however, immune to EAC. Intergranular cracking is produced at K levels exceeding both K_{TH} and K_{ICi} , which are achieved due to stable TG plane strain crack growth. The higher K level increases the volume at the crack tip subjected to high tensile stress and the finite crack growth rate produces higher $\dot{\epsilon}_{CT}$. In order to determine whether the latter variable promotes IG cracking, the following continuum solution is used to calculate the increase in $\dot{\delta}_{CT}$ for the propagating crack compared to the stationary crack for ST/A 3 h Beta-C [30,56]:

$$\dot{\delta}_{CT} = 2\alpha \frac{dK}{dt} \frac{K(1-\nu^2)}{E \sigma_{YS}} + \beta \frac{\sigma_{YS}}{E} \frac{da}{dt} \ln \left(0.2 \frac{K^2(1-\nu^2)}{\sigma_{YS}^2 r} \right)$$

The parameter, β , is a constant equal to 5.1 and r is distance behind the crack tip. Since IG cracking evolves gradually for ST/A 3 h Beta-C, it is difficult to define a K level where EAC begins. Thus, the point where rapid da/dt commences is selected. For the ST/A 3 h Beta-C specimen, dK/dt equals 4.5×10^{-3} MPa $\sqrt{m/s}$, da/dt equals 0.1 $\mu m/s$, and K equals 90 MPa \sqrt{m} at the onset of rapid da/dt . For

an arbitrarily selected distance, r , of $10\text{ }\mu\text{m}$, $\dot{\delta}_{CT}$ from Eq. 2 equals 58 nm/s .³ This crack tip deformation rate is nearly two orders of magnitude higher than for the stationary crack at a K level of $25\text{ MPa}\sqrt{\text{m}}$ ($\dot{\delta}_{CT} = 1\text{ nm/s}$). The increased $\dot{\delta}_{CT}$ is due to the finite crack growth rate, as dK/dt is nearly equal for the propagating ($4.5 \times 10^{-3}\text{ MPa}\sqrt{\text{m/s}}$) and stationary ($3.1 \times 10^{-3}\text{ MPa}\sqrt{\text{m/s}}$) cracks.

The previous analysis indicates that EAC in ST/A Beta-C aged 3 h and 4 h is promoted by enhanced $\dot{\epsilon}_{CT}$ accompanying stable crack growth, and implies that IG cracking may be produced from a stationary fatigue precrack if dK/dt is increased by higher applied $\dot{\delta}_m$. This analysis shows that $\dot{\epsilon}_{CT}$ must be considered in a study of metallurgical effects on EAC resistance. Experiments reported elsewhere extend the results of the present effort to include this important variable [17].

CONCLUSIONS

1. Aging renders immune solution-treated Beta-C susceptible to severe EAC in aqueous NaCl for conditions involving a fatigue precrack, intermediate loading rate, and fixed electrode potential near free corrosion. The threshold for EAC is about 40% of K_{ICi} , subcritical crack growth rates approach $100\text{ }\mu\text{m/s}$, and the crack path is fully intergranular, in microstructures aged longer than 7 h.
2. The σ_{YS} increase due to α precipitation does not govern the EAC susceptibility of ST/A Beta-C. Solution treated and cold worked Beta-C retains immunity to EAC for high σ_{YS} comparable to that developed by aging. For several levels of cold work, fracture of ST/CW Beta-C is by TG microvoid processes, with K_{TH} equaling K_{ICi} .
3. Cold work reduces the air fracture toughness of ST Beta-C below levels for ST/A microstructures at similar σ_{YS} , limiting the criticality of the EAC experiments.
4. Two explanations for the deleterious effect of aging on EAC susceptibility of high-strength β -Ti alloys are eliminated. Neither grain boundary α precipitates nor intragranular planar slip bands are present in sufficient number to explain the fully IG crack path and severe EAC in ST/A Beta-C.

³ The distance pertinent to the crack tip deformation rate and EAC is uncertain; for r equal to $100\text{ }\mu\text{m}$, $\dot{\delta}_{CT}$ equals 34 nm/s .

5. Crack tip strain rate must be considered in assessing the intrinsic EAC resistance of β -Ti alloys. Short-term-aged microstructures of Beta-C crack by IG separation in aqueous NaCl, but only after crack tip strain rate increases due to ductile crack extension.

ACKNOWLEDGMENTS

This research was supported by the Office of Naval Research (Grant N00014-91-J-4164), with Dr. A. John Sedriks as Scientific Monitor. Material was donated by the RMI Titanium Company and mechanical processing was provided by the General Electric Corporate Research and Development Center. Informative discussions were conducted with J.R. Scully, M.A. Gaudett, and J.R. Hughes. These contributions are gratefully acknowledged.

REFERENCES

- [1] B.P. Somerday, J.A. Grandle and R.P. Gangloff: in *Proceedings of the Tri-Service Conference on Corrosion*, T. Naguy, ed., Materials Laboratory, Wright-Patterson Air Force Base, OH, 1994, pp. 375-392.
- [2] L.M. Young, G.A. Young, J.R. Scully and R.P. Gangloff: *Metall. Mater. Trans A*, 1995, vol. 26A, pp. 1257-1271.
- [3] M.J. Blackburn, J.A. Feeney and T.R. Beck: in *Advances in Corrosion Science and Technology*, M.G. Fontana and R.W. Staehle, eds., Plenum Publishing, NY, NY, 1972, vol. 3, pp. 67-292.
- [4] M.J. Blackburn, W.H. Smyrl and J.A. Feeney: in *Stress Corrosion Cracking in High Strength Steel and in Titanium and Aluminum Alloys*, B.F. Brown, ed., Naval Research Laboratory, Washington, DC, 1972, pp. 245-363.
- [5] J.A. Feeney and M.J. Blackburn: *Metall. Trans*, 1970, vol. 1, pp. 3309-3323.
- [6] D.G. Kolman: PhD Thesis, University of Virginia, Charlottesville, VA, 1995.
- [7] R.P. Gangloff: in *Corrosion Prevention and Control*, M. Levy and S. Isserow, eds., US Army Laboratory Command, Watertown, MA, 1986, pp. 64-111.
- [8] *Atlas of Stress-Corrosion and Corrosion Fatigue Curves*, A.J. McEvily, Jr., ed., ASM, Materials Park, OH, 1990, pp. 457, 484.
- [9] D.A. Meyn and P.S. Pao: in *Slow Strain Rate Testing for the Evaluation of Environmentally Induced Cracking: Research and Engineering Applications*, ASTM STP 1210, R.D. Kane, ed., ASTM, Philadelphia, PA, 1993, pp. 158-169.
- [10] B.P. Somerday, L.M. Young and R.P. Gangloff: submitted to *Metall. Mater Trans. A*, 1995.
- [11] G.A. Young: MS Thesis, University of Virginia, Charlottesville, VA, 1993.
- [12] G.T. Terlinde, T.W. Duerig and J.C. Williams: *Metall. Trans. A*, vol. 14A, pp. 2101-2115.
- [13] A. Gysler, G. Lütjering and V. Gerhold: *Acta Metall.*, 1974, vol. 22, pp. 901-909.
- [14] D.G. Kolman and J.R. Scully: in *Effects of the Environment on the Initiation of Crack Growth*, ASTM STP 1298, W.A. Van der Sluys, R.S. Piascik, and R. Zawierucha, eds., ASTM, Philadelphia, PA, 1997, in review.

- [15] J.A. Moskovitz and R.M. Pelloux: *Corrosion*, 1979, vol. 35, pp. 509-514.
- [16] L.M. Young: MS Thesis, University of Virginia, Charlottesville, VA, 1993.
- [17] B.P. Somerday and R.P. Gangloff, submitted to *Corrosion*, 1996.
- [18] M.A. Gaudett and J.R. Scully, submitted to *Scripta Metall.*, 1996.
- [19] T.W. Duerig and J.C. Williams: in *Beta Titanium Alloys in the 80's*, R.R. Boyer and H.W. Rosenberg, eds., The Metallurgical Society of AIME, Warrendale, PA, 1984, pp. 19-67.
- [20] T.J. Headley and H.J. Rack: *Metall. Trans. A*, 1979, vol. 10A, pp. 909-920.
- [21] C.G. Rhodes and N.E. Paton: *Metall. Trans. A*, 1977, vol. 8A, pp. 1749-1761.
- [22] *Annual Book of ASTM Standards*, Designation E647-88, ASTM, Philadelphia, PA, 1989, vol. 3.01, pp. 646-666.
- [23] B.P. Somerday, Y. Leng and R.P. Gangloff: *Fatigue Fract. Engng Mater. Struct.*, 1995, vol. 18, pp. 565-582.
- [24] J.K. Donald and J. Ruschau: in *Fatigue Crack Measurement: Techniques and Applications*, K.J. Marsh, R.A. Smith and R.O. Ritchie, eds., EMAS, West Midlands, UK, 1991, pp. 11-37.
- [25] J.W. Hutchinson: *J. Appl. Mech. Trans. ASME*, 1983, vol. 50, pp. 1042-1051.
- [26] *Annual Book of ASTM Standards*, Designation E1152-87, ASTM, Philadelphia, PA, 1991, vol. 3.01, pp. 825-835.
- [27] R.J. Stokes: MS Thesis, University of Kentucky, Lexington, KY, 1976.
- [28] D.H. Wilson and C.M. Esler: in *Beta Titanium Alloys in the 80's*, R.R. Boyer and H.W. Rosenberg, eds., Metallurgical Society of AIME, Warrendale, PA, 1984, pp. 457-482.
- [29] H.J. Rack: in *Titanium '80 Science and Technology*, H. Kimura and O. Izumi, eds., Metallurgical Society of AIME, Warrendale, PA, 1980, pp. 1627-1635.
- [30] J.R. Rice, W.J. Drugan and T-L. Sham: in *Fracture Mechanics: 12th Conference, ASTM STP 700*, P.C. Paris, ed., ASTM, Philadelphia, PA, 1980, pp. 189-221.
- [31] S. Ankem, D. Banerjee, D.J. McNeish, J.C. Williams and S.R. Seagle: *Metall. Trans. A*, 1987, vol. 18A, pp. 2015-2025.

- [32] K.N. Akhurst and T.J. Baker: *Metall. Trans. A*, 1980, vol. 12A, pp. 1059-1070.
- [33] R.M. McMeeking: *J. Mech. Phys. Solids*, 1977, vol. 25, pp. 357-381.
- [34] P.F. Thomason: *Ductile Fracture of Metals*, Pergamon Press, New York, 1990.
- [35] M.J. Haynes and R.P. Gangloff: *Metall. Mater. Trans. A*, 1995, in review.
- [36] J.B. Guernsey, V.C. Petersen and F.H. Froes: *Metall. Trans.*, 1972, vol. 3, pp. 339-341.
- [37] K.S. Chan, C.C. Wojcik and D.A. Koss: *Metall. Trans. A*, 1981, vol. 12A, pp. 1899-1907.
- [38] T. Hamajima, G. Lütjering and S. Weissmann: *Metall. Trans.*, 1973, vol. 4, pp. 847-856.
- [39] M.A. Greenfield and H. Margolin: *Metall. Trans.*, 1972, vol. 3, pp. 2649-2659.
- [40] H.G. Nelson: *Metall. Trans. A*, 1976, vol. 7A, pp. 621-627.
- [41] D.P. Williams and H.G. Nelson: *Metall. Trans.*, 1972, vol. 3, pp. 2107-2113.
- [42] H.G. Nelson, D.P. Williams, and J.E. Stein: *Metall. Trans.*, 1972, vol. 3, pp. 469-475.
- [44] M. Young, E. Levine and H. Margolin: *Metall. Trans. A*, 1979, vol. 10A, pp. 359-365.
- [45] A.W. Thompson and I.M. Bernstein: in *Advances in Corrosion Science and Technology*, M.G. Fontana and R.W. Staehle, eds., Plenum Press, New York, 1980, pp. 53-175.
- [46] J.K. Tien, S.V. Nair and R.R. Jensen: in *Hydrogen Effects in Metals*, I.M. Bernstein and A.W. Thompson, eds., The Metallurgical Society of AIME, Warrendale, PA, 1981, pp. 37-56.
- [47] C.G. Rhodes and J.C. Williams: *Metall. Trans. A*, 1975, vol. 6A, pp. 2103-2114.
- [48] G. Terlinde, H.-J. Rathjen and K.-H. Schwalbe: *Metall. Trans. A*, vol. 19A, pp. 1037-1049.
- [49] R.H. Jones: in *Hydrogen Effects on Material Behavior*, N.R. Moody and A.W. Thompson, eds., TMS, Warrendale, PA, 1989, pp. 817-843.
- [50] S. Yu and J.R. Scully: unpublished research, University of Virginia, Charlottesville, VA, 1996.
- [51] S.P. Lynch: *Acta Metall.*, 1988, vol. 36, pp. 2639-2661.
- [52] R.M. Latanision and H. Opperhauser, Jr.: *Metall. Trans.*, 1974, vol. 5, pp. 483-492.

- [53] D.G. Kolman and J.R. Scully: *J. Electrochem. Soc.*, 1994, vol. 141, pp. 2633-2641.
- [54] F.P. Ford: in *Environment-Induced Cracking of Metals*, R.P. Gangloff and M.B. Ives, eds., NACE, Houston, TX, 1990, pp. 139-165.
- [55] D.P.G. Lidbury: in *Embrittlement by the Localized Crack Environment*, R.P. Gangloff, ed., The Metallurgical Society of AIME, Warrendale, PA, 1983, pp. 149-172.
- [56] J.R. Rice and E.P. Sorensen: *J. Mech. Phys. Solids*, 1978, vol. 26, pp. 163-186.
- [57] C.F. Shih: *J. Mech. Phys. Solids*, 1981, vol. 29, pp. 305-326.
- [58] H.J. Rack: *Metall. Trans. A*, 1975, vol. 6A, pp. 947-949.

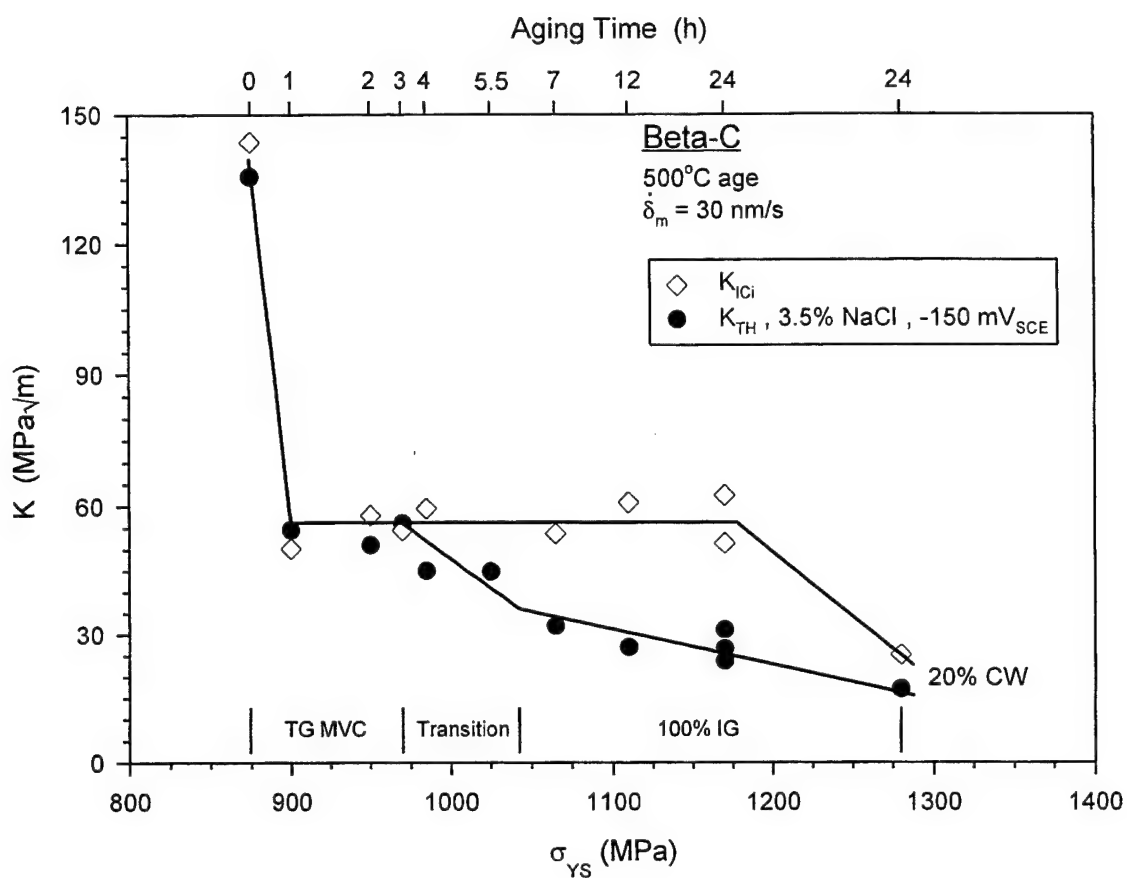


Fig. 1 Air fracture toughness (K_{ICi}) and EAC threshold stress-intensity factor (K_{TH}) for ST/A Beta-C as a function of yield strength (σ_{YS}) and aging time. The aqueous NaCl fracture modes for each range of σ_{YS} and aging time are indicated.

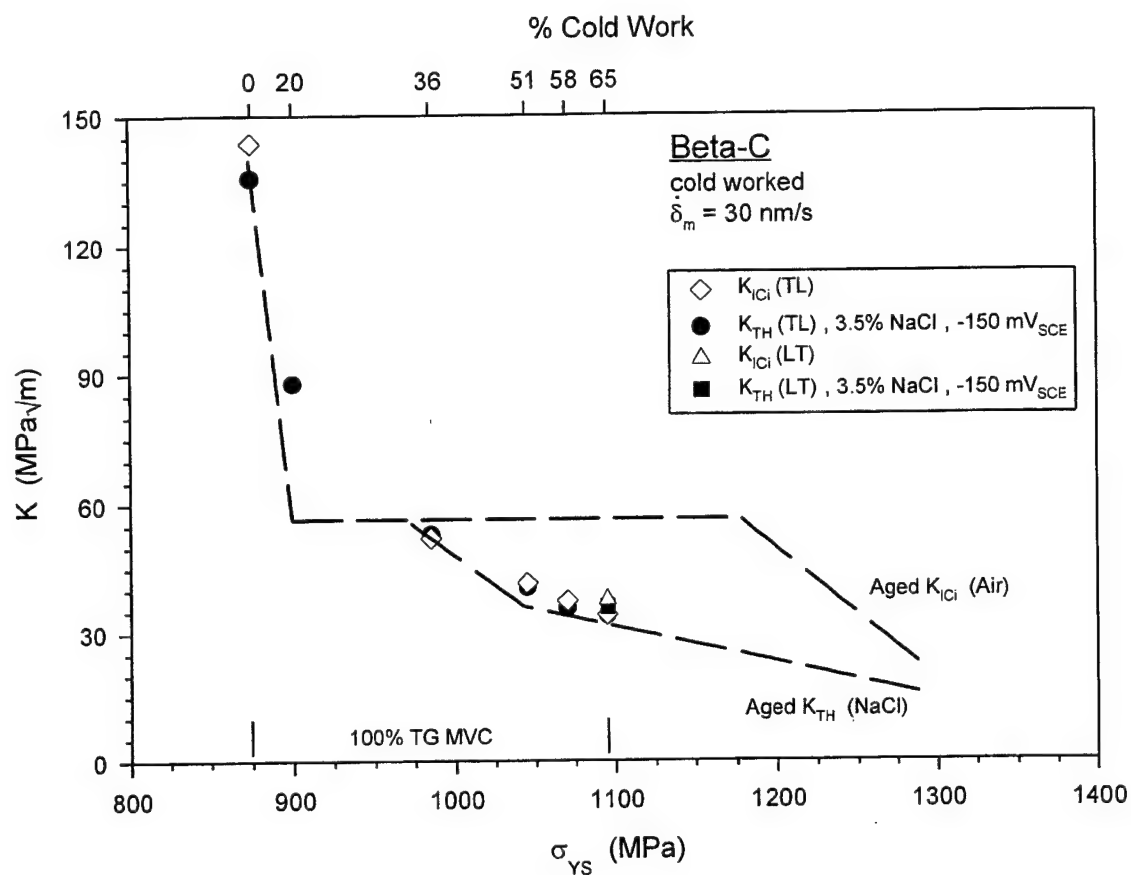


Fig.2 Air fracture toughness (K_{ICi}) and EAC threshold stress-intensity factor (K_{TH}) for ST/CW Beta-C as a function of yield strength (σ_{YS}) and cold-work reduction. The fracture mode for both air and aqueous NaCl exposures is indicated. Dashed trend lines for the ST/A data in Fig. 1 are shown.

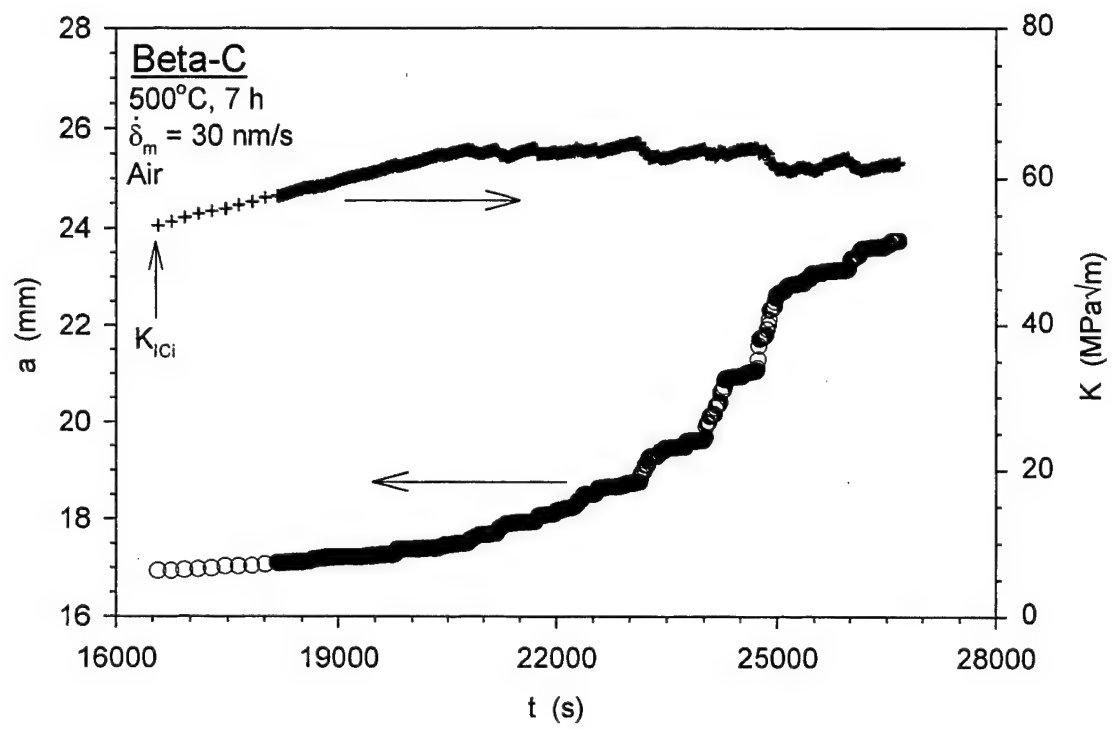


Fig. 3 Crack length (a) and applied stress-intensity factor (K) vs time (t) data for ST/A 7 h Beta-C in air.

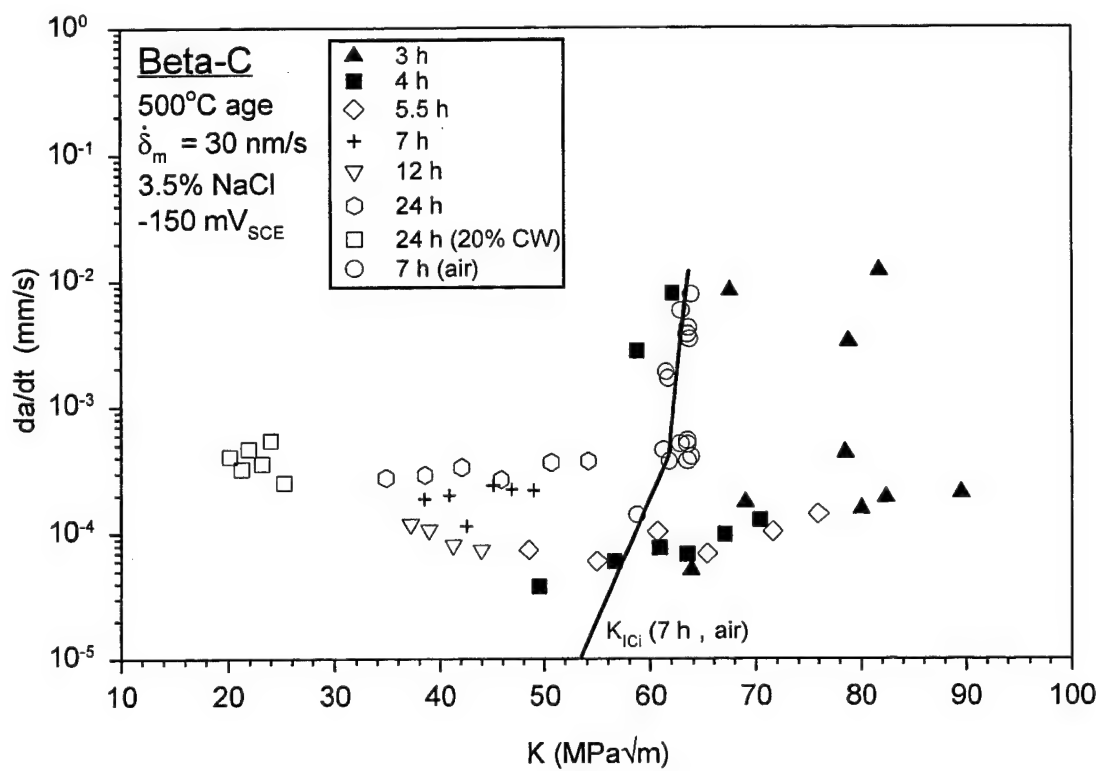


Fig. 4 Slow crack growth rate (da/dt) vs applied stress-intensity factor (K) data for ST/A and ST/CW/A Beta-C in aqueous NaCl and ST/A 7 h Beta-C in air.

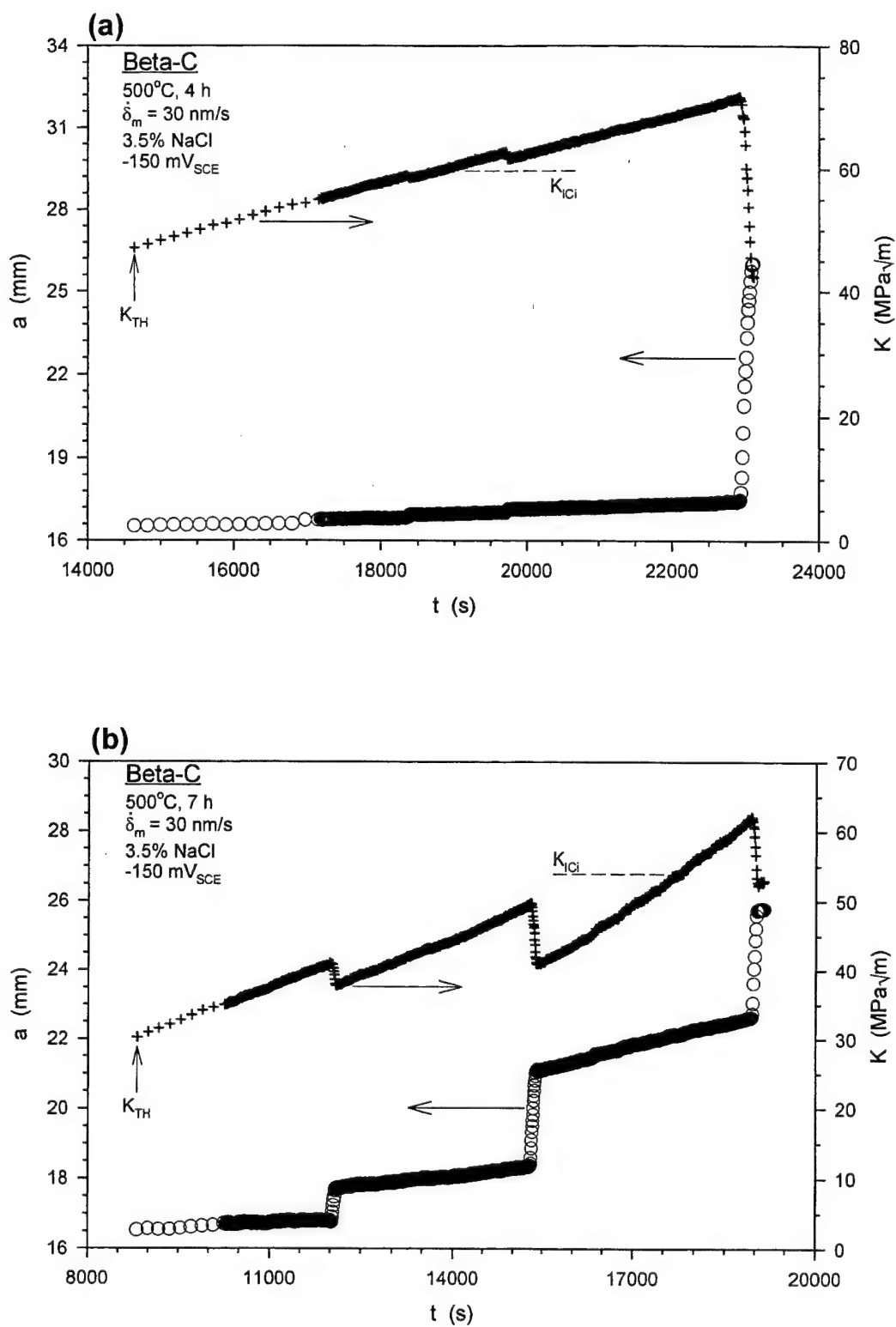


Fig. 5 Crack length (a) and applied stress-intensity factor (K) vs time (t) data for: a) ST/A 4 h Beta-C, and b) ST/A 7 h Beta-C in aqueous NaCl.

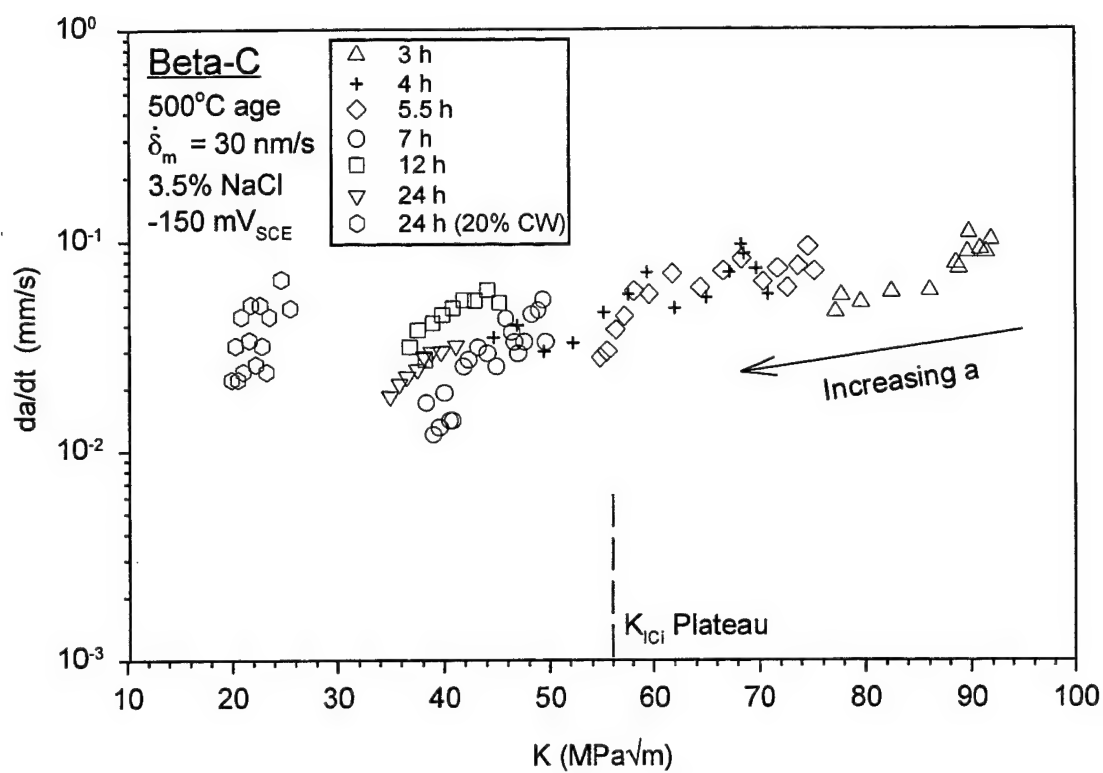
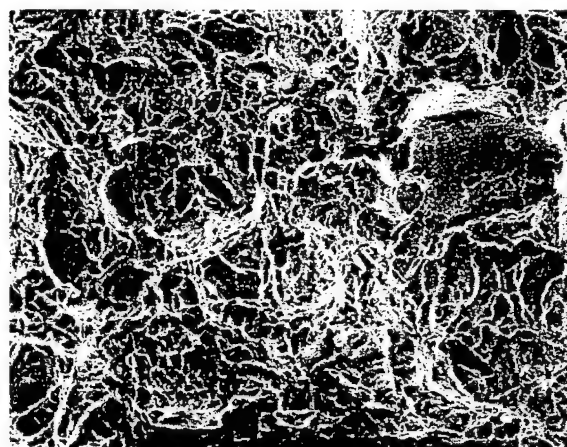


Fig. 6 Rapid crack growth rate (da/dt) vs applied stress-intensity factor (K) data for ST/A and ST/CW/A Beta-C in aqueous NaCl.

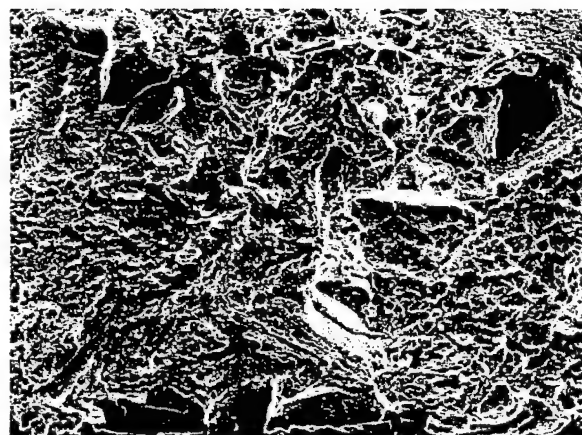


(a)



(b)

100 μm



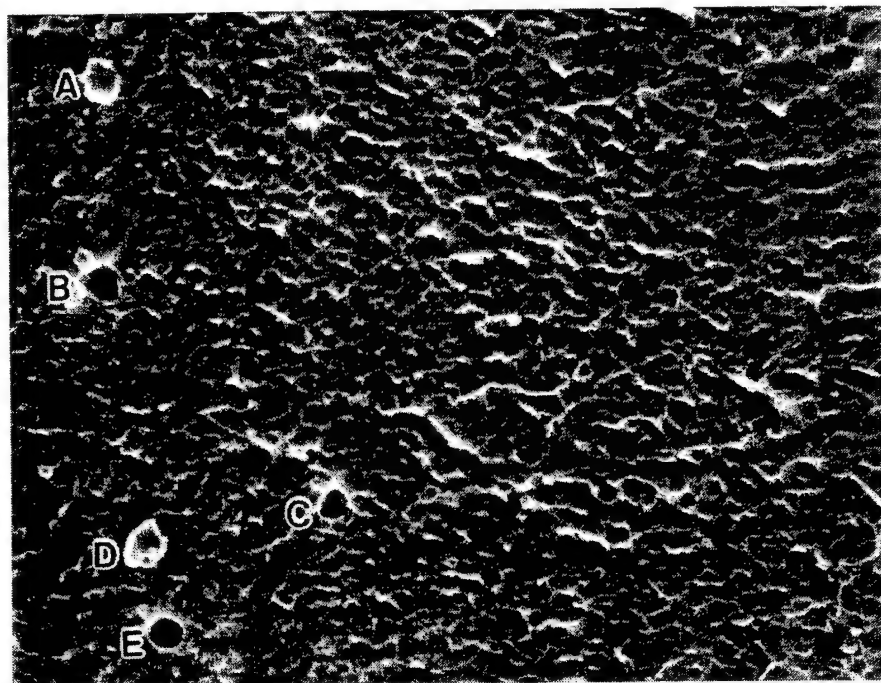
(c)



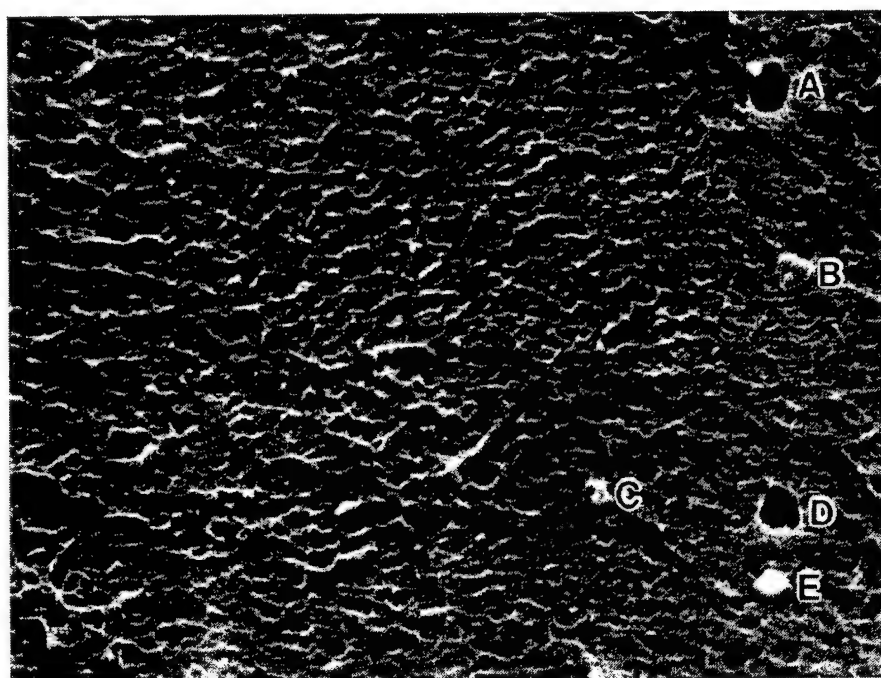
(d)

100 μm

Fig. 7 Low-magnification SEM fractographs for air fracture of: a) ST/A 1 h Beta-C, b) ST/A 3 h Beta-C, c) ST/A 24 h Beta-C, and d) ST/CW/A Beta-C.



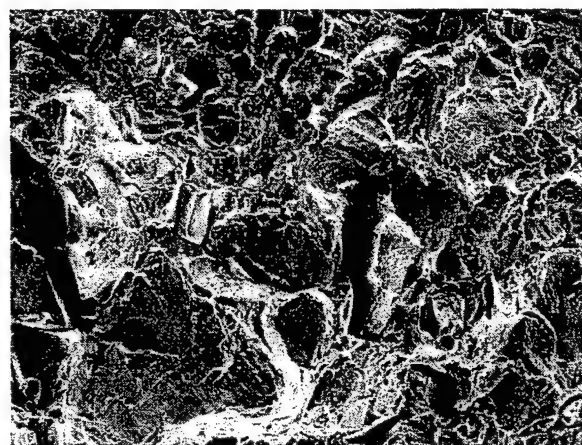
(a)



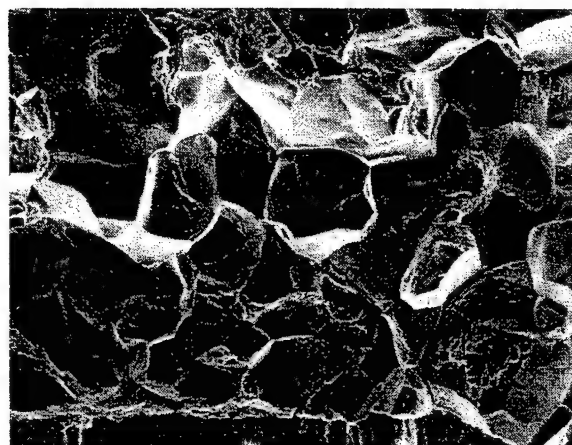
(b)

4 μm

Fig. 8 Matching SEM fractographs from opposite air fracture surfaces showing IG facets at high magnification. The letters A, B, C, D, E indicate matching protrusion/cavity pairs on opposite facets.

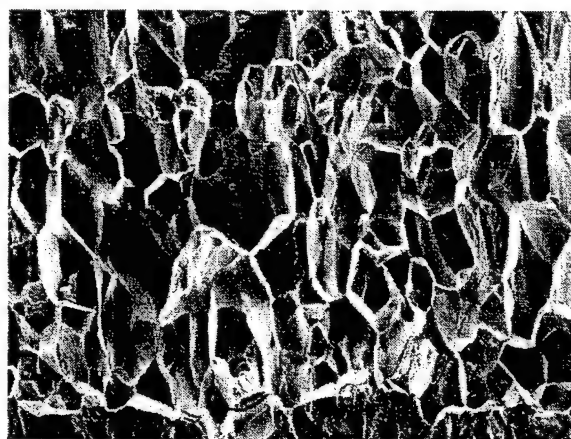


(a)



(b)

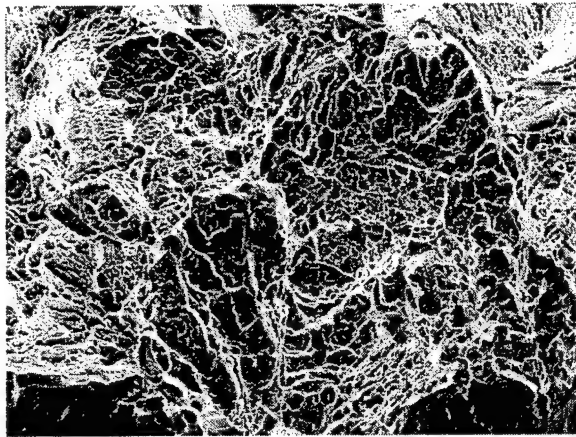
100 μm



(c)

100 μm

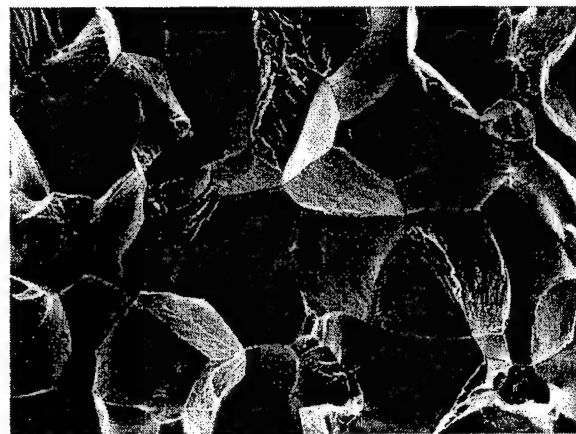
Fig. 9 Low-magnification SEM fractographs for aqueous NaCl EAC of: a) ST/A 2h Beta-C, b) ST/A 12 h Beta-C, and c) ST/CW/A Beta-C.



(a)



(b)



(c)

100 μm

Fig. 10 Low-magnification SEM fractographs for cracking of ST/A 4 h Beta-C in aqueous NaCl:
a) near fatigue precrack, b) at $\Delta a = 3.5$ mm, and c) at $\Delta a = 12$ mm.

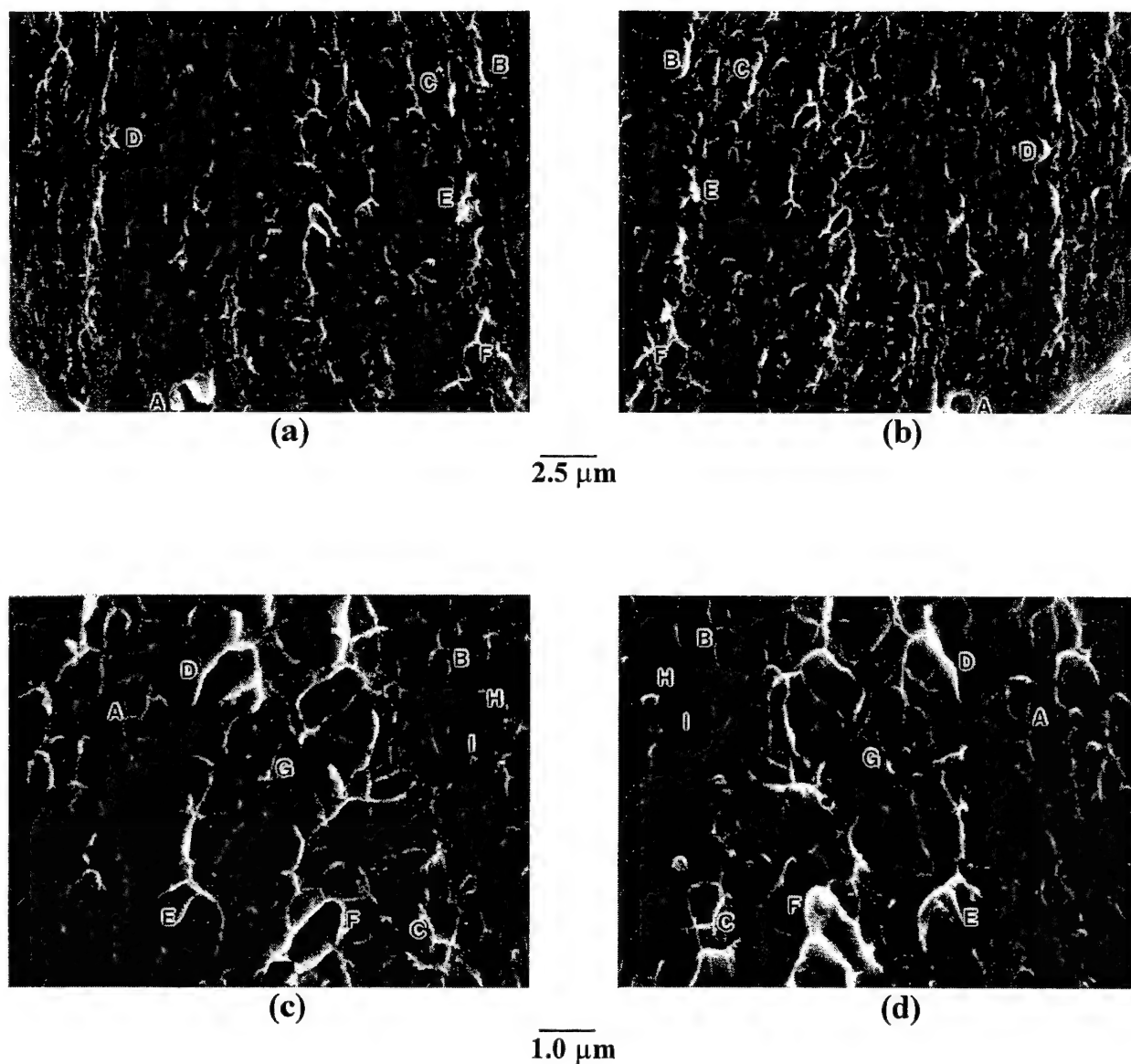
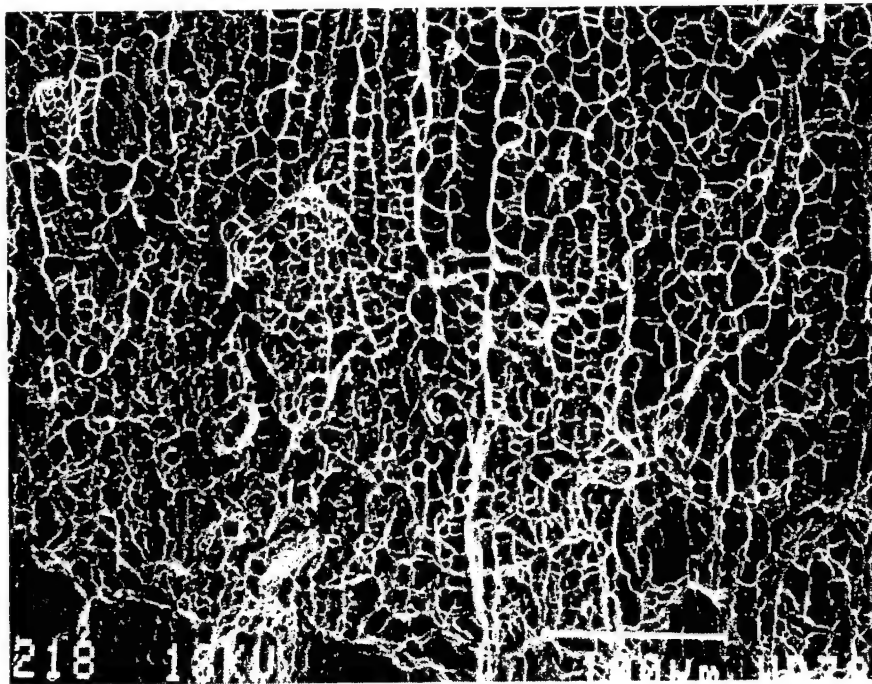
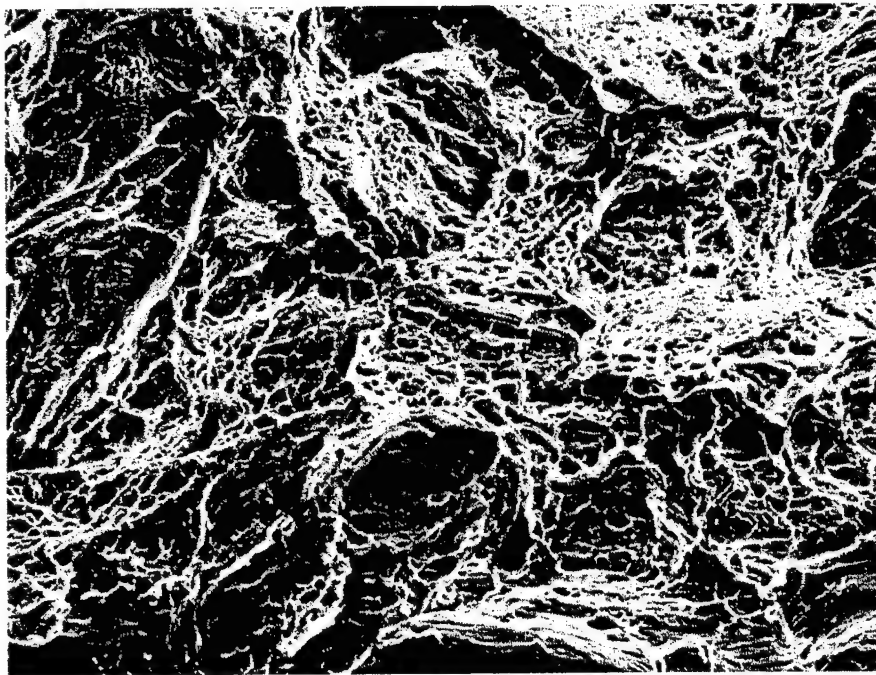


Fig. 11 Matching SEM fractographs from opposite fracture surfaces for ST/A 4 h Beta-C in aqueous NaCl showing the same area at two magnifications: a) and b) lower magnification; A,B,C,D,E,F are matching protrusion/cavity pairs; c) and d) higher magnification; A,B,C are matching pairs of ridge-like protrusions, and D,E,F,G,H,I are matching protrusion/cavity pairs.



(a)

100 μm



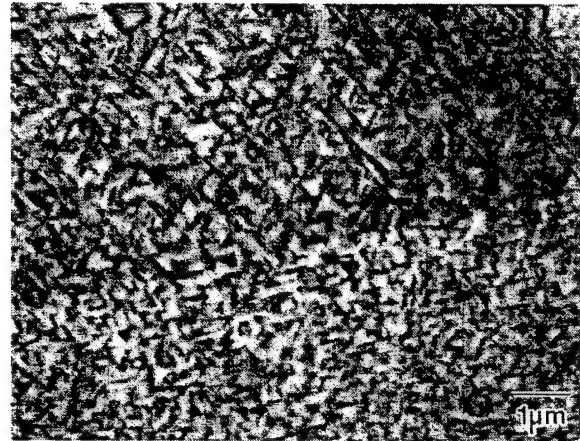
(b)

100 μm

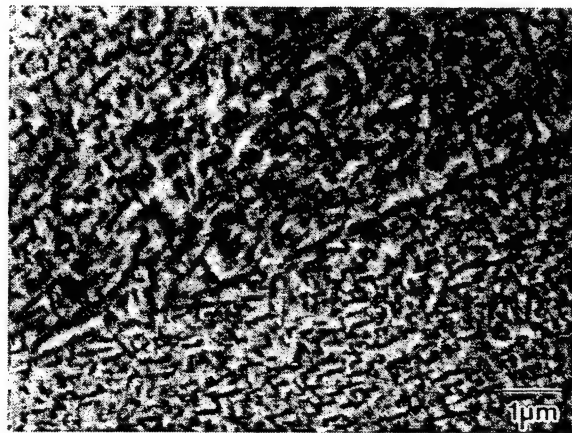
Fig. 12 Low-magnification SEM fractographs for both air and aqueous NaCl cracking of: a) ST/CW 58% Beta-C, and b) ST Beta-C.



(a)



(b)



(c)

Fig. 13 Back-scattered SEM micrographs of grain boundaries for: a) ST/A 4 h Beta-C; b) and c) ST/A 24 h Beta-C.

**The Effect of Crack Tip Strain Rate on Aqueous Environmental
Cracking Resistant Ti-3Al-8V-6Cr-4Mo-4Zr**

B. P. Somerday and R. P. Gangloff

**The Effect of Crack Tip Strain Rate on Aqueous Environmental
Cracking Resistant Ti-3Al-8V-6Cr-4Mo-4Zr**

B. P. Somerday and R. P. Gangloff

The Effect of Crack Tip Strain Rate on Aqueous Environmental-Cracking-Resistant Ti-3Al-8V-6Cr-4Mo-4Zr

Brian P. Somerday and Richard P. Gangloff

ABSTRACT

The objective of this study is to critically examine the intrinsic environment-assisted cracking (EAC) resistance of two microstructures of Ti-3Al-8V-6Cr-4Mo-4Zr (Beta-C) in aqueous NaCl through variations in crack tip strain rate. Single-phase- β Beta-C, cold worked to high strength, is immune to EAC in aqueous NaCl for a range of crack tip strain rates that should allow varying levels of atomic hydrogen production and accumulation. Intergranular EAC in short-term-aged β/α Beta-C is promoted by high crack tip strain rates from rapid loading rates and/or from stable crack growth. These results strengthen the notions that increased yield strength does not promote EAC in β/α Beta-C, and that crack tip strain rate and aging time govern EAC severity.

INTRODUCTION

Numerous variables affect the intergranular (IG) environment-assisted cracking (EAC) susceptibility of β -Ti alloys in neutral aqueous NaCl solutions. The effects of loading rate, crack/stress state configuration and electrode potential on EAC are understood phenomenologically, and mechanistic interpretations are based on crack tip atomic hydrogen (H) production, uptake and embrittlement (HE) [1-11]. The effects of metallurgical variables, such as yield strength (σ_{ys}), deformation mode and α microstructure, are less certain [1,2,7-10]. Experiments to identify the metallurgical properties which promote EAC must investigate a range of mechanical and electrochemical variables to ensure sufficient H production and uptake.

A recent study examined the mechanism for the deleterious effect of aging on the EAC susceptibility of Ti-3Al-8V-6Cr-4Mo-4Zr (Beta-C) in aqueous NaCl. Solution treated Beta-C was either cold worked (ST/CW condition) or isothermally aged (ST/A condition) to produce both β and β/α microstructures having a similar range of σ_{ys} [2]. An important conclusion was that increased alloy σ_{ys} did not cause the EAC susceptibility of β/α ST/A Beta-C compared to the immune single-phase- β ST condition. This conclusion was based on the immunity of ST/CW Beta-C at several levels of cold work. One possible shortcoming of the decisive EAC experiments on ST/CW Beta-C was the use of a single crack mouth opening displacement (δ_m) rate in testing the fracture mechanics specimens. The range of loading rates that produces maximum EAC susceptibility in β -Ti depends on alloy microstructure [4]. Additional experiments over a broad range of loading rates are needed to establish the intrinsic EAC immunity of ST/CW Beta-C.

An additional finding from this study was that Beta-C, aged for short times at 500°C, exhibited novel cracking in aqueous NaCl under constant δ_m rate [2]. Initial extension from the fatigue precrack was by transgranular (TG) microvoid coalescence (MVC), but as the crack propagated stably and the stress-intensity factor increased, an intergranular (IG) contribution to the fracture mode evolved. The fracture mode ultimately became 100% intergranular and the crack growth rate accelerated to nearly 100 $\mu\text{m/s}$. This cracking behavior was interpreted based on increased crack tip strain rate due to crack advance, but further experiments were needed.

The objective of this study is to characterize the EAC behavior of single-phase- β ST/CW Beta-C over a range of loading rates and to determine whether increasing crack tip strain rate

promotes IG EAC in short-term-aged ST/A Beta-C. Experiments are conducted on precracked specimens of Beta-C under constant δ_m rate in aqueous NaCl at fixed electrode potential.

EXPERIMENTAL PROCEDURES

Material

The alloy studied was Beta-C with a composition of Ti-3.4 Al-8.3 V-5.9 Cr-4.1 Mo-4.4 Zr (wt pct), as specified by the manufacturer, RMI Titanium Company. The product form was hot-rolled 41-mm-diameter round bar that was solution heat treated at 815°C for 1 h and air cooled to room temperature (ST condition). The resulting microstructure consisted of single-phase- β grains, equiaxed and 80 μm in size [12].

Two microstructures were studied. The first was produced by cold rolling ST Beta-C by a reduction of 65% (ST/CW condition). The microstructure consisted only of β grains, which were 40 μm by 90 μm in cross-section and 130 μm in length [12], and had a σ_{YS} of 1095 MPa [2]. Processing details are described elsewhere [2]. Although previous EAC experiments on Beta-C cold worked from 20% to 65% indicated that all conditions were equally immune [2], the ST/CW 65% microstructure had the highest σ_{YS} and greatest potential for EAC. The second microstructure was produced by heat treating ST Beta-C isothermally (ST/A condition) at 500°C for 4 h to precipitate a portion of the equilibrium amount of α phase. The α formed as fine plate-like particles (less than 1 μm in length) within β grains, and possibly as very thin layers on β -grain boundaries [1,12-15], and resulted in a σ_{YS} of 985 MPa [2]. Previous experiments showed that ST/A 4 h Beta-C exhibited unique EAC similar to other short-time-aged microstructures, and in contrast to behavior for longer aging times [2].

EAC-Fracture Mechanics

Sidegrooved compact-tension (CT) specimens were used for air fracture toughness as well as EAC measurements of both crack propagation threshold and kinetics. For the ST/A specimens, the crack plane was perpendicular to the longitudinal axis of the round bar with crack growth in the radial direction. The ST/CW specimens were in the TL orientation; viz, with the crack plane

perpendicular to the rolling plane and with crack growth parallel to the rolling direction (the original longitudinal axis). Specimen dimensions and precracking parameters are provided elsewhere [2].

Each fracture mechanics experiment was conducted under monotonically rising δ_m at a fixed rate ($\dot{\delta}_m$) using a servohydraulic mechanical test system operated in δ_m -feedback control. The loading rates for ST/CW 65% Beta-C EAC experiments ($\dot{\delta}_m$ equaling 3 nm/s, 30 nm/s and 4 $\mu\text{m/s}$) were selected to cover a broad range and produced IG EAC in Beta-C aged 24 h at 500°C [4]. The loading rates for ST/A 4 h Beta-C EAC experiments ($\dot{\delta}_m$ equaling 30 nm/s, 800 nm/s and 4 $\mu\text{m/s}$) were selected to achieve specific crack tip strain rates, as discussed in a later section. Experiments in air for both microstructures were conducted at $\dot{\delta}_m$ equaling 30 nm/s. The direct-current potential difference (DCPD) method was used to measure crack extension [4,16,17].

An elastic analysis (stress-intensity factor, K) was sufficient for characterizing the fracture mechanics and plane strain predominated [2]. The K level associated with initial crack extension in aqueous NaCl is a lower-bound threshold (K_{TH}), equivalent to $K_{TH/}$ in Ref. [4]. The K levels corresponding to initial crack extension in air (K_{ICi}) are lower bounds of the standardized values of fracture toughness [16]. The methods of defining K_{TH} and K_{ICi} from load, DCPD and δ_m data are described elsewhere [2]. Crack growth rates (da/dt) were calculated from DCPD-based crack length (a) vs time (t) data using three different methods [2,4]. The method selected depended on the number of a - t data pairs, the crack growth rate, and data variability.

Environment

Experiments were conducted at 25°C in either moist air or flowing neutral 0.6 M (3.5 wt pct) aqueous NaCl (pH = 5 to 6) at a fixed electrode potential of -150 mV (vs the saturated calomel electrode). This electrode potential produced severe IG EAC in both ST/A 24 h Beta-C and ST/A Beta-21S [3,7]. Details are provided in Refs. 3 and 4.

RESULTS

Initial Crack Extension

The effect of loading rate on the threshold for initial crack extension in aqueous NaCl, K_{TH} , is shown in Fig. 1 for both ST/A 4 h and ST/CW 65% Beta-C. Loading rate is expressed in Fig. 1 as the rate of change of stress intensity (dK/dt) prior to crack extension. Figure 1 shows that K_{TH} for both ST/A 4 h (○) and ST/CW 65% (□) Beta-C is nearly constant as loading rate changes over multiple orders of magnitude for each microstructure. A mild decrease in K_{TH} , from an average of 33 MPa \sqrt{m} to 30 MPa \sqrt{m} , is suggested for ST/CW 65% Beta-C as dK/dt decreases from the higher rates to the lowest. A similar decrease in K_{TH} , from 45 MPa \sqrt{m} to 41 MPa \sqrt{m} , is noted for ST/A 4 h Beta-C, but results from an increased loading rate.

Air fracture toughness values, K_{ICi} , are included in Fig. 1 for both microstructures (●, ■) at a single loading rate. Values of K_{TH} essentially equal K_{ICi} for ST/CW 65% Beta-C, but are less than K_{ICi} for ST/A 4 h Beta-C. Since K_{ICi} is likely independent of loading rate [4], the K_{TH} to K_{ICi} comparison in Fig. 1 suggests that ST/CW 65% Beta-C is not susceptible to EAC at any of the loading rates examined, while the aged condition is embrittled by the NaCl solution at each $\dot{\delta}_m$.

Crack Propagation

The crack growth behavior of ST/CW 65% Beta-C is identical for moist air and aqueous NaCl at each loading rate. Following initiation at K_{TH} or K_{ICi} , each crack grows by alternating increments of unstable and stable extension. The increments of unstable crack extension depend on loading rate. The unstable bursts are several millimeters long at $\dot{\delta}_m$ equaling 30 nm/s and 4 μ m/s, but are 1 mm or less at $\dot{\delta}_m$ equaling 3 nm/s. The first unstable event occurs almost immediately following initiation for each loading rate. These results establish that crack growth in ST/CW Beta-C is not environment-sensitive.

The crack growth behavior of ST/A 4 h Beta-C in aqueous NaCl at the slowest $\dot{\delta}_m$ of 30 nm/s was described previously; a vs t and K vs t resemble behavior in air for the first 1 mm of extension [2]. The applied K increases above K_{TH} as slow crack growth progresses, and K_{ICi} is exceeded after some extension. Following this slow da/dt sequence, at K equaling 72 MPa \sqrt{m} , the slope of the a

$vs t$ curve increases dramatically and K decreases. This rapid da/dt behavior is not characteristic of fracture instability, as crack length increases regularly between successive data points and da/dt is finite.

Increasing $\dot{\delta}_m$ from 30 nm/s to 800 nm/s does not alter the $a vs t$ and $K vs t$ trends for ST/A 4 h Beta-C in aqueous NaCl, as shown in Fig. 2(a). The K level at the onset of rapid da/dt decreases from 72 MPa \sqrt{m} to 61 MPa \sqrt{m} as $\dot{\delta}_m$ increases from 30 nm/s to 800 nm/s, although K_{TH} is equal for these two loading rates (Fig. 1). Similar behavior was observed for Beta-C aged 24 h at 500°C [4].

Increasing $\dot{\delta}_m$ further to 4 $\mu\text{m/s}$ results in significant changes to the $a vs t$ and $K vs t$ behaviors for ST/A 4 h Beta-C in aqueous NaCl compared to the lower loading rates, as shown in Fig. 2(b). For this high loading rate, only a brief increment of slow da/dt follows initiation before the crack growth rate accelerates. In contrast to the lower loading rates, K increases monotonically for all crack extension following initiation at K_{TH} . The constant $\dot{\delta}_m$ was interrupted during rapid da/dt for this experiment at K equaling 80 MPa \sqrt{m} , as indicated in Fig. 2(b). The crack growth rate decelerated immediately and the K level decreased continuously under fixed $\dot{\delta}_m$ until crack extension arrested.

The $da/dt vs K$ relationships measured for ST/A 4 h Beta-C in aqueous NaCl during rapid da/dt are presented in Fig. 3 for $\dot{\delta}_m$ equaling 30 nm/s (\square), 800 nm/s (\circ), and 4 $\mu\text{m/s}$ (\diamond). The K level decreased during rapid da/dt for the two lower loading rates, but increased for the highest loading rate. The K -decreasing segment under fixed $\dot{\delta}_m$ (Fig. 2(b)) is shown for the highest loading rate (\diamond). For $\dot{\delta}_m$ equaling 4 $\mu\text{m/s}$, crack growth rates (about 100 $\mu\text{m/s}$) are higher than those for the lower loading rates, and increase mildly as K increases. Data variability obscures the effect of loading rate on da/dt for lower $\dot{\delta}_m$, but the lowest da/dt as well as decreasing da/dt with decreasing K are suggested for $\dot{\delta}_m$ equaling 30 nm/s. The $da/dt vs K$ trend for $\dot{\delta}_m$ equaling 800 nm/s is unclear. The rapid crack growth rates in Fig. 3 are equal to those for severe IG NaCl EAC in other aged Beta-C microstructures at similar K levels [2,4].

Fractography

The ductile air fracture mode for ST/CW 65% Beta-C was not altered by loading in aqueous NaCl at any of the $\dot{\delta}_m$ rates. The fracture surface produced in aqueous NaCl at $\dot{\delta}_m$ equaling 3 nm/s

is shown in Fig. 4, and is identical to those observed for cracking in air as well as higher loading rates in solution [2]. (The fatigue precrack is evident at the bottom of the fractograph in Fig. 4.) The fracture surface morphology, typical of TG MVC, is found for all crack extensions. This result, consistent with equal K_{TH} and K_{ICi} (Fig. 1), establishes that single-phase- β ST/CW Beta-C is not susceptible to EAC.

The aqueous NaCl fracture mode for ST/A 4 h Beta-C changes as the crack extends and K increases at $\dot{\delta}_m$ equaling 30 nm/s, as reported previously [2]. A typical fractograph is presented in Fig. 5(a) and shows a region 1.3 mm beyond the fatigue precrack tip. Transgranular microvoid cracking, typical of air fracture [2], contributes substantially to the fracture mode in Fig. 5(a), but the remaining fracture surface is covered by IG facets, many of which exhibit microscopic plasticity. The proportion of IG fracture increases with increasing crack length and K , and microscopic plasticity on IG facets becomes more subtle [2]. The EAC fracture surface consists ultimately of 100% IG facets which appear smooth at lower magnification (Fig. 5(b)).

Increasing $\dot{\delta}_m$ to 800 nm/s produces a fracture mode (Fig. 6) similar to that for $\dot{\delta}_m$ equaling 30 nm/s (Fig. 5(a)), but a further increase of $\dot{\delta}_m$ rate to 4 $\mu\text{m/s}$ alters the fracture mode (Fig. 7) compared to the lower loading rates. The fracture surfaces represented in Figs. 6 and 7 are near the fatigue precracks, and are comparable to Fig. 5(a). Figure 6 shows significant contributions to the fracture mode from both TG MVC and IG cracking for $\dot{\delta}_m$ equaling 800 nm/s. Many of the facets exhibit microscopic plasticity. Figure 7 shows that increasing $\dot{\delta}_m$ to 4 $\mu\text{m/s}$ produces a fracture surface dominated by IG facets, with only a limited area very near to the fatigue precrack exhibiting evidence of TG MVC. There is an even balance between smooth facets and those with ductile features in Fig. 7. For both loading rates represented in Figs. 6 and 7, the aqueous NaCl fracture mode changes ultimately to 100% smooth IG facets with continued crack extension. The results presented in Figs. 5 through 7, coupled with the lowering of K_{TH} from K_{ICi} (Fig. 1), establish that ST/A 4 h Beta-C is susceptible to EAC in aqueous NaCl, for each $\dot{\delta}_m$ rate examined.

DISCUSSION

The EAC results for β -Ti alloys in aqueous NaCl are interpreted based on HE [1,5]. The H is produced by cathodic electrochemical reaction on the crack tip surface. Crack tip strain ruptures the passive surface film, which enhances the production and uptake of H by exposing the electrochemically active and diffusion-barrier-free base alloy. Atomic hydrogen may be transported from the crack tip surface to trap sites within the process zone. Traps may be either preexisting microstructural features such as α/β interfaces, or plastic strain-generated during crack tip deformation. The location of cracking, exact trap sites, and mechanism by which H lowers the IG fracture resistance of β -Ti have not been identified. The EAC susceptibility is a function of the amount of H in the process zone, the level of crack tip stress which can be sustained to drive HE, and the intrinsic "strength" of the grain boundary region [18].

Effect of Loading Rate on EAC of ST/CW Beta-C

The current results establish the intrinsic EAC resistance of ST/CW Beta-C. Values of K_{TH} equal K_{ICi} (Fig. 1), similar crack growth behaviors are observed for air and aqueous NaCl, and the air TG MVC fracture mode is not altered by aqueous NaCl exposure (Fig. 4) for $\dot{\delta}_m$ spanning three orders of magnitude. Since this ST/CW condition has the greatest EAC potential due to high σ_{YS} , other microstructures with lower amounts of cold work [2] are likely inherently immune.

Previous work used the EAC immunity of ST/CW Beta-C at $\dot{\delta}_m$ equaling 30 nm/s to conclude that increasing σ_{YS} with aging was not the cause of severe IG cracking of ST/A microstructures in aqueous NaCl [2]. One shortcoming was the use of a single loading rate to establish the EAC immunity of ST/CW Beta-C. The current results bolster the conclusion that σ_{YS} is not the critical variable for IG EAC of ST/A β -Ti alloys.

Characterizing the intrinsic EAC susceptibility of ST/CW Beta-C over a range of $\dot{\delta}_m$ is important because this variable governs crack tip strain rate ($\dot{\epsilon}_{CT}$). The crack tip strain rate (proportional to dK/dt) controls the duration of H accumulation in the process zone prior to loading to K_{TH} , as well as the frequency of exposure of the electrochemically active base alloy from surface film rupture. While metallurgical properties, such as α precipitation and elemental segregation at

grain boundaries [2], control the H production, uptake, accumulation and embrittlement that ultimately determine the intrinsic susceptibility of a given microstructure, EAC may be precluded if the salient extrinsic variables, i.e., $\dot{\epsilon}_{CT}$, are outside the window which permits HE to operate. For example, a single loading rate ($\dot{\epsilon}_{CT}$), may not be sufficient for determining the intrinsic EAC resistance of ST/CW Beta-C compared to the ST microstructure because increased trapping of H at dislocations, which inhibits bulk H transport to the grain boundaries, can occur for the former. A slower $\dot{\epsilon}_m$ prolongs the time for H accumulation at grain boundaries in ST/CW Beta-C and allows an intrinsic EAC mechanism to operate.

Effect of Loading Rate on EAC of ST/A 4 h Beta-C

It was proposed previously that the transition from aqueous NaCl fracture with a substantial contribution from TG MVC (Fig. 5(a)) to 100% IG cracking with smooth facets (Fig.5(b)) resulted from increased $\dot{\epsilon}_{CT}$ accompanying stable crack growth [2]. Relative crack tip deformation rates were compared at $\dot{\epsilon}_m$ equaling 30 nm/s for the stationary fatigue precrack at K_{TH} vs the propagating crack at the K level where da/dt accelerated to near 100 $\mu\text{m/s}$. These calculations were conducted using the following continuum solutions for crack tip opening displacement rate ($\dot{\delta}_{CT}$), which is proportional to $\dot{\epsilon}_{CT}$ [7,19-22]:

$$\dot{\delta}_{CT} = 2\alpha \frac{dK}{dt} \frac{K(1-\nu^2)}{\sigma_{ys} E} \quad (1)$$

for the stationary crack subjected to dK/dt at any K, and:

$$\dot{\delta}_{CT} = 2\alpha \frac{dK}{dt} \frac{K(1-\nu^2)}{E \sigma_{ys}} + \beta \frac{\sigma_{ys}}{E} \frac{da}{dt} \ln \left(0.2 \frac{K^2(1-\nu^2)}{\sigma_{ys}^2 r} \right) \quad (2)$$

for the propagating crack. The parameters, α and β , are constants equal to 0.65 and 5.1, ν is Poisson's ratio (0.33), E is elastic modulus, and r is distance behind the crack tip. Calculations of $\dot{\delta}_{CT}$ for $\dot{\epsilon}_m$ equaling 30 nm/s yielded a value of 1.8 nm/s for the stationary crack (Eq. 1) vs 27 nm/s

for the propagating crack (Eq. 2), assuming r equaled $10\text{ }\mu\text{m}$. The crack tip deformation rate increased by over an order of magnitude during stable crack growth. The primary contribution to the increased $\dot{\delta}_{CT}$ for the propagating crack was from the crack growth rate, da/dt , since dK/dt was nearly constant for all crack extension prior to rapid crack growth.

This analysis suggests that IG EAC may be produced from a stationary fatigue precrack in ST/A 4 h Beta-C if dK/dt is increased. Assuming that $\dot{\delta}_{CT}$ (27 nm/s) for the propagating crack in ST/A 4 h Beta-C is a threshold level for rapid IG EAC, then increasing dK/dt according to Eq. 1 to produce an equal $\dot{\delta}_{CT}$ for the stationary crack should promote similar IG cracking, at a K level sufficient to drive HE. This notion was tested by the EAC experiment on ST/A 4 h Beta-C with $\dot{\delta}_m$ equaling 800 nm/s. The $\dot{\delta}_{CT}$ calculated from Eq. 1 at this loading rate, for a K level (25 MPa/m) which produced IG cracking from the fatigue precrack in ST/A Beta-C aged at 500°C for 7 h and longer [2], is similar to that at the onset of IG rapid da/dt for $\dot{\delta}_m$ equaling 30 nm/s. Figure 6 shows, however, that the fracture mode near the fatigue precrack for this elevated loading rate is not fully intergranular, and is similar to that for $\dot{\delta}_m$ equaling 30 nm/s in Fig. 5(a). The K_{TH} values measured for both loading rates are equal (Fig. 1).

While the result of the EAC experiment on ST/A 4 h Beta-C with $\dot{\delta}_m$ equaling 800 nm/s suggests that a unique $\dot{\epsilon}_{CT}$ ($\dot{\delta}_{CT}$) does not govern IG cracking in aqueous NaCl, the following points must be considered. The continuum solutions given by Eqs. 1 and 2 may not represent the correct deformation rates at the tips of stationary and propagating cracks. The accuracy of these solutions and the validity of the J-integral depend on crack tip geometry and strain level, as well as the extent of crack growth [21-24]. The selection of r equal to $10\text{ }\mu\text{m}$ is arbitrary. Smaller values of r yield higher crack tip deformation rates for the propagating crack; for example, with r equal to $1\text{ }\mu\text{m}$, $\dot{\delta}_{CT}$ equals 40 nm/s for a $\dot{\delta}_m$ rate of 30 nm/s. This suggests that a $\dot{\delta}_m$ higher than 800 nm/s may be needed in order to achieve a deformation rate at the stationary crack tip that compares to the propagating crack. In addition microscopic deformation processes which are not described at the continuum scale may be more important.

The EAC experiment on ST/A 4 h Beta-C at $\dot{\delta}_m$ of $4\text{ }\mu\text{m/s}$ was conducted to further test the notion that increased crack tip deformation rate triggers the transition to fully IG EAC. This high loading rate is near the upper limit of experimental capabilities, but produces IG EAC at K_{TH} for

Beta-C aged 24 h at 500°C [4]. The crack tip deformation rate, $\dot{\epsilon}_{CT}$, produced at the stationary precrack tip for this $\dot{\epsilon}_m$ was 390 nm/s. Figure 7 shows that the fracture surface near the fatigue precrack for $\dot{\epsilon}_m$ equaling 4 $\mu\text{m/s}$ consists almost entirely of IG facets. Limited areas of TG MVC are noted and many facets exhibit microscopic plasticity in Fig. 7, but the fracture surface is clearly more intergranular compared to those produced at lower loading rates (Figs. 5(a) and 6). The K_{TH} for this high $\dot{\epsilon}_m$ is decreased compared to the lower loading rates (Fig. 1). The results for high $\dot{\epsilon}_m$ support the notion that increased deformation rate at the stationary crack tip, through increased dK/dt , promotes fully IG EAC from the fatigue precrack for ST/A 4 h Beta-C in aqueous NaCl.

Implications for K_{TH}

The current experiments on ST/A 4 h Beta-C in aqueous NaCl amplify results for other EAC-susceptible aged β -Ti alloys. The K_{TH} vs dK/dt relationship for Beta-C aged 24 h at 500°C (ST/A 24 h Beta-C) differs from that for Beta-21S aged 8 h at 538°C (ST/A Beta-21S) for cracking under rising $\dot{\epsilon}_m$ in neutral aqueous NaCl. A reduced K_{TH} below K_{IGI} and 100% IG separation for all crack lengths were found for ST/A 24 h Beta-C at dK/dt from 3×10^{-4} MPa $\sqrt{\text{m/s}}$ to 4 MPa $\sqrt{\text{m/s}}$, and for ST/A Beta-21S at dK/dt from 10^{-4} MPa $\sqrt{\text{m/s}}$ to 0.1 MPa $\sqrt{\text{m/s}}$. Loading rates above 2 MPa $\sqrt{\text{m/s}}$ precluded EAC for ST/A Beta-21S, but not for ST/A 24 h Beta-C. The EAC data for ST/A 4 h Beta-C show yet another dependency on dK/dt , as fully IG cracking from the fatigue precrack is not produced below 0.5 MPa $\sqrt{\text{m/s}}$. These results indicate collectively that the effect of $\dot{\epsilon}_{CT}$ on EAC depends on microstructure.

Comparison of K_{TH} values for fully IG fracture indicates that ST/A 4 h Beta-C is intrinsically more resistant to EAC compared to microstructures aged for longer times. The K_{TH} for ST/A 4 h Beta-C at $\dot{\epsilon}_m$ equaling 4 $\mu\text{m/s}$ (41 MPa $\sqrt{\text{m}}$) is higher than that for ST/A 24 h Beta-C (32 MPa $\sqrt{\text{m}}$) [4] at the same loading rate. Thus for similar crack tip film rupture frequencies, a higher driving force is needed for microstructures aged for shorter times. It is unclear whether EAC susceptibility is governed by a microstructural effect on H production and uptake, or trapping of H in the crack tip process zone [2].

Implications for da/dt

The rapid crack growth kinetics presented in Fig. 3 for ST/A 4 h Beta-C in aqueous NaCl support the explanation for similar EAC behavior in ST/A 24 h Beta-C under rising δ_m [4]. Loading rate-independent rapid da/dt was observed for ST/A 24 h Beta-C at $\dot{\delta}_m$ from 3 nm/s to 300 nm/s. These EAC kinetics contrasted to the dependence of K_{TH} on loading rate. The differences were resolved by considering the contributions to crack tip strain rate, $\dot{\epsilon}_{CT}$, for propagating vs stationary cracks. Crack growth rate was independent of $\dot{\delta}_m$ for the propagating crack because $\dot{\epsilon}_{CT}$ was dominated by da/dt compared to dK/dt (Eq. 2). Once rapid da/dt commenced, presumably because a threshold K was exceeded [4], the crack produced a moving high strain rate and contributions from external loading were not significant. This notion was supported by interrupting the constant $\dot{\delta}_m$ during rapid crack growth; rapid da/dt was not immediately arrested by fixed δ_m .

Loading rate-independent rapid EAC kinetics are shown for ST/A 4 h Beta-C in Fig. 3 at $\dot{\delta}_m$ equaling 30 nm/s (\square) and 800 nm/s (\circ), but da/dt is increased noticeably by raising $\dot{\delta}_m$ to 4 $\mu\text{m/s}$ (\diamond). In addition interrupting the constant $\dot{\delta}_m$ of 4 $\mu\text{m/s}$ causes da/dt to decrease immediately under fixed δ_m for ST/A 4 h Beta-C (Figs. 2(b) and 3). These results indicate that for sufficiently high loading rates, the contributions of dK/dt and da/dt to $\dot{\epsilon}_{CT}$ are comparable, and crack growth rate can increase for increasing $\dot{\delta}_m$ or decrease for fixed δ_m .

CONCLUSIONS

1. Single-phase- β Beta-C, cold worked to high strength, is intrinsically immune to EAC in aqueous NaCl for a range of crack tip strain rates that allow varying levels of crack tip H production and accumulation.
2. Intergranular EAC in underaged β/α Beta-C is promoted by high crack tip strain rates from rapid loading rates and/or from stable crack growth. Existing continuum solutions for crack tip strain rate are not sufficient to precisely reconcile dK/dt and da/dt contributions.
3. The severity of EAC in ST/A Beta-C, as measured by decreasing K_{TH} , increases with aging time for both high and low constant crack tip strain rates.
4. The K_{TH} vs crack tip strain rate relationship for EAC-susceptible ST/A β -Ti alloys depends

on microstructure. The microstructural variable which governs the strain rate-dependent EAC response has not been determined.

ACKNOWLEDGMENTS

This research was supported by the Office of Naval Research (Grant N00014-91-J-4164), with Dr. A. John Sedriks as Scientific Monitor. Material was donated by the RMI Titanium Company, and mechanical processing was conducted by J.R. Hughes of the General Electric Corporate Research and Development Center. These contributions are gratefully acknowledged.

REFERENCES

- [1] L.M. Young, G.A. Young, J.R. Scully and R.P. Gangloff: *Metall. Mater. Trans A*, 1995, vol. 26A, pp. 1257-1271.
- [2] B.P. Somerday and R.P. Gangloff: submitted to *Metall. Mater. Trans. A*, 1996.
- [3] B.P. Somerday, J.A. Grandle and R.P. Gangloff: in *Proceedings of the Tri-Service Conference on Corrosion*, T. Naguy, ed., Materials Laboratory, Wright-Patterson Air Force Base, OH, 1994, pp. 375-392.
- [4] B.P. Somerday, L.M. Young and R.P. Gangloff: submitted to *Metall. Mater. Trans. A*, 1995.
- [5] D.G. Kolman: PhD Thesis, University of Virginia, Charlottesville, VA, 1995.
- [6] D.G. Kolman and J.R. Scully: in *Effects of the Environment on the Initiation of Crack Growth, ASTM STP 1298*, W.A. Van der Sluys, R.S. Piascik, and R. Zawierucha, eds., ASTM, Philadelphia, PA, 1997, in review.
- [7] L.M. Young: MS Thesis, University of Virginia, Charlottesville, VA, 1993.
- [8] M.J. Blackburn, J.A. Feeney and T.R. Beck: in *Advances in Corrosion Science and Technology*, M.G. Fontana and R.W. Staehle, eds., Plenum Publishing, NY, NY, 1972, vol. 3, pp. 67-292.
- [9] M.J. Blackburn, W.H. Smyrl and J.A. Feeney: in *Stress Corrosion Cracking in High Strength Steel and in Titanium and Aluminum Alloys*, B.F. Brown, ed., Naval Research Laboratory, Washington, DC, 1972, pp. 245-363.
- [10] J.A. Feeney and M.J. Blackburn: *Metall. Trans*, 1970, vol. 1, pp. 3309-3323.
- [11] D.A. Meyn and P.S. Pao: in *Slow Strain Rate Testing for the Evaluation of Environmentally Induced Cracking: Research and Engineering Applications, ASTM STP 1210*, R.D. Kane, ed., ASTM, Philadelphia, PA, 1993, pp. 158-169.
- [12] M.A. Gaudett and J.R. Scully, submitted to *Scripta Metall.*, 1996.
- [13] T.J. Headley and H.J. Rack: *Metall. Trans. A*, 1979, vol. 10A, pp. 909-920.
- [14] C.G. Rhodes and N.E. Paton: *Metall. Trans. A*, 1977, vol. 8A, pp. 1749-1761.
- [15] T.W. Duerig and J.C. Williams: in *Beta Titanium Alloys in the 80's*, R.R. Boyer and H.W. Rosenberg, eds., The Metallurgical Society of AIME, Warrendale, PA, 1984, pp. 19-67.

- [16] B.P. Somerday, Y. Leng and R.P. Gangloff: *Fatigue Fract. Engng Mater. Struct.*, 1995, vol. 18, pp. 565-582.
- [17] J.K. Donald and J. Ruschau: in *Fatigue Crack Measurement: Techniques and Applications*, K.J. Marsh, R.A. Smith and R.O. Ritchie, eds., EMAS, West Midlands, UK, 1991, pp. 11-37.
- [18] K.N. Akhurst and T.J. Baker: *Metall. Trans. A*, 1980, vol. 12A, pp. 1059-1070.
- [19] D.P.G. Lidbury: in *Embrittlement by the Localized Crack Environment*, R.P. Gangloff, ed., The Metallurgical Society of AIME, Warrendale, PA, 1983, pp. 149-172.
- [20] C.F. Shih: *J. Mech. Phys. Solids*, 1981, vol. 29, pp. 305-326.
- [21] J.R. Rice, W.J. Drugan and T-L. Sham: in *Fracture Mechanics: 12th Conference, ASTM STP 700*, P.C. Paris, ed., ASTM, Philadelphia, PA, 1980, pp. 189-221.
- [22] J.R. Rice and E.P. Sorensen: *J. Mech. Phys. Solids*, 1978, vol. 26, pp. 163-186.
- [23] R.M. McMeeking: *J. Mech. Phys. Solids*, 1977, vol. 25, pp. 357-381.
- [24] J.W. Hutchinson: *J. Appl. Mech. Trans. ASME*, 1983, vol. 50, pp. 1042-1051.

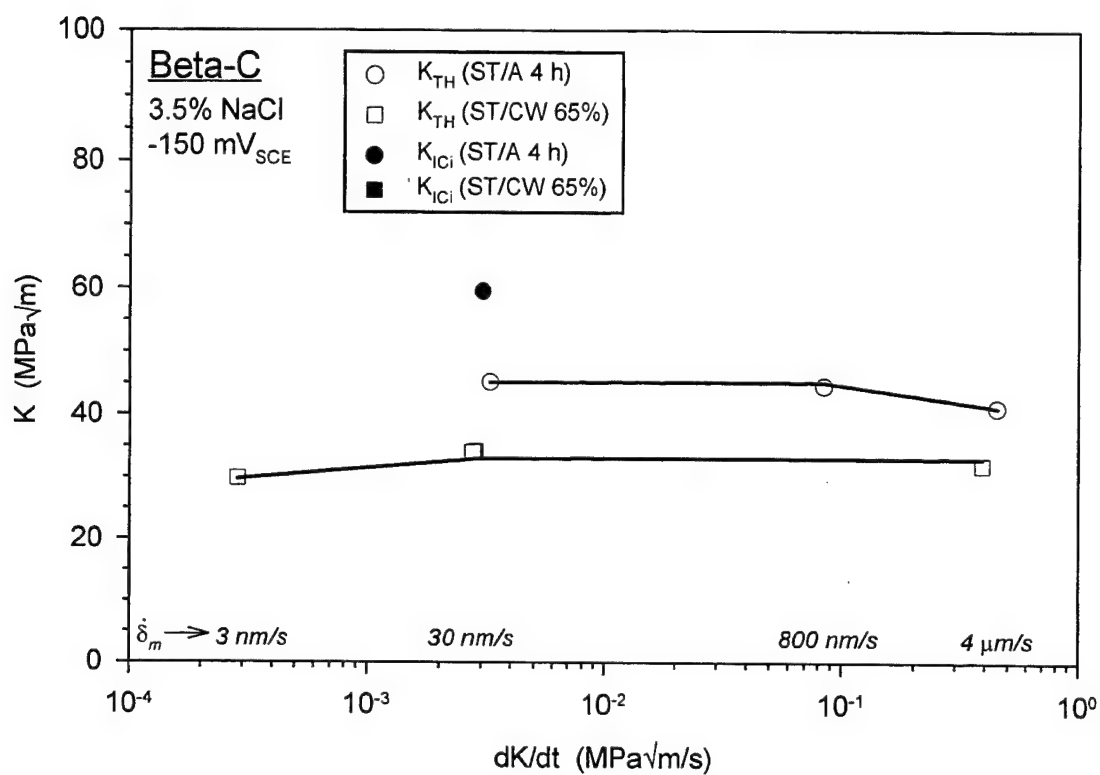


Fig. 1 Dependence of EAC threshold stress intensity (K_{TH}) on rate of change of stress intensity (dK/dt) prior to the onset of cracking for ST/A 4 h and ST/CW 65% Beta-C. Air fracture toughnesses (K_{ICi}) are shown for each microstructure at a constant loading rate.

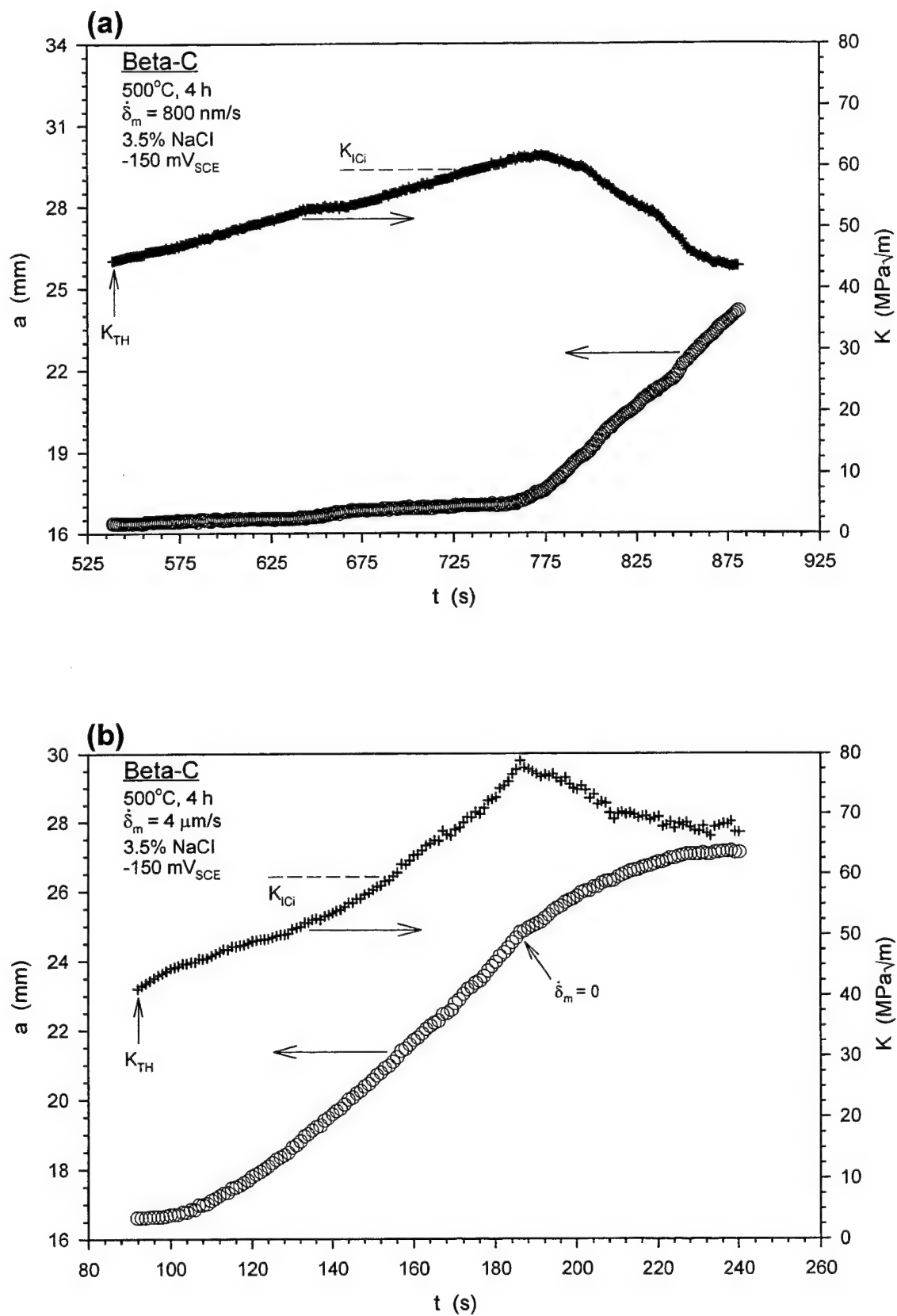


Fig. 2 Crack length (a) from DCPD and stress intensity (K) vs time (t) for ST/A 4 h Beta-C in aqueous NaCl at displacement rates of: a) 800 nm/s, and b) 4 $\mu\text{m/s}$.

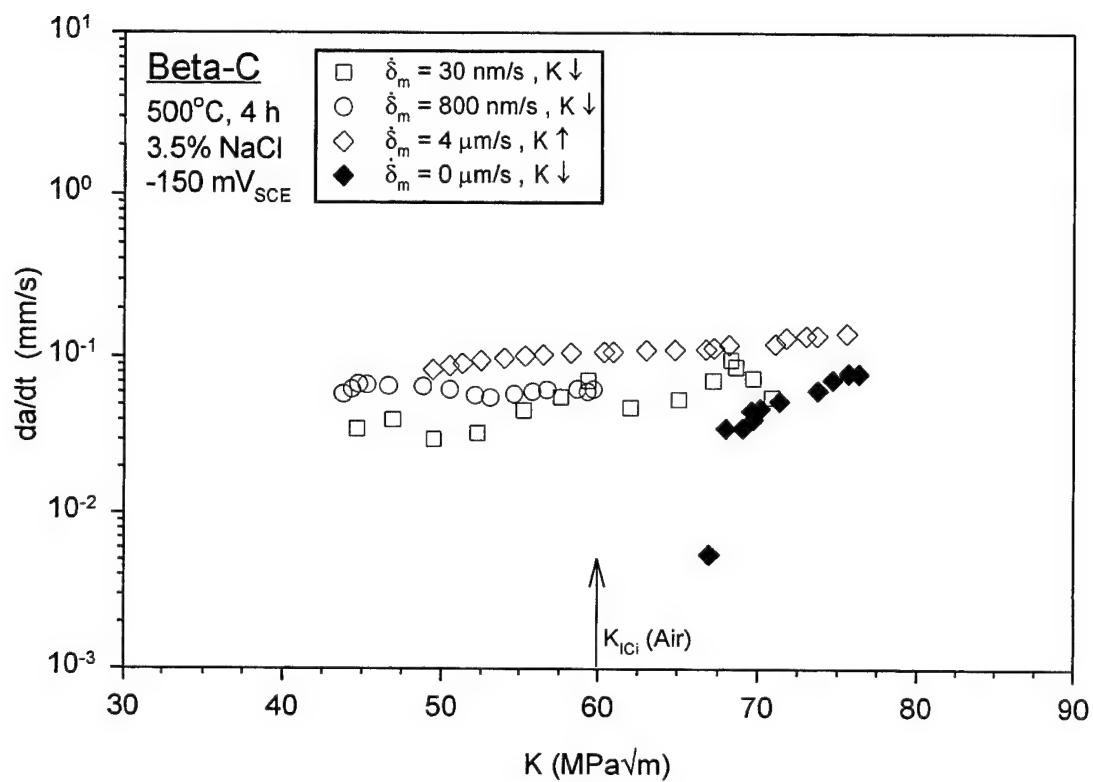
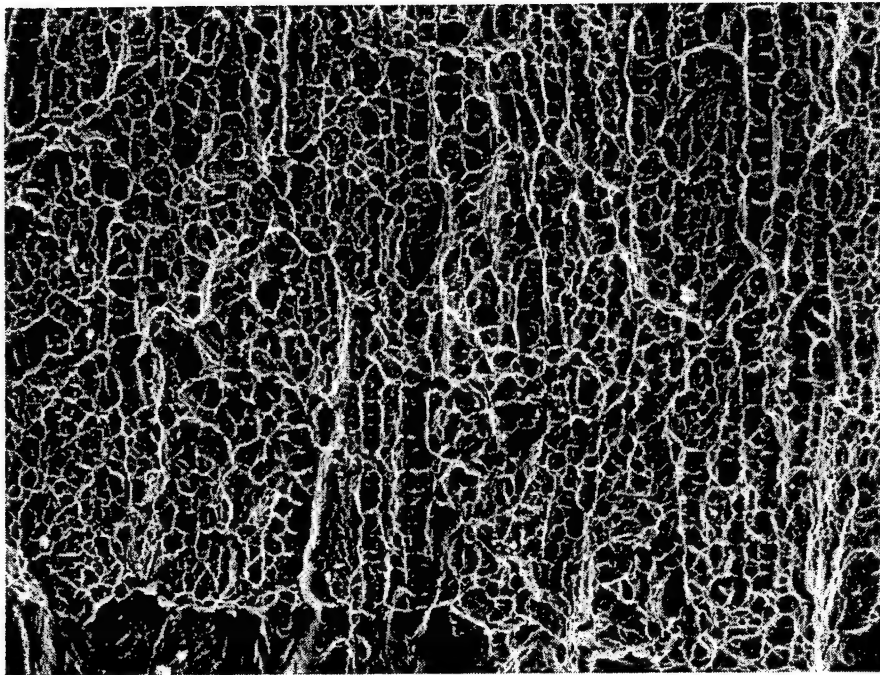
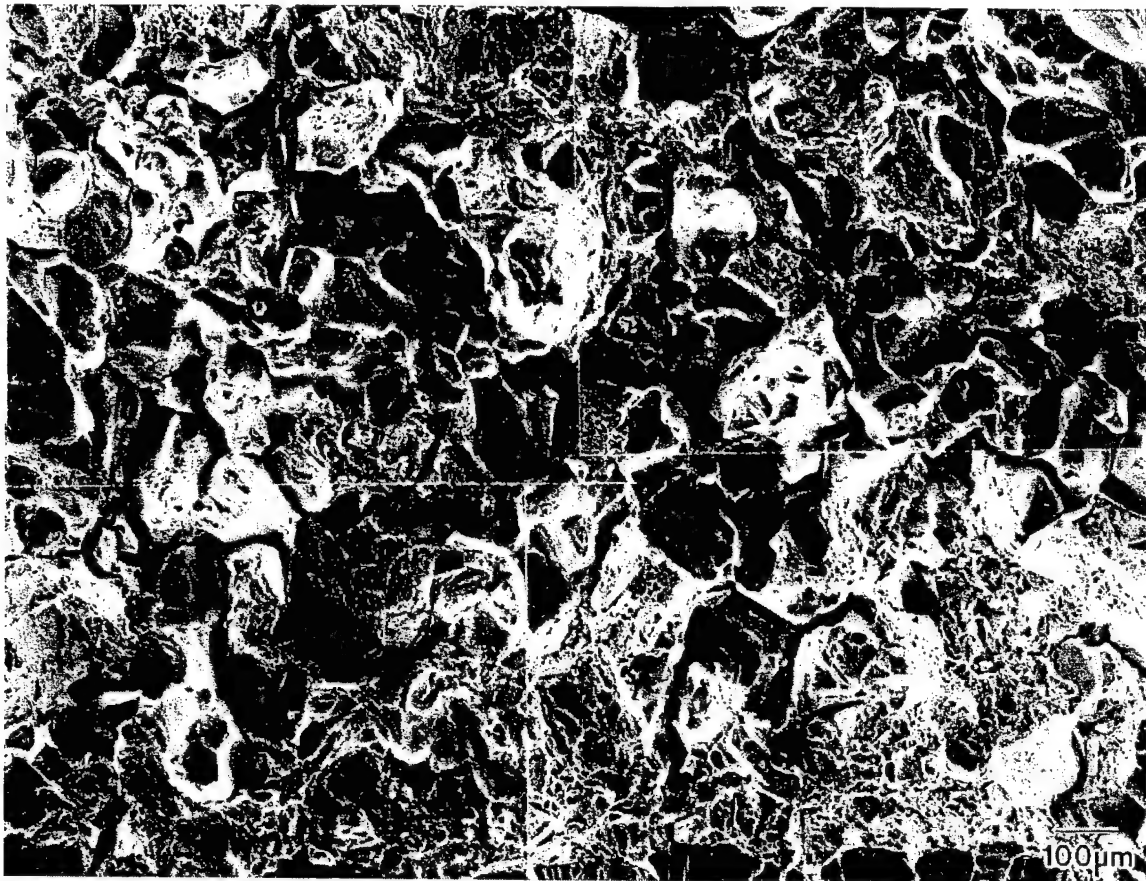


Fig. 3 The EAC growth rate (da/dt) vs stress intensity (K) relationships for ST/A 4 h Beta-C loaded at four displacement rates in aqueous NaCl.

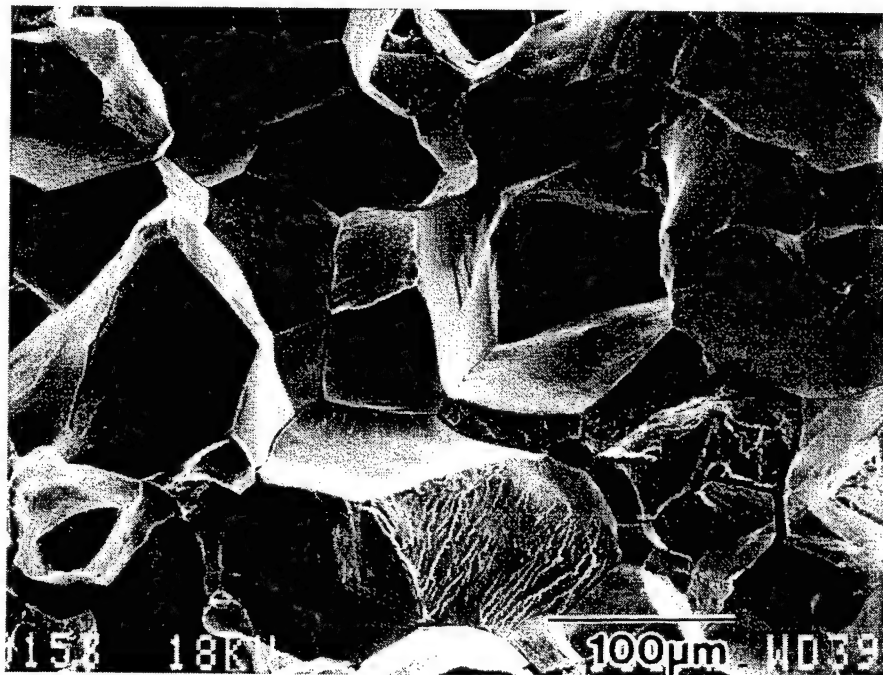


100 μm

Fig. 4 Fractograph of ST/CW 65% Beta-C cracked in aqueous NaCl at a displacement rate of 3 nm/s. The precrack is evident at the bottom of the fractograph.



(a)



(b)

Fig. 5 Fractographs of ST/A 4 h Beta-C cracked in aqueous NaCl at a displacement rate of 30 nm/s: a) near the fatigue precrack, and b) near the end of EAC. The precrack is evident at the bottom of the fractograph in a).

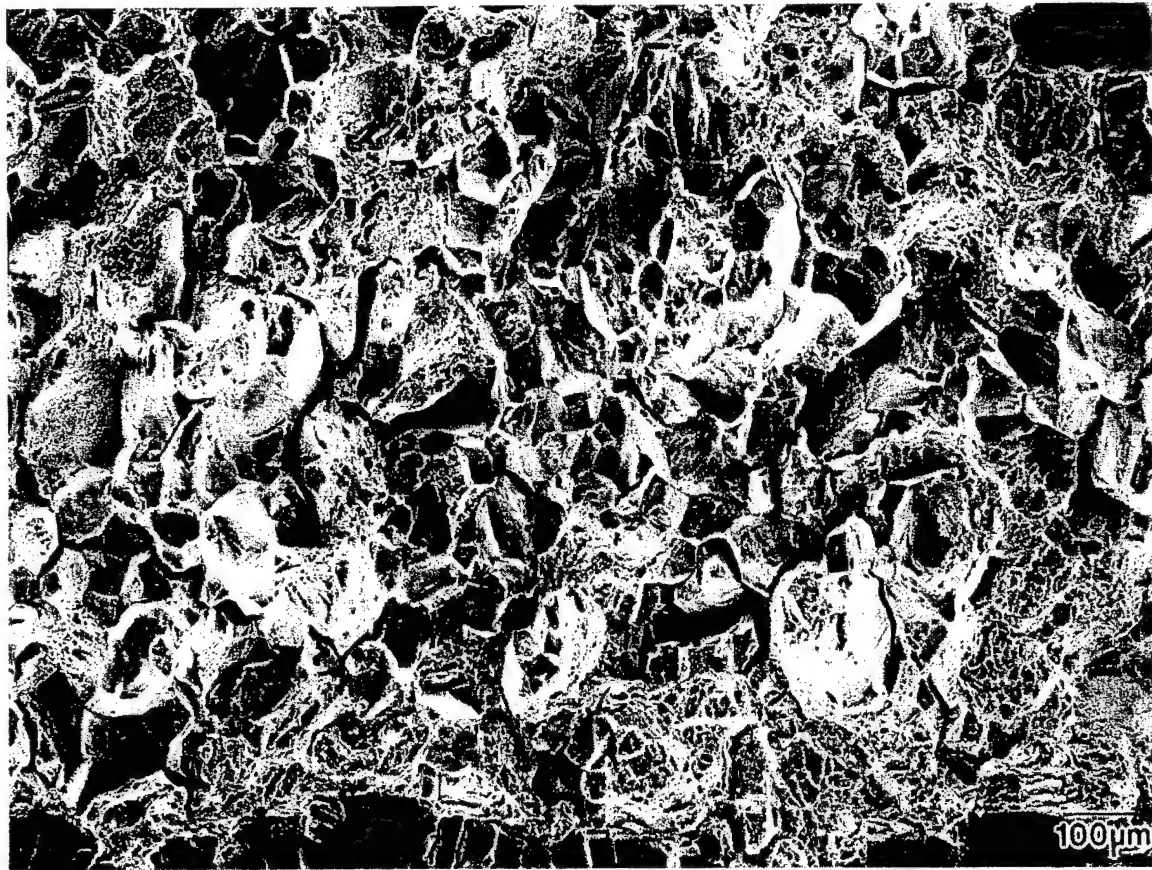


Fig. 6 Fractograph of ST/A 4 h Beta-C cracked in aqueous NaCl at a displacement rate of 800 nm/s. The precrack is evident at the bottom of the fractograph.

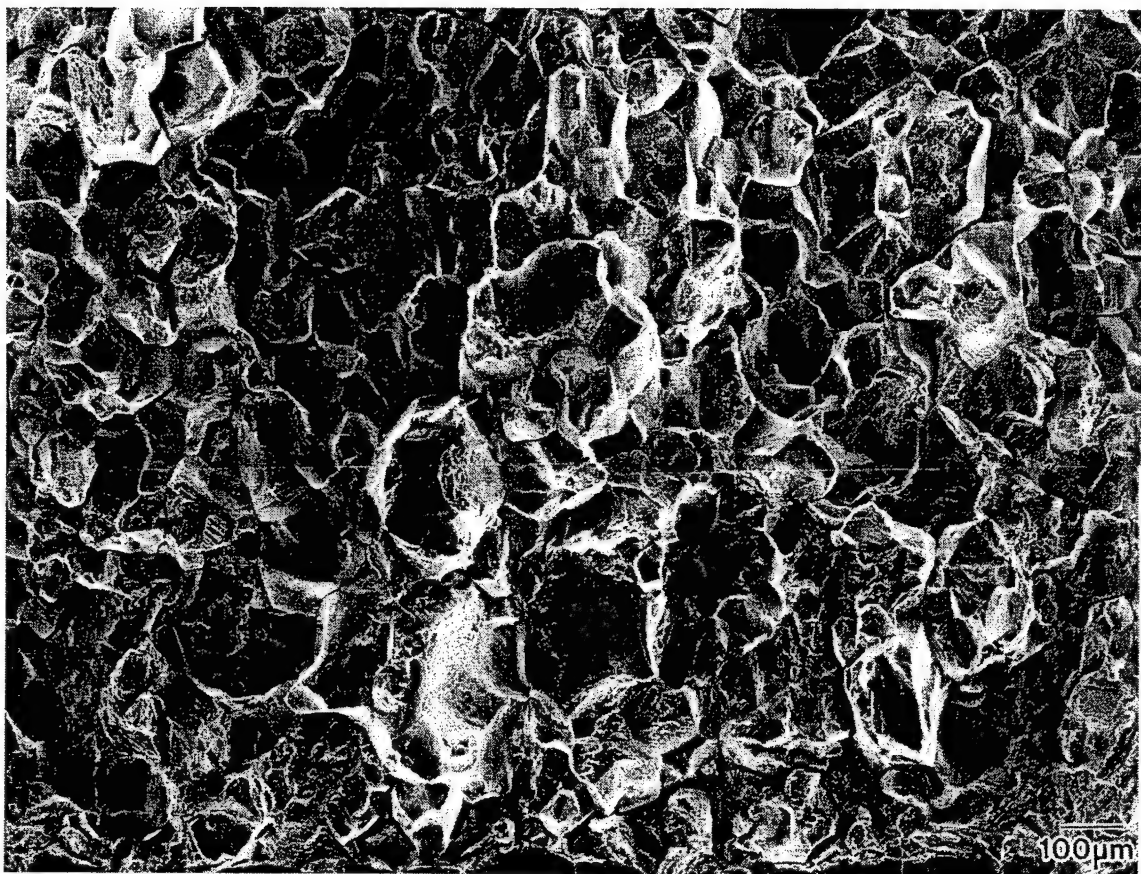


Fig. 7 Fractograph of ST/A 4 h Beta-C in aqueous NaCl at a displacement rate of 4 $\mu\text{m/s}$. The precrack is evident at the bottom of the fractograph.

Measurement of Crack Opening Displacement and Crack Tip Strain for Transgranular and Intergranular Cracks in Aged β -Ti

B. P. Somerday and R. P. Gangloff

MEASUREMENT OF CRACK OPENING DISPLACEMENT AND CRACK TIP STRAIN FOR TRANSGRANULAR AND INTERGRANULAR CRACKS IN AGED β -Ti

Brian P. Somerday and Richard P. Gangloff

ABSTRACT

The objective of this study is to measure the displacement and strain distributions near intergranular (IG) and transgranular (TG) crack tips as a function of stress intensity and time in order to better understand environmental embrittlement in a high-strength β/α Ti alloy. Measured crack opening displacements for TG fatigue cracks exceed those for IG environmental cracks at all stress intensities and distances behind the crack tip. Strains ahead of IG cracks can exceed those for TG cracks due to grain boundary discontinuities such as triple points. In the absence of such discontinuities, strain is lower for IG cracks compared to TG cracks, consistent with the crack openings. Larger strains ahead of TG cracks compared to IG cracks may explain why the former propagate under static loading in aqueous NaCl, but the latter remain stationary. The lack of measurable time-dependent deformation ahead of TG cracks suggests that continuum crack tip creep does not govern EAC; rather, local deformation processes are important.

INTRODUCTION

The experimental variables which govern environment-assisted cracking (EAC) of α -precipitation-hardened β -Ti alloys in aqueous NaCl have been studied extensively; including applied electrode potential, cracked vs smooth specimens, loading rate, crack growth rate, yield strength, and α -microstructure [1-12]. Mechanistic interpretations, based on a hydrogen embrittlement (HE) scenario for EAC, indicate that these variables affect the local mechanics or electrochemistry at the crack tip. For example, loading rate and crack growth rate control crack tip strain rate, which is critical for mechanically destabilizing the passive surface film to allow hydrogen (H) production and uptake into the process zone. Fracture mechanics modeling to date does not adequately describe the stress intensity (K) and position dependencies of crack tip strain and strain rate.

Effects of inert environment prestrain and fracture mode, i.e, transgranular (TG) vs intergranular (IG), on crack propagation in aqueous NaCl were demonstrated recently for β/α Ti alloys [13]. Fatigue-precracked compact-tension (CT) specimens of aged Ti-3Al-8V-6Cr-4Mo-4Zr (Beta-C) were loaded in air to a K which exceeded the threshold for EAC in aqueous NaCl, but was below the air fracture toughness. After maintaining this K level under fixed crack mouth opening displacement (δ_m) for various times, the specimens were exposed to aqueous NaCl. The TG fatigue precrack extended by IG separation in aqueous NaCl, after air exposure at constant δ_m for several minutes, but remained stationary in solution following a 24 h air hold time; i.e., EAC was precluded for the latter case. In addition similar experiments showed that IG cracks loaded in air to a fixed δ_m did not propagate in aqueous NaCl following hold times of any duration in the air environment. It was suggested that the time and crack tip shape dependencies of crack tip creep strain rates accounted for the observed behavior, but this conclusion was speculative.

The objective of this study is to measure the displacement and strain distributions near IG and TG crack tips, as a function of K and time, in order to ascertain whether local mechanics explain the effects of cracking mode and inert environment prestrain on the EAC response of aged β -Ti alloys. Displacement and strain distributions are measured from scanning electron microscope (SEM) images of the surfaces of loaded CT specimens containing IG or TG cracks using the stereoinaging technique.

EXPERIMENTAL PROCEDURES

Material

The alloy studied was Beta-C (Ti-3.4Al-8.3V-5.9Cr-4.1Mo-4.4Zr; wt pct). The product form was hot-rolled 41-mm-diameter round bar that was solution heat treated at 815°C for 1 h and air cooled to room temperature (ST condition). The resulting microstructure consisted of single-phase- β grains, equiaxed and 80 μm in size, and had a yield strength (σ_{YS}) of 875 MPa [5,14]. The ST microstructure was aged at 500°C for 24 h to produce fine (less than 1 μm in length) plate-like α precipitates within β grains, and occasional thin layers on β -grain boundaries, which increased the alloy σ_{YS} to 1175 MPa (ST/A 24 h condition) [3,5].

Test Specimens

Transgranular and intergranular cracks were produced in sidegrooved CT specimens typically used for fracture-mechanics experiments on Beta-C in air and aqueous NaCl [2-5,13]. The specimens had dimensions of width (W) = 30 mm, gross thickness (B) = 6 mm, and net thickness (B_N) = 5 mm. A TG crack was created in one specimen by fatigue in moist air, with the final K_{MAX} = 15 MPa $\sqrt{\text{m}}$, ΔK = 10 MPa $\sqrt{\text{m}}$, and crack length-to-width ratio (a/W) = 0.53. Two IG-cracked specimens were produced by loading fatigue-precracked CT specimens monotonically under constant crack mouth opening displacement rate ($\dot{\delta}_m$) in aqueous NaCl. Details of this procedure are described elsewhere [2,4,5]. Examination of CT specimens loaded in aqueous NaCl shows that the fracture surface is covered entirely by IG facets (Fig. 1), i.e., no other fracture mode contributes to crack extension. The EAC kinetics in ST/A 24 h Beta-C under constant $\dot{\delta}_m$ are characterized by alternating slow-rapid rates, with associated rising and falling K [4,5]. The IG cracks were terminated immediately following a rapid crack growth rate event under falling K ; final K levels were from 38 MPa $\sqrt{\text{m}}$ to 39 MPa $\sqrt{\text{m}}$, with a/W from 0.67 to 0.73.

The CT specimens containing TG and IG cracks were machined into smaller CT specimens (B = 3 mm and W = 16 mm) without sidegrooves, which were suitable for measuring crack tip displacement and strain. Material was removed from the larger CT specimens to produce a/W ratios

from 0.53 to 0.59 and thickness was reduced equally in both directions. The surfaces of each specimen were ground and polished, then ion milled. These procedures revealed the grain boundaries and produced fine, contrasting features on the surface which were needed for local displacement measurements.

Stereoimaging Measurements

Scanning electron micrographs were taken of the crack tip region (at magnifications up to 2000x) on the small CT specimen surface, which was subjected to controlled load *vs* time (*t*) conditions. Each specimen was loaded under servohydraulic-actuator displacement control in a stage which fit into the SEM [15]. Actuator displacement was interrupted several times while increasing the load monotonically to the maximum in order to photograph the crack tip at multiple *K* levels. Each TG or IG specimen was held at the maximum *K* level in order to photograph the crack tip periodically for up to 3 h. The maximum *K* levels were similar to those used for EAC experiments on TG and IG cracks [13].

Displacements within the CT specimen surface plane near the crack tip, induced by either active loading or time-dependent deformation, were measured from SEM photographs using the stereoimaging technique and DISMAP system [16-18]. Displacements in the crack wake were used to measure crack opening, whereas those ahead of the crack were used to calculate strain. A photograph of the unloaded crack was compared to those at increasing load levels to measure displacements as a function of *K*, while the first photograph taken upon reaching the maximum *K* level (*t* = 0) was used as the reference for displacements evolving over time at fixed *K*.

RESULTS

Crack Tip Profiles

The TG surface crack profile is characterized in Figures 2(a) through 2(d). Figure 2(a), an SEM micrograph at 400x magnification for *K* = 5 MPa√m, shows that the TG crack consists of a single macroscopic plane normal to the loading direction. Figures 2(b) through 2(d) are higher-magnification (1000x) micrographs which show two notable changes in the crack tip profile as *K*

increases to 44 MPa \sqrt{m} . First, the originally sharp TG fatigue crack tip progressively blunts as K increases due to intense deformation ahead of the tip. The crack tip does not blunt into a shape with smooth curvature, but rather exhibits vertices (Fig. 2(d)). Second, a band of intense shear (Figs. 2(c) and 2(d)), which intersects the crack tip at an angle of nearly 90° to the crack plane, forms at a K level of about 33 MPa \sqrt{m} . A 3-h hold at the maximum K level of 44 MPa \sqrt{m} and in vacuum at 25°C did not produce any noticeable change in the TG crack tip profile.

The surface profiles for both IG-cracked specimens (Figs. 3(a) through 3(c) and Figs. 4(a) through 4(d)) show contrasting features compared to the TG crack. While the TG crack is defined by a single plane, the IG cracks exhibit microscopic branching, as characterized by the SEM micrographs (300x to 500x) in Figs. 3(a) (K = 32 MPa \sqrt{m}) and 4(a) (K = 39 MPa \sqrt{m}) showing the ends of the cracks. The orientations of "local" IG crack planes can vary from that of the macroscopic crack plane, which is normal to the loading direction for both specimens, and the IG crack does not have a single tip. Higher-magnification (1000x) micrographs of Figs. 3(a) and 4(a) show that IG crack tips can respond to load differently. The IG crack tip in Fig. 3(a) ("A") remains sharp compared to the TG crack tip for similar K levels (Figs. 3(b) and 3(c) compared to Figs. 2(c) and 2(d)). The IG crack tip in Fig. 4(a), located at a grain boundary triple point ("A"), extends slightly by stable tearing into a neighboring grain as K increases (Figs. 3(b) through 3(d)), but is nonetheless much sharper than the TG crack (Figs. 2(c) through 2(d)) for similar K levels. The IG crack tip tearing was unexpected as the applied K levels (33 MPa \sqrt{m} to 47 MPa \sqrt{m}) were below K_{ICi} (56 MPa \sqrt{m} to 62 MPa \sqrt{m}) and the EAC IG fracture surfaces show no evidence of cracks meandering out of the grain boundary plane [2,5]. Similar to the TG crack, the IG crack tip profiles did not change during a vacuum hold time of 2.5 h at maximum K.

Crack Opening Displacement

Crack opening displacement parallel (COD_x) and perpendicular (COD_y) to the loading direction was measured as a function of positive distance behind the crack tip (y) for the TG and IG

cracks, and for increasing K , as summarized in Figs. 5 through 7.¹ The plots in Figs. 5 through 7 are intended to compare the following: 1) opening displacements of TG vs IG cracks, 2) the magnitude of opening displacement parallel vs perpendicular to the loading direction for each crack, and 3) the opening displacement as a function of distance ahead of the crack tip, compared to relationships determined for other materials. In order to accomplish the last goal, the data in Figs. 5 through 7 are evaluated based on an empirical relationship between COD and \sqrt{y} . This approach is broadly applicable, and was established from analyzing extensive data for both sharp and blunt crack tips [19]. Analytical models do not treat such varied stationary crack opening behavior [20-22].

The COD_x data for the TG crack in Figs. 2(b) through 2(d) are plotted vs \sqrt{y} in Fig. 5(a), and for increasing K . The data for each K level in Fig. 5(a) are well described by a solid-line regression fit. Extrapolating the regression fits in Fig. 5(a) to $\sqrt{y} = 0$ shows that the COD_x axis is intersected at higher values as K increases, which is consistent with evolving crack tip blunting in Figs. 2(b) through 2(d) [19]. The extrapolated regression fits for the lower K levels (15 MPa \sqrt{m} and 24 MPa \sqrt{m}) indicate that COD_x is negative for $\sqrt{y} = 0$, but such values are physically unrealistic. Lower-bound values for COD_x at the crack tip are equal to 0 and are predicted for an elastic crack. The opening of TG cracks at lower K levels may approximate elastic behavior, since crack tip blunting and associated deformation are limited (Fig. 2(b)).

The COD_x vs \sqrt{y} relationships for the tearing IG crack in Figs. 4(b) through 4(d) are shown in Fig. 6(a) for increasing K . Similar to the TG crack, linear regression fits represent the COD_x vs \sqrt{y} data for all K levels. (The line for $K = 33$ MPa \sqrt{m} in Fig. 6(a) was fit only to the first two data points.) Extrapolating the linear relationships to $\sqrt{y} = 0$ shows that the COD_x axis is intersected at progressively higher values as K increases. This result suggests that the crack tip blunts with increasing deformation. Figs. 4(b) through 4(d) show that some blunting is associated with tearing of the crack tip.

The IG crack tip in Figs. 3(b) and 3(c) is sharper than that in Figs. 4(b) through 4(d) as K

¹The coordinate system used for describing position near the crack tip and components of displacement is defined as follows. The origin is at the crack tip with x and y axes parallel and perpendicular to the mode I loading direction, respectively. The axes are not defined relative to the crack plane because IG cracks change orientation (Figs. 3(a) and 4(a)). The displacement components represent mode I and mode II opening for crack planes normal to the loading direction.

increases, and the latter is located at a triple point; thus different crack opening behavior is expected for these two cases. Comparison of COD_x vs \sqrt{y} for these crack tips at two K levels in Fig. 6(b) reveals both similarities and differences. While COD_x vs \sqrt{y} for the sharp IG crack tip (■,▲) is linear, less opening is measured at each position compared to the tearing tip (□,△). The dashed-line regression fits to the sharp IG crack tip data extrapolate closer to $COD_x = 0$ at $\sqrt{y} = 0$ compared to the tearing crack tip, which is expected for limited crack tip blunting.

Additional data in Fig. 6(b) at larger distances behind the sharp IG crack tip indicate that intersection of the linear regression fits at positive values on the COD_x axis does not necessarily imply crack tip blunting. These COD_x data at large \sqrt{y} were measured beyond the point where the two crack branches intersect in Fig. 3(a). The entire set of data for the sharp but microbranched IG crack tip show that COD_x is not a continuous function of \sqrt{y} . Rather, the dependence of COD_x on \sqrt{y} likely changes each time the local orientation of the IG crack is altered. Since the IG crack planes change orientation after a short distance behind the tips in Figs. 3 and 4, and the COD_x values at small \sqrt{y} in Fig. 6(b) were not measured solely along these initial crack segments, extrapolation of linear fits to these data do not necessarily pass through $COD_x = 0$ at $\sqrt{y} = 0$, even if the crack tip is sharp. Discontinuities in COD_x vs \sqrt{y} are not typically observed for stationary TG cracks [23].

Figure 7(a) compares COD_x vs \sqrt{y} for the TG and tearing IG cracks at $K = 44$ MPa/m. As expected from the qualitative observations of crack opening in Figs. 2 and 4, COD_x for the TG crack greatly exceeds that of the IG crack at constant K . The slope of the linear regression fit to COD_x vs \sqrt{y} for the TG crack is $0.95 \sqrt{\mu m}$ (solid line), compared to $0.23 \sqrt{\mu m}$ (dashed line) for the IG crack.

Measurements of COD_y for the TG and IG cracks in Figs. 2 through 4 are presented in Figs. 5(b), 6(c) and 7(b). The COD_y is the difference between the vector components of displacement normal to the loading direction for the two crack surfaces, at the same point (y) behind the crack tip. Figure 5(b) shows that a linear relationship does not fit the COD_y vs \sqrt{y} data for the TG crack, compared to the COD_x vs \sqrt{y} data in Fig. 5(a). This difference in the y -dependencies of COD_x and COD_y is observed commonly for TG cracks [19]. Evaluating the TG crack opening data at $K = 44$ MPa/m indicates that COD_y is between 20% to 40% of COD_x .

Similar to the TG crack, COD_y data for the sharp (■,▲) and tearing (□,△) IG cracks in Fig.

6(c) are not well represented by a linear relationship. Comparing the components of displacement in Fig. 6(c) to those in Fig. 6(b) at $K \approx 39 \text{ MPa}/\text{m}$ indicates that COD_y is between 30% to 40% of COD_x for the tearing IG crack tip, and 30% to 50% of COD_x for the sharp IG crack tip. The negative values of COD_y for the sharp IG crack tip in Fig. 6(c) (■) are not significant, but merely reflect that y -displacement is higher on opposite crack surfaces for the sharp IG crack compared to the TG and tearing IG cracks. Comparison of COD_y for the TG and tearing IG crack tips at $K = 44 \text{ MPa}/\text{m}$ in Fig. 7(b) shows a trend similar to COD_x in Fig. 7(a); opening displacements are larger for the TG crack tip.

The K -dependencies of COD_x and COD_y (at $y \approx 6 \text{ }\mu\text{m}$) are shown in Figs. 8(a) and 8(b) for the TG and IG crack cases. The COD_x data are plotted vs K^2 in order to compare the stereomaging measurements to modeling results. Figure 8(a) shows that a linear regression fit forced through the origin reasonably describes the dependence of COD_x on K^2 for the TG crack. This relationship, represented by the solid line through the data (○), is expected based on analytical and finite-element modeling predictions for small-scale yielding [22-25]. The modeling results indicate that mode I crack tip opening displacement (CTOD) equals $\alpha K^2/[\sigma_{ys}E]$, where α is a dimensionless constant which depends on both work hardening and stress state, and E is elastic modulus. The slope of the solid-line regression fit in Fig. 8(a) multiplied by $[\sigma_{ys}E]$, where $E = 105 \text{ GPa}$ [5], equals 0.2, which is less than predicted values of α for both plane strain (0.6 to 0.8) and plane stress (0.8 to 1.0) at low work hardening [22]. The COD_x vs K^2 data for the tearing IG crack (□) in Fig. 8(a) are not well-described by the dashed-line regression fit through the origin. Figure 8(a) shows that COD_x for the IG crack tip is substantially less than that for the TG crack tip at each K level.

The COD_y data are plotted vs K^2 in Fig. 8(b) only to compare the results to Fig. 8(a), since models of mode II-type crack opening induced by mode I loading do not exist. Similar to COD_x for the IG crack, COD_y data for both crack tips in Fig. 8(b) are not linear functions of K^2 . The COD_y for the IG crack tip is less than that for the TG crack tip at each K level.

Crack Tip Strain

The in-plane surface strains ahead of TG and IG cracks were calculated from displacement gradients measured using the stereomaging technique. While each component of the strain tensor

was calculated, these multiaxial quantities were combined into an effective strain ($\bar{\epsilon}$) in order to characterize crack tip deformation [16,19]. The first section below illustrates distributions of effective strain along different planes intersecting the TG and IG crack tips, and the effect of increasing K on effective strain at fixed positions ahead of each crack tip. Similar to the COD data, these results focus on comparing the behavior of TG vs IG cracks, as well as evaluating empirical and analytical relationships. The second section addresses changes in strain ahead of TG and IG crack tips as a function of time.

Effects of Angular Orientation and K on $\bar{\epsilon}$ The effective strain is plotted vs radial distance (r) ahead of the crack tip along planes which form angles (θ) of 45° , 0° , and -45° with respect to the y -plane (normal to mode I loading direction) in Figs. 9(a) through 9(c), as well as 10(a) and 10(b). Positive and negative θ refer to orientations "above" and "below" the main crack planes, respectively, in Figs. 2(a), 3(a), and 4(a). The relevance of the empirical relationship $\bar{\epsilon} \propto (r + B)^{-m}$ for describing the results in Figs. 9(a) through 9(c) was analyzed by fitting linear curves to the data plotted on log-log axes. This relationship fit extensive crack tip strain distribution measurements [19,26], and has a form similar to analytical expressions of $\bar{\epsilon}$ vs r [20,21,27]. The constant, B , is added to r in order to ensure that crack tip strain remains finite as r approaches 0; $B = 1 \mu\text{m}$ in Figs. 9(a) through 9(c).

Comparison of $\bar{\epsilon}$ distributions for the TG crack in Fig. 2 vs the tearing IG crack in Fig. 4 at $K = 44 \text{ MPa}/\text{m}$ reveals behavior which contrasts to the COD measurements. While both COD_x and COD_y for the TG crack exceed those for the IG crack at all K and y (Figs. 7 and 8), the trend of $\bar{\epsilon}$ in Figs. 9(a) through 9(c) is not as clear. The linear curve fits to the data indicate that $\bar{\epsilon}$ is higher near the tip for the tearing IG crack (dashed line through \square) compared to the TG crack (solid line through \circ) for $\theta = 45^\circ$ and 0° (Figs. 9(a) and 9(b)), while farther from the tip these trends are reversed. For $\theta = -45^\circ$ (Fig. 9(c)), $\bar{\epsilon}$ is lower for the IG crack for all r , except at the tip ($r = 0 \mu\text{m}$). It is difficult to evaluate whether the empirical relationship $\bar{\epsilon} \propto (r + B)^{-m}$ is relevant for either the TG or IG crack. Linear curves fit the TG data reasonably well at $\theta = 45^\circ$ and -45° (Figs. 9(a) and 9(c)), and the IG crack data at $\theta = 0^\circ$ (Fig. 9(b)).

Figures 10(a) and 10(b) compare $\bar{\epsilon}$ as a function of θ for the TG and tearing IG crack tips in Figs. 2 and 4. Figure 10(a) suggests that $\bar{\epsilon}$ is consistently highest at $\theta = 45^\circ$ (\circ), and lowest at $\theta =$

-45° (Δ), for the TG crack, although the differences are not significant. For the IG crack, $\bar{\epsilon}$ is essentially equal at $\theta = 45^\circ$ and 0° (\circ, \square) in Fig. 10(b), but is considerably lower at $\theta = -45^\circ$ (Δ).

Because of the CODx differences between the sharp and tearing IG crack tips at similar K (Fig. 6(b)), the strain distributions for these two cases are compared in Fig. 11. Crack tip $\bar{\epsilon}$ ($K \approx 39$ MPa $\sqrt{\text{m}}$) at $\theta = 0^\circ$ for the tearing IG crack (\square) is compared to that at $\theta = 45^\circ$ for the sharp IG crack (Δ) since these planes are oriented similarly relative to the respective local crack planes (Figs. 3(b) and 3(c) compared to Figs. 4(b) through 4(d)). Figure 11 shows that, similar to CODx, $\bar{\epsilon}$ is greater for the tearing IG crack tip compared to the sharp crack tip. Included in Fig. 11 are data for the sharp crack tip at $\theta = 0^\circ$ (\diamond) which indicate that strains are low for other orientations.

Figures 12(a) through 12(c) summarize the effect of increasing K on $\bar{\epsilon}$ for fixed positions ($r = 3 \mu\text{m}$ to $4 \mu\text{m}$) ahead of the crack tip at $\theta = 45^\circ$, 0° , and -45° . The $\bar{\epsilon}$ is plotted vs K^2 in order to compare the measurements to modeling predictions. Figures 12(a) and 12(b) show similar trends at $\theta = 45^\circ$ and 0° for the TG and tearing IG crack tips in Figs. 2 and 4. The $\bar{\epsilon}$ is considerably higher for the TG crack (\circ) compared to the IG crack (\square) at lower K, but $\bar{\epsilon}$ increases more rapidly with K for the IG crack. At higher K, $\bar{\epsilon}$ for the IG crack exceeds that for the TG crack, as indicated previously in Figs. 9(a) and 9(b). Two particular details are noted in Fig. 12(b) for $\theta = 0^\circ$. The $\bar{\epsilon}$ decreases noticeably at the highest K for the TG crack and $\bar{\epsilon}$ is nearly constant at higher K for the IG crack. At $\theta = -45^\circ$, $\bar{\epsilon}$ is lower for the IG crack compared to the TG crack for all K.

The solid and dashed lines in Figs. 12(a) through 12(c) are intended to show both the stereoimaging data trends as well as the relevance of analytical descriptions of $\bar{\epsilon}$ vs K. Models of crack tip strain suggest that $\bar{\epsilon}$ is directly proportional to K^2 on a log-log plot, where the slope is a function of the work-hardening exponent for all orientations [20,21,27]. Linear curve fits to the data in Figs. 12(a) through 12(c) show that the TG crack is well described by model predictions, except for the highest K at $\theta = 0^\circ$. (This point was excluded from the regression fit to the TG crack data.) In contrast, a linear curve fits the IG data well only at $\theta = 45^\circ$, and the slope of the regression line at $\theta = -45^\circ$ differs significantly compared to those at $\theta = 45^\circ$ and 0° .

Effect of Time on $\bar{\epsilon}$ at Constant K The effect of hold time in vacuum at constant K on crack tip $\bar{\epsilon}$ is evaluated from the displacement vector distributions in Figs. 13(a) and 13(b) for the TG and IG cracks. The vectors superimposed on images of the crack tip profiles represent changes in

displacement at each point from $t = 0$ to $t = 75$ min for the TG crack at $K = 44$ MPa $\sqrt{\text{m}}$ (Fig. 13(a)); and from $t = 0$ to $t = 150$ min for the tearing IG crack at $K = 47$ MPa $\sqrt{\text{m}}$ (Fig. 13(b)). The displacement vector distributions in Figs. 13(a) and 13(b) indicate that very limited deformation occurred during the hold times. For the TG crack, the time-dependent displacement vectors are very small (less than $0.002 \mu\text{m}$) compared to those due to increasing K , and do not form smooth gradients. The strain-change distributions calculated from this displacement field are erratic compared to the trends shown in Figs. 9(a) through 9(c). These characteristics suggest that changes in the measured displacement field resulted from small errors in the stereoimaging technique.

Small vectors are likewise measured for the IG crack (less than $0.09 \mu\text{m}$), particularly above the crack plane; calculated strain changes in this region are nearly zero. The displacement gradients below the crack plane yield higher strain changes, but it is expected that deformation should more limited in this region based on the results in Figs. 9(c), 10(b), and 12(c). Similar to the TG crack, it is likely that time-dependent displacement measured below the crack plane resulted from errors in the stereoimaging technique.

DISCUSSION

TG Crack

The following crack opening and crack tip strain results, established for the TG crack in Fig. 2, are consistent with observed and modeled behaviors of stationary TG cracks loaded monotonically [19-24,27]: 1) COD $_x$ increases linearly with both increasing square root of distance behind the crack tip and K^2 in Figs. 5(a) and 8(a); 2) crack tip blunting evolves with increasing K , as characterized by the profiles in Figs. 2(b) through 2(d), as well as the intersection of linear curve fits at progressively higher values on the COD $_x$ axis in Fig. 5(a); 3) crack opening displacement has a component normal to the mode I loading direction, as illustrated in Fig. 5(b); 4) $\bar{\epsilon}$ is finite at the crack tip and decreases continuously with increasing r in Figs. 9(a) through 9(c); and 5) $\bar{\epsilon}$ increases linearly with increasing K^2 in Figs. 12(a) through 12(c). Empirical and analytical models for TG cracks fit the data well in Figs. 5(a), 8(a), 9(a), 9(c), and 12(a) through 12(c). These correlations have been observed in other studies of TG crack opening and deformation [19,23,27].

Some unexpected results are noted. For example, $\bar{\epsilon}$ decreases abruptly at $K = 44 \text{ MPa}/\text{m}$ in Fig. 12(b), in contrast to the behavior at lower K and for crack plane orientations of $\theta = 45^\circ$ and -45° (Figs. 12(a) and 12(c)). It is speculated that this decrease in $\bar{\epsilon}$ along $\theta = 0^\circ$ at high K results from crack tip blunting. The magnitude of crack tip strain along a given plane is a strong function of crack tip shape [28]. The crack tip profile in Figs. 2(b) through 2(d) does not evolve into a smoothly curved shape, but rather develops vertices. Strain parallel to the crack plane ($\theta = 0^\circ$ for the TG crack) can be very low for this type of crack tip profile [28]. It is possible that the crack tip in Fig. 2(d) develops vertices which lower $\bar{\epsilon}$ compared to that in Fig. 2(c).

Another result which contradicts predicted behavior is the asymmetry of crack tip strain at $\theta = 45^\circ$ and -45° in Fig. 10(a). Analytical and finite-element models of TG cracks loaded monotonically in mode I suggest that strain distributions should be identical at equal angles above and below the crack plane ($\theta = 0^\circ$ for the TG crack) [20,21,24]. It is likely that the $\bar{\epsilon}$ asymmetry in Fig. 10(a) results from the shear crack which develops as K increases (Figs. 2(b) through 2(d)).

Finally, the measured proportionality constant (0.2) between COD_x (at $y \approx 6 \text{ }\mu\text{m}$) and K^2 (Fig. 8(a)) is lower than expected from modeling results (0.8 to 1.0 for plane stress) [22]. While the reason for this discrepancy is unclear, other studies have found similar unfavorable correlations [27].

IG Crack

Unlike the TG crack, measured COD and $\bar{\epsilon}$ behaviors for the IG cracks in Figs. 3 and 4 cannot be easily compared to expected results since few studies have focused on describing the mechanics of this cracking mode. Nonetheless, some inconsistencies in the results for IG cracks are noted in this section.

The IG crack tip in Figs. 3(b) and 3(c) responds to load differently compared to that in Figs. 4(b) through 4(d); *viz*, the latter tears locally into a neighboring grain while the former remains intact. Transgranular ductile tearing similar to that in air initiates at $K = 33 \text{ MPa}/\text{m}$ in Fig. 4(b), which is less than K_{ICi} (56 MPa/m to 62 MPa/m) for this aged microstructure [5]. Crack tip tearing at low K can be explained by considering that ductile-fracture K_{ICi} is governed by the interplay between crack tip strain and microstructural fracture resistance [29,30]. Although K_{ICi} was measured from a TG fatigue precrack [5], the magnitude of IG crack tip strain can approach that for a TG crack

as K increases (Figs. 12(a) and 12(b)). Given these similar crack tip driving forces, tearing could occur if the microstructural fracture resistance is intrinsically lower near the grain boundary compared to the grain interior. An explanation for why the crack does not extend along the grain boundary is proposed in a later section.

The IG crack tip in Figs. 3(b) and 3(c) likely remains on the boundary because strains are lower compared to the tip in Figs. 4(b) through 4(d), as shown by the data Fig. 11. The reason for these differences in crack tip strain for nominally similar fracture modes and applied K levels results from the location of each IG crack tip on the grain boundary. The IG crack tip in Figs. 4(b) through 4(d) lies at a grain boundary triple point, while the crack plane in Figs. 3(b) and 3(c) is coincident with the boundary ahead of the tip. Maintaining strain compatibility at the intersecting grain boundaries concentrates stress and strain near the IG crack tip in Figs. 4(b) through 4(d) compared to that in Figs. 3(b) and 3(c).

Another result of note for the IG crack tip in Figs. 4(b) through 4(d) is that strain at $\theta = -45^\circ$ is significantly less than at $\theta = 45^\circ$ and 0° (Fig. 10(b)). This result is interpreted based on the crack profile in Fig. 4(a). The two IG crack microbranches which diverge from the "main" crack in Fig. 4(a) are nearly parallel to each other on opposite sides of the same grain. The lower crack provides a free surface which spans most of the length of the upper crack. This free surface may lower the strain for the upper crack tip at $\theta = -45^\circ$.

TG vs IG Cracks

Differences between the TG crack tip profile in Fig. 2 and the IG profiles in Figs. 3 and 4 are consistent with measurements of COD in Figs. 7 and 8; viz, crack opening is significantly greater for the TG crack compared to the IG cracks. Based on these results and the notion that crack tip strain scales with crack opening, similar trends were expected for measurements of $\bar{\epsilon}$. The results in Figs. 9 and 12 show, however, that $\bar{\epsilon}$ for an IG crack tip can exceed that for a TG crack tip. For the IG crack which terminates at a grain boundary triple point in Figs. 4(b) through 4(d), $\bar{\epsilon}$ is greater near the crack tip compared to the TG crack in Figs. 2(b) through 2(d) at higher K . Strain is enhanced ahead of this IG crack tip because strain compatibility must be maintained at the grain boundary intersection. The incompatibility is a function of the degree of deformation and proximity

to the grain boundary triple point and thus increases with increasing K and decreasing r . Strains ahead of IG cracks are less than those for TG cracks when the former are not affected by microstructural incompatibility (sharp crack in Fig. 11) and for orientations which are influenced by microscopic crack branching ($\theta = -45^\circ$ in Figs. 9(c), 10(b), and 12(c)).

Figure 14 illustrates that crack tip opening displacement is not necessarily a reliable “remote” measurement of crack tip driving force. Measured $\bar{\epsilon}$ vs COD_x relationships are shown for the TG crack and tearing IG crack. The slope is greater for the IG crack tip (\square) compared to the TG crack tip (\circ) and both sets of data are reasonably described by a linear curve fit forced through the origin. This result suggests that applied K is similarly not a complete descriptor of the local crack tip stress and strain distributions. This behavior is analogous to the relationships between applied stress, local stress and local strain in polycrystalline plasticity of an uncracked microstructure.

Implications for EAC of ST/A 24 h Beta-C

The measurements of $\bar{\epsilon}$ for TG and IG cracks in ST/A 24 h Beta-C may explain the difference in EAC response of these two “precrack” fracture modes. An existing IG crack does not propagate under static δ_m in aqueous NaCl, while a TG crack exhibits EAC during aqueous NaCl exposure following short hold times in air at constant K . Statistically, it is likely that most of the IG crack front consists of separated grain boundaries which do not terminate at grain boundary discontinuities. Based on this premise, strain ahead of TG cracks is higher compared to IG cracks at a given K , and the surface passive film is mechanically destabilized to allow EAC in the former case, but not the latter. One issue which must be resolved is why IG cracks will propagate under rising δ_m .

Measurement of TG crack tip $\bar{\epsilon}$ as a function of hold time at constant K does not explain the EAC behavior of ST/A 24 h Beta-C specimens prestrained in air for various times and subsequently exposed to aqueous NaCl. Results for steel show that EAC is precluded by prolonged inert environment prestrain because the crack tip creep strain rate decays below the minimum level needed to maintain passive film rupture [31-33]. The measured displacements ahead of the TG crack tip in Fig. 13(a) show that no resolvable strain accumulates for ST/A 24 h Beta-C at times up to 75 min, but static-loading EAC occurs for similar hold times in air followed by exposure to aqueous NaCl.

These results suggest that local deformation processes, which cannot be measured by the stereomaging technique, are important for EAC. This notion is supported by work which proposes that discrete dislocation intersections with the crack tip are responsible for passive film rupture [6].

The tearing of the IG crack tip in Figs. 4(b) through 4(d) into a neighboring grain provides an insight into EAC of ST/A 24 h Beta-C. This result indicates that grain boundaries may not be intrinsically preferred mechanical fracture paths, and thus the EAC fracture mode is intergranular because the boundaries are selectively embrittled. This result is easily interpreted if the EAC mechanism is anodic dissolution as opposed to HE, since mechanically driven cracks which are not exposed to the environment propagate through the grain interior. Alternately, if HE is the pertinent mechanism, propagation of the IG crack in Figs. 4(b) through 4(d) into the grain indicates that H penetration was highly localized during cracking in aqueous NaCl. The presence of residual H over a distance on the order of the plastic zone size would have lowered the grain boundary fracture resistance and promoted some crack extension along the boundary during testing in air.

CONCLUSIONS

1. Measured crack opening displacements for TG cracks exceed those for IG cracks at similar K and distance behind the crack tip, consistent with qualitative observations of the crack tip profiles.
2. Strains ahead of IG cracks can exceed those for TG cracks due to grain boundary discontinuities such as triple points. In the absence of such discontinuities, strain is lower for IG cracks compared to TG cracks, consistent with crack opening.
3. Crack tip opening displacement may not be an adequate "remote" measure of deformation because microstructural features promote different levels of strain concentration.
4. Larger strains ahead of TG cracks compared to IG cracks may explain why the former propagate under static loading in aqueous NaCl, but the latter remain stationary. Low strains for the IG crack are insufficient to mechanically rupture the crack tip surface film and allow EAC.
5. The lack of measurable time-dependent deformation ahead of TG cracks suggests that

continuum crack tip creep does not govern EAC; rather, local deformation processes are important.

ACKNOWLEDGMENTS

This research was supported by the Office of Naval Research (Grant N00014-91-J-4164), with Dr. A. John Sedriks as Scientific Monitor. Material was donated by the RMI Titanium Company. Stereoimaging measurements were performed at Southwest Research Institute with Dr. David L. Davidson. These contributions are gratefully acknowledged.

REFERENCES

- [1] L.M. Young, G.A. Young, J.R. Scully and R.P. Gangloff: *Metall. Mater. Trans. A*, 1995, vol. 26A, pp. 1257-1271.
- [2] B.P. Somerday and R.P. Gangloff: *Metall. Mater. Trans. A*, 1996, in preparation.
- [3] B.P. Somerday and R.P. Gangloff: *Corrosion*, 1996, in preparation.
- [4] B.P. Somerday, J.A. Grandle and R.P. Gangloff: in *Proceedings of the Tri-Service Conference on Corrosion*, T. Naguy, ed., Materials Laboratory, Wright-Patterson Air Force Base, OH, 1994, pp. 375-392.
- [5] B.P. Somerday, L.M. Young and R.P. Gangloff: submitted to *Metall. Mater. Trans. A*, 1995.
- [6] D.G. Kolman: PhD Dissertation, University of Virginia, Charlottesville, VA, 1995.
- [7] D.G. Kolman and J.R. Scully: in *Effects of the Environment on the Initiation of Crack Growth*, ASTM STP 1298, W.A. Van der Sluys, R.S. Piascik, and R. Zawierucha, eds., ASTM, Philadelphia, PA, 1997, in review.
- [8] L.M. Young: MS Thesis, University of Virginia, Charlottesville, VA, 1993.
- [9] M.J. Blackburn, J.A. Feeney and T.R. Beck: in *Advances in Corrosion Science and Technology*, M.G. Fontana and R.W. Staehle, eds., Plenum Publishing, NY, NY, 1972, vol. 3, pp. 67-292.
- [10] M.J. Blackburn, W.H. Smyrl and J.A. Feeney: in *Stress Corrosion Cracking in High Strength Steel and in Titanium and Aluminum Alloys*, B.F. Brown, ed., Naval Research Laboratory, Washington, DC, 1972, pp. 245-363.
- [11] J.A. Feeney and M.J. Blackburn: *Metall. Trans.*, 1970, vol. 1, pp. 3309-3323.
- [12] D.A. Meyn and P.S. Pao: in *Slow Strain Rate Testing for the Evaluation of Environmentally Induced Cracking: Research and Engineering Applications*, ASTM STP 1210, R.D. Kane, ed., ASTM, Philadelphia, PA, 1993, pp. 158-169.
- [13] B.P. Somerday and R.P. Gangloff: *Scripta Metall.*, 1996, in preparation.
- [14] M.A. Gaudett and J.R. Scully, submitted to *Scripta Metall.*, 1996.
- [15] D.L. Davidson and A. Nagy: *J. Physics E.*, 1978, vol. 11, pp. 207-210.

- [16] D.R. Williams, D.L. Davidson and J. Lankford: *Exper. Mech.*, 1980, vol. 20, pp. 134-139.
- [17] D.L. Davidson: in *Scanning Electron Microscopy/1979/II*, SEM, Inc., AMF O'Hare, IL, 1979, pp. 79-86.
- [18] E.A. Franke, D.J. Wenzel and D.L. Davidson: *Rev. Sci. Instruments*, 1991, vol. 62, pp. 1270-1279.
- [19] D.L. Davidson and J. Lankford: *Int. Mat. Rev.*, 1992, vol. 37, pp. 45-76.
- [20] J.W. Hutchinson: *J. Mech. Phys. Solids*, 1968, vol. 16, pp. 337-347.
- [21] J.R. Rice and G.F. Rosengren: *J. Mech. Phys. Solids*, 1968, vol. 16, pp. 1-12.
- [22] C.F. Shih: *J. Mech. Phys. Solids*, 1981, vol. 29, pp. 305-326.
- [23] K.S. Chan: *Metall. Trans. A*, 1990, vol. 21A, pp. 81-86.
- [24] R.M. McMeeking: *J. Mech. Phys. Solids*, 1977, vol. 25, pp. 357-381.
- [25] J.W. Hutchinson: *J. Appl. Mech. Trans. ASME*, 1983, vol. 50, pp. 1042-1051.
- [26] D.L. Davidson: *Eng. Fract. Mech.*, 1986, vol. 25, pp. 123-132.
- [27] K.S. Chan: *Metall. Trans. A*, 1990, vol. 21A, pp. 69-80.
- [28] R.M. McMeeking: *J. Engng Mater. Tech. Trans. ASME*, 1977, vol. 99, pp. 290-297.
- [29] B.P. Somerday, Y. Leng and R.P. Gangloff: *Fatigue Fract. Engng Mater. Struct.*, 1995, vol. 18, pp. 1031-1050.
- [30] M.J. Haynes, B.P. Somerday, C.L. Lach and R.P. Gangloff: in *Elevated Temperature Effects on Fatigue and Fracture Toughness in Advanced Aluminum Alloys*, ASTM STP 1296, R.S. Piascik, R.P. Gangloff, N.E. Dowling and A. Saxena, eds., ASTM, Philadelphia, PA, 1995, to be published.
- [31] R.N. Parkins: in *Stress Corrosion Cracking - The Slow Strain-Rate Technique*, ASTM STP 665, G.M. Ugiansky and J.H. Payer, eds., ASTM, Philadelphia, PA, 1979, pp. 5-25.
- [32] R.N. Parkins, G.P. Marsh and J.T. Evans: in *Predictive Methods for Assessing Corrosion Damage to BWR Piping and PWR Steam Generators*, H. Okada and R. Staehle, eds., NACE, Houston, TX, 1982, pp. 249-260.

- [33] J.T. Evans: *Acta Metall.*, 1977, vol. 25, pp. 805-808.

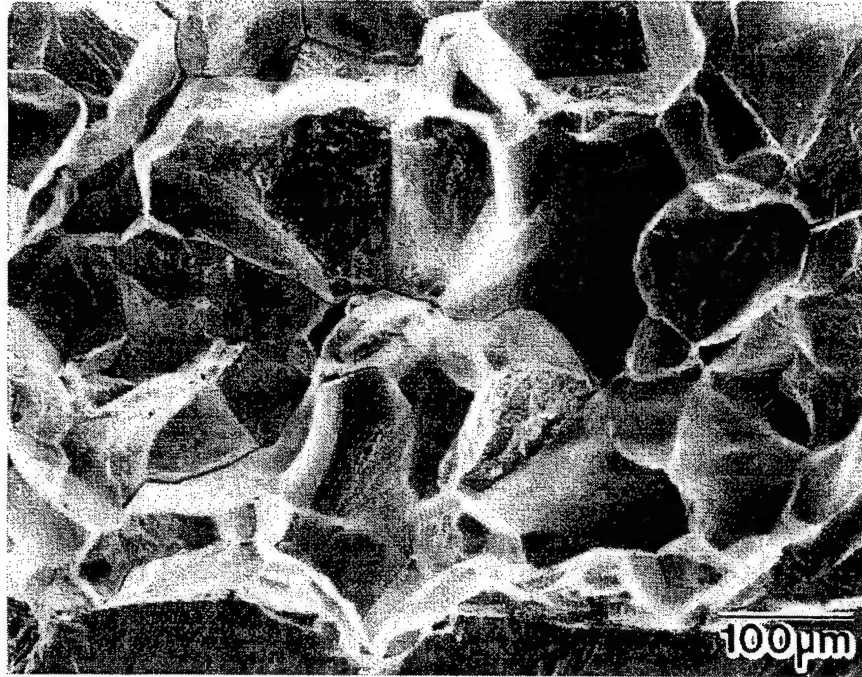


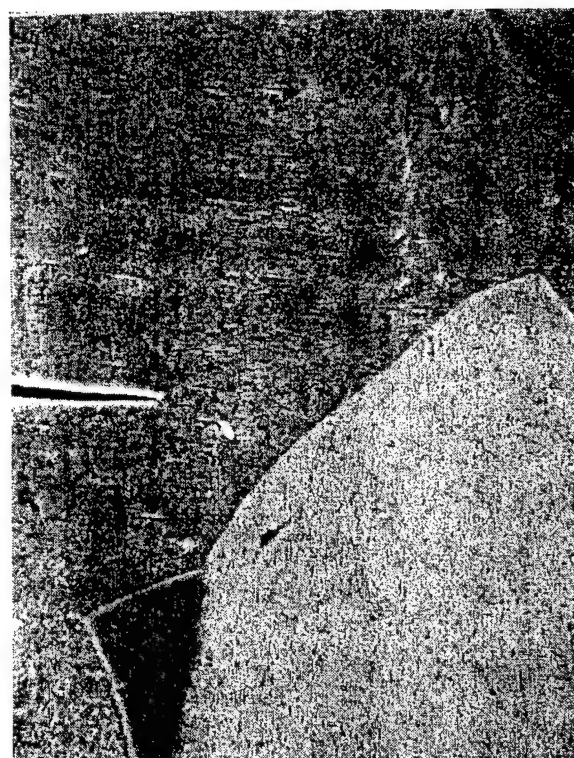
Fig. 1 Fractograph of ST/A 24 h Beta-C cracked in aqueous NaCl showing EAC IG fracture mode near fatigue precrack. Crack growth is from bottom to top.

↑
Loading direction; x



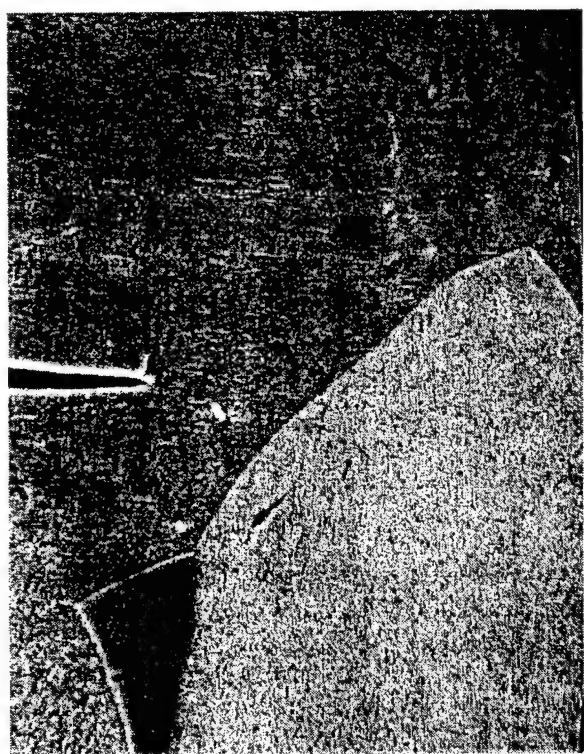
(a)

50 μm



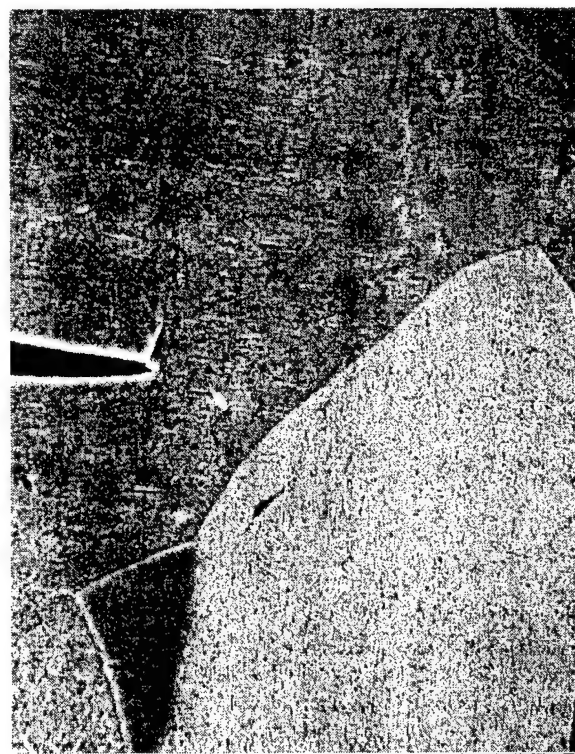
(b)

20 μm



(c)

20 μm



(d)

20 μm

Fig. 2 SEM images of loaded transgranular fatigue crack at low and high magnification: a) $K = 5 \text{ MPa}\sqrt{\text{m}}$, b) $K = 24 \text{ MPa}\sqrt{\text{m}}$, c) $K = 33 \text{ MPa}\sqrt{\text{m}}$, and d) $K = 44 \text{ MPa}\sqrt{\text{m}}$.

↑
Loading direction; x

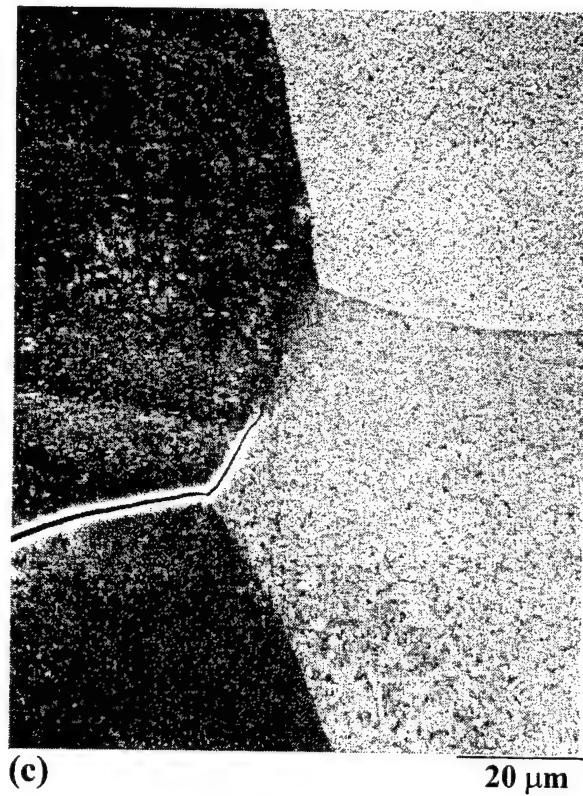
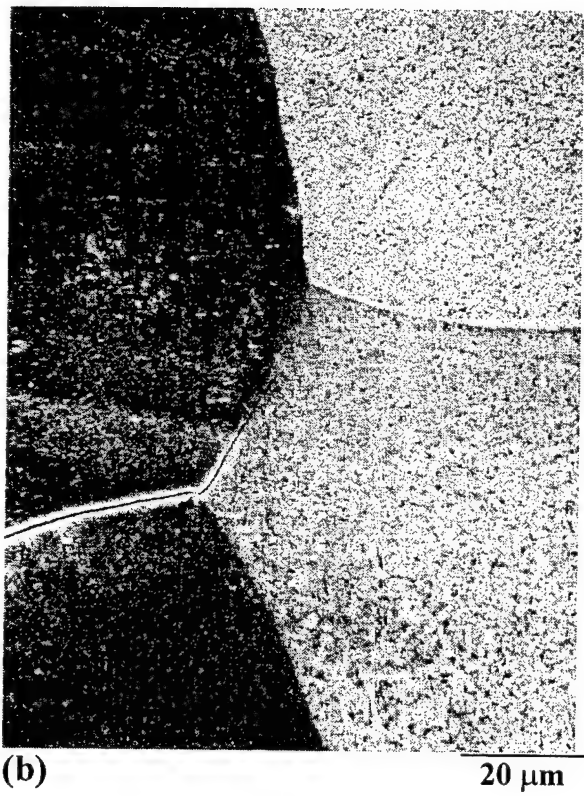
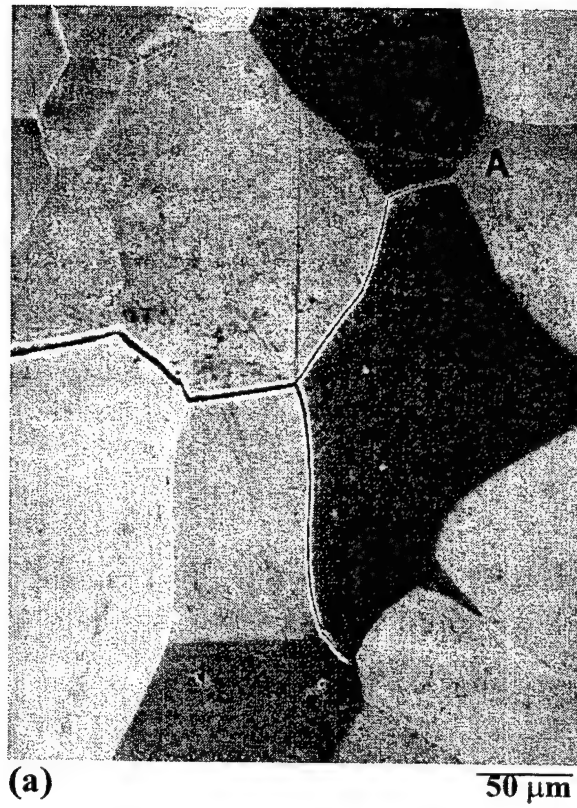


Fig. 3 SEM images of loaded IG-cracked specimen at low and high magnification: a) and b) $K = 32 \text{ MPa}\sqrt{\text{m}}$, c) $K = 38 \text{ MPa}\sqrt{\text{m}}$.

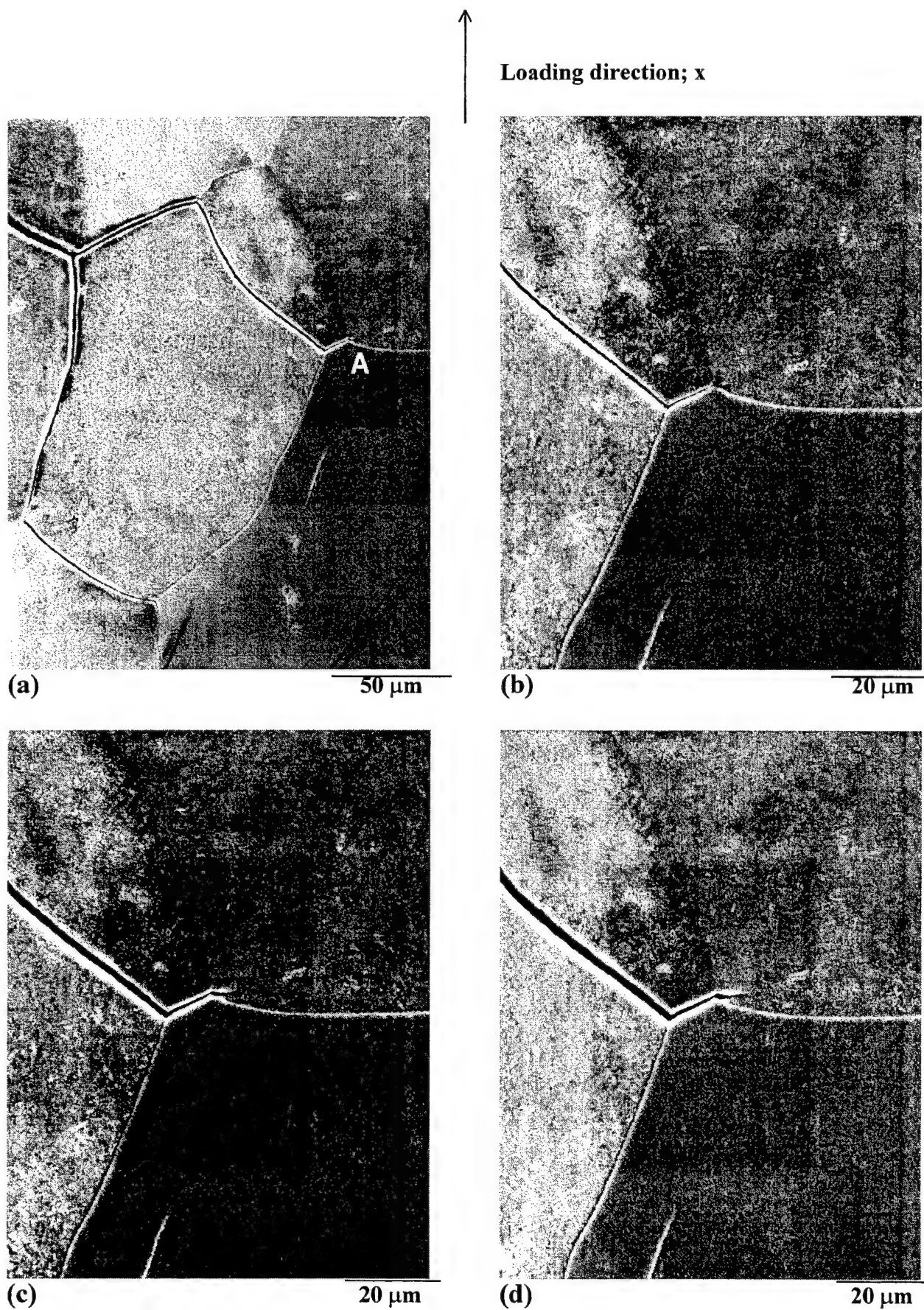


Fig. 4 SEM images of loaded IG-cracked specimen at low and high magnification: a) $K = 39 \text{ MPa}\sqrt{\text{m}}$, b) $K = 33 \text{ MPa}\sqrt{\text{m}}$, c) $K = 44 \text{ MPa}\sqrt{\text{m}}$, and d) $K = 47 \text{ MPa}\sqrt{\text{m}}$.

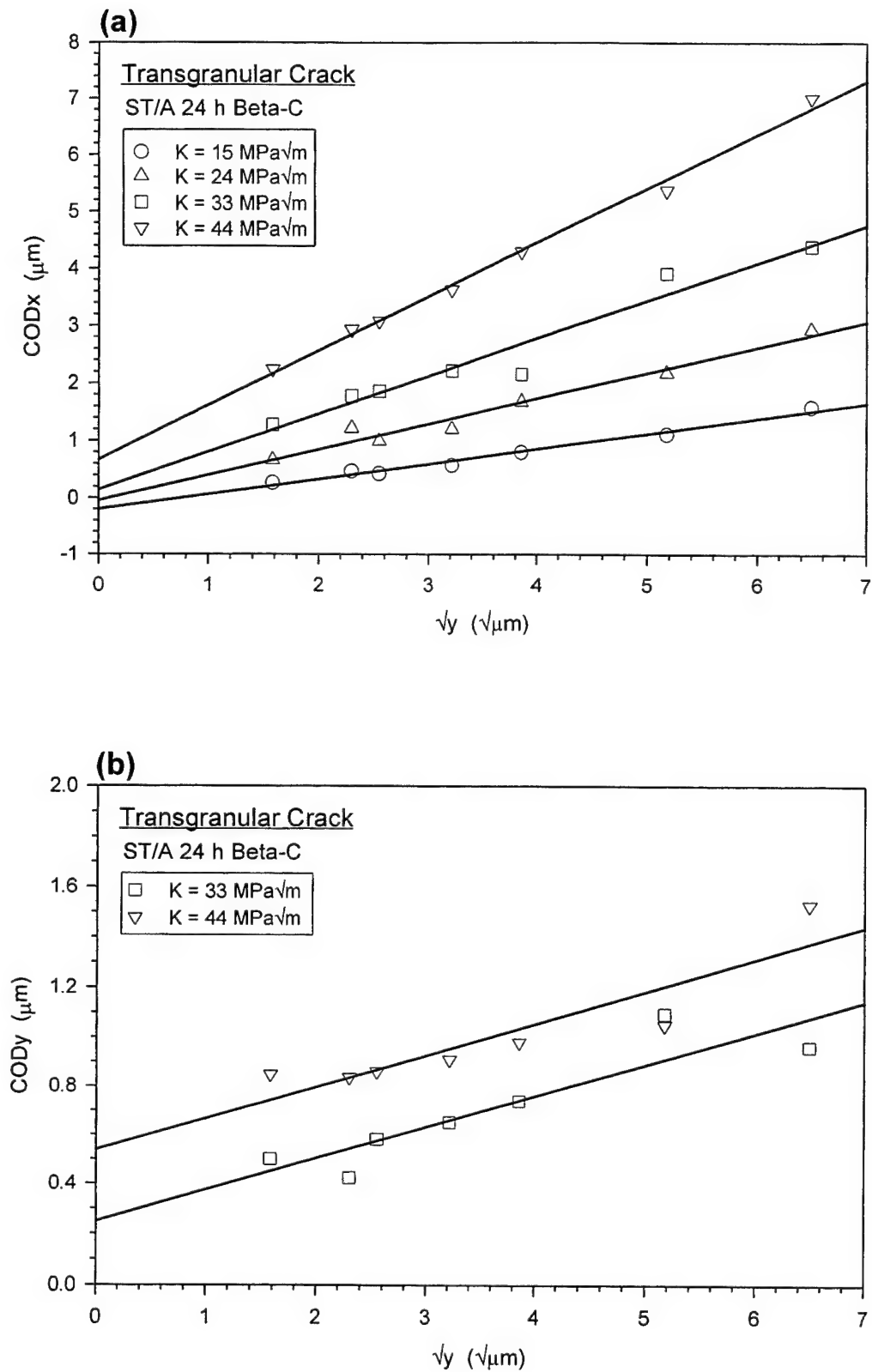


Fig. 5 Crack opening displacement as a function of \sqrt{y} at several K levels for TG crack: a) displacement parallel to loading direction (COD_x), and b) displacement perpendicular to loading direction (COD_y). Solid lines are linear regression fits to the data.

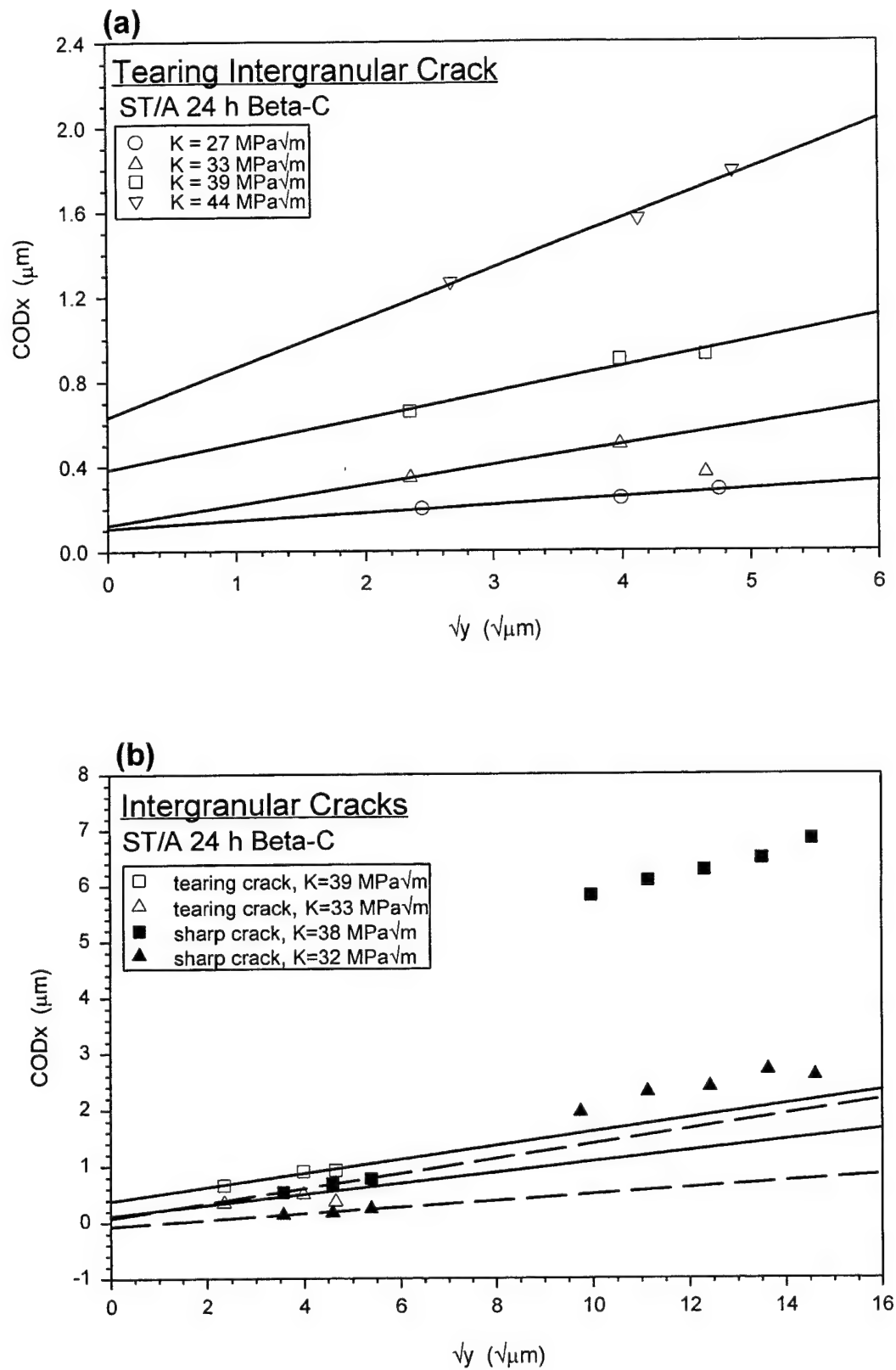


Fig. 6 Crack opening displacement as a function of \sqrt{y} at several K levels for IG cracks: a) displacement parallel to loading direction (COD_x) for tearing IG crack, b) COD_x for tearing IG crack vs sharp IG crack, and c) displacement perpendicular to loading direction (COD_y) for tearing IG crack vs sharp IG crack. Solid and dashed lines are regression fits.

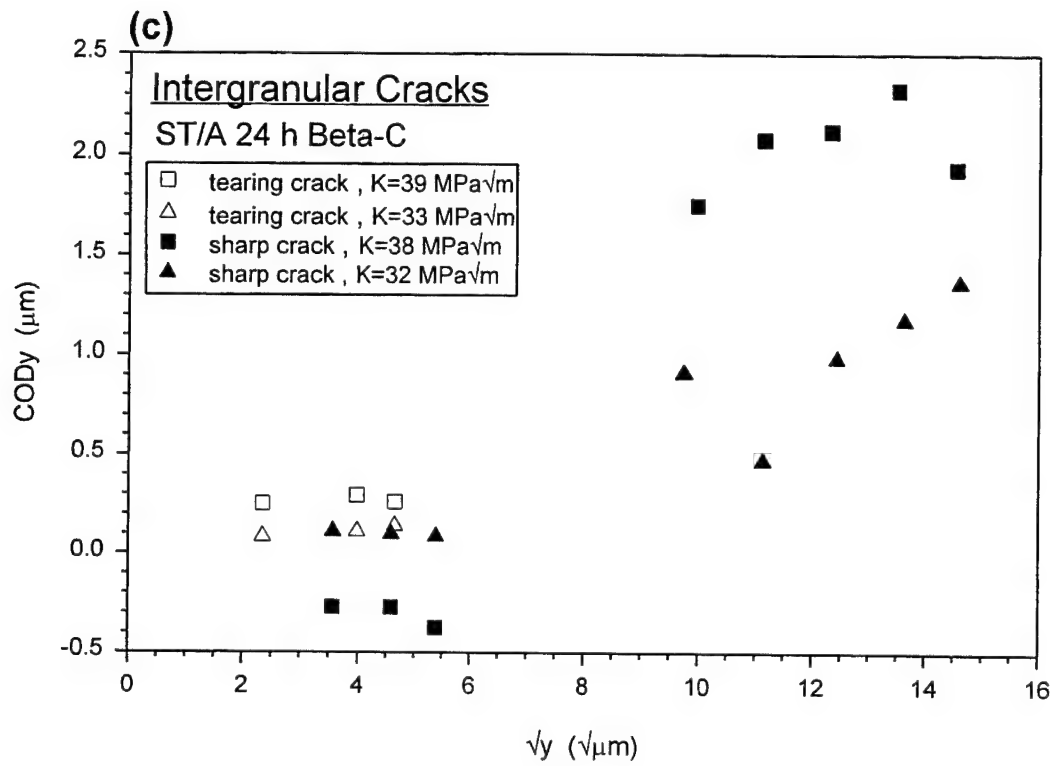


Fig. 6 (continued)

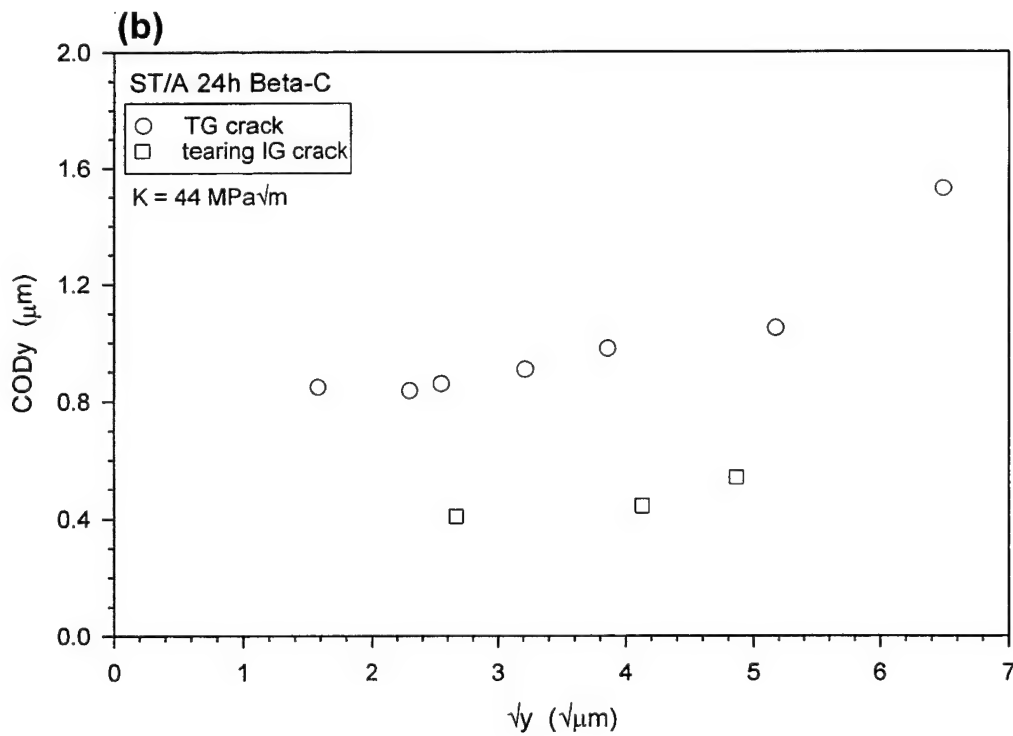
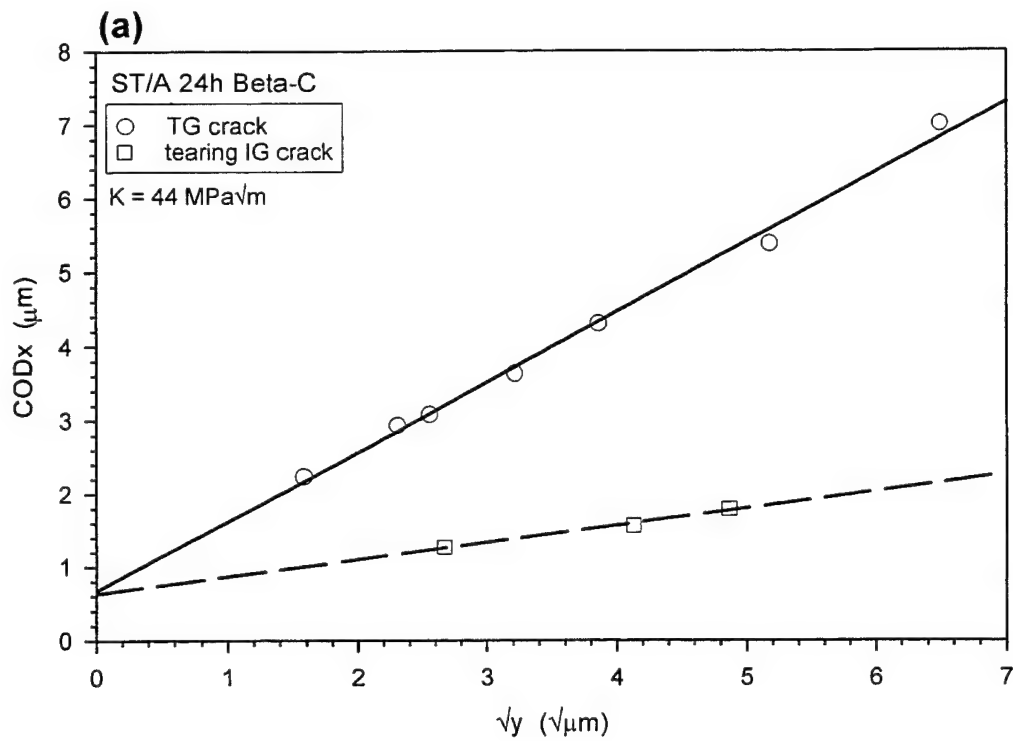


Fig. 7 Comparison of crack opening displacement as a function of \sqrt{y} for TG vs IG cracks at fixed K : a) displacement parallel to loading direction (COD_x), and b) displacement perpendicular to loading direction (COD_y). Solid and dashed lines are regression fits to the data.

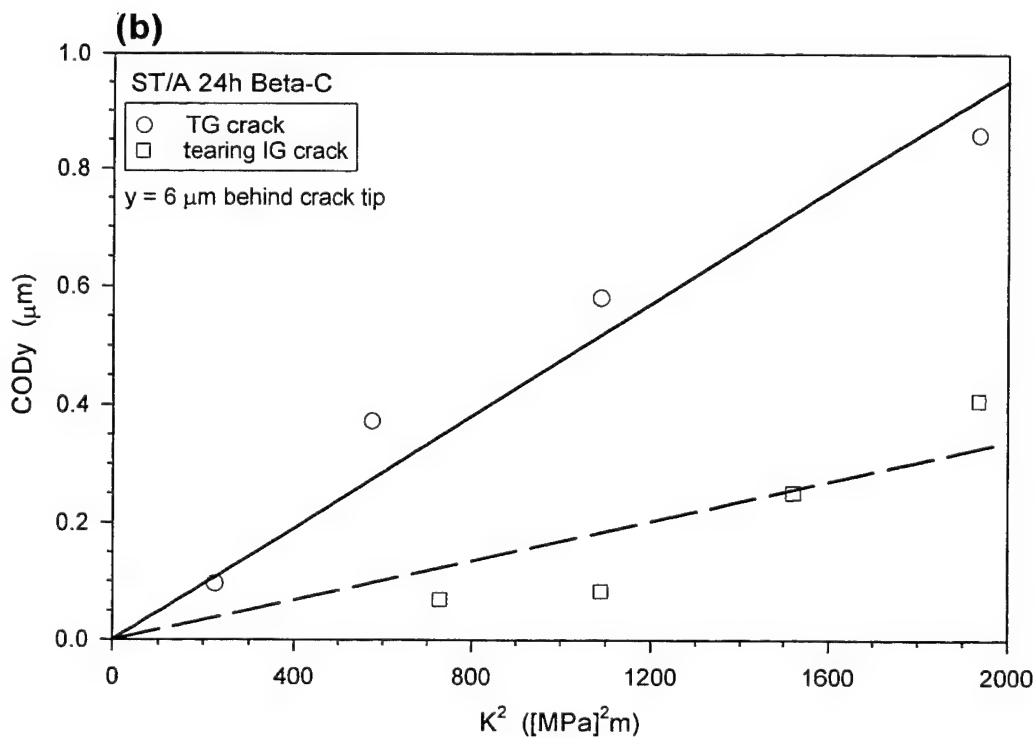
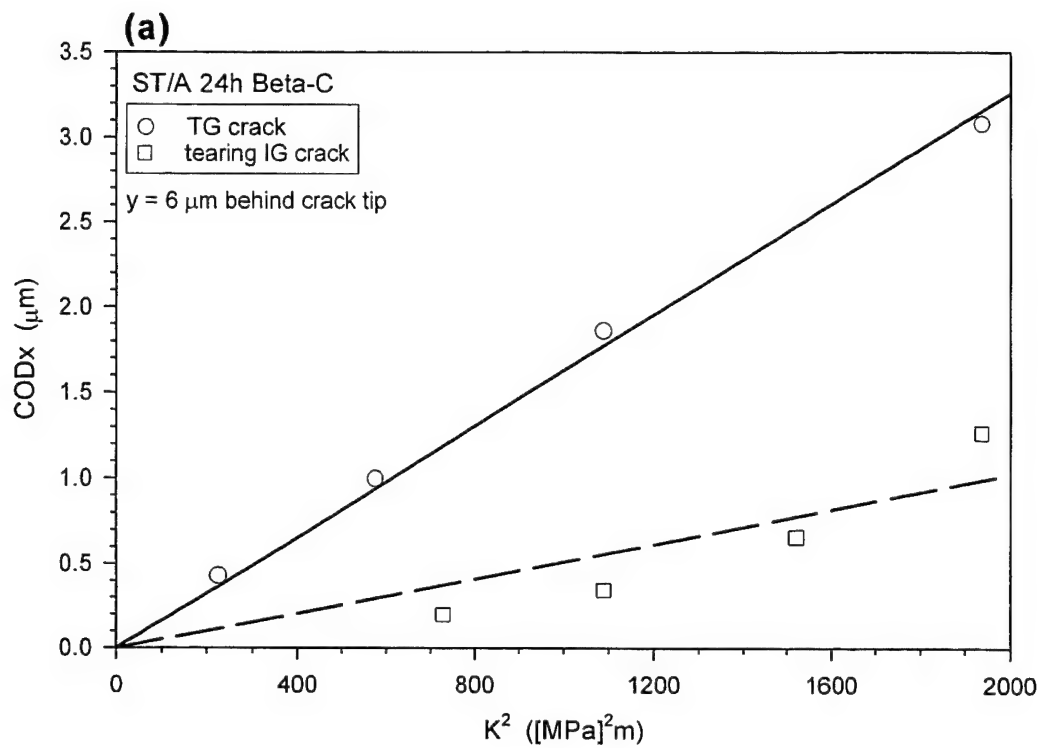


Fig. 8 Comparison of crack opening displacement as a function of K^2 for TG vs IG cracks at a fixed distance behind the crack tip: a) displacement parallel to the loading direction (CODx), and b) displacement perpendicular to the loading direction (CODy). Solid and dashed lines are regression fits to the data.

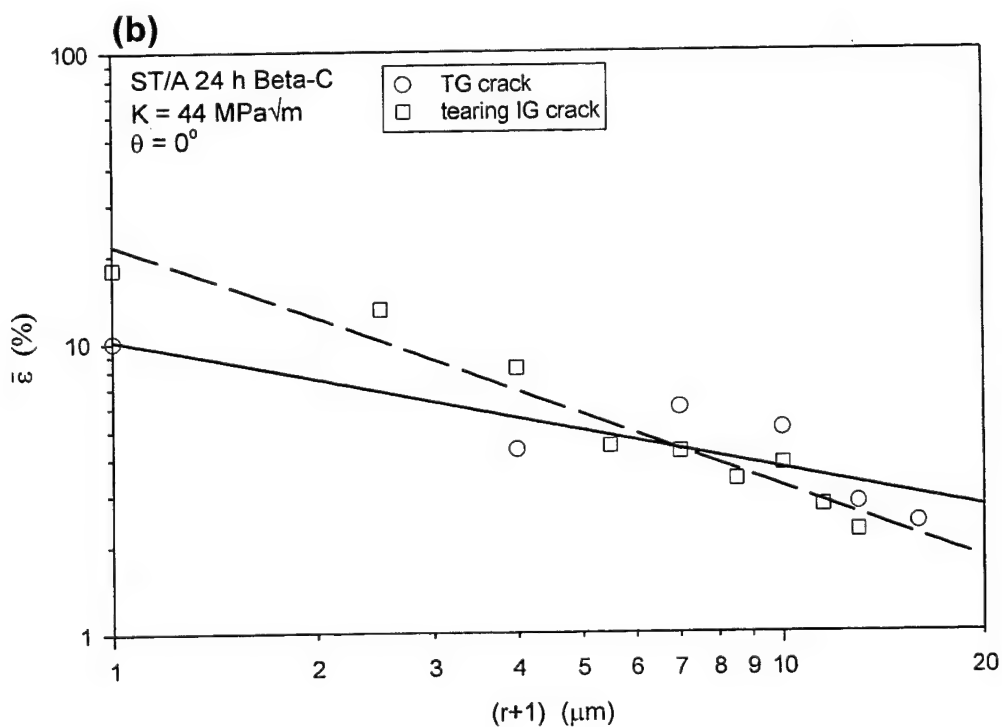
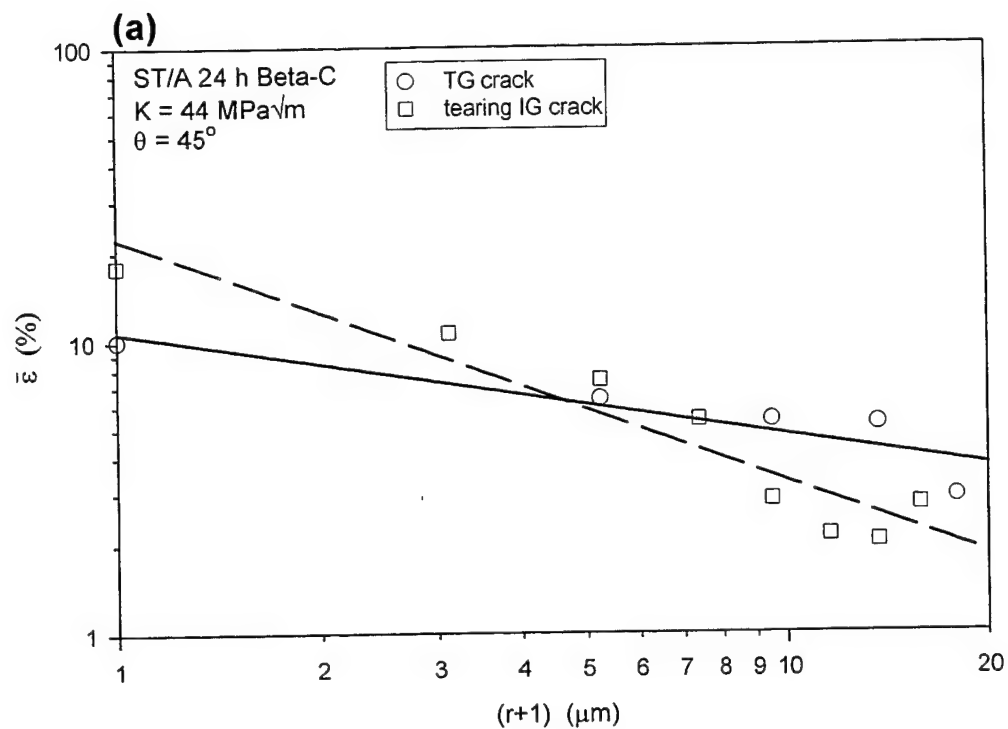


Fig. 9 Comparison of effective strain as a function of radial distance ahead of the crack tip for TG vs IG cracks at fixed K : a) $\theta = 45^\circ$, b) $\theta = 0^\circ$, and c) $\theta = -45^\circ$. Solid and dashed lines are regression fits to the data.

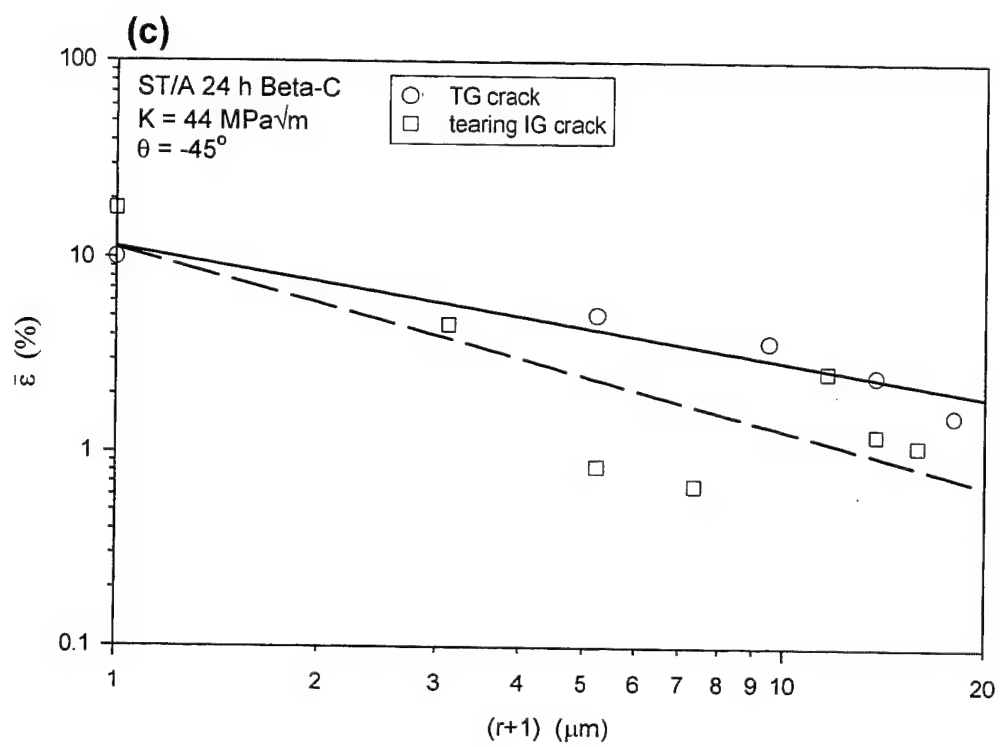


Fig. 9 (continued)

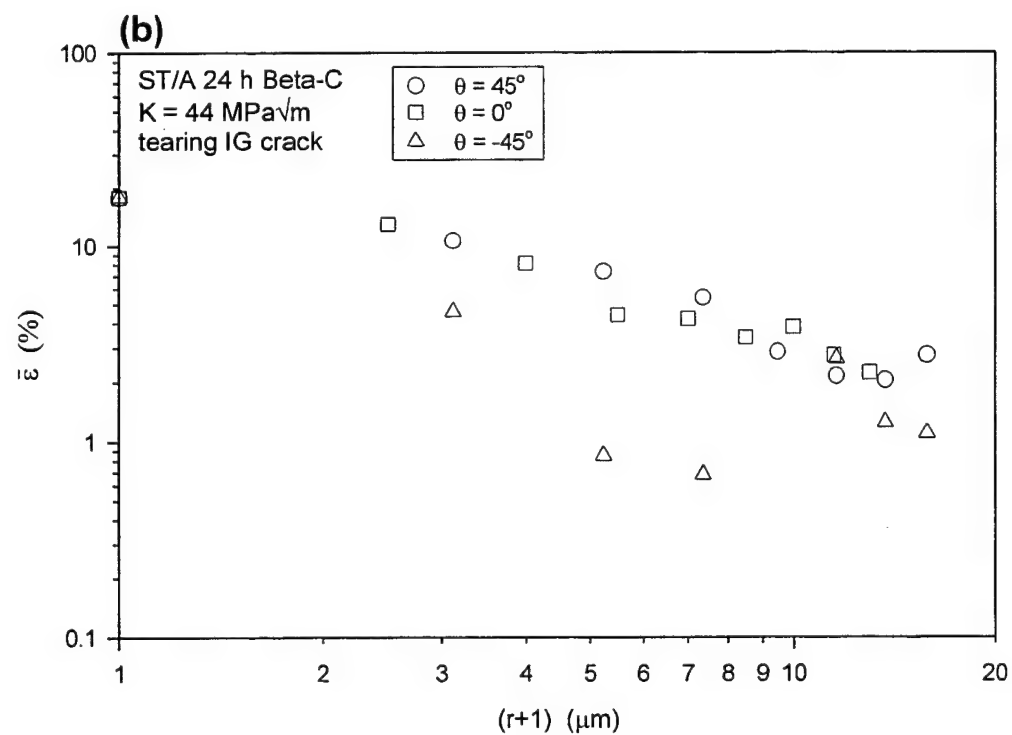
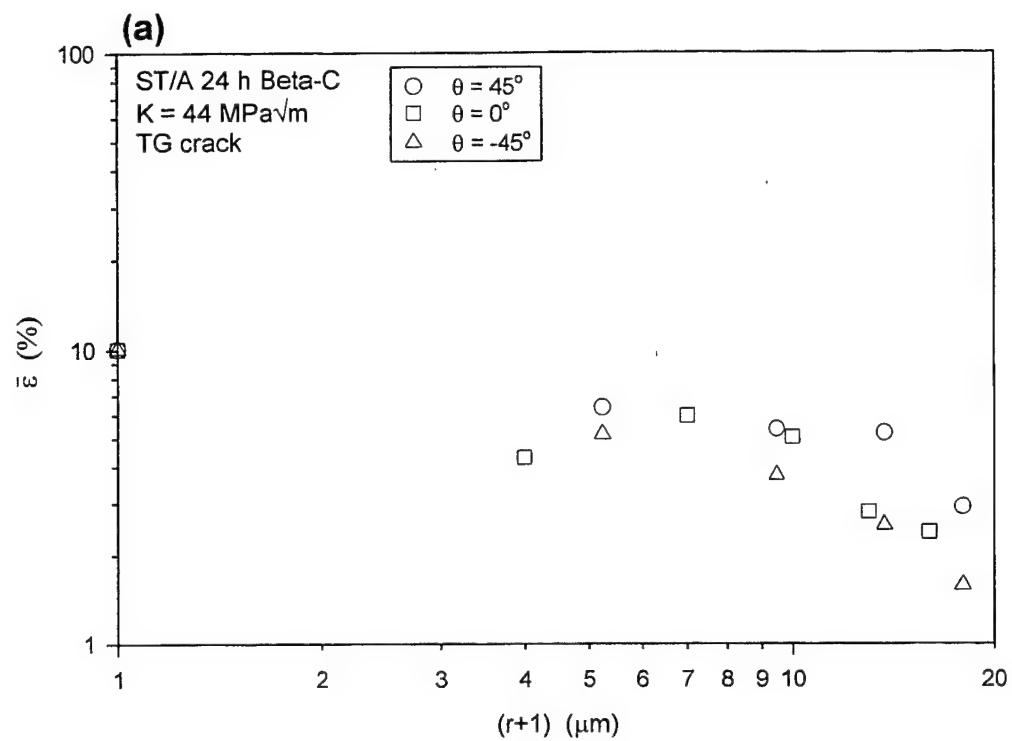


Fig. 10 Comparison of effective strain as a function of radial distance ahead of the crack tip at varying angular orientation for fixed K : a) transgranular crack, and b) intergranular crack.

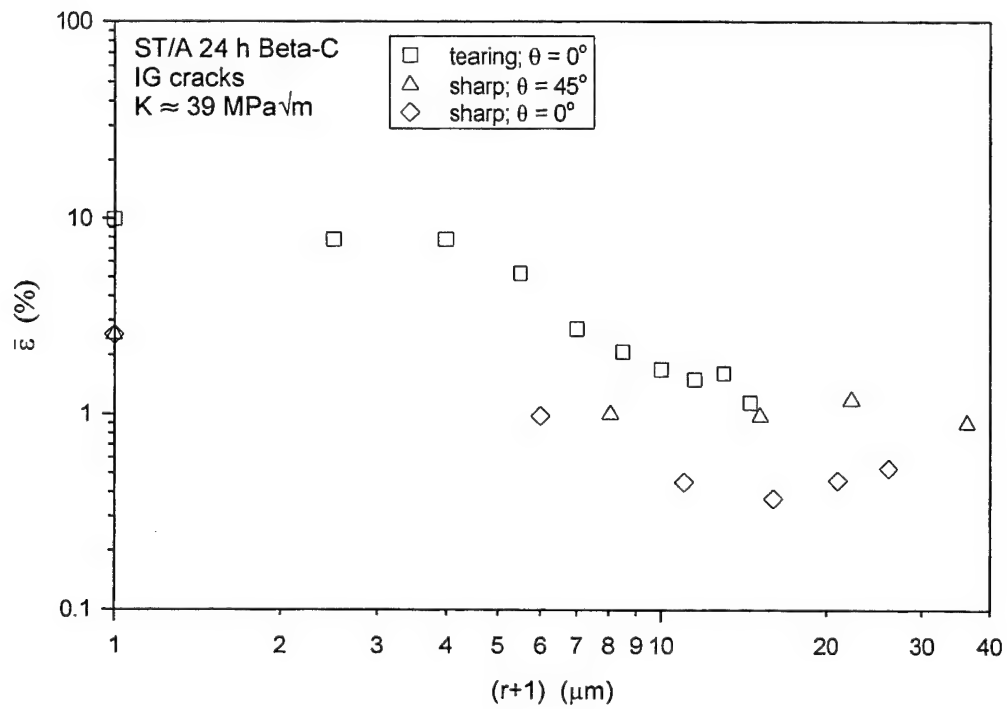


Fig. 11 Comparison of effective strain as a function of radial distance ahead of the crack tip for tearing vs sharp IG cracks at fixed K .

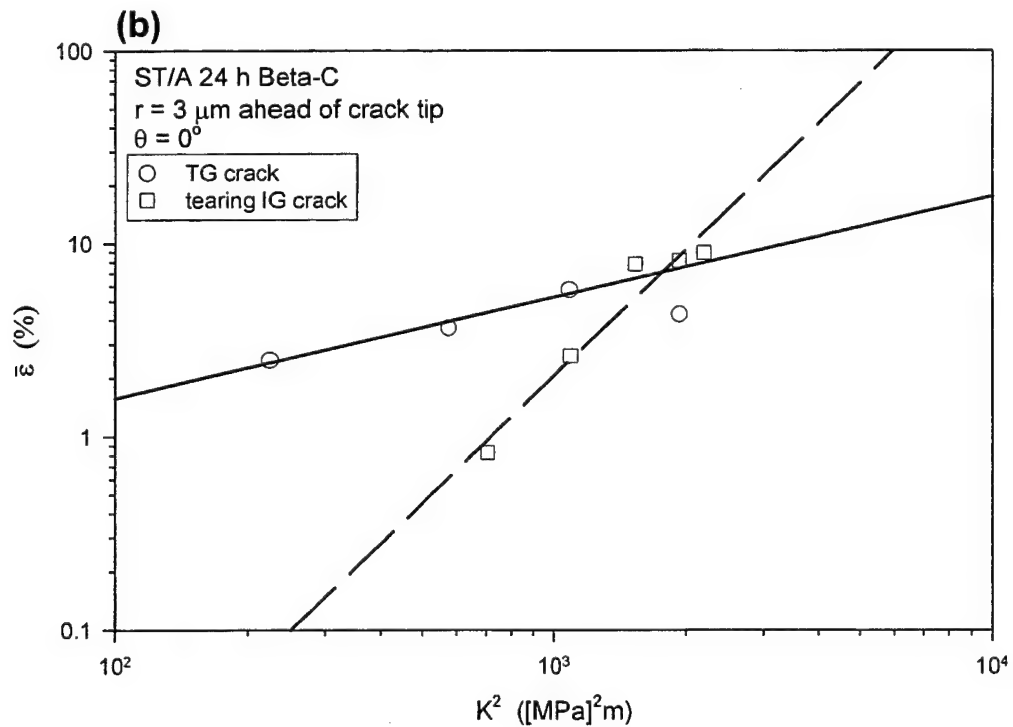
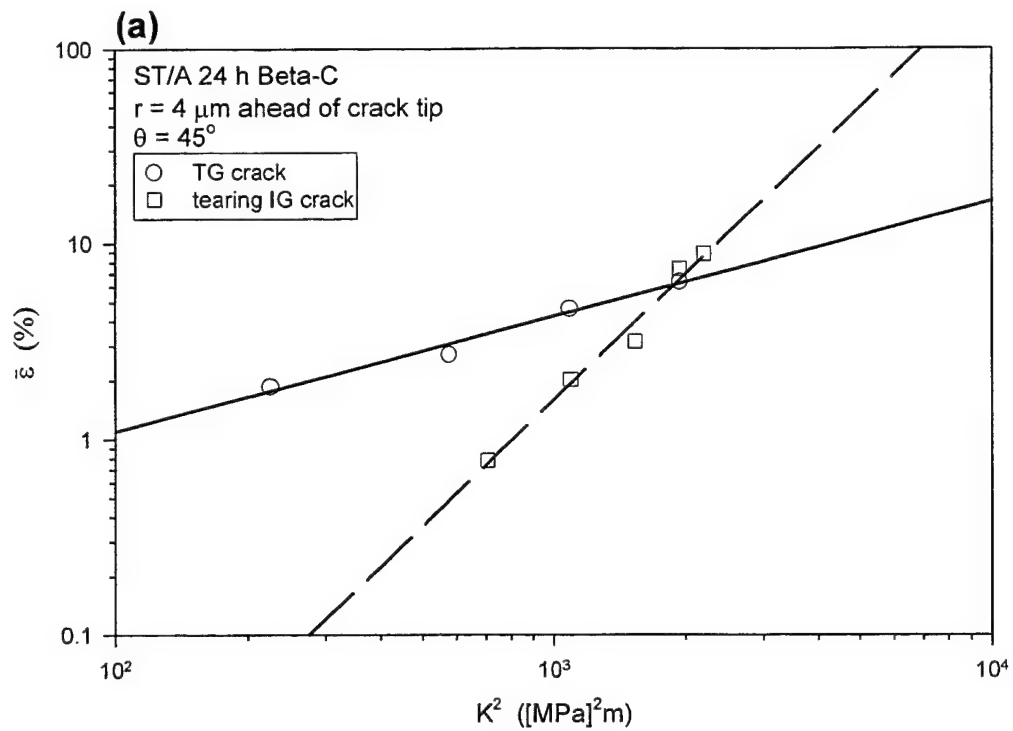


Fig. 12 Comparison of effective strain as a function of K^2 for TG vs IG cracks at fixed position ahead of the crack tip: a) $\theta = 45^\circ$, b) $\theta = 0^\circ$, and c) $\theta = -45^\circ$. Solid and dashed lines are regression fits to the data.

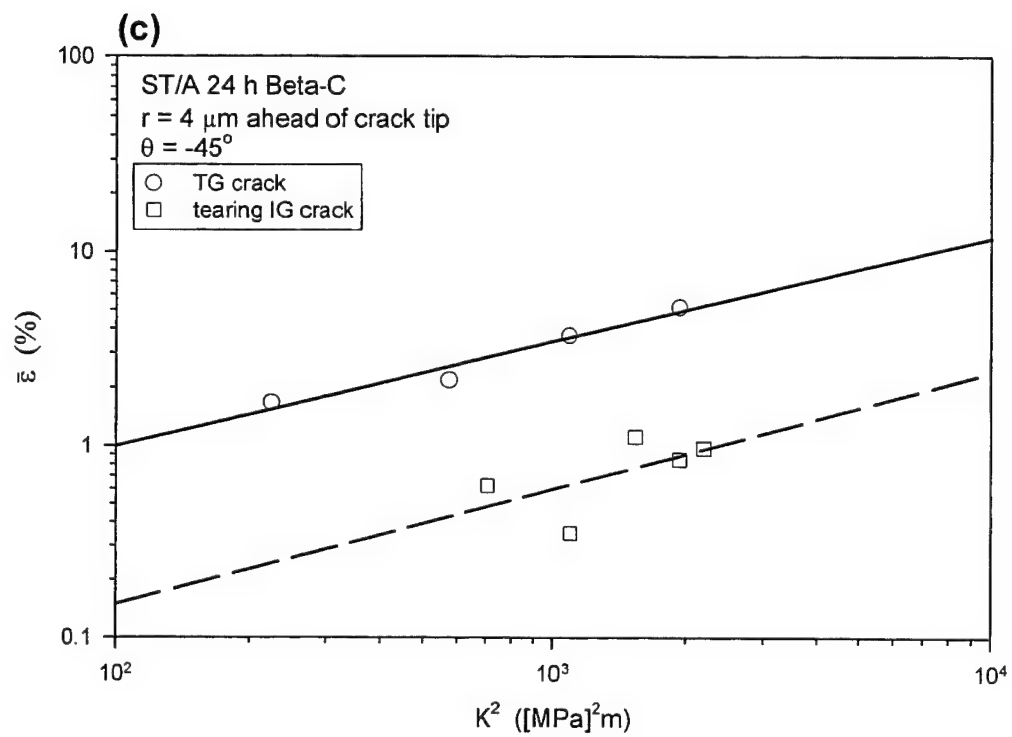


Fig. 12(continued)

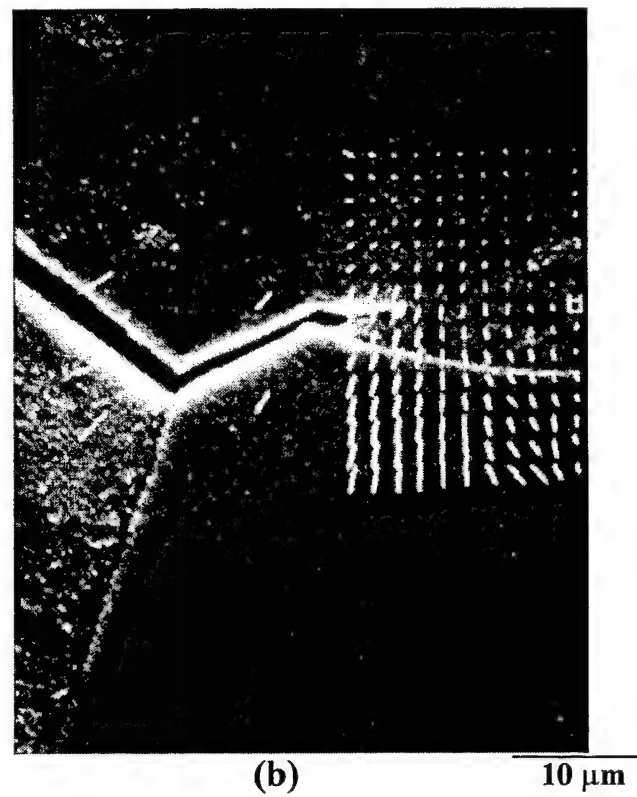
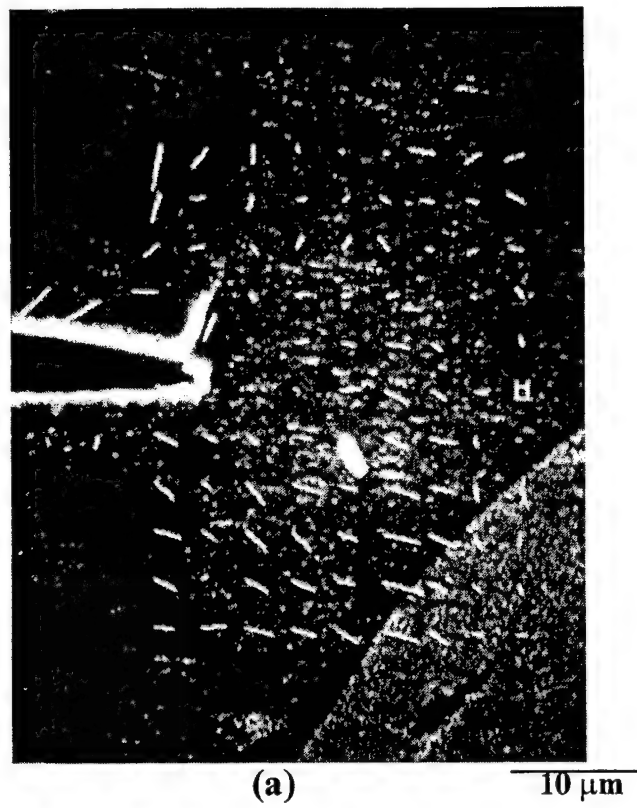


Fig. 13 Vectors representing time-dependent displacement changes superimposed on crack profiles: a) transgranular crack, $K = 44\ \text{MPa}\sqrt{\text{m}}$; and b) intergranular crack, $K = 47\ \text{MPa}\sqrt{\text{m}}$.

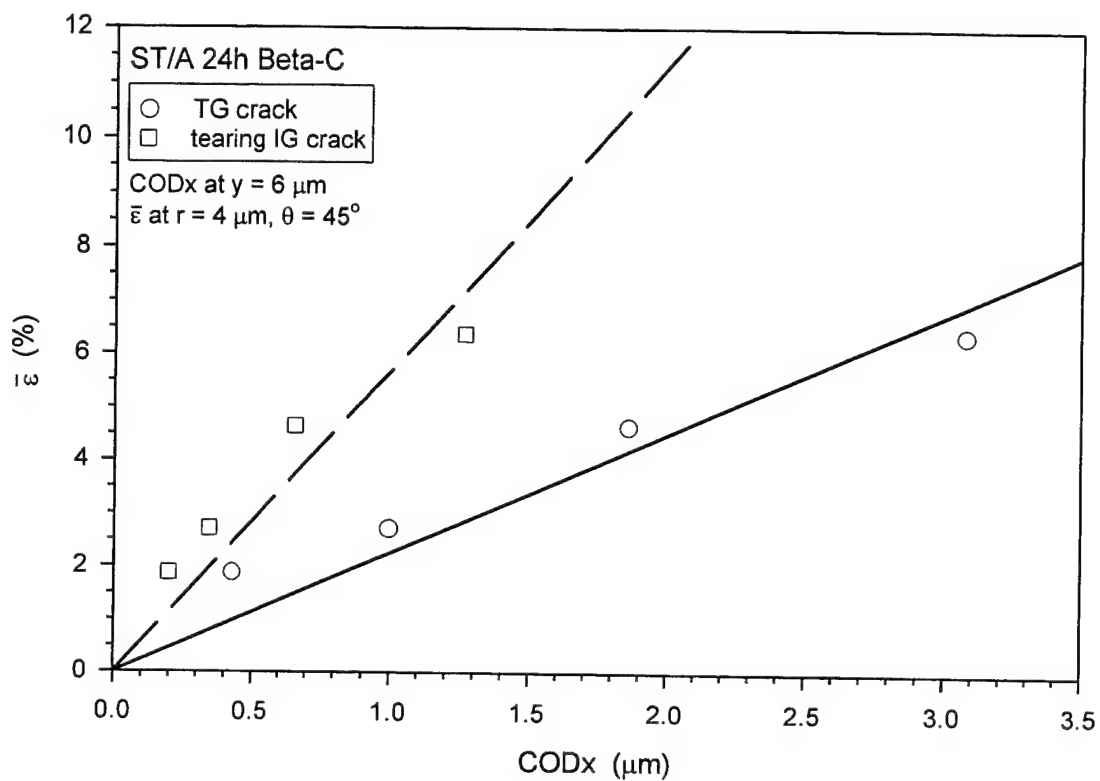


Fig. 14 Effective strain vs CODx for TG and IG cracks. The effective strain and CODx are measured at fixed positions about the crack tips. The solid and dashed lines are regression fits to the data.

Understanding Crack Tip Strain Rate Effects in Hydrogen Embrittlement for Improved Fitness-for-Service Modeling

R. P. Gangloff, B. P. Somerday and D. L. Cooke

R.P. Gangloff, B.P. Somerday and D.L. Cooke, *Understanding Crack Tip Strain Rate Effects in Hydrogen Embrittlement for Improved Fitness-for-Service Modeling*, in Life Prediction of Structures Subject to Environmental Degradation, R.N. Parkins and P.L. Andresen, eds., NACE, Houston, TX, in press (1996).

Understanding Crack Tip Strain Rate Effects in Hydrogen Embrittlement for Improved Fitness-for-Service Modeling

Richard P. Gangloff and Brian P. Somerday

**Department of Materials Science and Engineering
University of Virginia
Charlottesville, Virginia 22903-2442**

David L. Cooke

**Chevron Research and Technology Company
Richmond, California 94802-0627**

Problem

Fitness-for-service modeling is complicated greatly when a flawed component is exposed to a gas or electrolyte that produces atomic hydrogen through (electro)chemical reactions on crack and boldly-exposed surfaces, and is subsequently or concurrently stressed. The fracture mechanics approach to this problem is effective for high strength alloys, particularly steels; laboratory measurements over the past 30 years described time-dependent subcritical hydrogen cracking in terms of threshold stress intensity and growth rate parameters.^{1,2} These material-environment properties are modeled mechanistically based on considerations of material crack tip hydrogen concentration, occluded crack chemistry, the extent of bare surface reactions to produce hydrogen, and trapping-modified hydrogen diffusion in the crack tip process zone.³ This research has proven beneficial to fitness-for-service modeling of flawed components.⁴

Fracture mechanics-based life prediction is more complicated for hydrogen cracking involving low strength ductile alloys or crack tip passive film formation. In these materials, the threshold stress intensity for the onset of cracking and the rate of crack propagation depend on the applied loading rate, and more basically on crack tip strain rate. Materials that resist hydrogen cracking under quasi-static loading are susceptible to embrittlement within a window of active crack tip strain rates. Accordingly, the laboratory data base and fitness-for-service modeling method must include the interactive effects of applied stress intensity and crack tip strain rate. Crack tip strain rate is central to the film rupture and transient-dissolution model of environmental cracking, and provides a reasonable basis for engineering predictions.⁴ A similar framework has not been developed for hydrogen cracking.

In hydrogen embrittlement, deleterious crack tip strain rate effects are believed to result from loading rate effects on crack tip stress and strain fields, process zone deformation morphology, and hydrogen interactions with dislocations,⁵ as well as by the rupture of otherwise protective crack tip surface films.⁶ Detailed damage mechanisms have not been developed. Lacking a fundamental and

quantitative understanding of strain rate effects, fitness-for-service modeling must rely on laboratory measurements for conditions similar to component operation. Systematic studies are needed to develop data to more broadly support such analyses in complex industrial applications.

Objective

The objective of this review is to define research contributions that enable life prediction for material-environment systems where both stress intensity and crack tip strain rate govern hydrogen-enhanced crack propagation. Three elements of this problem are considered, including: a) a modern laboratory method to develop a fitness-for-service data base capturing loading rate effects in hydrogen embrittlement, b) loading rate effects in internal hydrogen embrittlement from prior environmental exposure, and c) crack tip strain rate effects in hydrogen embrittlement due to *in situ* environmental exposure. Research on crack propagation is emphasized and limiting uncertainties are cited.

Laboratory Test Method

Fracture mechanics laboratory methods have been developed over the past 10 years to define loading rate and crack tip strain rate effects on hydrogen embrittlement resistance.⁷⁻¹⁰ Several issues are central to such work. First, elastic-plastic analysis is necessary to define the proper macroscopic crack tip driving force for low strength materials as well as the stress, strain and strain rate fields about the crack tip. Second, high precision methods that continuously monitor crack growth are necessary to determine transient and steady-state material-cracking behavior. Third, computer-programmed loading experiments, with varying solution exposure, provide a probe of crack tip strain rate effects.

These attributes are combined in a constant extension rate method with a precracked and instrumented specimen. Measurements of load (P), crack mouth opening displacement (δ_m), and crack length (a) from direct current electrical potential difference yield the data shown in Figure 1.¹¹ Analysis of these data yields the threshold J-integral and elastic stress intensity for the onset of crack propagation, the time-based rate of crack extension, and the stress intensity dependence of crack growth, all for a known-fixed displacement rate but less well-defined crack tip strain rate. This method can be applied to specimens that are hydrogen precharged then fractured in moist air, fractured in an electrolyte without environmental preexposure, or a combination of both forms of hydrogen embrittlement. The results of this laboratory approach are relevant quantitatively to fitness-for-service modeling, provided that the laboratory and component loading rates are matched.

While fracture mechanics laboratory methods are well-developed, crack tip strain rate must be better defined from both the continuum and dislocation perspectives.^{12,13} The effects of crack tip shape, crack path, time-dependent deformation, and localized slip must be included in strain-rate calculations. Additional complexities include the dependence of strain rate on position ahead of the crack tip and on crack growth rate. Fracture mechanics experiments must be supplemented with microscopic studies of hydrogen effects on crack tip deformation and fracture.

Crack Tip Strain Rate Effects on Internal Hydrogen Embrittlement

Recent laboratory studies,¹⁴ as well as detailed analyses of a 1984 catastrophic fracture of a carbon steel pressure vessel in oil-refinery service,^{15,16} establish that low strength ferritic steels can be embrittled severely by either hydrogen predissolved in the microstructure from long-term environmental exposure, or by loading in the environment. Examples include brittle cracking of low strength C-Mn steels in wet H_2S service¹⁵⁻¹⁸ and in high pressure hydrogen gas at near-25°C,^{19,20} Cr-Mo alloy steels in

H₂ at elevated temperature,²¹ and cathodically polarized microalloyed steels in marine applications.^{10,18} While J-integral and CTOD-based methods provide a quantitative basis for fitness-for-service evaluations of flawed pressure components in each of these technologies, the effect of hydrogen is not incorporated sufficiently in such codes.

Embrittlement of low strength steels, from either predissolved or environmental hydrogen, is exacerbated by active crack tip straining, as first suggested based on fatigue crack growth experiments.^{20,22} Constant load or displacement experiments lead to the oft-cited observation that low strength steels are not prone to embrittlement; the threshold stress intensity for hydrogen cracking approaches the steel fracture toughness.^{2,14} This widely observed trend is established by the lower bounds on the results of several hundred laboratory experiments involving steels in hydrogen producing gases and electrolytes; Figure 2.^{1,2} In sharp contrast severe intergranular and transgranular hydrogen embrittlement is produced if the stress intensity is increased monotonically at a slow to modest rate.^{14,15,17-21} The threshold stress intensity for the onset of such cracking is low, perhaps 10% to 30% of K_{IC} , and the resistance to stable crack propagation is reduced compared to the hydrogen-free case. This trend is represented for hydrogen-precharged Cr-Mo alloy steels by the line marked "JSW" in Figure 2, and by the specific R-curve results shown in Figure 3. In this latter figure, the ductile fracture resistance of a hydrogen-free low-strength C-Mn steel in moist air (\blacktriangle and \bullet) is reduced substantially by either prior hydrogen charging in wet H₂S (\blacksquare), or by *in situ* loading in high pressure H₂ (\square and Δ). If active loading is interrupted, hydrogen cracking ceases and does not appear to occur during constant-load hold-times.¹⁴ This form of hydrogen embrittlement is exacerbated by decreasing steel yield strength,² decreasing crack tip strain rate through a minimum (Figure 4), and increased hydrogen concentration within the steel or on the straining crack tip surface (Figure 5). The effects of varying temperature, modestly above and below 25°C, and constraint, from plane strain to plane stress, are uncertain.

Since extreme embrittlement is produced in these steels by electrochemical or H₂ precharging, followed by active loading in an inert environment (Figures 2 and 3), the important strain rate effect is associated with crack tip plasticity and hydrogen redistribution to microstructural fracture sites. The additional effect of crack tip strain rate in promoting hydrogen production and uptake during loading of hydrogen-free or precharged steels in the environment is unlikely for H₂. If an alkaline electrolyte with H₂S or NaCl produces a crack tip passive film, or if a sulfide film is produced in acidified wet H₂S, then strain rate could additionally degrade surface-film integrity.

Fitness-for-service analyses of low strength steels, hydrogen charged by environmental exposure,¹⁵ are complicated by several uncertainties. A range of crack tip strain rates and multiple-loading cycles can be encountered in service and hydrogen concentration gradients exist in the walls of pipes and pressure vessels containing hydrogen-producing environments. Additionally, stress state may vary, and distributed hydrogen delamination, microcracking and blister-damage can affect crack propagation. The behavior of surface and through-wall cracks in such instances is difficult to model. There is presently no accepted mechanistic explanation for the effect of crack tip strain rate on internal hydrogen embrittlement, and there are no mechanism-based models that predict the loading rate effect on material-property parameters necessary for component life prediction. Dislocations may transport H; promote cleavage, slip-band cracking, or intergranular microcracking; or accelerate microvoid growth and coalescence by plastic instability.

Crack Tip Strain Rate Effects on Hydrogen Environment Embrittlement

Alloy embrittlement behavior and component life prediction are complicated when hydrogen

production and uptake are affected by the stability of a passive film at the crack tip.⁶ An example is provided by the brittle cracking of high strength body-centered-cubic β -titanium alloys intended for a variety of high performance applications, including fasteners in marine environments.^{9,11,12,23} Severe intergranular crack growth can be produced by exposure of these alloys to neutral NaCl solution, at stress intensity levels above a threshold.^{9,11} The rising load experiment represented in Figure 1 provides an important tool for alloy development and damage tolerant life prediction. For example, the data summarized in Figure 6 show that the rising load threshold for brittle cracking of several β -titanium alloys in aqueous chloride solution can be well below K_{IC} , depending on alloy composition, microstructure, and yield strength.¹¹ Brittle cracking in this material-environment system is attributed to hydrogen environment embrittlement based on circumstantial evidence.

Experiments with precracked specimens subjected to either constant or monotonically rising load demonstrate that the threshold stress intensity for environmental crack growth depends on loading rate, and more basically on crack tip strain rate. Typical threshold data, of the type presented in Figure 6, are plotted vs dK/dt in Figure 7 for two high strength β -titanium alloys in NaCl.¹¹ The strain rate regime for hydrogen embrittlement is surprisingly wide, and depends on crack path and alloy composition or microstructure. Environmental cracking is promoted by increasing crack tip strain rate, above the level typical of constant load, but cracking is eliminated at very high loading rates.

Brittle cracking may or may not be produced by environmental exposure under constant load. The key factor appears to be if the magnitude of the crack tip strain rate from creep is sufficient to sustain hydrogen production and damage. This behavior is evidenced by experiments that vary the time between load application and exposure to the solution; an environmental crack will not propagate if sufficient creep occurs to reduce the crack tip strain rate prior to solution introduction. An example of this effect is presented in Figure 8 for high strength Beta-C in NaCl.¹¹ Environmental cracking occurred under fixed crack mouth opening displacement if the specimen was exposed to solution within 4 minutes of loading to a high stress intensity. Cracking did not occur for the same loading, but with a 24 hour creep-period before solution introduction.

While a transgranular fatigue precrack will grow when rapidly subjected to constant load in NaCl solution, an intergranular crack will not propagate, suggesting an important difference in the strain rates about the tips of these two types of crack. Fracture mechanics does not recognize such a difference, supporting the importance of measurements of crack tip deformation. These experiments show that the kinetics of crack propagation depend on both stress intensity and crack tip strain rate, rather than a unique growth rate vs stress intensity relationship. This behavior leads to complex patterns of crack propagation and arrest, depending on specimen or component compliance. A typical example is provided by the crack length data in Figure 1.

The effect of strain rate is attributed to enhanced hydrogen uptake that follows from destabilization of the crack tip passive film, as well as to hydrogen damage within the process zone and that depends on active plastic deformation. The relative contributions of these factors is not understood for titanium alloys in aqueous chloride. Limited results suggest a similar important role of crack tip strain rate for α/β -titanium alloys fractured in neutral NaCl solution,²⁴ but not for aluminum alloys that should form a similar crack-tip passive film in NaCl at free corrosion potentials.²⁵ Experiments with low strength β -titanium alloys in acidic solutions with H_2S suggest that process zone hydrogen damage is not promoted by active crack tip plasticity, in contrast to the behavior of low strength steels, Figure 3.²³

Component life prediction in this case requires measurements and modeling of the three dimensional relationship between applied stress intensity, crack tip strain rate and subcritical crack

growth rate. This problem is complex because these parameters are interrelated. Crack growth kinetics must be defined empirically because of a lack of a quantitative model of hydrogen embrittlement.

Conclusion

Active crack tip strain rate promotes severe intergranular and transgranular hydrogen embrittlement in low strength steels, and in alloys that form a passive crack tip film during environmental exposure. Fitness-for-service and remaining-life models are accordingly complicated. A rising load fracture mechanics experiment provides important data for hydrogen-resistant alloy development and quantitative component performance predictions. Loading rate effects are explained qualitatively by crack tip strain rate and active plasticity that enhance hydrogen production and uptake, and that promote process zone hydrogen transport and microscopic damage. Mechanism-based models of the hydrogen cracking threshold and stable crack growth rate parameters do not exist. Lacking fundamental understanding, fitness-for-service modeling must rely on laboratory measurements for conditions similar to component operation. Systematic laboratory studies to define the pertinent variables are limited.

Acknowledgement

Research on fitness-for-service of steels in wet H₂S was supported by the Chevron Research and Technology Company. Research on high strength titanium alloys in marine environments was sponsored by the Office of Naval Research (Grant N00014-91-J-4164), with Dr. A. John Sedriks as Scientific Monitor. This support is gratefully acknowledged.

References

1. R.P. Gangloff, *Materials Science and Engineering*, A103 (1988): p. 157.
2. R.P. Gangloff, *Corrosion Prevention and Control*, ed. M. Levy, S. Isserow, (Watertown, MA: US Army Laboratory Command, 1986): p. 64.
3. R.P. Wei, R.P. Gangloff, *Fracture Mechanics: Perspectives and Directions*, ASTM STP 1020, ed. R.P. Wei, R.P. Gangloff (Philadelphia, PA: ASTM, 1989): p. 233.
4. P.L. Andresen, R.P. Gangloff, L.F. Coffin, F.P. Ford, *Fatigue 87*, Vol. III-A, ed. R.O. Ritchie, E.A. Starke, Jr. (West Midlands, UK: EMAS, 1987): p. 1723.
5. J.K. Tien, S.V. Nair, R.R. Jensen, *Hydrogen Effects in Metals*, ed. I.M. Bernstein and A.W. Thompson (Warrendale, PA: TMS-AIME, 1981): p. 37.
6. J.R. Scully, P.J. Moran, *Environmentally Assisted Cracking: Science and Engineering*, ASTM STP 1049, ed. W.B. Lisagor, T.W. Crooker, B.N. Leis (Philadelphia, PA: ASTM, 1990): p. 5.
7. G. Abramson, J.T. Evans, R.N. Parkins, *Metallurgical Transactions*, A, 16A (1985): p. 101.
8. E.M. Hackett, P.J. Moran, J.P. Gudas, *Fracture Mechanics, Seventeenth Volume*, ASTM STP 905, ed. J.H. Underwood, et al. (Philadelphia, PA: ASTM, 1986): p. 512.
9. L.M. Young, G.A. Young, Jr., J.R. Scully, R.P. Gangloff, *Metallurgical and Materials Transactions*, A, 26A (1995): p. 1257.

10. W. Dietzel and M. Pfuff, Hydrogen Transport and Cracking in Metals, ed. A. Turnbull (London, UK: Institute of Metals, 1995): p. 77.
11. B.P. Somerday, L.M. Young, R.P. Gangloff, *The Effects of Crack Tip Strain Rate and Stress Intensity on Environment-Assisted Cracking of Beta-Titanium Alloys in Aqueous NaCl*, Metallurgical and Materials Transactions (1996): in review.
12. L.M. Young, *Environment-Assisted Cracking in Beta Titanium Alloys*, MS Thesis (Charlottesville, VA: University of Virginia, 1993).
13. T. Shoji, S. Suzuki and R.G. Ballinger, *Theoretical Predictions of SCC Growth Behavior*, Proceedings, 7th International Conference on Degradation of Materials in Nuclear Power Systems-Water Reactors (Houston, TX: NACE, 1995): in press.
14. R.P. Gangloff, *Critical Assessment of Hydrogen Embrittlement in Pressure Vessel Steels*, Draft Report HPV-59 (New York, NY: Materials Properties Council, 1991).
15. H.I. McHenry, D.T. Read, T.R. Shrivs, Materials Performance, August (1987): p. 18.
16. H.I. McHenry, P.T. Purtscher, T.R. Shrivs, Corrosion Science, 27 (1987): p. 1041.
17. L. Coudreuse, A. Ponsot, P. Bocquet, Second International Conference on Interaction of Steels with Hydrogen in Petroleum Industry Pressure Vessel and Pipeline Service, (New York, NY: Materials Properties Council, 1994): p. 759.
18. *Use of Fracture Mechanics Concepts in the Case of Hydrogen Charged Materials*, Final Report, ECSC Steel Research Program (Commission of the European Communities, 1995).
19. S.L. Robinson, R.E. Stoltz, Hydrogen Effects in Metals, ed. I.M. Bernstein, A.W. Thompson (Warrendale, PA: TMS-AIME, 1981): p. 987.
20. H.J. Cialone, J.H. Holbrook, Metallurgical Transactions A, 16A (1985): p. 115.
21. L. Coudreuse, R. Blondeau, A. Cheviet, Memoires et Etudes Scientifiques Revue de Metallurgie, 86 (1989): p. 35.
22. H.G. Nelson, Effect of Hydrogen on Behavior of Materials, ed. A.W. Thompson and I.M. Bernstein (Warrendale, PA: TMS-AIME, 1976): p. 602.
23. J.A. Grandle, B.P. Somerday, R.P. Gangloff, Proceedings of the Tri-Service Conference on Corrosion, ed. T. Naguy, (Wright-Patterson Air Force Base, OH: USAF, 1994): p. 375.
24. J.A. Muskovitz, R.M. Pelloux, Corrosion, 35 (1979): p. 509.
25. W. Dietzel, K.-H. Schwalbe, D. Wu, Fatigue and Fracture of Engineering Materials and Structures, 12 (1989): p. 139.

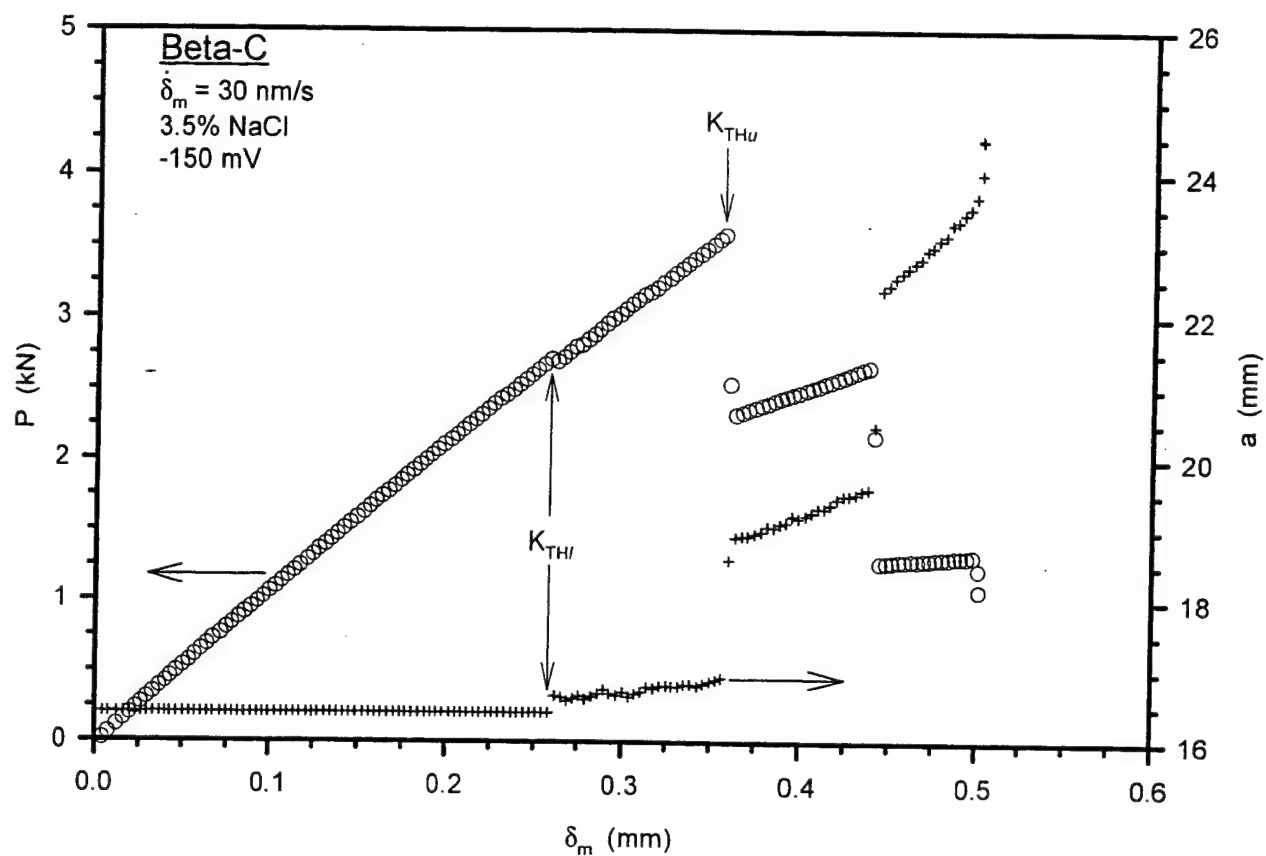


Figure 1 Measured load (P), as well as crack length (a), vs crack mouth opening displacement (δ_m) for a fatigue precracked compact tension specimen of peak-aged Beta-C subjected to constant crack mouth opening displacement rate-controlled ($d\delta_m/dt = 30 \text{ nm/s}$) loading in aqueous 3.5% NaCl at -150 mV_{SCE} .¹¹

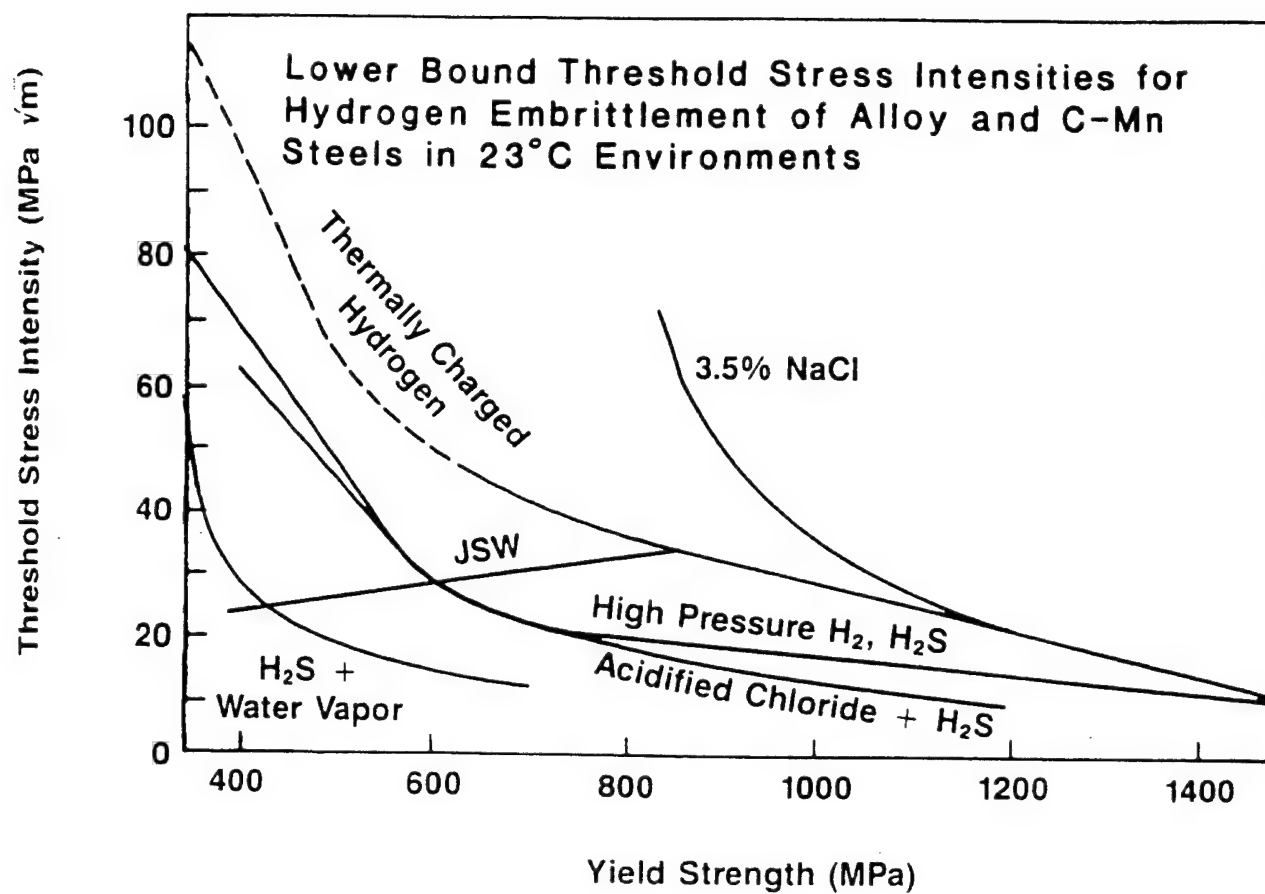


Figure 2

Lower bounds on the yield strength dependence of the threshold stress intensity for hydrogen embrittlement for ferrite-pearlite, bainitic and tempered martensitic steels stressed in five hydrogen producing environments, or after pre-exposure to dissolved hydrogen in the steel.^{1,2}

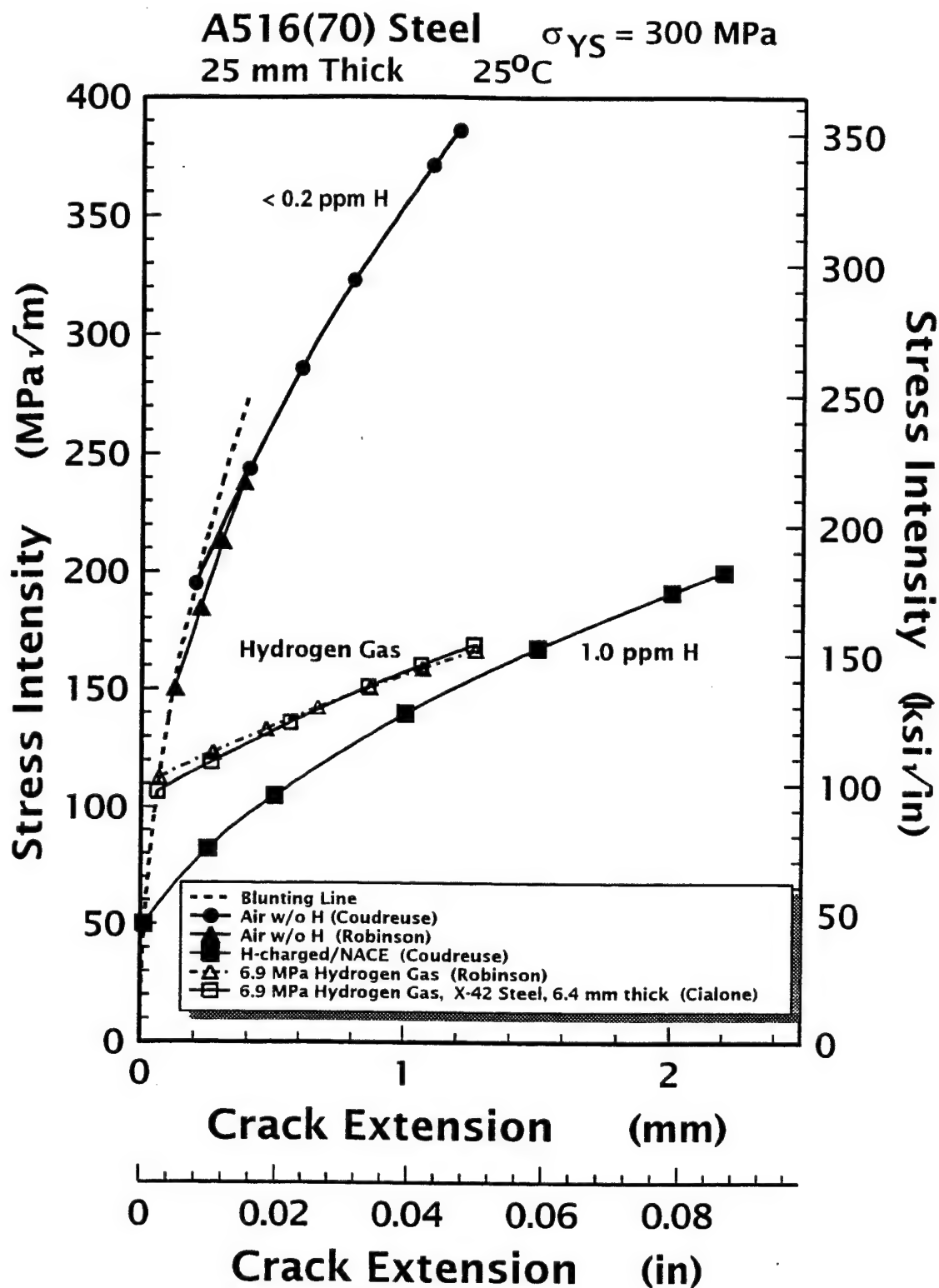


Figure 3

The effect of concurrent H_2 -environment exposure, or hydrogen precharging in wet H_2S , on the ductile fracture initiation and growth toughness of a low strength C-Mn steel subjected to constant crack mouth opening displacement rate loading at 25°C.¹⁷⁻²⁰ The threshold stress intensity for the onset of hydrogen embrittlement is given by the point of departure from the blunting line. This threshold is plotted in Figures 4 and 5.

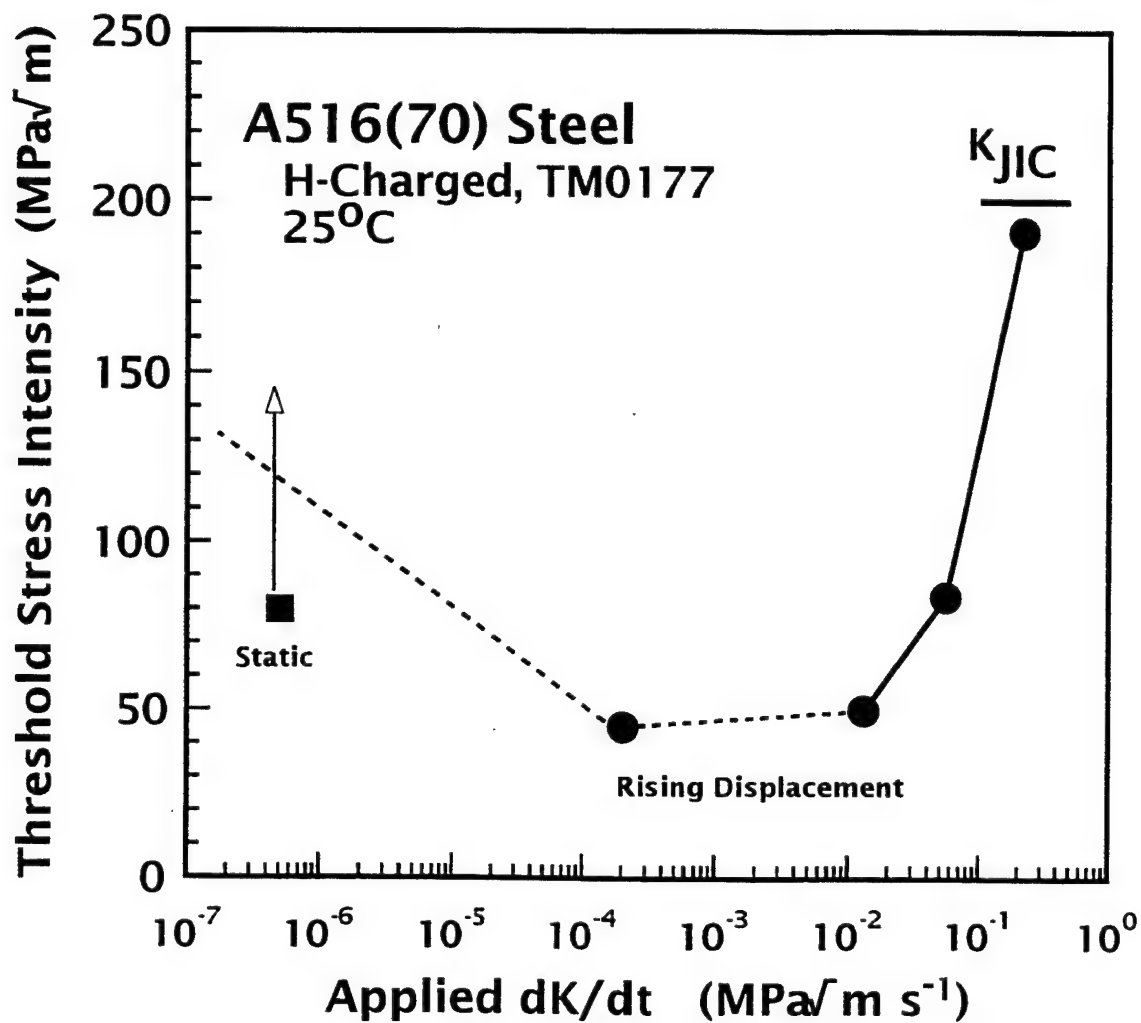


Figure 4

The effect of load-line displacement rate on the threshold stress intensity for crack propagation in A516(70) steel, precharged with 1 part-per-million (weight) hydrogen.

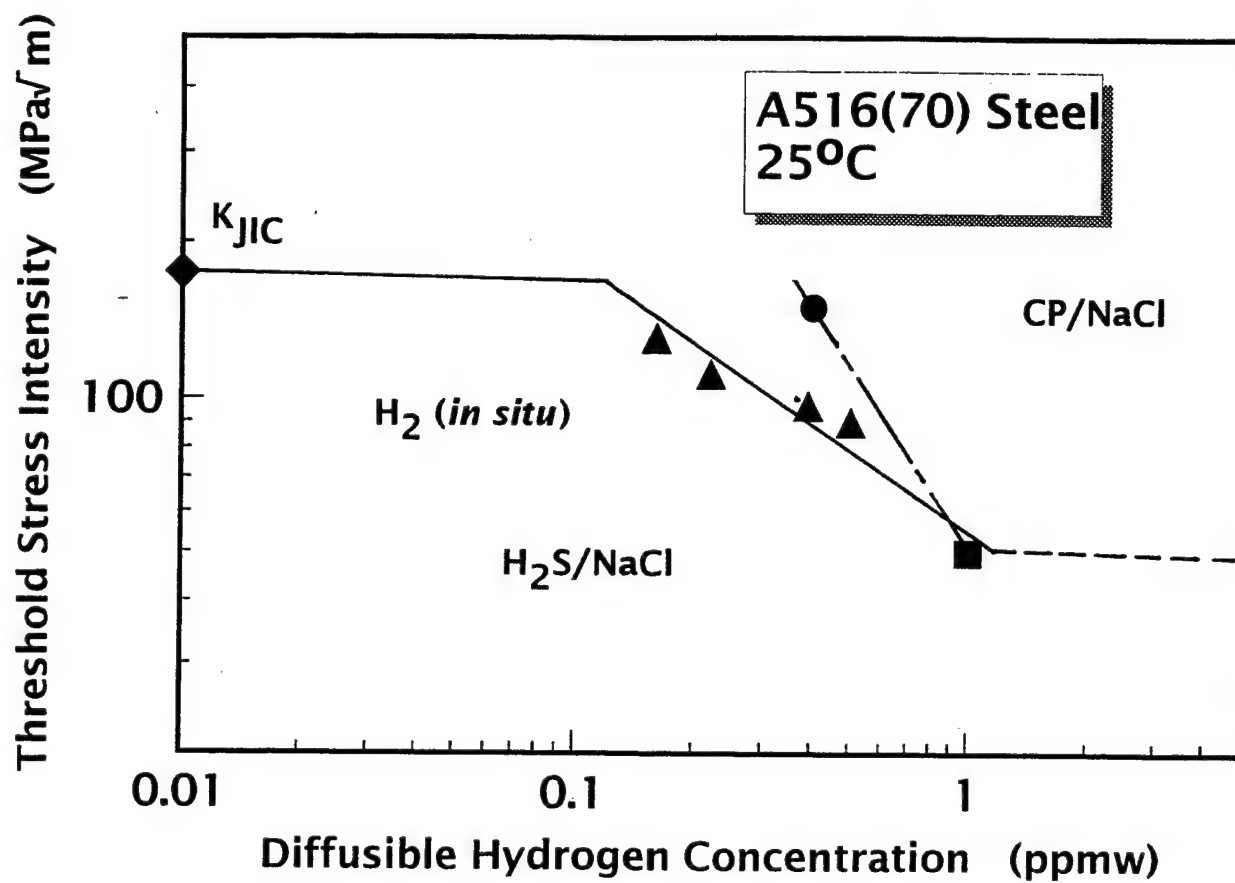


Figure 5

The effect of precharged hydrogen concentration on the threshold stress intensity for crack propagation in A516(70) steel, loaded at a fixed slow displacement rate.

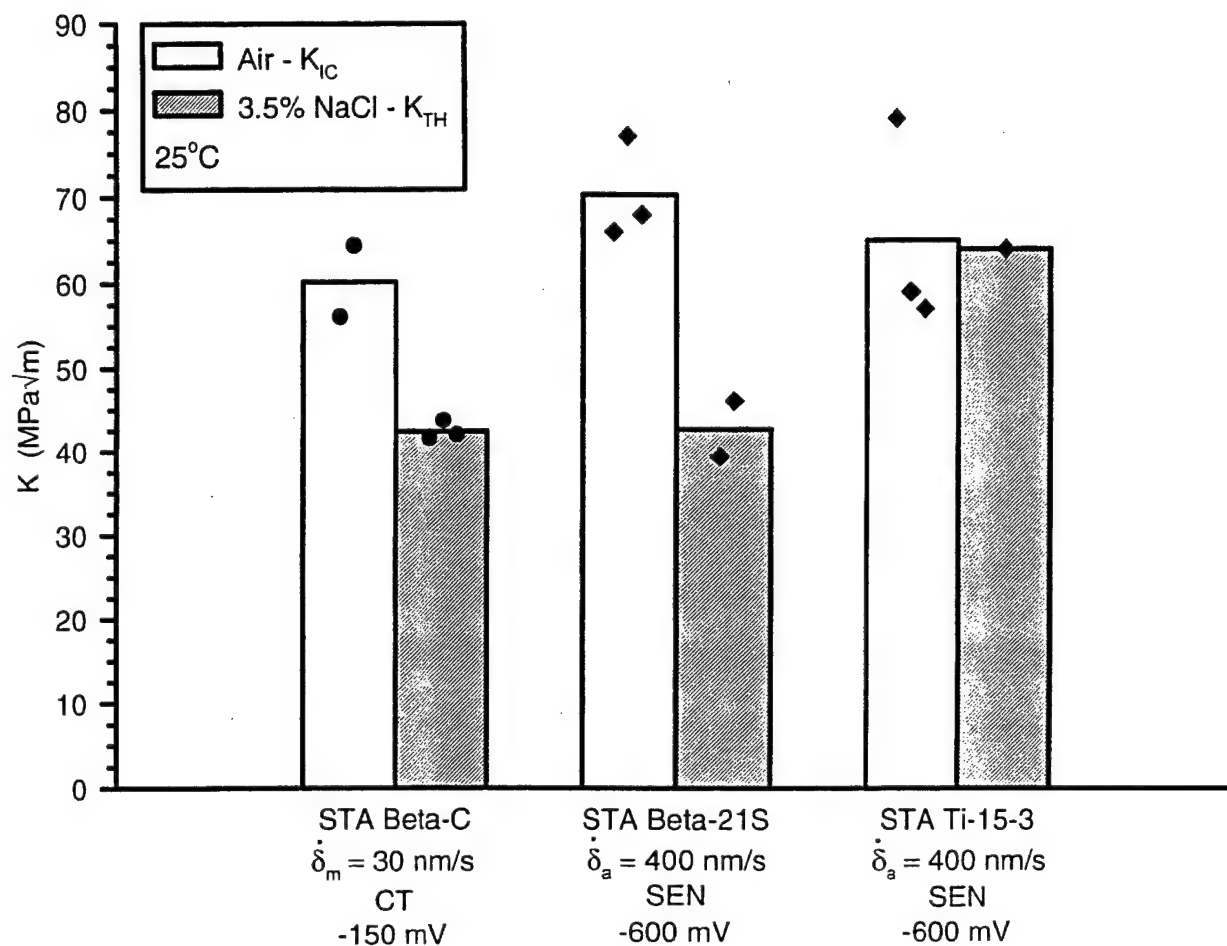


Figure 6

Comparison of the constant displacement rate threshold stress intensity (K_{TH}) for crack extension in aqueous 3.5% NaCl at fixed electrode potential, to the air fracture toughness (K_{IC}), for solution heat-treated and aged (STA) compact tension specimens of Ti-3Al-8V-6Cr-4Mo-4Zr (Beta-C), as well as single-edge cracked specimens of Ti-15Mo-3Nb-3Al (Beta-21S) and Ti-15V-3Cr-3Al (Ti-15-3).^{11,23}

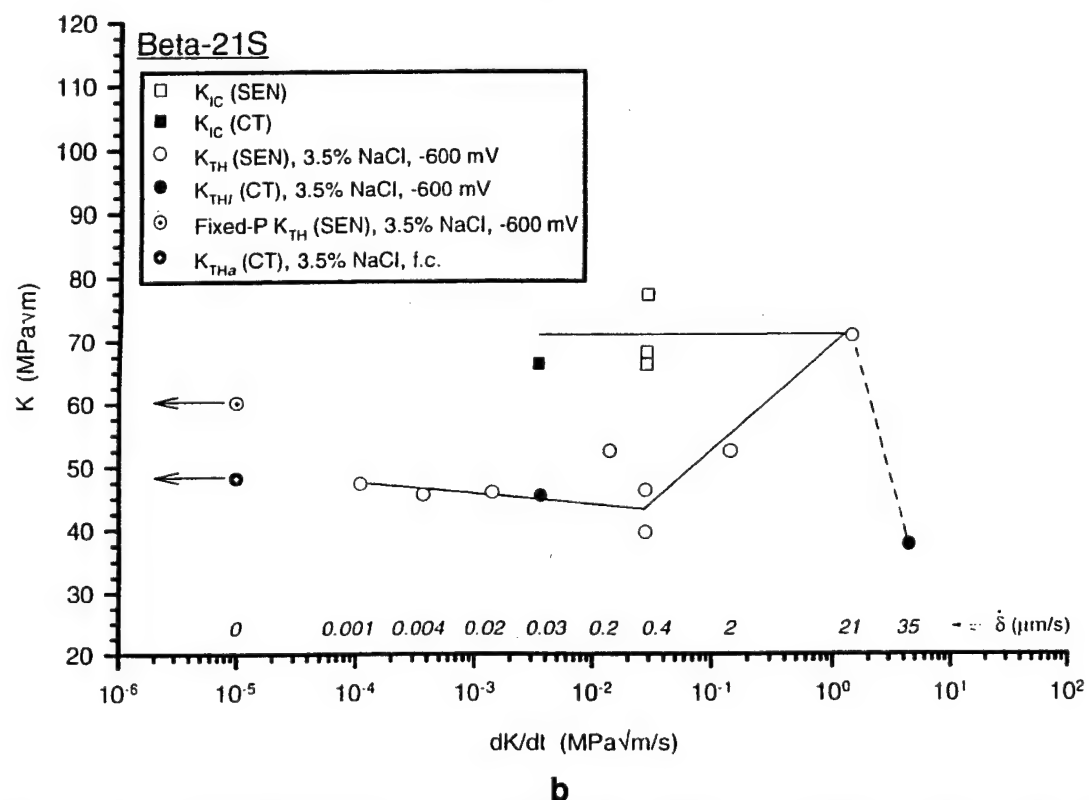
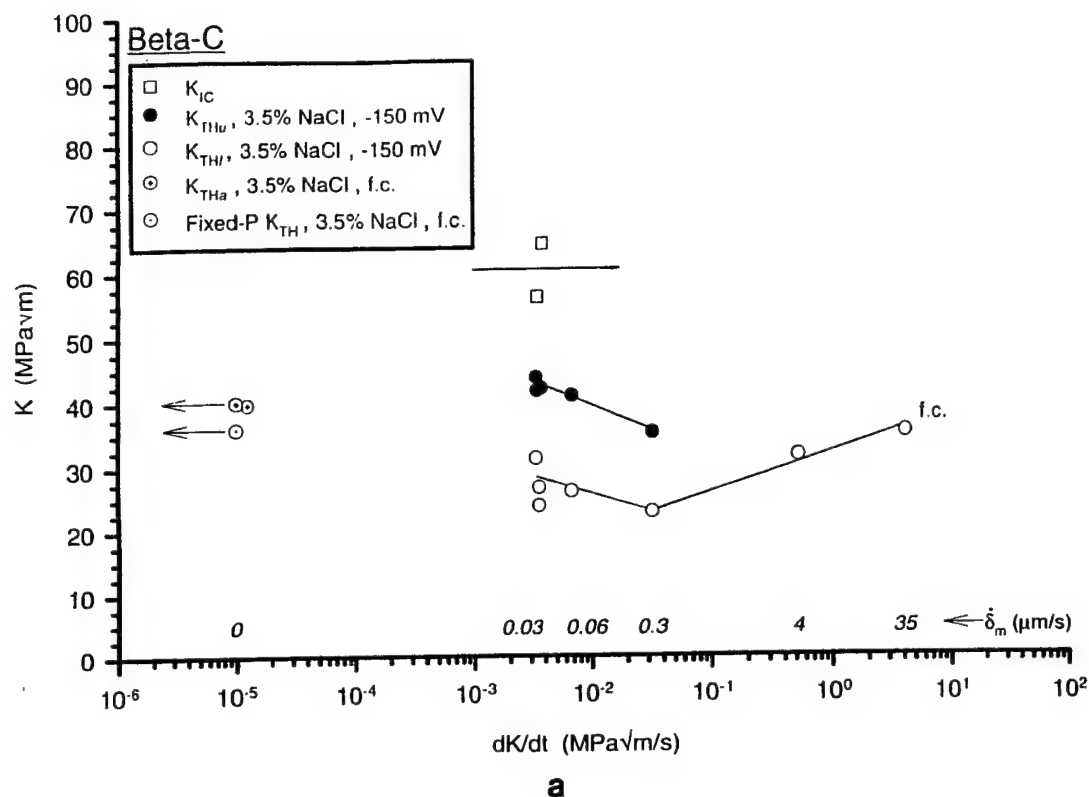


Figure 7

The constant displacement rate threshold stress intensity for cracking in aqueous 3.5% NaCl at fixed electrode potential, as a function of the rate of change of stress intensity (dK/dt) for: (a) peak-aged Beta-C under constant δ_m/dt , and (b) peak-aged Beta-21S under both constant crack-mouth-opening and test-machine-actuator displacement rate control. Static-loading results are included and the displacement rate is indicated for each dK/dt .^{11,12}

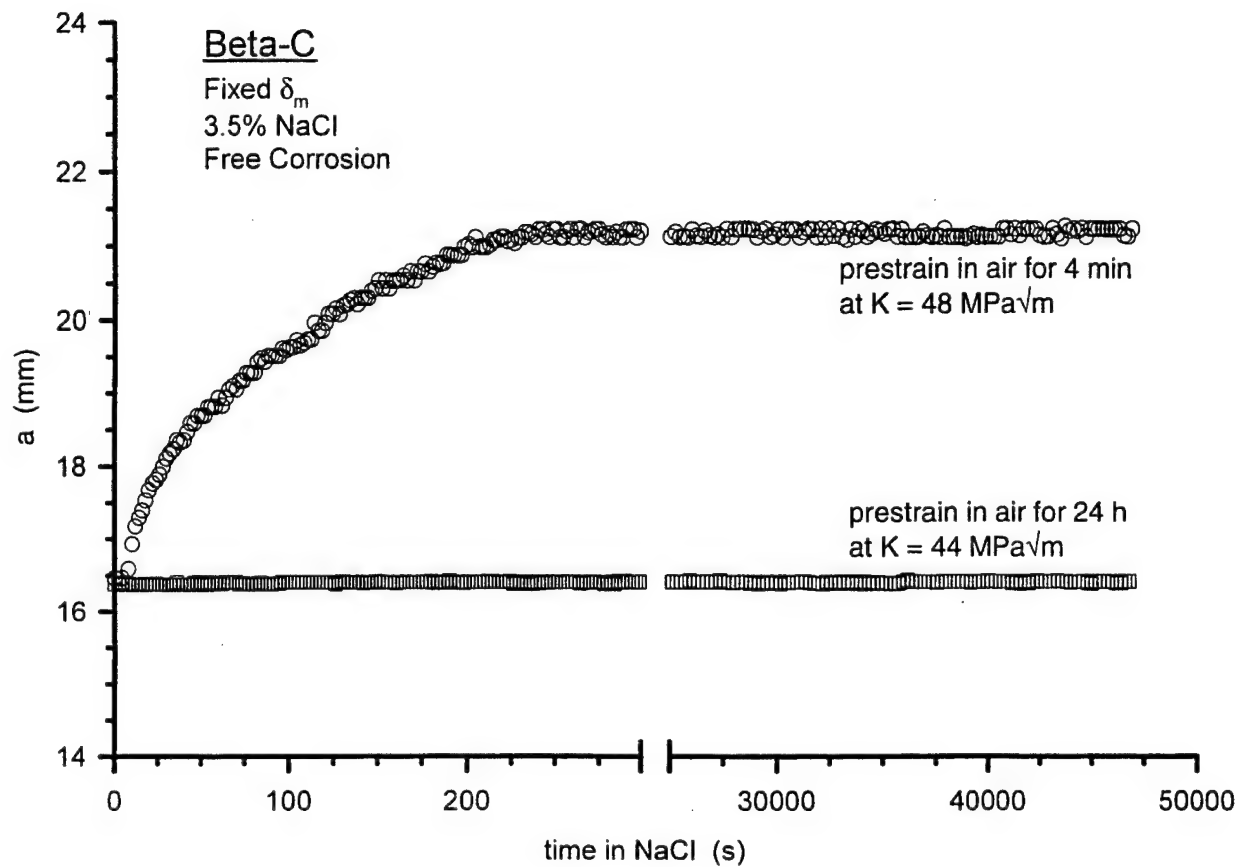


Figure 8 The effect of air prestrain duration, at fixed crack mouth opening displacement, on subsequent subcritical crack propagation in Beta-C exposed to 3.5% NaCl at free corrosion.¹¹

**Effect of Pre-dissolved Hydrogen on Fracture Initiation in Metastable
Beta Ti-3Al-8V-6Cr-4Mo-4Zr**

M. A. Gaudett and J. R. Scully

ENHANCED RESISTANCE TO STEADY STATE ACTIVE DISSOLUTION AND PASSIVITY OF TI ALLOYED WITH NB AND ZR

Steven Y. Yu and John R. Scully
University of Virginia
Department of Materials Science and Engineering
Center for Electrochemical Science and Engineering
Charlottesville, VA 22903-2442

Alloying of Ti with Nb and Zr resulted in improved resistance to active dissolution and improved passivation in comparison to Ti in 5 M HCl solution at 37°C. The improved resistance to active dissolution was attributed to the enrichment of elemental Nb and Zr on the active surface of Ti which resulted in reduced dissolution rates and led to the formation of a passivating coverage by Nb containing oxides and ZrO₂. XPS revealed that the surfaces of Ti-45% Nb and Ti-50% Zr were enriched with Nb and Zr, after long exposures to 5 M HCl in the active region. Open circuit potentials and impedance data suggested that enrichment occurred after chemical dissolution of native or anodic oxides and surface activation of the alloys. The mechanisms by which Nb and Zr enrich the surface are: i) preferential dissolution of Ti in the active state and ii) the slow chemical dissolution rate of ZrO₂ relative to TiO₂. The two mechanisms account for improved resistance to active dissolution and passivation of Ti-Zr-Nb ternary alloys with moderate alloying additions (11% to 13% by weight) of Nb and Zr.

INTRODUCTION

Commercially pure titanium (C.P. Ti) is widely utilized in biomedical implants due to its good corrosion resistance. However, the modular design of modern orthopedic implants results in tight joints where crevices can form. In addition, the mechanical abrasion experienced by implants during their service life can introduce oxidized alloying elements into the surrounding tissues. Beck showed that Ti⁺³ was the dominant dissolved species resulting from the scratch repassivation of Ti, and Baes and Mesmer reported that Ti⁺³ is hydrolyzable (1,2). The hydrolysis of Ti⁺³ has been shown to result in a pH as low as 0, as found in 1 M TiCl₃ dissolved in deaerated water (3). Moreover, Kolman and

Scully have shown that Ti^{+3} production occurs over the duration of repassivation due to the low overall current efficiency of TiO_2 formation (3). Therefore, the hydrolysis of titanium ions during passive dissolution and abrasion-repassivation can result in local acidification and a high Cl^- concentration adjacent to the implant. In addition, Beck reported a $pH < 1.3$ near a corroding pit exposed to neutral chloride solution (4). Consequently, an improved implant alloy that exhibits enhanced active corrosion resistance, reduced passive dissolution, and improved repassivation behavior in both physiological and aggressive crevice simulating environments is of technological interest.

Ti-13% Nb-13% Zr, a near-beta titanium alloy, has been developed by Smith & Nephew, Inc., specifically for use in orthopedic implants. Ti-13% Nb-13% Zr contains elements, which exhibit high corrosion resistance due to the formation of protective oxide films (5,6,7,8,9,10,11,12,13,14). Okazaki, and Ito showed that the alloying addition of Nb and Zr to Ti results in improved resistance to active dissolution and/or passivity of Ti (15). In addition, alloying with Nb has been shown to reduce the active anodic dissolution of Ti in both reducing and oxidizing acid solutions (16). However, the mechanisms by which the alloying additions of Nb and Zr to Ti resulted in reduced active dissolution and improved passivity have not been clarified (15,16). In this investigation, the mechanisms by which Nb and Zr improve the corrosion resistance and passivity of Ti were studied in 5 M hydrochloric acid (HCl). In addition, the mechanisms by which moderate (10 to 15 wt. %) bulk alloying concentrations of Nb and/or Zr provide sufficient surface coverage to alter active dissolution rates and improve the passivation of Ti were investigated.

EXPERIMENTAL PROCEDURE

Materials

The effects of Nb and Zr alloying additions on the electrochemical characteristics of Ti-13% Nb-13% Zr (wt. pct.) (Table I), were investigated. A second Ti-Zr-Nb based alloy, Ti-35% Zr-10% Nb (wt. pct.), was also examined. In addition, commercially pure Ti, Nb, Zr, as well as Ti-Zr and Ti-Nb binary alloys (Table II) were tested.

Two thermo-mechanical variants of Ti-13% Nb-13% Zr were tested: solution treated (ST), and solution treated and aged (STA). The ST Ti-13% Nb-13% Zr was hot rolled above the beta transus ($> 735^\circ C$), in vacuum and water quenched to room temperature. The STA Ti-13% Nb-13% Zr was hot rolled above the beta transus, water quenched to room temperature, and then aged for six hours at $500^\circ C$ in vacuum.

The microstructural phases present in ST and STA Ti-13% Nb-13% Zr were determined by X-ray diffraction (XRD) and transmission electron microscopy (TEM). α' (martensitic h.c.p) and β (b.c.c.) phases were present in ST Ti-13% Nb-13% Zr. The

STA heat treatment resulted in the partial phase transformation of the $\alpha' + \beta \rightarrow \alpha' + \alpha$ (diffusional h.c.p.) + β .

Nb functions as a beta phase stabilizer, and Zr is a neutral or mild beta stabilizer, in titanium (17). Therefore, Nb should partition to the β phase resulting in a Nb-rich β phase and a Nb-poor diffusional α phase in STA Ti-13% Nb-13% Zr. In contrast, Gegel showed that there was no partitioning of Zr between the β and α phases in Ti-6% Al-2% Sn-4% Zr-2% Mo (18). Therefore, partitioning of Zr between the α and the β phases was not expected in the STA Ti-13% Nb-13% Zr. Moreover, there should be no diffusional partitioning of Zr and Nb between martensitic α' and β in ST Ti-13% Nb-13% Zr due to the diffusionless nature of the martensitic transformation. The compositions of the α , and β phases in the STA Ti-13% Nb-13% Zr were determined by TEM/EDS.

Experimental Techniques

The electrochemical samples were mechanically polished with abrasive paper, polished with 0.05 μm SiC to a mirror finish, and ultrasonically cleaned with 18 M Ω -cm ultrapure water prior to electrochemical tests. The electrochemical tests were conducted in lactated Ringer's, and 5 M HCl solution. Lactated Ringer's solution was selected to simulate physiological fluid, and the 5 M HCl solution was selected to provide a bulk analog which simulates an aggressive crevice type environment. The solutions were deaerated with nitrogen for 12 hours prior to the experiments and were maintained at 37°C during the experiments. In addition, all the potentials were recorded with respect to saturated calomel reference electrodes (SCE).

The OCP's in 5 M HCl were recorded as a function of time for Ti, Nb and Zr, as well as Ti-Nb and Ti-Zr binary alloys with native air formed oxides. In addition, the OCP's of samples with anodically grown oxides, formed in a borate buffer solution at +3.33 V_{OCP} were recorded. [The polarization of the Ti-Nb and Ti-Zr alloys to +3.33 V_{OCP} produced approximately 10 nm thick oxides given that Ti, Nb, and Zr each exhibited anodization ratios of 2.5 to 3 nm/V (19,20,21).] Electrochemical impedance spectroscopy (EIS) was conducted at OCP and at various potentials in the active region. A 10 mV AC signal was applied with a frequency range from 50 kHz to 1 mHz. Anodic potentiodynamic polarization scans were conducted on the alloys and pure metals at a scan rate of 0.1 mV/sec, after depassivation and surface activation was observed.

X-ray photoelectron spectroscopy (XPS) was utilized for *ex-situ* surface analysis of the native and anodically formed oxides. XPS tests were conducted on Ti-45% Nb, Ti-50% Zr, and Ti-13% Nb-13% Zr (ST) which were: *i*) held at OCP for 12 hours in 5 M HCl, *ii*) held at OCP for 12 hours and then anodically polarized to -0.1 V_{SCE} for 3 hours in 5M HCl, *iii*) instantaneously polarized to -0.1 V_{SCE} without a hold at OCP in 5 M HCl, and *iv*) polished and held in air to create an air formed oxide. The samples were then placed in a Perkin-Elmer 560 ESCA/SAM system for XPS analysis. High resolution

scans of 0.1 eV/step were conducted near localized electron binding energies: i) 470 to 450 eV for the $2p_{3/2}$ electron shell of Ti at 458.8 eV, ii) 220 to 190 eV for the $3d_{5/2}$ of Nb at 202.4 eV, iii) 190 to 170 eV for the $3d_{5/2}$ of Zr at 178.9 eV, iv) 300 to 270 eV for the 1s of C at 284.8 eV and, v) 540 to 520 eV for the 1s of O at 531 eV. A Shirley-type background correction was conducted on the resulting XPS spectra to remove the background contributions from inelastically scattered electrons (22). Surface charging was accounted for by using the adventitious carbon 1s peak at 284.8 eV as a reference. Analysis of XPS spectra was conducted by fitting Gaussian type peaks to the XPS data to determine the areas under the XPS peaks. The atomic ratio of oxidized Ti:Nb or Ti:Zr was determined by the following:

$$Ti:X = \frac{\Sigma \left(I_{Ti-oxidized} / \phi_{Ti} \right)}{\Sigma \left(I_{X-oxidized} / \phi_X \right)} \quad [1]$$

where Ti:X = the atomic ratios of oxidized Ti:Nb, or Ti:Zr, $I_{X-oxidized}$ = the XPS intensity of oxidized species x, and ϕ_x = the specific sensitivity factor of species X, which is a function of the element and electron shell, the specific XPS system, and spatial relationship between the X-ray source and photoelectron detector (23). Mg K_{α} X-rays with an energy of 1253.64 eV were utilized.

RESULTS

Depassivation and activation of Ti in comparison to Ti-Nb and Ti-Zr

Oxide film dissolution and the subsequent surface activation of C.P. Ti, Nb, Zr, as well as Ti-45% Nb, and Ti-50% Zr with native air-formed oxides (approximately 0.2 to 0.3 nm in thickness) in 5 M HCl were indicated by decreasing OCP's, as shown in Figures 1 and 2. The OCP's of Ti-45% Nb and Ti-50% Zr in 5 M HCl with 10 nm anodic oxides are shown in Figure 3. C.P. Ti, Ti-45% Nb and Ti-50% Zr exhibited surface activation after chemical dissolution of the oxides while Nb and Zr resisted oxide dissolution.

Several potential regions were observed in the OCP vs. time behaviors of Ti-45% Nb and Ti-50% Zr (Figures 1, 2, and 3). Prior to surface activation, both Ti-45% Nb and Ti-50% Zr exhibited gradually decreasing OCP's which was attributed to chemical dissolution and thinning of the anodically formed oxides (24). The dissolution and subsequent thinning of the anodically formed oxides on Ti-45% Nb and Ti-50% Zr was confirmed by EIS data which revealed decreases in both the impedance parameters,

$1/C_{\text{oxide/interface}}$ and $R_{\text{oxide/interface}}$ prior to surface activation (Figure 4).ⁱ There was good correlation between the decreases in $1/C_{\text{oxide/interface}}$ and $R_{\text{oxide/interface}}$ and the active shift in the OCPs. This was followed by rapidly changing potentials which were attributed to a transition from a limiting thin oxide to an adsorbed monolayer species (24). The open circuit potentials of the samples reached minimas of $-0.5 V_{\text{SCE}}$ and $-0.7 V_{\text{SCE}}$ for Ti-45% Nb and Ti-50% Zr, respectively. The minimas were followed by gradual increases in the open circuit potentials of both the alloys. The gradual increases in the OCPs of Ti-45% Nb and Ti-50% Zr correlate with gradual increases in $R_{\text{oxide/interface}}$ (Figure 4). The increases in $R_{\text{oxide/interface}}$ and the rises in the OCP's of Ti-45% Nb and Ti-50% Zr suggest the presence of an active Ti alloy surface which enriches in Nb and Zr and thereby *i*) exhibits lower dissolution rates with respect to Ti, or *ii*) undergoes passivation by Nb or Zr compact oxides. The Ti-50% Zr samples required longer times for complete oxide dissolution and to surface activation in comparison to Ti-45% Nb samples. (Figures 2, and 3) The slow decreases in OCP, $1/C_{\text{oxide/interface}}$ and $R_{\text{oxide/interface}}$ as a function of time suggests that ZrO_2 has a slower oxide dissolution rate than TiO_2 or Nb_2O_5 .

Effects of Nb and Zr alloying on the active corrosion and passivation of Ti

The effects of Nb and Zr on the corrosion and passivity characteristics of Ti were investigated using anodic potentiodynamic polarization scans after a 12 hour period at OCP which allowed for surface enrichment by Nb or Zr. Emphasis was placed on the 5 M HCl solution since all the Ti-based alloys were spontaneously passive and exhibited similar passive $E\text{-log}(i)$ behaviors in the lactated Ringer's solution ($\text{pH} \approx 6.8$) but became activated in 5 M HCl. In 5 M HCl, Ti exhibited an active/passive regime with a critical current density (i_{crit}) of approximately $3.3 \times 10^{-4} \text{ A/cm}^2$ at $-0.4 V_{\text{SCE}}$, while Nb was spontaneously passive (*ii*). All alloys with the exception of Zr were passive within the potential range from $0.0 V_{\text{SCE}}$ to $+2.5 V_{\text{SCE}}$, as shown in Figures 5 and 6. Zr experienced crevice corrosion at $E > +0.1 V_{\text{SCE}}$. However, Zr was also spontaneously passive and exhibited lower anodic dissolution rates than Ti and Nb at $E < +0.1 V_{\text{SCE}}$ (Figure 6). The alloying of Nb and Zr with Ti, as in Ti-15% Nb and Ti-15% Zr, resulted in the reduction of i_{crit} from $3.3 \times 10^{-4} \text{ A/cm}^2$ to approximately $1 \times 10^{-4} \text{ A/cm}^2$ and reduced active dissolution rates compared to Ti (Figures 5 and 6). The alloying of Ti with 45% Nb (wt. pct.) and 50% Zr (wt. pct.) resulted in reduced active anodic dissolution rates or spontaneous passivation in comparison to Ti, Ti-15% Nb, or Ti-15% Zr (Figures 5 and 6). Therefore, Zr may act cooperatively with Ti where Zr

ⁱ Prior to surface activation, C_{oxide} and R_{oxide} were determined by fitting EIS data to a two time constant model of the solution/oxide/metal interface, as shown by Kolman and Scully (19). The $C_{\text{interface}}$ and $R_{\text{interface}}$ were measured after oxide dissolution and surface activation.

ⁱⁱ The anodic current density, i_{anodic} , including i_{crit} , was corrected for the cathodic current density, i_{cathodic} , associated with the measured current density: $i_{\text{measured}} = i_{\text{anodic}} - |i_{\text{cathodic}}|$.

improves the passivity at potentials where Ti is active, and TiO_2 minimizes the breakdown of passivity at higher potentials.

Active anodic dissolution and passivation characteristics of Ti-Nb-Zr ternary alloys

The corrosion and passivity characteristics of the Ti-Nb and Ti-Zr alloys in 5 M HCl indicated that alloying of Ti with both Nb and Zr should yield a Ti-Nb-Zr alloy with improved corrosion resistance and passivity compared to C.P. Ti. ST and STA Ti-13% Nb-13% Zr exhibited lower active dissolution rates compared to C.P. Ti in 5 M HCl, as shown in Figure 7.

ST and STA Ti-13% Nb-13% Zr exhibited similar anodic polarization behaviors in 5 M HCl. The good corrosion resistance of STA Ti-13% Nb-13% Zr in a reducing acid in comparison to other STA β -Ti alloys was attributed to the lack of partitioning of the Zr and Nb between the α and β phases, as shown in Table 3 (25). There was only a slight enrichment of Nb in the β phase present in STA Ti-13% Nb-13% Zr and no partitioning of Zr between the α and β phases, as expected from Giegel's work (17). The presence of Zr and Nb, in both phases at greater than 11 % (wt. pct.) or approximately 6 % (atomic percent), results in improved corrosion resistance relative to C.P. Ti.

Ex-Situ investigation of oxide compositions on Ti-Nb and Ti-Zr

Electrochemical data indirectly suggested that the improved resistance to active dissolution and improved passivity of Ti-Nb and Ti-Zr alloys were the result of surface enrichment by Nb and Zr. Therefore, XPS studies were conducted on the Ti-45% Nb and Ti-50% Zr samples which were prepared, as indicated in Table IV, to determine if enrichment could be detected.

The atomic ratio of elemental Ti:Nb in the Ti-45% Nb bulk alloy was 2.3. In comparison, the atomic ratio of all oxidized Ti:Nb species in the native air formed oxide was 2.4 (Table IV). Therefore, there was no tendency to preferentially form oxides of Ti compared to Nb oxides. However, the ratio of oxidized Ti:Nb on the instantaneously polarized Ti-45% Nb sample was approximately 1.9, while the ratio of oxidized Ti:Nb on Ti-45% Nb which was held at OCP to activate Ti and enrich Nb, and then polarized to $-0.1 \text{ V}_{\text{SCE}}$ was approximately 1.2. Moreover, the ratio of oxidized Ti:Nb on the sample which was held at OCP in 5M HCl for 12 hours prior to air oxidation was approximately 1.2. These atomic ratios suggest that enrichment of the Ti alloy by Nb occurs primarily near the OCP. The change in the oxidized Ti:Nb atomic ratio may indicate the preferential dissolution of Ti to limit its availability for oxidation during $-0.1 \text{ V}_{\text{SCE}}$ anodization.

The elemental Ti:Zr atomic ratio of the Ti-50% Zr bulk alloy was 1.9. In contrast, the oxidized Ti:Zr atomic ratio of the air formed oxide was 2.63, which indicates

preferential air oxidation of Ti. The oxidized Ti:Zr atomic ratio of Ti-50% Zr which was held at OCP and then anodically polarized to $-0.1 V_{SCE}$ was 1.96, while the atomic ratio of oxidized Ti:Zr of the instantaneously anodically polarized Ti-50% Zr sample was 2.1. Furthermore, a Ti-50% Zr sample which was held at OCP for 12 hours to enrich Zr prior to air oxidation exhibited at Ti:Zr ratio of 1.8. Therefore, the tendency to preferentially form TiO_2 was offset by both the enrichment of Zr at the surface and preferential dissolution of TiO_2 compared to ZrO_2 during potential hold at $-0.1 V_{SCE}$.

XPS was conducted on Ti-13% Nb-13% Zr (ST), which was held at OCP for 12 hours and then polarized to $-0.1 V_{SCE}$ in 5 M HCl. The atomic ratio of elemental Ti:Nb atomic ratio in the bulk alloy was 11, while the ratio of oxidized Ti:Nb was 7.5. In contrast, the elemental Ti:Zr atomic ratio in the bulk alloy was 10.9 while the oxidized Ti:Zr atomic ratio was 14.5. This also indicates increased Nb_2O_5 formation due to Nb enrichment during active dissolution. Less ZrO_2 formation is observed either due to less Zr enrichment than Nb or due to the preferential formation of TiO_2 compared to ZrO_2 .

DISCUSSION

The alloying of Ti with Nb resulted in improved passivity of Ti-45% Nb compared to Ti (Figure 6). Ti-50% Zr exhibited improved passivity compared to C.P. Ti at potentials above $+2.0 V_{SCE}$, and below $0.0 V_{SCE}$ (Figure 6).

It is clear that the corrosion resistance and passivity of Ti are improved by either *i*) the presence of elemental Nb and Zr on the surface of active Ti, or *ii*) the formation of a sufficient surface coverage by Nb-containing oxides and/or ZrO_2 . It is interesting to note that the improvements in active dissolution rate and i_{crit} are brought about by only ~ 11 % Nb to 15 % Nb (wt. pct.), as shown in Figure 5, and Table III (iii). Therefore, at issue regarding the corrosion and passivity characteristics of Ti-Nb-Zr ternary alloys are the mechanisms by which sufficient enrichment occur on the alloy surface with elemental Nb and/or Zr, and in the oxide film by Nb-containing oxides and ZrO_2 to impact the corrosion resistance and passivity for alloys of modest Nb and Zr alloying.

Three scenarios can be listed to describe the mechanisms by which Nb and Zr enrich the surface of Ti: *i*) oxides of Nb and Zr, or elemental Nb and Zr preferentially enrich the activated surface of Ti due to the preferential dissolution of Ti, *ii*) Nb, Zr, and Ti maintain stoichiometric balance during active dissolution, and oxidize at similar rates at $E > E_{pp}$, but at $E > E_{pp}$, TiO_2 undergoes more rapid chemical dissolution than oxides of Nb and Zr, and/or *iii*) Nb and Zr have higher oxidation rates than Ti at $E > E_{pp}$, resulting in the preferential formation of Nb and Zr oxides. Ti:Nb and Ti:Zr atomic ratios

iii. It is also interesting to note that significant changes in Fe passivity occur at 12 % (wt. pct.) Cr.

determined from the series of XPS experiments strongly suggest that the primary mechanism by which Nb and Zr enrich the surface film is by the preferential dissolution of Ti at $E < E_{pp}$. The evidence for this is that the instantaneous anodic polarization of Ti-45% Nb to $-0.1 V_{SCE}$, which minimized the active dissolution of Ti, did not yield decreased Ti:Nb ratios. Ti is apparently preferentially dissolved in Ti-Nb alloys during active anodic dissolution. This results in the enrichment of the surface with Nb, the formation of a thin protective Nb film during active dissolution of Ti, and subsequently, enhanced formation of Nb-containing oxides during anodic polarization due to the higher availability of elemental Nb. The oxidized Ti:Zr atomic ratio of the instantaneously polarized Ti-50% Zr showed a slight increase of the surface oxide by ZrO_2 relative to TiO_2 , in comparison to the air formed oxide (from 2.6 vs. 2.1). This is attributed primarily to the dissolution rate of TiO_2 being higher than ZrO_2 . Therefore, two mechanisms account for the enhanced corrosion resistance and passivity of Ti-13% Nb-13% Zr: i) significant Nb surface enrichment and Nb-containing oxide formation, and ii) a slight increase in the presence of Zr on the surface and the resistance of ZrO_2 to chemical dissolution.

CONCLUSIONS

Anodic polarization behavior of Ti-13% Nb-13% Zr (ST and STA) in 5 M HCl revealed that the alloying additions of Nb and Zr to Ti resulted in improved resistance to active dissolution and enhanced passivation relative to C.P. Ti. The enhanced resistance to active dissolution and improved passivity was attributed to the presence of sufficient elemental Nb and Zr, and sufficient oxidized Nb_2O_5 and ZrO_2 , respectively. EIS tests on Ti-45% Nb and Ti-50% Zr alloys held at OCP in 5 M HCl revealed gradual increases in the $R_{surface}$, $1/C_{surface}$, and OCPs after oxide dissolution and surface activation. This suggests enrichment of the surface by Nb and Zr, which was confirmed by XPS. In summary, beneficial Nb-containing oxides formation was promoted by sufficient alloying with Nb and/or surface enrichment of Nb during preferential Ti dissolution in its active state. Beneficial ZrO_2 formation was promoted by sufficient alloying with isomorphous Zr. Preferential dissolution of Ti to enrich Zr was only observed after long times in the active state. Instead, enrichment of ZrO_2 relative to TiO_2 occurred more readily due to the slow chemical dissolution rate of ZrO_2 . A combination of these mechanisms is theorized to protect Ti-Zr-Nb ternary alloys.

ACKNOWLEDGMENTS

The authors would like to acknowledge the sponsorship of Smith & Nephew, Inc., in particular, Dr. Paul Kovacs. The authors would like thank Teledyne Wah Chang, Inc.,

for their generous donation of alloys and Princeton Applied Research for their on-going support of the electrochemical instrumentation in the CESE.

REFERENCES

1. T.R. Beck, *Electrochim. Acta*, **18**, 807, (1973).
2. C. Baes, and R. Mesmer, *The Hydrolysis of Cations*, p. 47, New York, John Wiley & Sons, (1975).
3. D.G. Kolman, and J.R. Scully, *J. Electrochem. Soc.*, **143**, 1847, (1996).
4. T.R. Beck, *Localized Corrosion*, B.F. Brown, Editor, p. 644, Houston, NACE, (1974).
5. T. Hurlen, H. Bentzen, and S. Hornkjol, *Electrochim Acta.*, **32**, 1613, (1987).
6. S. Hornkjol, *Electrochim. Acta*, **36**, 1443, (1991).
7. M.S. El-Basiouny, and A.M. Bekheet, *Brit. Corr. J.*, **15**, 89, (1980).
8. C.V. D'Alkaine, L.M.M. DeSouza, and F.C. Nart, *Corr. Sci.*, **34**, 109, (1993).
9. B. Cox, *J. Electrochem. Soc.*, **117**, 654, (1970).
10. V.G. Jangg, R.T. Webster, and M. Simon, *Werkstoffe und Korrosion*, **29**, 16, (1978).
11. D.R. Knittel, and A. Bronson, *Corr.*, **40**, 9, (1984).
12. T. Hurlen, and S. Hornkjol, *Electrochim. Acta*, **32**, 811, (1987).
13. G.C. Palit, and H.S. Gadiyar, *Corr.*, **43**, 140, (1987).
14. S. Hornkjol, *Electrochim. Acta*, **33**, 289, (1988).
15. Y. Okazaki, A. Ito, T. Tateishi, and Y. Ito, *Mat. Trans.*, **35**, 58, (1994).
16. V.V. Andreeva, et. al., *Corrosion of Metals and Alloys*, N.D. Tomashov and E.N. Mirollybev, p. 43, Israel Program for Scientific Programs, Jerusalem, (1966).
17. E.W. Collings, *The Physical Metallurgy of Titanium Alloys*, pp. 42, Metals Park, Ohio, ASM, (1984).
18. H. Gegel, S. Nativ, and R. Raj, *Scripta. Met.*, **14**, 241, (1980).
19. D.G. Kolman, and J.R. Scully, *J. Electrochem Soc.*, **140**, 2773, 1993.
20. T. Hurlen, H. Bentzen, and S. Hornkjol, *Electrochim Acta*, **32**, 1613, (1987).
21. A. Goosen, M. Vazquez., and D. MacDonald, *Electrochim Acta*, **41**, 35, (1996).
22. J. Vegh, *Journal of Electron Spectroscopy and Related Phenomena*, **46**, 411, (1988)
23. J. F. Moulder, W. F. Stickle, P.E. Sobol, and K.D. Bomben, *Handbook of X-ray Photoelectron Spectroscopy*, J. Chastain, editor, p. 25, Eden Prairie, Minnesota, Perkin-Elmer Corporation, 1992.
24. E. Kelly, *J. Electrochem. Soc.*, **126**, 2067, 1979.
25. S. Yu and J. R. Scully, *Corr. J.*, submitted for publication, March 1996.

TABLES

Table I: The composition of Ti-13% Nb-13% Zr alloy in weight percent--based on vendor's information.

Ti	Nb	Zr	Ta	Fe	Al	O	N
balance	13-14	13-14	0.1	0.1	0.02	0.15	0.02

Table II: Composition and the phases present in the binary alloys of Ti-Nb and Ti-Zr which were selected for electrochemical testing.

Binary alloys tested (wt. pct.)	Phases present
Ti-15% Nb	$\alpha' + \beta$
Ti-45% Nb	β
Ti-15% Zr	$\alpha' + \beta$
Ti-50% Zr	$\alpha' + \beta$

Table III: Weight percentages of alloying elements present in the α and β phases due to partitioning in the STA Ti-13% Nb-13% Zr (wt. pct.) calculated from energy dispersive spectroscopy analysis (EDS) and transmission electron microscopy (TEM).

Phase	Ti (wt. pct.)	Nb (wt. pct.)	Zr (wt. pct.)
α	74.2 ± 1.6	11.8 ± 0.6	13.2 ± 0.2
β	71.1 ± 0.3	15.6 ± 0.5	13.3 ± 0.3

Table IV: The ratios of all forms of oxidized Ti to oxidized Nb or Zr in the near surface region of the respective binary alloys after various sample preparation methods conducted on Ti-45% Nb and Ti-50% Zr prior to XPS surface analysis.

Alloy	Pre-treatment	Final Experiment	$\frac{\Sigma \text{ oxidized Ti}}{\Sigma \text{ oxidized Nb or Zr}}$
Ti-45% Nb	exposure to lab air	exposure to lab air	2.4
Ti-45% Nb	none	$-0.1 V_{SCE}$ for 3 hours	1.9
Ti-45% Nb	12 hours at OCP	$-0.1 V_{SCE}$ for 3 hours	1.2
Ti-45% Nb	12 hours at OCP	exposure to lab air	1.2
Ti-50% Zr	exposure to lab air	exposure to lab air	2.6
Ti-50% Zr	none	$-0.1 V_{SCE}$ for 3 hours	2.1
Ti-50% Zr	12 hours at OCP	$-0.1 V_{SCE}$ for 3 hours	1.9
Ti-50% Zr	12 hours at OCP	exposure to lab air	1.8

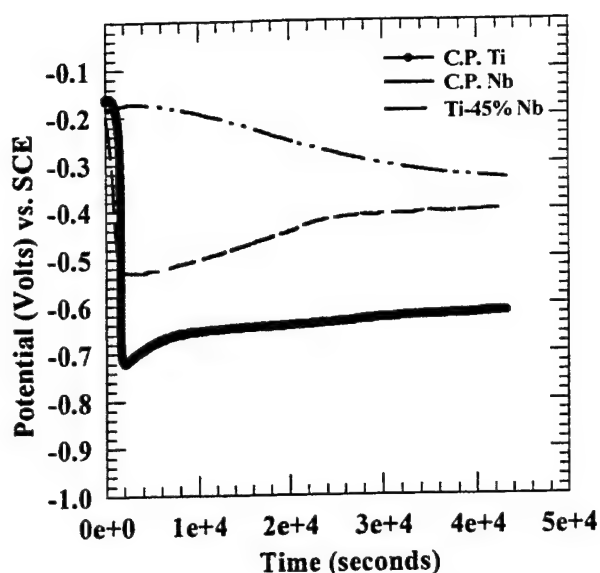


Figure 1: Open circuit potentials of C.P. Ti, C.P. Nb, and Ti-45% Nb, initially with air-formed oxides, in deaerated 5 M HCl solution at 37°C for 12 hours

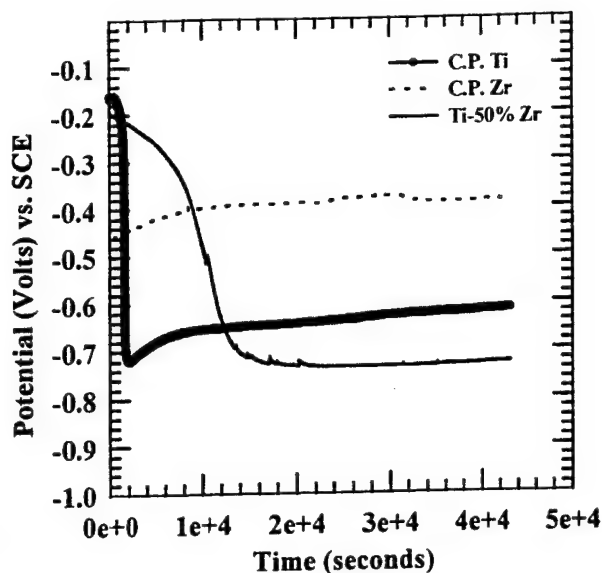


Figure 2: Open circuit potentials of C.P. Ti, C.P. Zr, and Ti-50% Zr, initially with air-formed oxides in, deaerated 5 M HCl solution at 37°C for 12 hours.

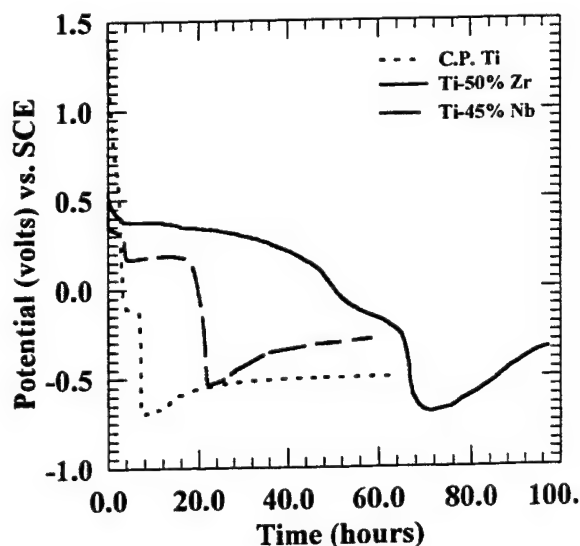


Figure 3: Open circuit potentials of C.P. Ti, Ti-45% Nb, and Ti-50% Zr with an anodic oxide film (anodically polarized in deaerated borate buffer at 37°C at +3.33 V_{OCP}) held at open circuit in 5M HCl solution at 37°C.

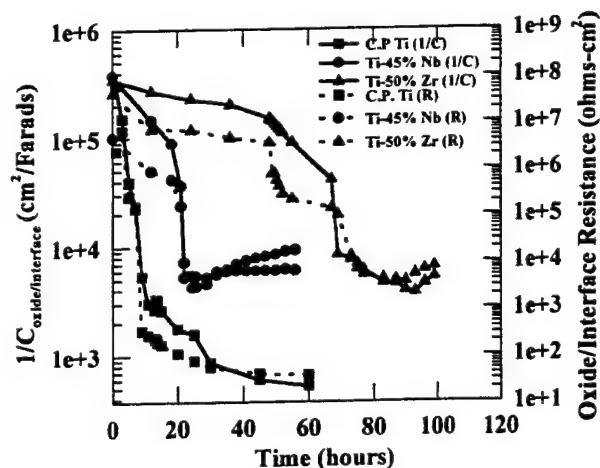


Figure 4: Plots of $1/C_{\text{oxide/interface}}$ and $R_{\text{oxide/interface}}$ with time for C.P. Ti, Ti-45% Nb and Ti-50% Zr with anodic oxides (~ 10 nm) formed by anodic polarization to +3.33 V_{OCP} in borate buffer) held at OCP in deaerated 5 M HCl solution at 37°C.

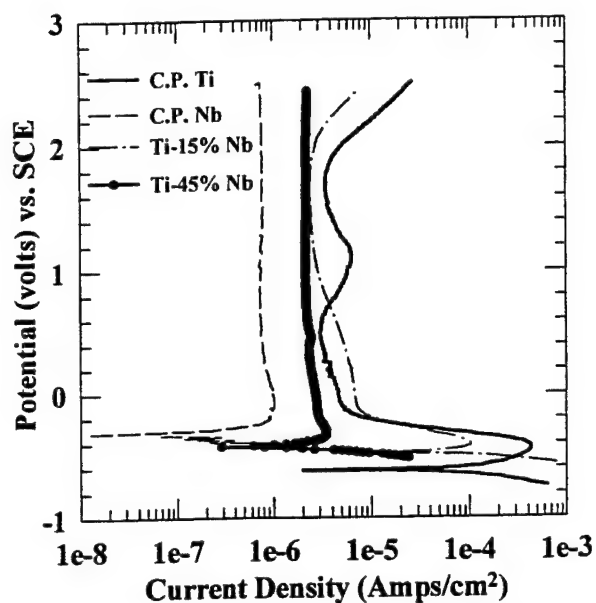


Figure 5: Anodic polarization behaviors of C.P. Ti, C.P. Nb, Ti-15% Nb, and Ti-45% Nb in deaerated 5 M HCl solution at 37°C. (scan rate = 0.1 mV/sec)

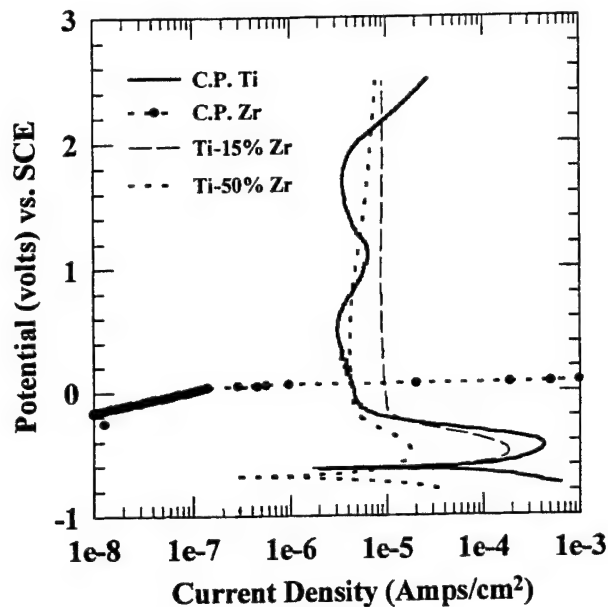


Figure 6: Anodic polarization behaviors of C.P. Ti, C.P. Zr, Ti-15% Zr, and Ti-50% Zr in deaerated 5 M HCl solution at 37°C. (scan rate = 0.1 mV/sec)

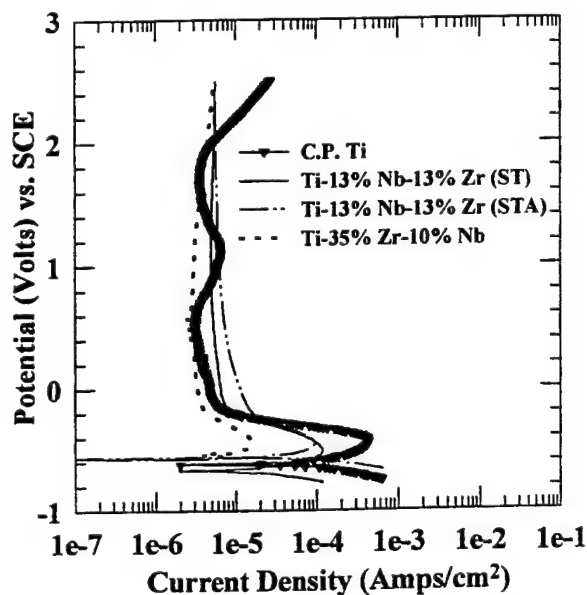


Figure 7: Anodic polarization behaviors of C.P. Ti, Ti-13% Nb-13% Zr (ST, and STA), and Ti-35% Zr-10% Nb in deaerated 5 M HCl solution at 37°C. (scan rate = 0.1 mV/sec)

**Understanding the pH and Potential Dependency of β -Titanium Alloy
Environmental Crack Initiation in 0.6 M NaCl through Investigation
of Crack Tip Electrode Kinetics**

D. G. Kolman and J. R. Scully

Submitted to Metallurgical and Materials Transactions A

Understanding the Potential and pH Dependency of High Strength β -Titanium Alloy Environmental Crack Initiation

D.G. Kolman* and J.R. Scully

Center for Electrochemical Science and Engineering

Department of Materials Science

University of Virginia

Charlottesville, VA 22903-2442

An explanation for the strong dependency of crack initiation of pre-cracked high strength β -titanium alloys in room temperature 0.6 M NaCl on applied potential and bulk solution pH is presented. It is proposed that environment assisted cracking (EAC) susceptibility in neutral environments results from the following series of events: 1) film rupture due to plastic deformation at actively deformed crack tips, 2) accelerated dissolution of titanium, 3) crack tip acidification by hydrolysis of titanium ions, 4) crack tip potential excursions towards bare metal open circuit potentials during film rupture due to large ohmic voltages in the crack solution, 5) accelerated crack tip proton or water reduction concurrent with titanium dissolution, 6) bare surface-dominated hydrogen ingress into a fracture process zone, and 7) crack initiation by hydrogen embrittlement. Evidence for each of the above elements of the crack initiation scenario is presented, with special emphasis on crack tip electrode kinetics and ohmic voltage calculations which govern process zone-controlled hydrogen uptake. The proposed EAC scenario is consistent with the strong dependencies of crack initiation and growth in pre-cracked high strength β -titanium alloys on (i) solution pH, (ii) applied potential and (iii) strain rate. This scenario also explains the observed propensity for EAC in fatigue-precracked, modern β -titanium alloys as compared to the "apparent" EAC-resistance of smooth and blunt notch counterparts. The latter lack both occluded crack tip geometries to promote acidification and ohmic voltage drops below reversible hydrogen, as well as localization of dynamic plastic strain. Hydrogen uptake is, subsequently, limited.

*Current address: Materials Corrosion and Environmental Effects Laboratory Los Alamos National Laboratories, MS G755, Los Alamos, NM 87544

I. INTRODUCTION

The susceptibility of precracked metastable β and $\beta + \alpha$ titanium ⁽¹⁾ alloys to intergranular, transgranular cleavage, or quasi-cleavage environment assisted cracking (EAC) in room temperature aqueous halide solutions has been reported¹⁻⁸. Susceptibility and crack path depend on alloy composition and microstructure¹⁻⁸. It is widely accepted that EAC of α -titanium alloys is controlled by hydrogen effects and/or the well-known tendency of the α phase to hydride⁹⁻¹⁴. In contrast to α -titanium, a large hydrogen concentration (> 40 at. pct.) is required to induce hydride formation in the bcc titanium phase according to the Ti-H binary phase diagram¹⁵. Much lower total hydrogen concentrations (e.g. > 1000 wt. ppm., > 4.8 at. pct.) have been found to promote intergranular cracking¹⁶⁻¹⁸ after electrochemical precharging of STA β -titanium alloys. These tests were completely decoupled from aqueous dissolution since pre-dissolved hydrogen was retained by the oxide hydrogen permeation barrier and testing was in lab air. For susceptible microstructures in NaCl (i.e., STA $\beta + \alpha$ Ti-15Mo-3Nb-3Al and Beta-C), increasing the hydrogen content of the material severely lowered the maximum longitudinal stress and effective plastic strain in pre-charged notched specimens and resulted in a change of fracture mode from transgranular to intergranular¹⁶. However, solution treated (ST) β -titanium resists intergranular cracking after hydrogen precharging¹⁶⁻¹⁸. Therefore, the alloy and heat treatment specificity of hydrogen embrittlement exactly mirrors that observed during EAC in 0.6 M NaCl. Thus, experimental evidence clearly indicates that pre-dissolved hydrogen embrittles β -titanium alloys in the same conditions which render them susceptible to aqueous EAC and both can result in an intergranular fracture path. Hydriding of volume fractions of the β or α phases detectable by x-ray diffraction was not observed after intergranular cracking¹⁶⁻¹⁸. Consequently, EAC by hydriding of substantial volumes of the bcc phase can be discounted. Local hydriding of grain boundary α films remains possible, but a proposed fracture path along hydrided α/β interfaces at α -titanium precipitates grown heterogeneously from β grain boundaries^{19,20} is not well supported by fractographic evidence^{1,18}. The established effect of hydrogen on the ductile-to-brittle transition in bcc titanium controls observed cleavage cracking at higher hydrogen concentrations but does not explain intergranular cracking.¹⁴ Beck proposed an alternative theory for EAC of α -titanium involving a salt film-based mass transport mechanism where cracking occurred due to the rapid dissolution rate of Ti following film rupture accompanied by salt film formation^{7,21}. No path-

(1) β -titanium matrix (bcc) for β solution heat treated (ST) condition with α -titanium precipitates (hcp) for the solution treated and aged condition (STA).

specific mechanism for intergranular cracking of β -Ti was proposed. Moreover, Beck²² and others², subsequently, argued against this theory. Green and Sedriks identified the critical species in the EAC of $\alpha+\beta$ Ti-8Al-1Mo-1V as hydrogen not chloride ions¹¹. It was argued that a hydrogen embrittlement mechanism controlled intergranular EAC of STA β -titanium alloys in neutral NaCl solution¹, in light of work¹⁶⁻¹⁸ which showed that hydrogen precharged specimens were intergranularly cracked with total hydrogen concentrations greater than 1000 wt. ppm. Intergranular fractography was similar¹⁶⁻¹⁸ to that observed for EAC in 0.6 M NaCl^{1,3}. Intergranular hydrogen embrittlement of β -titanium alloys might also be linked with observed coplanar slip and dislocation pile-ups at grain boundaries, undetected but possible local hydriding of thin grain boundary α films, or an as-yet unidentified grain boundary segregation phenomenon upon α precipitation¹⁸.

A variety of pre-cracked $\beta+\alpha$ alloys and $\alpha+\beta$ alloys have been observed to be susceptible to EAC with intergranular or transgranular cleavage cracking paths when held between $-0.8 V_{SCE}$ and $+0.5 V_{SCE}$ in neutral pH aqueous environments. A susceptibility maximum is observed at $-0.6V_{SCE}$ ¹⁻⁸ (see Figure 1). It has also been shown that: 1) precracked $\alpha+\beta$ titanium alloys are immune to cracking at $-1V_{SCE}$ in neutral solution but susceptible to cracking at $-1V_{SCE}$ when exposed to strongly acidic bulk environments^{2, 23, 25}; 2) at potentials where cracking is observed, cracking can be slowed or eliminated in strongly alkaline bulk environments²³; and 3) an acidic crack tip chemistry forms in a neutral bulk environment without cathodic polarization²⁶. The EAC dependence on potential and pH are likely linked because conditions favoring acidic crack tips conditions generally promote EAC while those that promote alkaline crack tip chemistries promote EAC inhibition¹⁻³. In contrast to the case of cathodically polarized steels, bulk hydrogen charging through TiO_2 passivated Ti surfaces exposed to neutral NaCl solution is unlikely at room temperature over the range of potentials shown in Figure 1 because the stable oxide is a strong barrier to hydrogen uptake^{23,24,27}. Therefore, the very slow transport of hydrogen through the oxide on β -titanium^{23,27} and through the β -titanium matrix itself¹⁶⁻¹⁹ make uniform bulk charging by cathodic polarization of an entire precracked specimen or the large fracture process zone ahead of a blunt notch by volume diffusional processes difficult. This, partially, explains the observed immunity to EAC at cathodic potentials. Passive films are not chemically destabilized or readily cathodically reduced at room temperature to enable bulk hydrogen uptake at cathodic potentials except under strongly acidic conditions (e.g. 5 M HCl). Such an acid concentration is not observed in crack tip solutions²⁶. Therefore, it is reasonable to expect that H uptake in near-neutral solutions must occur at the bare crack tip surface following mechanically-induced depassivation

in order to support hydrogen-controlled EAC. The strong strain rate dependency of EAC susceptibility for β -Ti alloys in NaCl supports this notion^{1,3}.

The mechanism of intergranular cracking in precracked high strength STA β -Ti remains unclear as does the origins of the observed applied potential dependency on crack initiation in neutral NaCl. Interestingly, EAC is observed in both $\alpha + \beta$ and $\beta + \alpha$ alloys during potentiostatic tests in neutral NaCl at intermediate potentials where the applied potential is more positive than the reversible hydrogen potential^{1-3,5,11}. An explanation for the potential dependency of crack initiation in neutral NaCl that explains both cathodic and anodic inhibition² of EAC initiation is required especially in light of the established link between lattice and trapped hydrogen and intergranular cracking¹⁶⁻¹⁸. This paper seeks to present evidence for anodic and cathodic inhibition of EAC in neutral NaCl based on factors controlling crack tip hydrogen uptake. We examine both the passive and bare surface dissolution and hydrogen production kinetics on selected β -titanium alloys in solutions of acidic, neutral and alkaline pH. The effect of pre-cracked compact tension sample geometry on ohmic solution resistance has also been explored to estimate transiently bare crack-tip potentials as a function of external applied potentials. The results support the notion of local crack tip hydrogen controlled EAC and are consistent with all experimental observations. Slip - film rupture - dissolution is shown to be inconsistent with these observations.

II. EXPERIMENTAL PROCEDURE

A. Materials

The metallurgical conditions for the metastable β -titanium alloys studied, Ti-15Mo-3Nb-3Al (Ti-14.9Mo-2.64Nb-3.15Al, wt%), and Ti-15V-3Cr-3Al-3Sn (Ti-15.0V-2.99Cr-3.14Al-2.81Sn, wt%), have been discussed elsewhere^{16-18,28,29}. Ti-15Mo-3Nb-3Al was solution heat treated (ST) for 8 hours at 871°C (1600 F) followed by an air cool. Ti-15V-3Cr-3Al-3Sn was solution heat treated for 30 minutes at 816°C (1500°F) followed by an air cool. Peak aging following solutionization (STA) for both alloys comprised a subsequent single step heat treatment at 538°C (1000°F) for 8 hours followed by an air cool. The presence of a β/α microstructure, and the absence of ω phase, was confirmed by both x-ray diffraction experiments, TEM/selected area diffraction, and optical microscopy on the STA β alloys^{1,18}. The physical metallurgy of STA Ti-3Al-8V-6Cr-4Zr-4Mo (Ti-3.4 Al-8.3V-5.9Cr-4.4Zr-4.1 Mo, wt%) has also been detailed elsewhere^{30,31}. STA Ti-3Al-8V-6Cr-4Zr-4Mo was solutionized at 815°C for 1 hour followed by an air cool. STA material was aged at 500°C for 24 hours followed by air

cooling. Grade 2 (commercially pure) titanium (Ti-0.16Fe-0.13O-0.005N) and grade 6 titanium (Ti-5.20Al-2.30Sn-0.46Fe-0.13O-0.010N) were also examined.

B. Environments

0.6 M NaCl solutions ($\kappa = 0.0521 (\Omega\text{-cm})^{-1}$) incorporated reagent grade NaCl added to distilled, deionized, 18 M Ω water. Other 0.6 M NaCl solutions were adjusted to alkaline pH values with reagent grade NaOH or to acidic pH values with reagent grade HCl. Solution pH was measured with a Corning 350 pH analyzer. 5M HCl solutions ($\kappa = 0.602 (\Omega\text{-cm})^{-1}$, calculated pH = -1.64³²) incorporated reagent grade HCl added to distilled, deionized, 18 M Ω water.

C. Repassivation Tests

Experimental procedure for potentiostatic scratch depassivation and fractured thin film tests are detailed elsewhere^{33,34}. The limitations of these tests have been thoroughly discussed by the authors³³.

D. Fracture Specimen and Model Compact Tension Specimen Tests

The experimental setup and high speed current acquisition procedures for actual fatigue pre-cracked compact tension tests has been previously detailed elsewhere^{3,35}. An apparatus which models the geometry of a compact tension specimen was utilized to examine the solution resistance down a crack. Figure 2 shows the model compact tension specimen fixture. The fixture, which is made of a nonconducting polymer, is screwed to an epoxy disk and mounted within a cell containing remotely positioned reference and counter electrodes. The screws were torqued to 0.014 N-m. The fixture is comprised of a simulated crack tip, and electrically coupled passive β -Ti surfaces. A working electrode within a well comprises the simulated crack tip⁽¹⁾. The working electrode is held potentiostatically by the remote counter and reference electrodes. A gap 30 μm in height and 5.08 mm in width exists at the thin film well / crack interface. The gap is roughly 6 times larger than the crack tip opening displacement (CTOD)³⁶ at K_{Ic} for STA Ti-15Mo-3Nb-3Al. The gap is the only pathway through solution from the well to the bulk solution where

(1) A fractured titanium thin film is shown as the working electrode in Figure 2. This working electrode is utilized to model film rupture at a crack tip. For the tests discussed here, an aluminum working electrode was utilized in order to generate large currents that cause ohmic limitation to assess the ohmic resistance of a crack geometry.

the reference and counter electrodes are positioned. This gap generates solution resistances similar to those at a crack tip, in theory. A measurement of the potential of the working electrode vs. a Ag/AgCl auxiliary reference electrode positioned within the well enables calculation of the potential drop between the well and the bulk solution. This value can be divided by the measured current to obtain the solution resistance.

III. RESULTS AND DISCUSSION

A. Proposed Scenario for EAC of β -Titanium Alloys in Chloride Solutions

It is proposed that EAC susceptibility in neutral or acidic environments results from the following series of events: 1) film rupture during dynamic plastic straining, 2) enhanced dissolution of titanium, 3) crack tip solution acidification due to hydrolysis of titanium ions (except when exposed to high pH solutions or strong cathodic polarization), 4) transient loss of potentiostatic control of the transiently-bare crack tip due to ohmic voltage drop in solution, 5) proton or water reduction concurrent with titanium dissolution, 6) bare surface-dominated hydrogen uptake into the metal following proton or water reduction, 7) hydrogen controlled intergranular crack initiation. The purpose of this paper will be to present evidence for components (1)-(6). Some of these elements have been presented in detail, previously^{37,38,39}. Element 7 is supported by the literature¹⁶⁻¹⁹ and beyond the scope of this paper.

B. The role of film rupture in crack initiation

Results from a monotonically rising CMOD test on STA Ti-15Mo-3Nb-3Al exposed to 0.6 M NaCl at an applied potential (E_{app}) of $-0.10V_{SCE}$ indicate that film rupture precedes crack initiation in β -titanium alloys³⁵ (see Figure 3). This was always observed prior to crack initiation. K_{Ih} (42.8 MPa \sqrt{m}) for this specimen, which had an R_c hardness of 45, is much lower than the moist air fracture toughness K_{ICi} (66-68 MPa \sqrt{m} , $R_c = 44.25$)¹, indicative of EAC. Both high speed current transient detection and background current measurement indicate that repeated overlapping film rupture events occur well before crack initiation as determined by DCPD measurement (Figure 3a). Such events decrease in intensity when active straining is stopped (Figure 3b) so that only creep strain remains. Film rupture is inferred from such current spikes because such transients are absent during exposure without straining or loading. Small area film rupture events can be detected because the bare surface current density following depassivation

can be as large as 10^9 times greater than the passive current density on filmed surfaces³⁴.

Film rupture is required for EAC of β -titanium alloys regardless of the controlling mechanism^{1,3}. If hydrogen embrittlement is the cause of cracking, film rupture would be required for hydrogen entry as the passive oxide on titanium is a strong hydrogen permeation barrier in room temperature solutions, as discussed above. If film-induced cleavage is the controlling EAC mechanism then film rupture is an inherent part of crack initiation and growth. If a dissolution mechanism controls cracking, then film rupture would be the source of crack growth. Steady state passive current densities are too low to account for even the slowest observed crack growth rates^{28,29}.

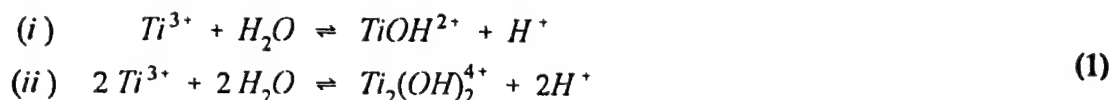
C. Dissolution of titanium at the crack tip

Previous researchers^{40,41} have shown that a large majority of the total anodic charge passed following depassivation of titanium exposed to chloride environments generates soluble dissolution products. Research in this laboratory indicates that at least 90% of the charge is associated with dissolution ($\text{Ti} \rightarrow \text{Ti}^{3+} + 3\text{e}^-$) and does not contribute to oxide formation ($\text{Ti} + 2\text{H}_2\text{O} \rightarrow \text{TiO}_2 + 4\text{H}^+ + 4\text{e}^-$)^{33,34}. This was determined by integration of a fractured titanium thin film current transient over time, compared to the charge required to reform an oxide layer consisting of TiO_2 of a certain thickness^{28,29,34}. The anodic charge density passed until the current density decayed to the previous passive current density following thin film fracture in 0.6 M NaCl was found to be 27-32 mC/cm² at E_{app} from 0 to -0.6 V_{SCE}. The total charge density required for oxide formation is 1.7 mC/cm², assuming a 1 nm oxide thickness^{28,29}, 0.52 nm monolayer thickness⁴², and 3.4 g/cm³ oxide density⁴². Therefore, the large majority of charge is attributed to dissolution of titanium during repassivation and not to barrier oxide formation.

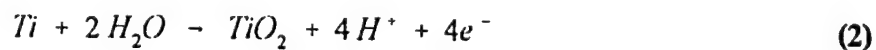
D. Crack tip acidification due to hydrolysis of titanium ions

Figure 4a illustrates pH shifts monitored from the inside of a Ti 15Mo-3Nb-3Al crevice created by inserting a pH electrode into a solution-filled hole drilled in the β -Ti alloy. The external solution was 0.6 M NaCl, as in crack growth experiments, and the indicated external potentials were applied. An alkaline pH shift is observed inside the crevice upon cathodic polarization. An acidic pH shift is observed upon anodic polarization. Crack tip solution acidification following cracking of Ti has been observed elsewhere^{26,37}. Film rupture is expected

to acidify crack tips further than in the case of crevices unless dominated by OH^- production on crack flanks due to strong cathodic protection. Moreover, the crevice gap and depth of the occluded cell is not as severe as at an actual crack tip (see next section), so acidification is not as extensive as theoretically calculated for a sharp crack tip in Ti with a 0.011 radian crack angle (Figure 4a). Trivalent titanium is produced following depassivation at the potential likely to be encountered at the deaerated crack tip⁴⁰ (see next section). The trivalent titanium may then hydrolyze. Two hydrolysis reactions of Ti^{3+} are possible⁴³:



Using published hydrolysis constants⁴³, a distribution diagram of hydrolysis products was calculated for Ti^{3+} ions³⁴. The distribution diagram indicated that Ti^{3+} additions to neutral, deaerated 0.6 M NaCl solution readily hydrolyze and that TiOH^{2+} is the dominant hydrolysis product over all pH. TiCl_3 was added to distilled, deionized water in an oxygen free atmosphere in order to confirm this calculation. The solution pH was recorded when it reached steady state (2-5 minutes). Concentrations of 10^{-4} M to 1 M TiCl_3 were examined (see Figure 4b). The pH of the solution was found to decrease from neutral to about pH 3 when 10^{-4} M TiCl_3 was added. At 1 M TiCl_3 , the pH approached 0. Thus, observed crack tip acidification following cracking is likely attributable to the hydrolysis of Ti^{3+} ions in the crack tip solution. Following depassivation, concurrent oxide formation and dissolution occur, as discussed above. Oxide formation also results in crack tip acidification. For the case of barrier oxide formation the reaction



is predominant over the potential range where EAC occurs. Thus, the production of H^+ and resulting crack tip acidification is assured following dissolution and oxide formation at anodic potentials.

E. Hydrogen production at crack tips due to ohmic voltage drop in solution

EAC initiation of β -titanium alloys exposed to 0.6 M NaCl has been observed during

potentiostatic tests at applied potentials of -0.10 and -0.15 V_{SCE} and open circuit potentials near $-.650$ V_{SCE} ¹⁻³. These potentials are more positive than the reversible potential for hydrogen production in this solution. At issue is whether crack tip acidification and an ohmic voltage drop can place the crack tip potential below the reversible potential for hydrogen production.

Large ohmic voltages between reference and the external filmed surfaces of a compact tension specimen is not possible given the passive current density on β -titanium alloys ($< 1 \mu A/cm^2$ in 0.6 M NaCl)^{28,29}, an exposed external area of approximately 10 cm^2 , and a solution resistance of 10 Ω . Therefore, bulk hydrogen charging of β -titanium alloys external surfaces is precluded at applied potentials of $-0.10V_{SCE}$ and $-0.15V_{SCE}$. Hydrogen production within the crack is possible, however because ohmic solution resistances within the crack are larger. Also, the local crack tip currents can be large following film rupture; the bare surface anodic current density (as measured from fractured titanium thin film tests)³⁴ is approximately 9 orders of magnitude larger than on film covered surfaces at $-0.10V_{SCE}$ (Figure 5). Further, crack tip acidification increases the reversible potential for hydrogen production.

Crack initiation is observed 1000 s after significant current transients are observed in Figure 3a. Diffusivities in β -titanium alloys are near or below 10^{-7} cm^2/s for many different alloys^{16,19}. The unfilmed transport distance $\sqrt{\pi Dt}$ into Ti is > 100 μm after 1000 s. However, hydrogen diffusivity in TiO_2 is six orders of magnitude lower than through the β -titanium lattice at room temperature⁴⁴⁻⁴⁶. Therefore, even if the filmed surfaces along the crack flank experienced a significant enough voltage drop to support hydrogen production, only the bare surfaces nearest the crack tip would be expected to contribute to crack tip hydrogen accumulation (see below).

It remains to be determined whether sufficient ohmic voltage drops are present to enable hydrogen production at transiently bare crack tips when external applied potentials are positive of reversible hydrogen. The voltage difference between the bare crack tip open circuit potential and some externally applied potential during a film rupture event can be described by the following expression:

$$E_{app} - E_{tip} = \eta_{act} + \left(\int_0^L \frac{i(x)dx}{\kappa(x)} \right) + \left(\frac{RT}{3F} \int_{C_{bulk}}^{C_{tip}} d \ln(C(x)) \right) \quad (3)$$

Where E_{tip} describes the open circuit potential of the bare crack tip. η_{act} describes the charge transfer overpotential for the bare tip. The relationships describing η_{act} vs. $\log(I)$ and E_{tip} for bare β -Ti are known as a function of pH³⁵. The second right hand term describes the ohmic voltage contribution obtained from integrating the total current density (tip and passive wall) flowing to the crack mouth from each increment of crack tip and wall (dx) given a local conductivity, $\kappa(x)$ for all increments equaling the crack length L. The third term describes any contribution from concentration overpotentials due to accumulation of Ti^{3+} at the crack tip and concentration differences along the crack from the tip to the mouth. The Ti^{3+} concentration present at various crack tip pH values was estimated from Figure 4b for expected tip pH levels³⁵. From these the concentration overpotential was found to be small in comparison to $E_{app}-E_{tip}$ suggesting dominance of Eq. 3 by the ohmic and charge transfer terms. To determine the extent of polarization of the crack tip (η_{act}) and whether it is more negative than the reversible hydrogen potential ($E_{tip} + \eta_{act} < E_{H/H_2O}$) requires understanding the ohmic voltage component. According to Eq. 3 this requires knowledge of the incremental currents flowing to the mouth, conductivities, and crack geometry as a function of incremental distance from the crack tip. The crack geometry was investigated through calculations of crack tip opening displacements (CTOD)³⁶ and SEM imaging of crack tips in STA β -Ti alloys actively loaded to K_{th} (e.g. 40-45 MPa/m)³⁶. The following expression describes the CTOD for a low work hardening material.

$$CTOD = 0.5 \left(\frac{K^2}{\sigma_{ys} E} \right) \quad (4)$$

For STA Ti 15Mo-3Nb-3Al and Beta-C, a CTOD of approximately 5-9 μm is calculated for K_{th} of 40-45 MPa/m, an elastic modulus, E, from 98-105 GPa and yield strength from 1200-1400 MPa. However, loaded intergranular cracks in STA Beta-C ($E = 104$ GPa, $\sigma_{ys} = 1170$ MPa, $K_{app} = 44$ MPa/m) have crack opening dimensions over a range of distances from the crack tip that are much smaller than their transgranular counterparts at the same σ_{ys} and K_{app} . The intergranular crack half angle is also much smaller at about 1-2 degrees³⁶. The ohmic resistance and voltage were, subsequently, estimated using a theoretical transport calculation for a trapezoidal crack

geometry⁴⁷ and experimentally using a compact tension specimen geometry⁽¹⁾. The following relationship was used for the calculated ohmic voltage⁴⁷:

$$V_{ohmic} = \frac{w_o i_{bare}}{\kappa 2\theta} \left[\ln \left(\frac{1+2\theta L}{w_o} \right) \right] \quad (5)$$

Where, w_o is the non-conservative CTOD of 5 μm , i_{bare} is the peak bare current density, θ is the crack opening half-angle in radians, and L is the crack length. R_s was found to be 4160 Ω for a estimated compact tension specimen crack opening angle at K_{th} of 0.011 radians⁽¹⁾. This overestimates the true ohmic resistance of an actual compact tension specimen since one-dimensional transport is assumed but underestimates it because it doesn't account for the smaller crack opening of an intergranular crack and its extensive tortuosity³⁶.

The solution resistance down a crack in a compact tension specimen was also experimentally determined from a model compact tension specimen. Here, a model compact tension specimen was polarized anodically with the reference and counter electrodes located in the bulk solution, 0.6 M NaCl (Figure 2). The potential of the simulated crack tip working electrode was measured with an auxiliary reference electrode placed at the tip. A linear dependence of the current was noted over the applied potential range, indicative of ohmically controlled E-I relationship, yielding a solution resistance of approximately 370 Ω (Figure 6). This solution resistance is a lower bound of the true solution resistance in a compact tension specimen because it is generated by a 30 μm high rectangular aperture between the crack tip well and the bulk solution (Figure 2). A real crack tip has a more tortuous geometry, a CTOD six to thirty times smaller, and current flow from both the transiently bare crack tip and the filmed crack walls. The solution resistance should be at least six times larger, 2200 Ω , for a CTOD of 5 μm . This value is within a factor of two of the theoretical value calculated above. Crack tortuosity, again, could not be factored into the experimental estimation⁽²⁾.

(1) The calculation involving the trapezoidal crack geometry was performed with and without inclusion of the passive current density of the crack flank. No difference in ohmic voltage was found as expected since the passive c.d. of Ti in strong acid is 9 orders of magnitude below the bare anodic c.d. and, therefore, may be assumed to act as an insulator having no effect on the crack tip ohmic voltage drop. Experimental determinations included passive current from crack walls.

(2) The question may arise as to how the crack tip potential can fall below the reversible potential for hydrogen production before crack initiation for the small net anodic currents of 0.3 to 3 μA that are detected (Figure 3a) flowing from the crack preceding EAC initiation (Currents as large as 1 mA have been noted during fast environmental crack

The true potential at a transiently bare crack tip surface can be calculated from knowledge of the peak current and solution resistance. Although the peak current density on bare titanium exposed to neutral 0.6M NaCl is known as a function of IR-corrected potential (Figure 5), the crack-tip current is unknown because the bare surface area is undetermined. Therefore the bare crack area was systematically varied in calculations. Assuming a crack-tip bare area of one CTOD at K_{th} (5 μm) times the CT sample thickness and the experimental solution resistance, 2200 Ω , the crack tip potential can be calculated as a function of applied potential. Figure 7a (2200 Ω) indicates that there is almost complete loss of potentiostatic control of the crack tip for this area ($2.5 \times 10^{-4} \text{ cm}^2$)-solution resistance combination. That is, the crack tip potential always approaches the bare surface open circuit potential, regardless of applied potential. Even if an bare area 100 times smaller is considered, the crack tip potential always remains negative of the reversible potential for water/proton reduction (Figure 7a). Thus, crack tip hydrogen production is assured for these area-solution resistance combinations, regardless of applied potential. If the bared area is even smaller (e.g., 10^{-3} and 10^{-4} CTOD), the crack tip potential may remain more positive than the reversible hydrogen potential at applied potentials $>0.5 V_{sce}$. Hydrogen production is thermodynamically precluded in these cases even if passive anodic currents from crack flanks (about 1 cm^2 area) are included given their low magnitudes (Figure 5). Similar trends are observed for the theoretical crack solution resistance of 4160 Ω (Figure 7b). Here, the crack tip bare area small enough such that the crack tip potential remains above reversible hydrogen is decreased. The connection between the results of Figure 7 and anodic inhibition of EAC of the β -Ti alloys shown in Figure 1, for Ti-8Al-1Mo-1V¹¹ and by others² suggests that raising the crack tip potential above the reversible hydrogen potential profoundly affects crack initiation and growth. Shifting the pH of the crack tip to more acidic conditions produces a positive shift in the reversible hydrogen potential, while a more alkaline crack tip pH has the opposite effect. Thus,

growth on STA Ti 15Mo-3Nb-3Al). The measured current (by the potentiostat at the counter electrode) can underestimate the true anodic current at the crack tip by a very large fractions, as the passive crack walls and CT specimen surface capacitively and faradaically couple with the bare crack tip. This fraction of the anodic current still contributes to IR drop since there is still anode (tip)-cathode (wall) separation, but is not measured by the potentiostat. A larger solution resistance than cited above is also possible without any alteration of solution resistivity (i.e. by salt film precipitation or hydrogen bubbles which may, in fact, form). Crack-tip film rupture and dissolution occurs prior to EAC initiation (Figure 3a). Integration of selected current spikes preceding initiation indicates that $1.2 \times 10^{-4} \text{ C}$ of anodic charge is detected at the crack tip. This corresponds to a crack advance from the transgranular fatigue precrack of 200 nm, assuming dissolution occurs uniformly over an area of 1 CTOD by the effective sample width (the whole crack front). Such crack advance precedes crack initiation as determined by DCPD and load data (Figure 3). If some of this dissolution is preferential at one grain boundary, a tight solution pathway will form between grains and, consequently, the IR voltage drop is further increased.

the critical applied potential for anodic inhibition should become more positive under more acidic conditions and more negative under more alkaline conditions. Such shifts in the critical applied potential have, also, been observed⁴⁸.

All calculations in Figure 7 were for peak current densities. Further calculations could be performed at lower current densities representative of various time during repassivation³⁴. For instance, at a applied potential of 0 V_{sce} it is seen that hydrogen production occurs at the bare crack tip at its peak current density. However, tens of seconds later when the current density has decayed 4 orders of magnitude, the crack tip potential is shifted above reversible hydrogen⁽¹⁾. Thus, hydrogen production does not occur at more anodic applied potentials during the entire repassivation event but only when the film rupture-repassivation current density is high. Hence, some hydrogen may still enter the Ti lattice and thus anodic inhibition may be incomplete or only partial as observed at anodic potentials in Figure 1 and also elsewhere^{2,11}. Since pitting of Ti is unlikely at even +1V_{sce} in room temperature 0.6 M NaCl^{27a-d} (Table 1), acidified pit sites may be ruled out as a source of both hydrolytic acidification and persistent large anodic current densities that can sustain IR voltage drops.

Table 1 Pitting Potentials for Ti-base alloys

Material	Heat treatment	E _{pit} (V _{sce})	Solution/Temp.	Ref.
C.P. Ti	annealed	13.2	5 M HCl (22°C)	27b
Ti-6Al-4V	annealed	1.7	5% NaCl, boiling, pH 3	27c
Ti-6Al-4V	hot rolled, forged	>5.9	2 M HCl (37°C)	27d
Ti-15Mo-2.7Nb-3Al-0.2Si	solution treated	2.9	5% NaCl, boiling, pH 3	27c
Ti-15Mo-2.7Nb-3Al-0.2Si	solution treated	13	5 M HCl (22°C)	27e
Ti -3Al-8V-6Cr-4Zr-4Mo	solution treated	3.1	5% NaCl, boiling, pH 3	27c

(1) An additional factor not explicitly included in this discussion is that the open circuit potential of the crack tip becomes more positive as an oxide film is reformed, this also contributes to making it easier to polarize the crack tip above the reversible hydrogen potential during the later stages of repassivation.

Other have shown that a sharp notch or crack is required for EAC of β -titanium alloys in 0.6 M NaCl^{5,49}. The surface crack half-angle for a smooth or blunt notch sample can become quite large during plastic straining^{47, 50}. This can limit both acidification and the ohmic voltage drop according to Eq. 5. Since a restricted geometry is required for significant potential drop in solution and hydrogen uptake (for $E_{app} > E_{r,HER}$), it is possible that only a sharp notch or fatigue pre-cracks can generate a large enough IR potential drop to enable hydrogen production at occluded sites. This may explain the requirement of a sharp notch or fatigue precrack for EAC of Ti. Thus, EAC is typically not observed on smooth or blunt notched high strength β -titanium⁵⁰. In addition, as Table 1 illustrates, smooth specimens will be extremely resistant to pit formation which could serve as a crack initiation site.

F. Proton or water reduction concurrent with titanium dissolution at the crack tip

The production of hydrogen on the bare crack tip surface following film rupture occurs at applied anodic potentials approaching 0 V_{SCE} given sufficient ohmic voltage loss in solution. The bare surface cathodic current density is 4 to 5 orders of magnitude larger than on a filmed titanium surface, depending on potential (Figure 5). The following pH dependency of the bare surface cathodic current density at the bare open circuit (i.e. the corrosion current density) is obtained from the bare surface polarization curves of fractured titanium thin films exposed to solutions of varying pH³⁴:

$$i_{cath_{O.C.P.}} \left(\frac{A}{cm^2} \right) = 10^{(0.68 - 0.15 pH)} \quad (6)$$

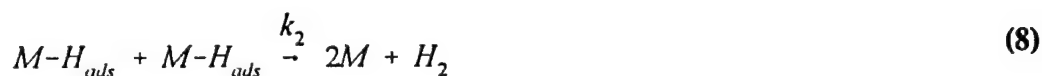
The crack tip cathodic current density, therefore, ranges from 0.4 A/cm² in neutral solution to 8 A/cm² in acidic solution. Thus, reduction of water kinetics are enhanced under acidic crack tip conditions.

G. Hydrogen uptake into titanium following crack tip proton or water reduction

The observation of cathodic inhibition of an HEAC phenomena requires further discussion. In order for cathodic inhibition of HEAC of β -Ti to be possible (Figure 1), it must first be shown that bulk charging through external Ti oxide covered surfaces at near-neutral pH is negligible.

This section compares relative lattice hydrogen concentrations achievable for bulk versus crack tip charging. As discussed above, the literature indicates that significant hydrogen ingress through the oxide on titanium and its alloys is unlikely in room temperature neutral solutions above $-1V_{SCE}$ because the oxide is a strong barrier to hydrogen uptake^{44,46}.

The exact flux of hydrogen into the lattice is dependent upon the production rate of hydrogen or the hydrogen evolution mechanism,⁵¹ as well as other factors. Only a fraction of the discharging hydrogen will enter the metal lattice. A slow discharge-fast recombination mechanism has been proposed for film-covered titanium in acidic chloride solutions⁵². However, the reaction mechanism on bare titanium is likely different due to the presence of a bare metal surface instead of a charge transfer-limiting semiconducting oxide. Recall, also, that the proton or water reduction cathodic current density at a bare crack tip is many orders of magnitude larger than that on a filmed surface (Figure 5). The IR-corrected cathodic Tafel slopes on bare titanium have been found to increase with increasing pH from fractured thin film tests³⁴. Tafel slopes were found to range from -182 (in 5M HCl) to -221 mV/decade (0.6M NaCl adjusted to pH 10). Therefore, the hydrogen evolution reaction mechanism on bare titanium could be attributed to a conventional hydrogen evolution mechanism, such as the coupled discharge-recombination mechanism⁵¹:



The current density for this reaction is⁽¹⁾:

$$i = k_1 C_{H^+} (1-\theta) \exp\left[\frac{-\beta \eta F}{R T}\right] = k_2 \theta^2 \quad (9)$$

where θ is the surface coverage of hydrogen, k_1 and k_2 are rate constants, and C_{H^+} is the H^+ concentration in solution. Assuming $\beta = 1/2$, a Tafel slope of 177 mV/decade (activated Temkin isotherm) would be observed for this mechanism⁵¹. Larger Tafel slopes would be obtained for $\beta < 1/2$. Therefore, the coupled discharge-recombination mechanism is consistent with the Tafel

(1) Water reduction, in place of proton reduction, is likely at neutral and alkaline pH.

slopes on bare titanium surfaces (-182 to -221 mV/decade).

At steady state the absorption of hydrogen into metal is usually a relatively fast process relative to diffusion and can be considered to be in "quasi-equilibrium" in the overall permeation process⁵¹. Thus, for the quasi-equilibrium reaction



the subsurface hydrogen concentration C_0 can be related to the hydrogen surface coverage by

$$C_0 = \left(\frac{k_a}{k_{-a}} \right) \left(\frac{\theta}{1 - \theta} \right) \quad (11)$$

The subsurface hydrogen concentration, C_0 , can be calculated, therefore, if the rate constants and coverages are known. To the authors' knowledge, neither such parameters nor experimental permeation data on bare titanium are known. However, knowledge of the reduction of water kinetic mechanism provides the relationship between θ and hydrogen production kinetic parameters (equation 9). The hydrogen concentration a depth x from the charging surface at time t can then be calculated from

$$C_{(x,t)} = \left(1 - \operatorname{erf} \left(\frac{x}{2\sqrt{D_{eff}t}} \right) \right) C_0 \quad (12)$$

where D_{eff} is the effective diffusivity through the metal in the case of a bare surface and through both the oxide and metal if the surface is passivated. For the case of a low hydrogen coverage and Langmuir isotherm, following equations describes the accumulation of hydrogen as a function of time and distance for the given reduction of water kinetics.

$$C_{(x,t)} = \left(1 - \operatorname{erf} \left(\frac{x}{2\sqrt{D_{eff}t}} \right) \right) \left(\frac{k_a}{k_{-a}} \right) \left(\frac{j^{1/2}}{k_2} \right) \quad (13)$$

Equation 13 predicts that the hydrogen concentration, $C(x,t)$, is a function of both the bare surface hydrogen production, recombination kinetics, absorption kinetics, the hydrogen diffusivity and time. Comparison of the *relative* hydrogen concentrations in the fracture process zone that results

from proton/water reduction on bare and filmed surfaces can be made to address whether hydrogen entry is local to the crack tip. Absolute concentrations cannot be calculated because the exact rate constants, surface coverages, etc. are not known. However, the relative concentrations can be calculated if it is assumed that the subsurface hydrogen concentrations are proportional to the water/proton reduction rates on both bare and filmed surfaces⁽¹⁾. Using $x = 48 \mu\text{m}$ (the plastic zone size at K_{th} of 44 MPa $\sqrt{\text{m}}$) and an oxide film thickness of 1 nm^{28,29}, D_{eff} is calculated to be $2.11 \times 10^{-13} \text{ cm}^2/\text{s}$, assuming a hydrogen diffusivity in the metal of $10^{-7} \text{ cm}^2/\text{s}$ ¹⁶ and a hydrogen diffusivity through the oxide of $4.4 \times 10^{-18} \text{ cm}^2/\text{s}$ ⁴⁴. Thus, both the hydrogen transport rate by diffusion and the hydrogen production rate (as seen from Figure 5) are much slower when a passivated surface is present. Figure 8 is a plot of the relative hydrogen concentrations at a 48 μm depth as a function of time for the filmed and bare surfaces, assuming that C_0 is proportional to the cathodic water/proton reduction current density on each surface in 0.6 M NaCl. Calculations were performed at two different applied potentials; the bare surface open circuit potential ($-1.58 \text{ V}_{\text{SCE}}$) and the reversible potential for hydrogen production ($-0.655 \text{ V}_{\text{SCE}}$) in neutral 0.6 M NaCl. These are the lower and upper bounds, respectively, on the potential range over which hydrogen can be produced for any applied potential greater than the bare surface open circuit potential. All calculations are normalized to the largest value of $C(x=48 \mu\text{m}, t \rightarrow \infty)$, the concentration at steady state on the bare surface at the bare surface open circuit potential. It is seen that hydrogen accumulation through the bare surface is always orders of magnitude larger than that through the passive surface. The oxide significantly delays hydrogen uptake at $t < 10^6 \text{ s}$ typical of HEAC testing. At steady state ($t > 10^9 \text{ s}$), hydrogen accumulation through the passive surface is still much smaller due to the smaller cathodic current density on the filmed surface (viz: 10^{-7} to 10^{-4} A/cm^2 depending on potential). At steady state, $C(x=48 \mu\text{m}, t \rightarrow \infty) = C_{\text{ss}} = C_0$. Although values for C_{ss} cannot be calculated, it is apparent from equations 9, 11 and 12 that C_{ss} increases exponentially with cathodic (hydrogen) overpotential. If the ohmic voltage is large enough so that the crack tip approaches the bare surface open circuit potential, the overpotential for hydrogen production can be calculated. In 0.6 M NaCl ($\text{pH} = 6$), the overpotential is $-0.596 \text{ V}_{\text{SCE}} - (-1.577 \text{ V}_{\text{SCE}}) = 0.98 \text{ V}$. This cathodic overpotential produces enormous hydrogen fugacities at the bare crack tip.

(1) If the bare surface proton / water reduction reaction were the activated Temkin isotherm instead of Langmuir, C_0 would be proportional to $(i^2)^{-1}$. This magnifies the difference between filmed and unfilmed hydrogen accumulations. Moreover, the hydrogen evolution mechanism on filmed titanium, slow discharge - fast recombination³², is theoretically non-embrittling because recombination is assumed to be instantaneous with respect to discharge.

In order to confirm that bulk hydrogen uptake through the oxide is negligible, STA Ti 15Mo-3Nb-3Al foils (thickness = 0.38 mm) were cathodically polarized for 5 days (> saturation times without oxide) at $-1V_{SCE}$ in a variety of room temperature chloride solutions and subsequently analyzed for hydrogen content. Hydrogen accumulations in 0.6 M NaCl adjusted to pH 10, 0.6 M NaCl, 0.6M NaCl adjusted to pH 1 and 5M HCl are seen in Figure 9. No hydrogen uptake occurs on STA Ti-15Mo-3Nb-3Al exposed to pH 1, neutral and pH 10 0.6 M NaCl solutions, as the concentrations measured from these samples are identical (177-188 ppm) to the as-received material (195 ± 20 ppm) within experimental error. These results agree with the prediction of Figure 8. This is expected because, electrochemical kinetic data confirm that Ti is spontaneously passive in water at pH 1^{28,29}. Moreover, cathodic reduction-induced thinning of TiO_2 does not occur in neutral solutions at 25°C⁵³. Recall that a crack tip solution pH of 1.8 has been measured in a Ti-8Al-1Mo-1V crack following crack propagation²⁶. Therefore, it can be concluded that hydrogen uptake through the oxide would be precluded at this pH and this is, in fact, observed in Figure 9. Moreover, Powell et al. cite evidence which indicates that hydrogen entry is much reduced or eliminated following film reformation²⁵. In summary, although the exact hydrogen flux into titanium following film rupture cannot be calculated, evidence suggests that hydrogen absorption is local to deforming crack tips at room temperature unless solutions are much more acidic than pH 1.⁽¹⁾

The minimal amount of bulk hydrogen charging also contributes to the observed lack of EAC susceptibility in constant extension rate tests on smooth β -Ti specimens⁵⁰. Since hydrogen uptake is limited through oxide covered Ti⁵⁰ and smooth specimens lack long, sharp^{47,50}, IR-producing crack tips (see above), hydrogen uptake is limited and "apparent" immunity is observed. Indeed, CERT testing of blunt notched Beta-C at -0.15, -0.6 and -1.0 V_{SCE} in 0.6 M NaCl produced small load drops and notched hydrogen concentrations that were indistinguishable from the as-received levels.

(1) This differs markedly from the case of high strength steels where oxide films are readily reduced thermodynamically and kinetically and bulk external hydrogen charging may dominate over crack tip charging at potentials negative to -900 mV_{SCE} except in cases of very high crack tip deformation⁵⁴. HEAC of steels is well-known to be enhanced by both strong cathodic polarization and anodic polarization and inhibited at intermediate potentials in neutral NaCl, unlike the case of high strength β -titanium.

H. Explanation for Cathodic Inhibition of high strength β -Ti EAC

If hydrogen controls crack initiation in high strength β -Ti, it must be explained why crack initiation is suppressed at cathodic applied potentials for long, sharp cracks subjected to applied cathodic potentials (Figure 1). Partial explanation has been provided above where it has been shown that hydrogen uptake is local to sharp cracks and controlled by processes occurring at the crack tip. It remains to be explained why local crack tip hydrogen uptake might be inhibited for cathodically polarized, actively strained crack tips where crack tip hydrogen production is shown to be thermodynamically possible (Figure 7).

Recall that cathodically polarized crack tips are well known³⁷ to become more alkaline (Figure 4a). Figure 10 shows the bare surface open circuit potentials obtained from fractured titanium thin films exposed to 0.6M NaCl solutions of various pH, from pH 1 to pH 13.7. The "bare metal" open circuit potential was taken as the most negative potential in the open circuit potential transients after film rupture. The intersections of the anodic and cathodic Tafel lines obtained by fitting of bare surface polarization curves in pH -1.64, 6 and 10³⁴ are also plotted in Figure 10. Linear regression of both data sets yields $E_{OCp} = -1.20V_{SCE} (pH = 0) - 0.043V_{SCE} * pH^{(1)}$. Thus, the bare surface open circuit potential decreases 43 mV/pH unit. The reversible potential for hydrogen evolution decreases 59 mV/pH. Thus, the overpotential for hydrogen production at the bare open circuit potential ($E_{HER} - E_{OCp}$) decreases 16 mV/pH (see Figure 10). When ohmic loss in solution is large such that the potential at the crack tip approaches its open circuit potential, an increased driving force for hydrogen production will exist at a crack tip in acidic solution (viz. anodically polarized) compared to an alkaline solution (viz. cathodically polarized).

Assuming that the hydrogen evolution mechanism on bare titanium is the coupled discharge-recombination mechanism, that the adsorption isotherm is either Langmuir, non-activated or the activated Temkin isotherm, and that all of the rate constants are independent of pH (or vary equally with pH), a relative subsurface hydrogen concentration, C_{ss} , can be calculated

(1) Statistical analysis indicates that the linear correlation coefficient (r^2) for the open circuit potential data is 0.92 and that there is a greater than 95% confidence that the magnitude of the slope is less than 50 mV/decade.

as a function of pH at the crack tip open circuit potential⁽¹⁾:

$$C_{ss} \propto (i_{c, OCP})^n = \left(i_{0_c} \cdot \exp 2.3 \left(\frac{(E_{0, HER}) - (E_{bare OCP})}{b_c} \right) \right)^n \quad (14)$$

where the c subscript represents the cathodic reaction, i_0 is the reduction of water exchange current density (A/cm^2) b_c is the cathodic Tafel slope (V/decade), and $n=0.5$, 1, or 2 depending upon whether Langmuir, Temkin, or activated Temkin isotherms apply. Since b_c increases with pH^{34} and the overpotential for hydrogen production decreases with pH, it is apparent that $i_{c, OCP}$ should decrease with pH. Indeed, earlier work³⁴ indicated that $\log(i_{c, OCP} (A/cm^2)) = 0.68 - 0.15 * pH$ ($r^2 = 0.999$). Good correlation between the fit to Eq. 6 and actual $i_{c, OCP}$ data is observed (Figure 11). These atomic hydrogen production current densities can be related to C_{ss} via equation 13. A normalized steady state hydrogen concentration, $C_{ss}/C_{ss, pH 14}$ is calculated by dividing the steady state concentration calculated at each pH by that at pH 14. Figure 11 illustrates that C_{ss} in a crack tip solution acidified to a pH of 1.8 is theoretically 10^1 to 10^4 times larger than that at pH 10 solution (activated Tempkin case) due to both a smaller (more shallow) Tafel slope and a larger overpotential for hydrogen production. The 10^1 to 10^4 theoretical increase may exceed the actual value due to some other limitation such as a lack of correspondence between hydrogen overpotential and fugacity beyond a certain hydrogen overpotential^{51,55}. However, the crucial point is that hydrogen absorption appears to be much greater in acidic crack-tip solutions and hydrogen embrittlement experiments indicate that a sizeable hydrogen concentration of 1000 wt. ppm is required to cause intergranular cracking¹⁶⁻¹⁸.

Previous research has shown that various titanium alloys are susceptible to EAC in acidic and neutral media but not in alkaline media for a given potential^{2,5,25}. As stated in the introduction, the immunity observed at more negative potentials in neutral solutions is attributable to an increase in crack tip solution pH. This is confirmed by the fact that tests at cathodic potentials in strongly acidic solutions (> 7 M HCl), where cathodic reactions likely would be

(2) This equation assumes that the fugacity varies linearly with pressure. At very high fugacities, this relationship does not hold true^{51,53}. Since the absolute fugacity values are not known, these calculations might overestimate the true steady state hydrogen concentration at high fugacity. An exact hydrogen concentration in β -titanium cannot be calculated because the rate constants for the hydrogen evolution and hydrogen absorption reactions on bare titanium are unknown and permeation experiments are plagued by oxide or carbide contamination.

unable to overcome the strong bulk acidity to produce an alkaline occluded chemistry, are susceptible to EAC^{2,5,25}. Moreover, the crack tip solution has been shown to acidify (pH 1-2) during testing of a titanium alloy at open circuit in near neutral 0.6 M NaCl^{26,37}. It is also reasonable to expect that the presence of a strongly alkaline bulk chemistry increases cracking resistance by preventing the crack tip solution from acidifying due to hydrolysis. This situation results in large differences in hydrogen flux into the lattice as a function of pH. EAC susceptibility in acidic media may also be explained by increased hydrogen absorption efficiency in acidic media. Galvanostatic tests on grade 2 titanium in sulfate solutions at 82°C have shown that hydrogen uptake is an order of magnitude larger in pH 0 solution than in neutral solution at identical cathodic current densities²⁴. This result indicates that hydrogen absorption is more efficient in acidic environments even though the hydrogen production reaction rate was equivalent to that in the neutral solutions. The same trend has been noted for steels as well⁵⁴.

In summary, acidic environments enhance the crack tip hydrogen production rate and likely the hydrogen absorption rate, leading to increased hydrogen concentrations within the titanium metal and increased EAC susceptibility under acidic conditions. Alkaline conditions decrease production rates and likely absorption rates leading to lower subsurface hydrogen concentrations. It should be noted that alkaline solutions do not enhance β -Ti alloy repassivation rates,³⁴ nor lower film rupture rates³⁵. It is apparent from Figures 7 and 8 that hydrogen concentrations, while minimized, will be non-zero under alkaline conditions. Therefore, cathodic inhibition based on short term laboratory results (Figure 1) should be further explored.

IV. CONCLUSIONS

An explanation for the dependency of crack initiation of precracked β -titanium alloys on solution pH and applied potential in room temperature aqueous 0.6 M NaCl has been presented. It is proposed that EAC susceptibility of precracked specimens in neutral environments results from the following series of events: 1) film rupture promoted by dynamic plastic strain, 2) dissolution of titanium, 3) crack tip solution acidification due to hydrolysis of titanium ions, 4) loss of potentiostatic control of the crack tip during film rupture transients due to ohmic drop in solution, 5) crack-tip water reduction concurrent with titanium dissolution during negative potential excursions, 6) bare surface dominated hydrogen ingress into the fracture process zone at the crack tip, 7) intergranular cracking by hydrogen embrittlement.

Hydrogen production and uptake on surfaces with native oxides was shown to be very slow and EAC is dominated by bare crack tip electrode kinetics. Film rupture was shown to precede EAC initiation providing a bare surface for enhanced hydrogen uptake. Production and uptake are limited on oxide covered bulk surfaces during cathodic polarization except in strongly acidic, depassivating solutions. Solution resistances can be large enough for precracked specimens to generate sufficient ohmic drop in solution to enable hydrogen production even when the applied potential is more positive than the reversible potential for hydrogen production.

The dependency of crack initiation in precracked specimens on pH and applied potential appear to be linked. Anodic inhibition was explained based on polarization of crack tips above reversible hydrogen. Cathodic inhibition was explained based on limited bulk hydrogen charging through oxide covered external surfaces, reduced crack tip production, and, speculatively, reduced uptake as a result of an alkaline crack tip chemistry. These critical factors also help explain the apparent "immunity" to EAC observed in smooth or blunt notch high strength β -titanium alloys in room temperature NaCl. In smooth specimens, the absence of repeated localized film rupture events in an occluded zone which can support both acidification and ohmic potential drop below the reversible hydrogen potential all conspire to limit hydrogen production and uptake.

ACKNOWLEDGMENTS

This work was supported by the Office of Naval Research (Grant No. N00014-91-J-4164). Electrochemical instrumentation support was provided by EG&G PAR. Alloys were supplied by TIMET and RMI Inc. Crack initiation experiments were conducted with the help of B.P. Somerday. This support is gratefully acknowledged. Further, we would like to acknowledge B.P. Somerday, R.P. Gangloff, R.G. Kelly and L.L. Scribner for their helpful discussions and F.D. Wall for writing the transient detection software used for this research.

Appendix A. Arguments Against Slip - Film Rupture - Dissolution Control of EAC

A wide variety of evidence supports the proposed scenario for hydrogen embrittlement of β -titanium alloys in aqueous chloride solutions. Additional support of this hypothesis arises from results which indicate that slip - film rupture - dissolution control of cracking is unlikely. It has been shown that bare surface anodic current densities are similar in solutions of widely varying pH when the curves are corrected for overpotential³⁴. Additionally, the anodic current densities are similar (e.g., $\pm 25\%$ at $-0.6V_{scv}$) in the different solutions over the potential range where EAC is generally observed³⁴. Moreover, the anodic charge densities passed in the first 30 ms following fracture of titanium thin films are similar³⁴. Therefore, both the bare surface anodic dissolution rate and the repassivation behavior are comparable in the solutions of different pH. Moreover, the film rupture rates are similar in solutions of widely varying pH³⁵. These results

argue against dissolution control of cracking, as dissolution behavior is similar between solutions wherein the extremes of EAC susceptibility and immunity are observed. Repassivation tests in solutions that more closely approximate crack tip solutions (i.e. contain TiCl_3) do not alter this conclusion³⁴.

Scratch repassivation tests on EAC susceptible and immune alloys in 0.6 M NaCl have been performed³⁴. Experiments incorporated ST and STA Ti-15Mo-3Nb-3Al, ST and STA Ti-15V-3Cr-3Al-3Sn, grade 2 (commercially pure) titanium and grade 6 titanium which roughly models the composition of α precipitates within the β matrix²⁹. It was observed that the bare surface current densities³⁴, anodic charge densities³⁴ and film rupture frequencies³⁵ were similar on all of the examined materials. These results argue against dissolution control of EAC because both susceptible and immune microstructures reveal similar bare surface current densities and repassivation behavior.

REFERENCES

- 1) L.M. Young, G.A. Young, Jr., J.R. Scully and R.P. Gangloff, *Metallurgical Transactions A*, 1995, 26A, pp. 1257-1271.
- 2) R.J.H. Wanhill, *Br. Corrosion Journal*, 1975, 10(2), pp. 69-78.
- 3) B.P. Somerday, J.P. Grandle and R.P. Gangloff in "Proceedings of the Tri-Service Conference on Corrosion", T. Naguy, ed., 1994, Materials Laboratory, Wright Patterson Air Force Base, OH, pp.375-392.
- 4) D.N. Fager, W.F. Spurr, *Trans ASM*, 1968, 61, pp. 283-292.
- 5) M.J. Blackburn, J.A. Feeney, and T.R. Beck in "Advances in Corrosion Science and Technology, Vol. 3", 1972, M.G. Fontana and R.W. Staehle, eds., Plenum Press, New York, pp. 67-292.
- 6) J.A. Feeney and M.J. Blackburn, *Metall. Trans.*, 1970, vol. 1, pp. 3309-3323.
- 7) T.R. Beck in "The Theory of Stress Corrosion Cracking", J.C. Scully ed., 1971, NATO Scientific Affairs Division, Brussels, pp. 64-85.
- 8) D.A. Meyn and P.S. Pao in "Slow Strain Rate Testing for the Evaluation of Environmentally Induced Cracking: Research and Engineering Applications, ASTM STP 1210", R.D. Kane ed., 1993, ASTM, Philadelphia, p.158-169.
- 9) G. Sanderson and J.C. Scully, *Corrosion Science*, 1966, vol. 6, pp. 541-542.
- 10) D. Hardie in "Environment-Induced Cracking of Metals", R.P. Gangloff and M.B. Ives eds., 1990, NACE, Houston, TX, pp. 347-361.
- 11) J.A.S. Green, A.J. Sedriks, *Corrosion*, 1972, 28(6), pp. 226-230.
- 12) I.I. Phillips, P. Poole and L.L. Shrier, *Corrosion Science*, (1972), 12, pp. 855-.
- 13) D.N. Williams, *J. Inst. of Metals*, 1962-63, 91, pp. 147-152.
- 14) H.G. Nelson, in *First Thermal Structures Conference*, E. Thornton ed., 1990, University of Virginia, Charlottesville, VA, pp. 301- 311.
- 15) A.D. McQuillan, *Proc. R. Soc. London, Ser. A*, 1950, vol. 204, pp. 309-323.
- 16) G.A. Young, *Scripta Met.*, 1993, vol. 28, pp. 507-512.
- 17) G.A. Young, Jr. and J.R. Scully in "Beta Titanium Alloys in the 1990's", D. Eylon, R.R.

- Boyer and D.A. Koss eds., 1993, TMS, Warrendale, PA, p. 147-158.
- 18) G.A. Young, Jr. and J.R. Scully, *Corrosion*, 1994, 50, 919-933.
 - 19) J.E. Costa, D. Banerjee and J.C. Williams in "Beta Titanium Alloys in the 80's", R.R. Boyer and H.W. Rosenberg eds., 1984, TMS, Warrendale, PA, p. 69-84.
 - 20) B.G. Pound, *Corrosion J.*, 1991, 47, p. 99-104.
 - 21) T.R. Beck in "Proceedings of Conference, Fundamental Aspects of Stress Corrosion Cracking", R.W. Staehle, A.J. Forty and D. VanRooyen eds., NACE, Houston, TX, p. 608 (1969).
 - 22) T.R. Beck in "Passivity of Metals", R.P. Frankenthal and J. Kruger eds., 1978, The Electrochemical Society, Pennington, NJ, pp. 1035-1052.
 - 23) R.W. Schutz and D.E. Thomas in "ASM Handbook, Vol. 13, Corrosion", 1992, ASM International, Metals Park, OH, p. 669-706.
 - 24) Z.A. Foroulis in "Titanium '80 Science and Technology, Proceedings of the Fourth International Conference on Titanium, Vol. 4", H. Kimura and O. Izumi eds., TMS, Warrendale, PA, p. 2705 (1980).
 - 25) D.T. Powell and J.C. Scully, *Corrosion*, 1968, 24, pp. 151- .
 - 26) B.F. Brown, C.T. Fujii, and E.P. Dahlberg, *J. Electrochem. Soc.*, 1969, 116, pp. 218-.
 - 27) (a) R.W. Schutz and L.C. Covington, *Corrosion*, 1981, 37, pp. 585-591. (b) I. Dugdale and J.B. Cotton, *Corros. Science*, 1964, vol. 4, pp. 397-411. (c) R.W. Schutz, in *Beta Titanium Alloys in the 1990's*, D. Eylon, R.R. Boyer, D.A. Koss, 1993, TMS, Warrendale, PA, pp. 75-91. (d) J.P. Simpson, in *Biological and Biomechanical Performances of Biomaterials*, P. Christel, A. Meunier, A.J.C. Lee, 1956, Elsevier Scientific Publishers, Amsterdam, 1956. (e) S. Yu and J.R. Scully, private communication, University of Virginia, 1996.
 - 28) D.G. Kolman and J.R. Scully, *J. Electrochem. Soc.*, 1993, 140, pp. 2771-2779.
 - 29) D.G. Kolman and J.R. Scully, *J. Electrochem. Soc.*, 1994, 141, pp. 2633-2641.
 - 30) T.J. Headley, H.J. Rack, *Metall Trans. A*, 1979, 10A, pp. 909-920.
 - 31) J.R. Wood, J.G. Ferrero, P.A. Russo and R.W. Schutz in "Beta Titanium Alloys in the 1990's", D. Eylon, R.R. Boyer and D.A. Koss eds., TMS, Warrendale, PA, p. 463 (1993).
 - 32) P.O. Gartland, SINTEF publication STF16-A88085, Trondheim, Norway (1988).
 - 33) D.G. Kolman and J.R. Scully, *J. Electrochem. Soc.*, 1995, 142, pp. 2179-2188.
 - 34) D.G. Kolman and J.R. Scully, *J. Electrochem. Soc.*, 1996, 143, pp. 1847-1860.
 - 35) D.G. Kolman and J.R. Scully, *Phil. Mag. A*, in preparation.
 - 36) (a) C.F. Shih, *J. Mech. Phys. Solids*, 1981, 29, pp. 305-326. (b) B.P. Somerday, R.P. Gangloff, "Measurement of Crack Opening Displacement and Crack Tip Strain for Transgranular and Intergranular Cracks in Aged β -Ti," *Scripta Metallurgica et Materialia*, in. prep. (1996).
 - 37) A. Turnbull, In "Embrittlement by the Localized Crack Environment", R.P. Gangloff, ed., 1984, TMS Warrendale, PA, pp. 3-31.
 - 38) R.P. Gangloff and A. Turnbull in "Modeling Environmental Effects on Crack Growth Processes", R.H. Jones and W.W. Gerberich eds., 1986, TMS, Warrendale, PA, p.55.
 - 39) B.F. Brown in "Stress Corrosion Cracking and Hydrogen Embrittlement of Iron Base Alloys", R.W. Staehle, J. Hochmann, R.D. McCright and J.E. Slater eds., 1977, NACE, Houston, TX, pp. 747-750.
 - 40) T.R. Beck, *Electrochim. Acta*, 1973, 18, pp. 807-814.
 - 41) J.R. Ambrose and J. Kruger, *J. Electrochem. Soc.*, 1974, 121, pp. 599-604.

- 42) D. Laser, M. Yaniv and S. Gottesfeld, *J. Electrochem. Soc.*, 1978, 125, pp. 358-.
- 43) C.F. Baes, Jr. and R.E. Mesmer, "The Hydrolysis of Cations", Krieger Publishing Co., Malabar, FL (1986).
- 44) O.W. Johnson, S.H. Paek and J.W. DeFord, *J. Appl. Physics*, 1975, 46, pp. 1026-.
- 45) J.L. Waisman, G. Sines and L.B. Robinson, *Metallurgical Transactions A*, 1973, 4A, pp. 291-302.
- 46) R.J. Wasilewski and G.L. Kehl, *Metallurgia*, 1954, 50, pp. 225-230.
- 47) RC Newman, *Corrosion*, 1994, 50(9), pp. 682-686.
- 48) J.A.S. Green, A.J. Sedriks, *Metall. Transactions A*, 1971, 2A, pp. 1807-1812.
- 49) R.W. Schutz, in Beta Titanium Alloys in the 1990's, D. Eylon, R.R. Boyer, D.A. Koss, eds., 1993, TMS, Warrendale, PA, pp. 75-91.
- 50) D.G. Kolman, J.R. Scully, in "Effects of the Environment on the Initiation of Crack Growth," ASTM STP 1298, 1997, W.A. Van der Slays, R.S. Piascik, and R. Zawierucha, ASTM, West Conshocken, PA, pp. TBA.
- 51) P.K. Subramanyan in "Comprehensive Treatise of Electrochemistry, Vol. 4, Electrochemical Materials Science", J.O'M. Bockris et al. eds., 1981, Plenum Press, New York, pp. 411-462.
- 52) E.J. Kelly and H.R. Bronstein, *J. Electrochem. Soc.*, 1984, 131, pp. 2232-2238.
- 53) T. Ohtsuka, M. Masudo, N. Sato, *J. Electrochem. Soc.*, 1987, 134, pp. 2406-2410.
- 54) A. Turnbull, M. Saenz de Santa Maria, *Metall. Transactions A*, 1988, 19A, pp. 1795-1806.
- 55) R.D. McCright in "Stress Corrosion Cracking and Hydrogen Embrittlement of Iron Base Alloys", R.W. Staehle, J. Hochmann, R.D. McCright and J.E. Slater eds., 1977, NACE, Houston, TX, pp. 306-325.

Figure Captions

Figure 1 - Plot of threshold stress intensities for various precracked β -titanium alloys exposed to 0.6 M NaCl. All data are from reference 5 except Ti-15Mo-3Nb-3Al data (reference 1) and Ti-3Al-8V-6Cr-4Zr-4Mo data (reference 3). All alloys are in the STA condition ($\beta + \alpha$ microstructure) except the Ti-13V-11Cr-3Al which was Beta solution treated.

Figure 2 - Experimental setup for experimental verification of crack tip IR voltages using a model compact tension geometry. The simulated crack tip electrode is in the well along with a crack tip auxiliary sensing reference electrode. The crack tip is shorted to the shaded half compact tension specimen. The applied potential is controlled by the reference electrode in the external solution. The solution can access the crack tip through a 30 μm wide slot the length of a typical fatigue pre-crack.

Figure 3 - (a) Results from monotonically increasing CMOD test (5.9×10^{-5} mm/s) on a STA Ti-15 Mo-3Nb-3Al compact tension specimens exposed to 0.6 M NaCl at $E_{\text{app}} = -0.10V_{\text{SCE}}$. The plot of current shows the times at which current transients above threshold were detected (small vertical lines at bottom of plot). Current measurement using the 100 nA current measuring resistor was switched to the 1000 nA scale at 7800 s. K_{th} (42.8 MPa $\sqrt{\text{m}}$) and $\Delta a = 0$ were chosen as the point at which intergranular cracking initiated, determined from the load and DCPD data. Film rupture current transients precede crack initiation. (b) Experimental data before, during, and after interruption of a rising CMOD on an STA Ti-3Al-8V-6Cr-4Zr-4Mo alloy compact tension specimen exposed to 0.6 M NaCl at $E_{\text{app}} = -0.11 V_{\text{SCE}}$ prior to crack initiation. Film rupture transients are observed above the background noise limit of ± 10 nA.

Figure 4 - (a) Measured occluded cell pH in a Ti-15Mo-3Nb-3Al alloy crevice subjected to the various applied potentials. (b) variation of measured pH as a function of TiCl_3 concentration exposed to distilled deionized water in an inert atmosphere which minimizes oxidation of Ti^{3+} .

Figure 5 - Comparison of the bare metal surface polarization curve obtained from fractured titanium thin film testing with that observed from a surface containing the native oxide after slow polarization in 0.6 M NaCl. Note that the oxide film is chemically stable over the entire potential range shown in Figure 1. All data is corrected for ohmic voltage error.

Figure 6 - Plot of the anodic current and "simulated crack tip" working electrode potential as a function of applied potential from a model compact tension specimen test (top). The model crack tip solution resistance, $\Delta V/I$, was calculated using the difference between the true and applied potentials (bottom).

Figure 7 - Calculation of the true bare crack tip potential as a function of applied potential for different exposed bare areas. Bare surface areas are calculated using the compact tension sample thickness and various fractions of the CTOD. The total bare area used for calculation is shown in parentheses. The reversible potential for hydrogen production and the interfacial kinetic data utilized (Figure 5) are based on the results in a neutral pH solution³⁵. (a) 2200 ohm experimental crack solution resistance, (b) 4160 ohm theoretical resistance.

Figure 8 - Calculation of the relative hydrogen concentration at a distance of 48 μm below filmed and bare β -titanium surfaces exposed to 0.6 M NaCl as a function of time using the hydrogen production kinetics shown in Figure 5. Concentrations are calculated for two different applied potentials, $E_{\text{bare OCP}} (-1.58V_{\text{SCE}})$ and $E_{\text{HER}} (-0.655V_{\text{SCE}})$, which represent the upper and lower bounds at which proton/water reduction can occur during potentiostatic tests where $E_{\text{app}} > -1.58V_{\text{SCE}}$.

Figure 9 - Accumulated total hydrogen concentrations measured in STA Ti 15Mo-3Nb-3Al foils (thickness = 0.38 mm) following cathodic polarization to $-1V_{\text{SCE}}$ for 5 days. Solutions are 0.6 M NaCl (pH adjusted the indicated value with either HCl or NaOH), except 5 M HCl at a pH of -1.64 . The results imply that oxide films are not chemically destabilized except in 5 M HCl.

Figure 10 - Plot of bare metal open circuit potentials from fractured titanium thin film electrode tests as a function of bulk solution pH. The overpotential for hydrogen production from water discharge is the difference between the reversible potential for hydrogen production and the open circuit potential.

Figure 11 - Plot of cathodic reduction of water current density at the bare open circuit potential ($i_{\text{c, OCP}}$) and the normalized steady state sub-surface hydrogen concentration ($C_{\text{ss}}/C_{\text{ss, pH 14}}$) as a function of solution pH. $i_{\text{c, OCP}}$ was calculated from the intersection of the anodic and cathodic Tafel lines using the bare surface polarization curves³⁴. $C_{\text{ss}}/C_{\text{ss, pH 14}}$ data are determined for the coupled-discharge recombination mechanism using the Langmuir [$C_{\text{ss}} = f(i^{1/2})$], Temkin non-activated [$C_{\text{ss}} = f(I)$], and Temkin activated [$C_{\text{ss}} = f(i^2)$] adsorption isotherms.

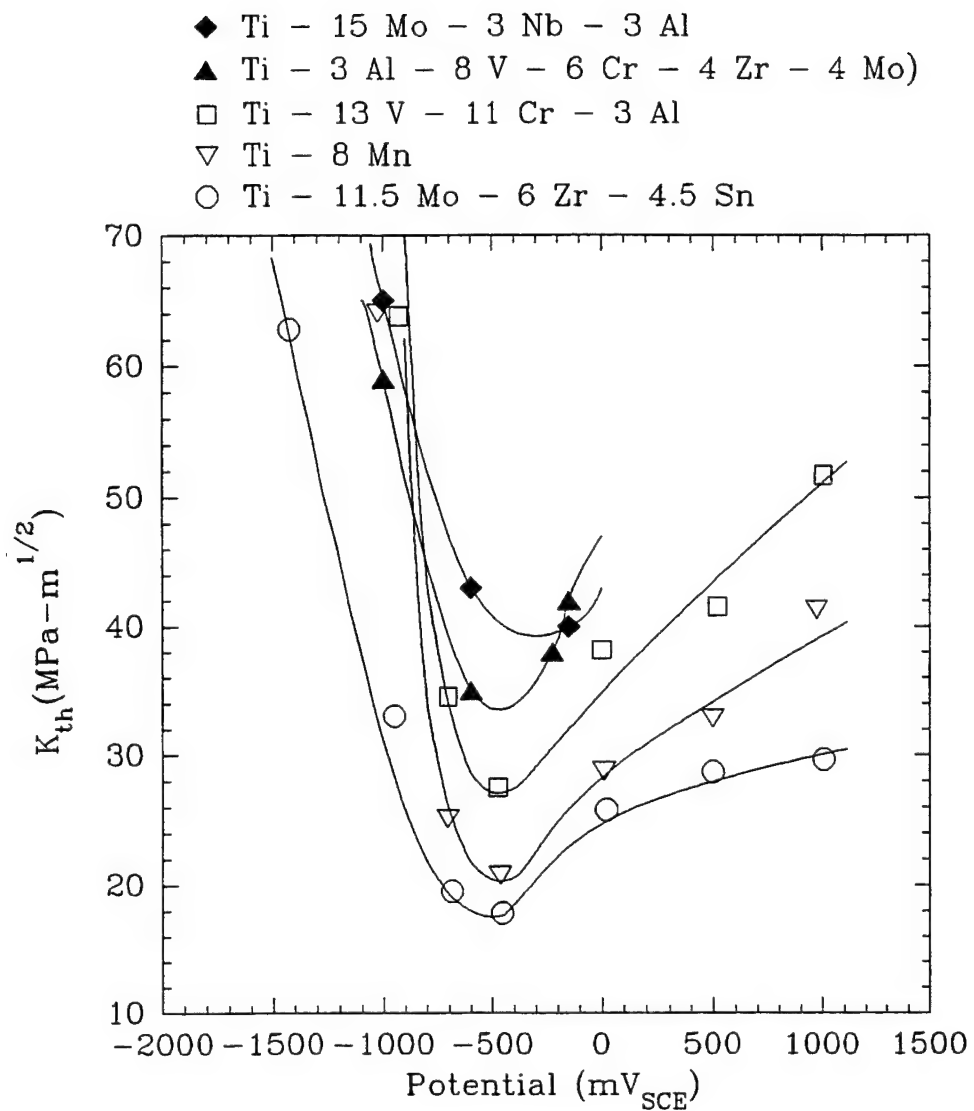


Figure 1 - Plot of threshold stress intensities for various precracked β -titanium alloys exposed to 0.6 M NaCl. All data are from reference 5 except Ti-15Mo-3Nb-3Al data (reference 1) and Ti-3Al-8V-6Cr-4Zr-4Mo data (reference 3). All alloys are in the STA condition ($\beta + \alpha$ microstructure) except the Ti-13V-11Cr-3Al which was Beta solution treated.

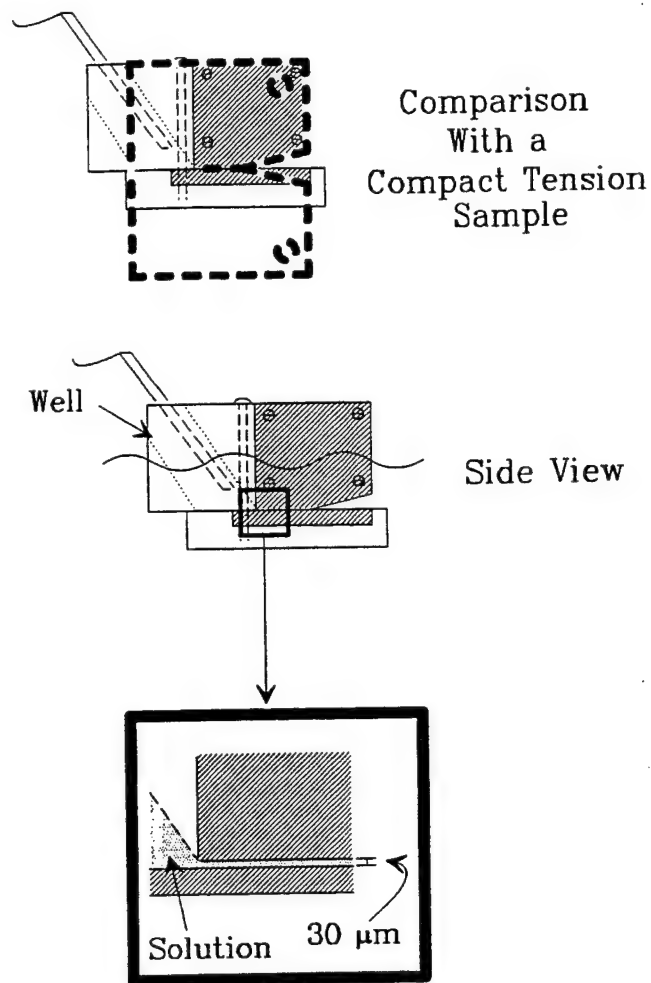


Figure 2 - Experimental setup for experimental verification of crack tip IR voltages using a model compact tension geometry. The simulated crack tip electrode is in the well along with a crack tip auxiliary sensing reference electrode. The crack tip is shorted to the shaded half compact tension specimen. The applied potential is controlled by the reference electrode in the external solution. The solution can access the crack tip through a 30 μm wide slot the length of a typical fatigue pre-crack.

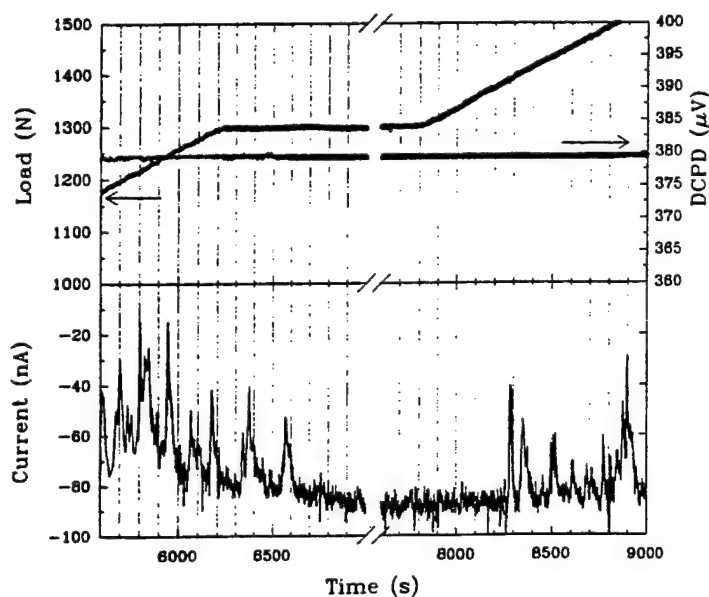
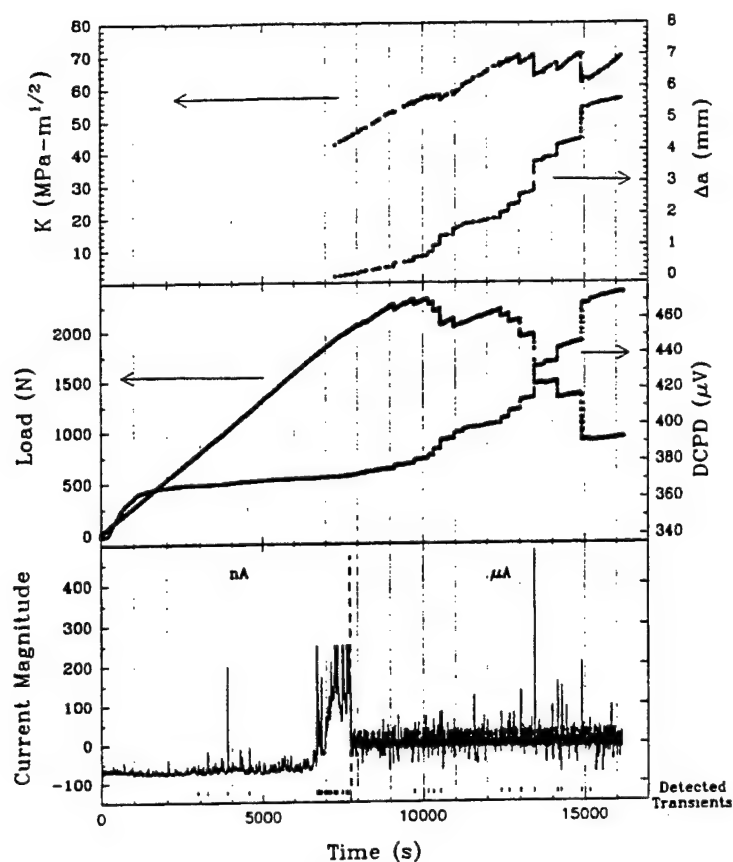


Figure 3 - (a) Results from monotonically increasing CMOD test (5.9×10^{-5} mm/s) on a STA Ti-15 Mo-3Nb-3Al compact tension specimens exposed to 0.6 M NaCl at $E_{app} = -0.10V_{SCE}$. The plot of current shows the times at which current transients above threshold were detected (small vertical lines at bottom of plot). Current measurement using the 100 nA current measuring resistor was switched to the 1000 nA scale at 7800 s. K_{th} (42.8 MPa/m) and $\Delta a = 0$ were chosen as the point at which intergranular cracking initiated, determined from the load and DCPD data. Film rupture current transients precede crack initiation. **(b)** Experimental data before, during, and after interruption of a rising CMOD on an STA Ti-3Al-8V-6Cr-4Zr-4Mo alloy compact tension specimen exposed to 0.6 M NaCl at $E_{app} = -0.11 V_{SCE}$ prior to crack initiation. Film rupture transients are observed above the background noise limit of ± 10 nA.

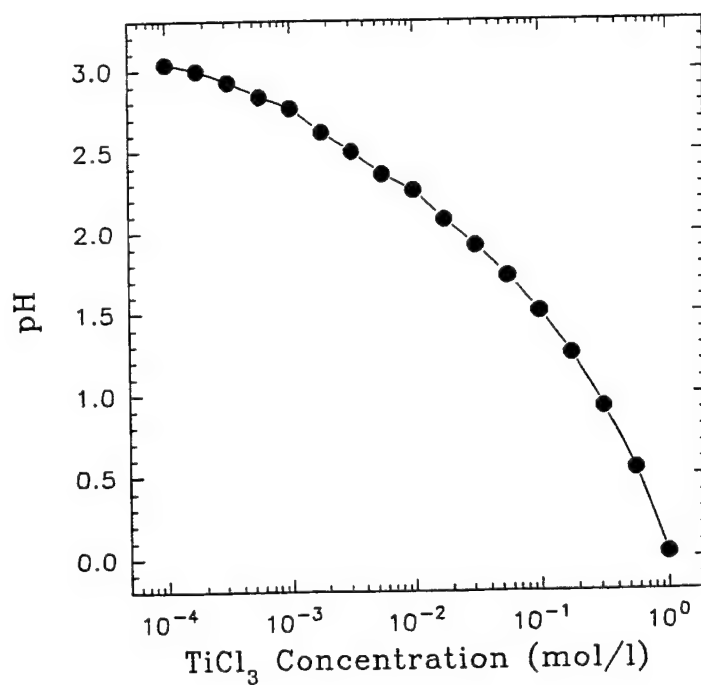
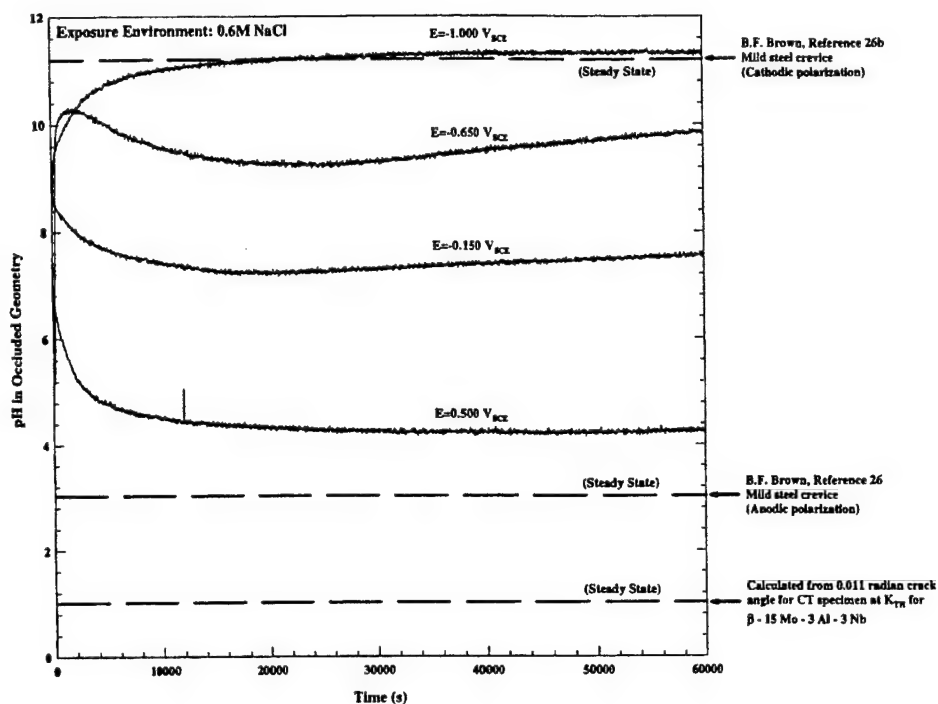


Figure 4 - (a) Measured occluded cell pH in a Ti-15Mo-3Nb-3Al alloy crevice subjected to the various applied potentials. **(b)** variation of measured pH as a function of $TiCl_3$ concentration exposed to distilled deionized water in an inert atmosphere which minimizes oxidation of Ti^{3+} .

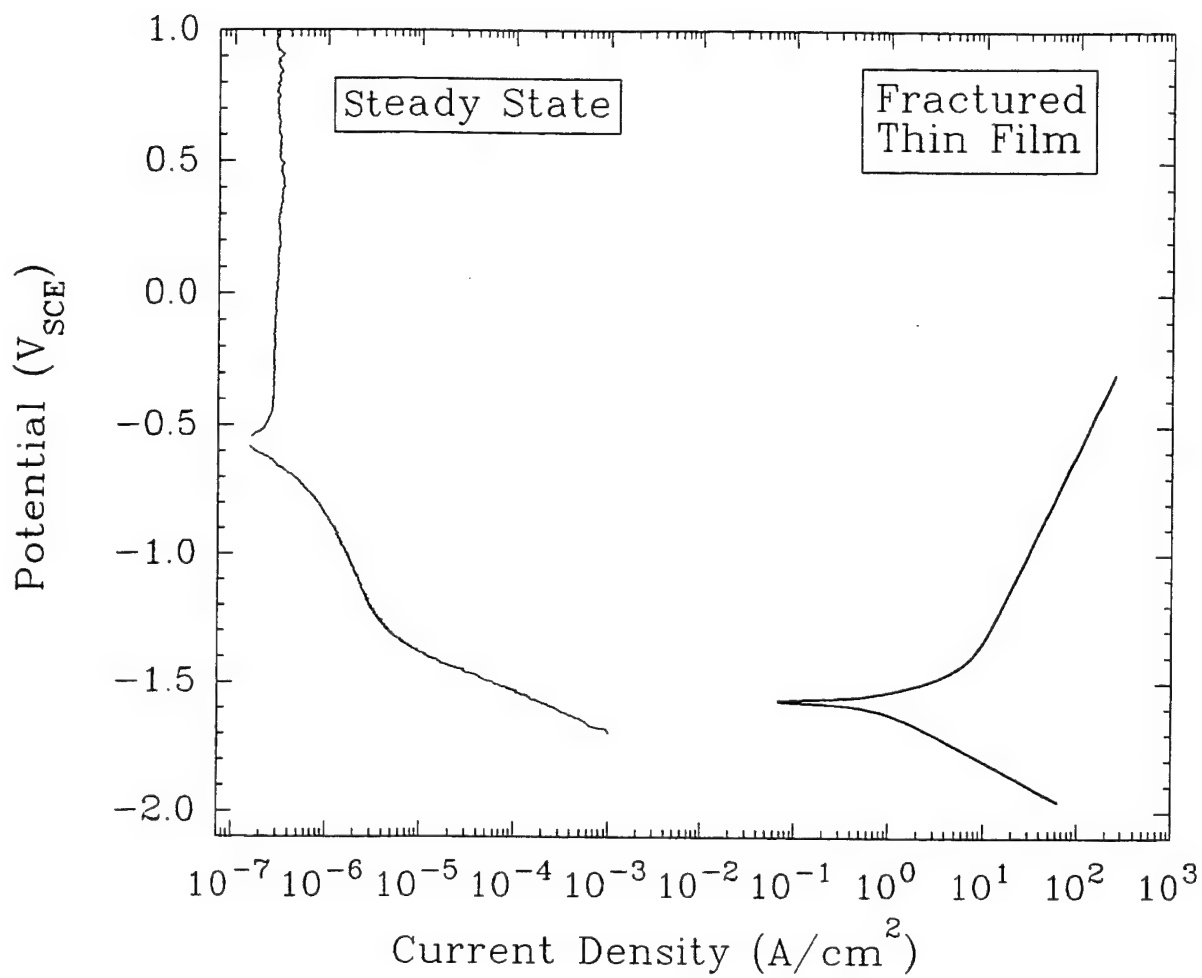


Figure 5 - Comparison of the bare metal surface polarization curve obtained from fractured titanium thin film testing with that observed from a surface containing the native oxide after slow polarization in 0.6 M NaCl. Note that the oxide film is chemically stable over the entire potential range shown in Figure 1. All data is corrected for ohmic voltages.

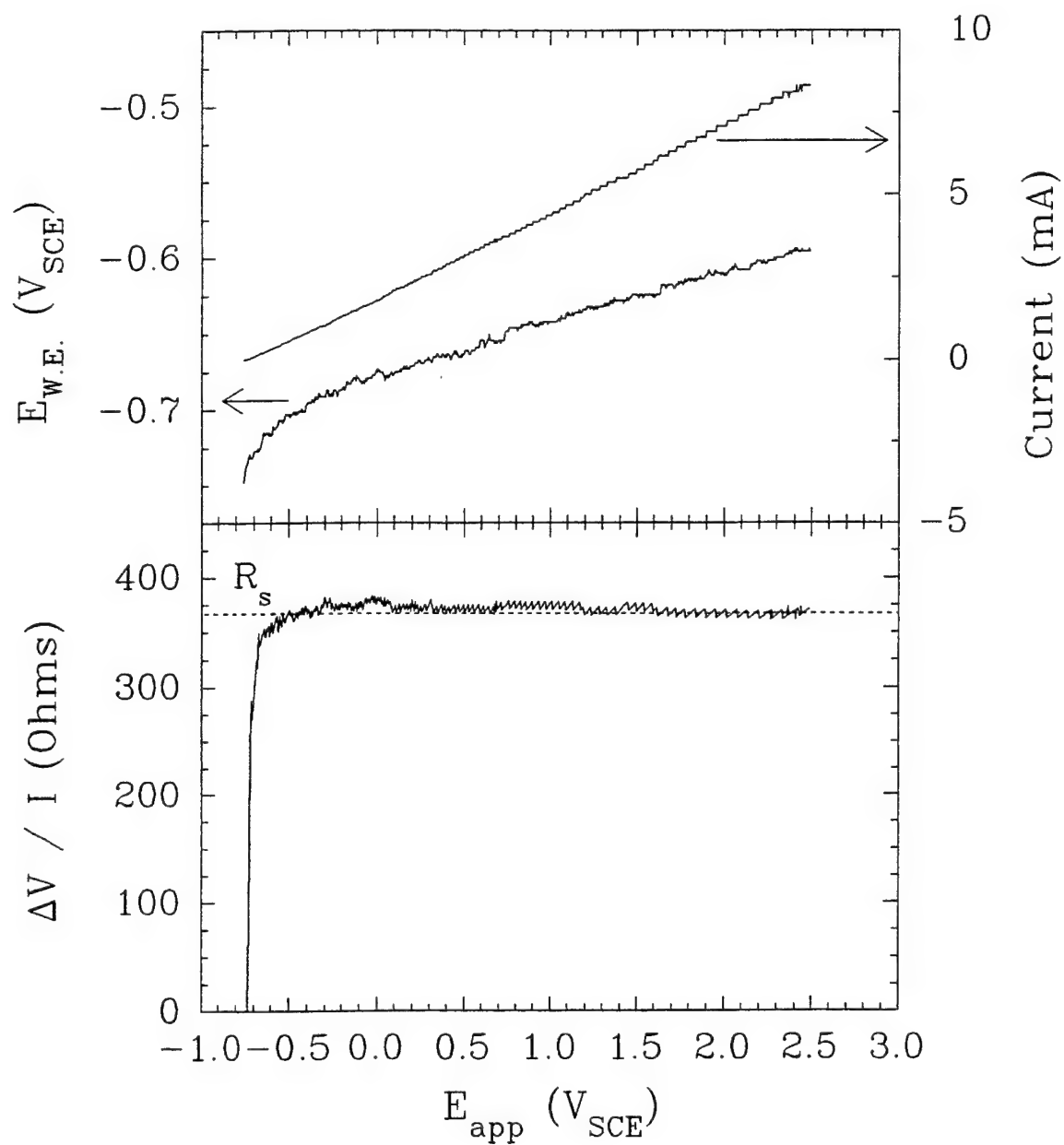


Figure 6 - Plot of the anodic current and "simulated crack tip" working electrode potential as a function of applied potential from a model compact tension specimen test (top). The model crack tip solution resistance, $\Delta V/I$, was calculated using the difference between the true and applied potentials (bottom).

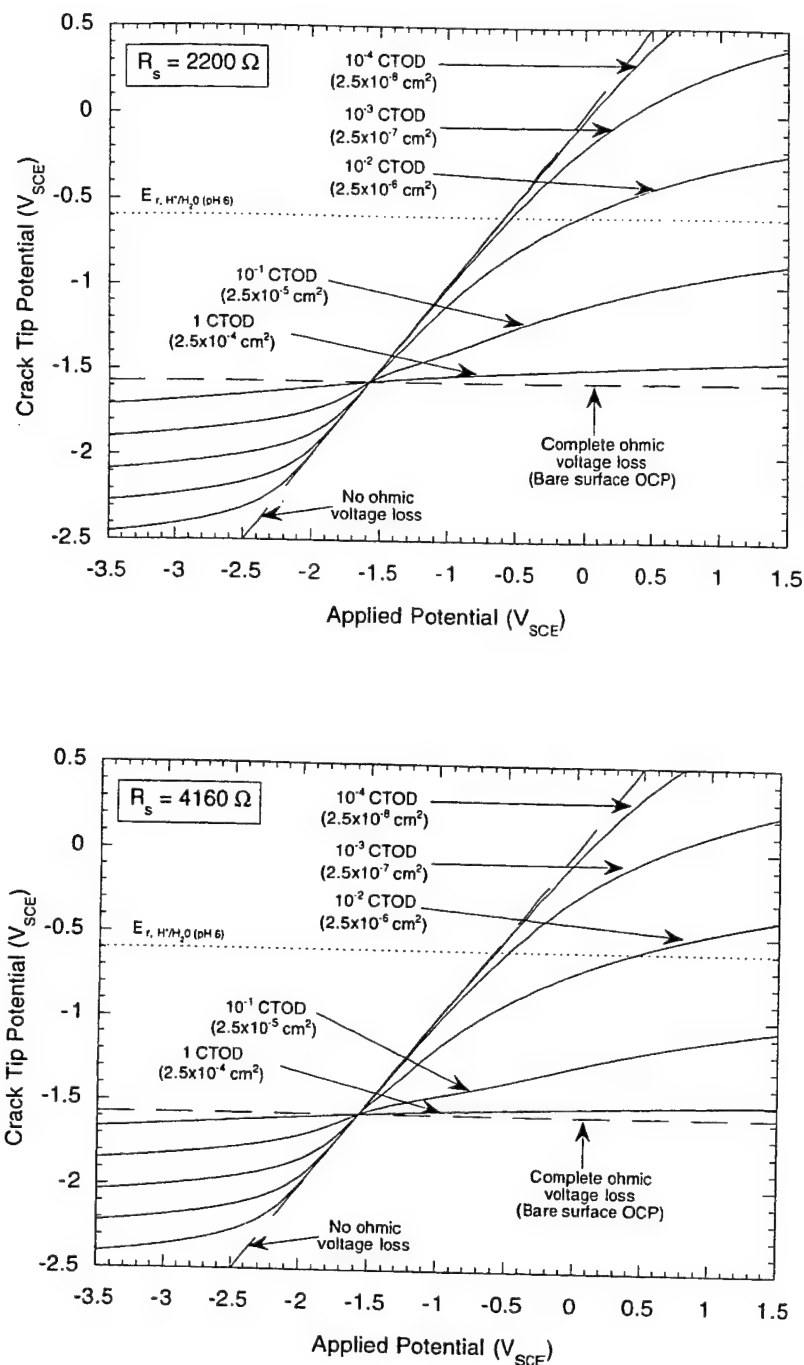


Figure 7 - Calculation of the true bare crack tip potential as a function of applied potential for different exposed bare areas. Bare surface areas are calculated using the compact tension sample thickness and various fractions of the CTOD. The total bare area used for calculation is shown in parentheses. The reversible potential for hydrogen production and the interfacial kinetic data utilized (Figure 5) are based on the results in a neutral pH solution³⁵. (a) 2200 ohm experimental crack solution resistance, (b) 4160 ohm theoretical resistance.

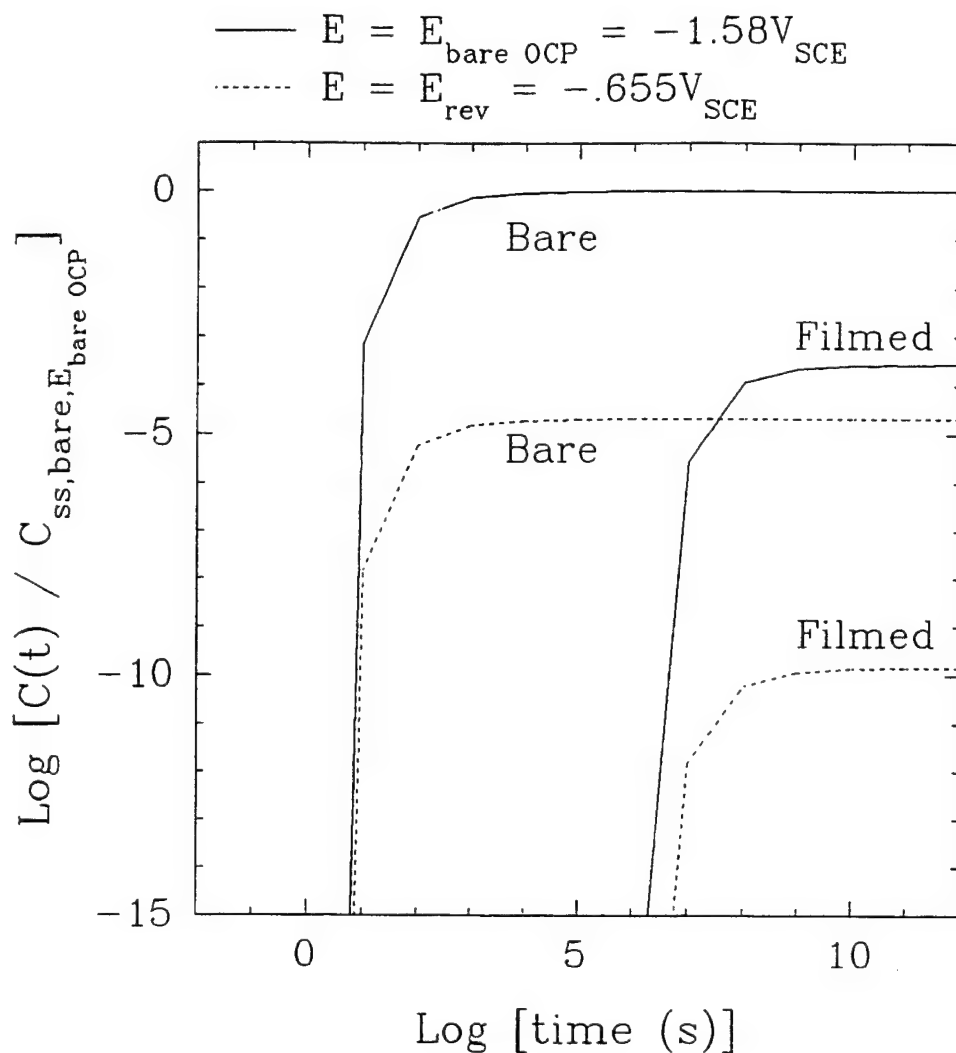


Figure 8 - Calculation of the relative hydrogen concentration at a distance of $48 \mu\text{m}$ below filmed and bare β -titanium surfaces exposed to 0.6 M NaCl as a function of time using the hydrogen production kinetics shown in Figure 5. Concentrations are calculated for two different applied potentials, $E_{\text{bare OCP}} (-1.58V_{\text{SCE}})$ and $E_{\text{HER}} (-0.655V_{\text{SCE}})$, which represent the upper and lower bounds at which proton/water reduction can occur during potentiostatic tests where $E_{\text{app}} > -1.58V_{\text{SCE}}$

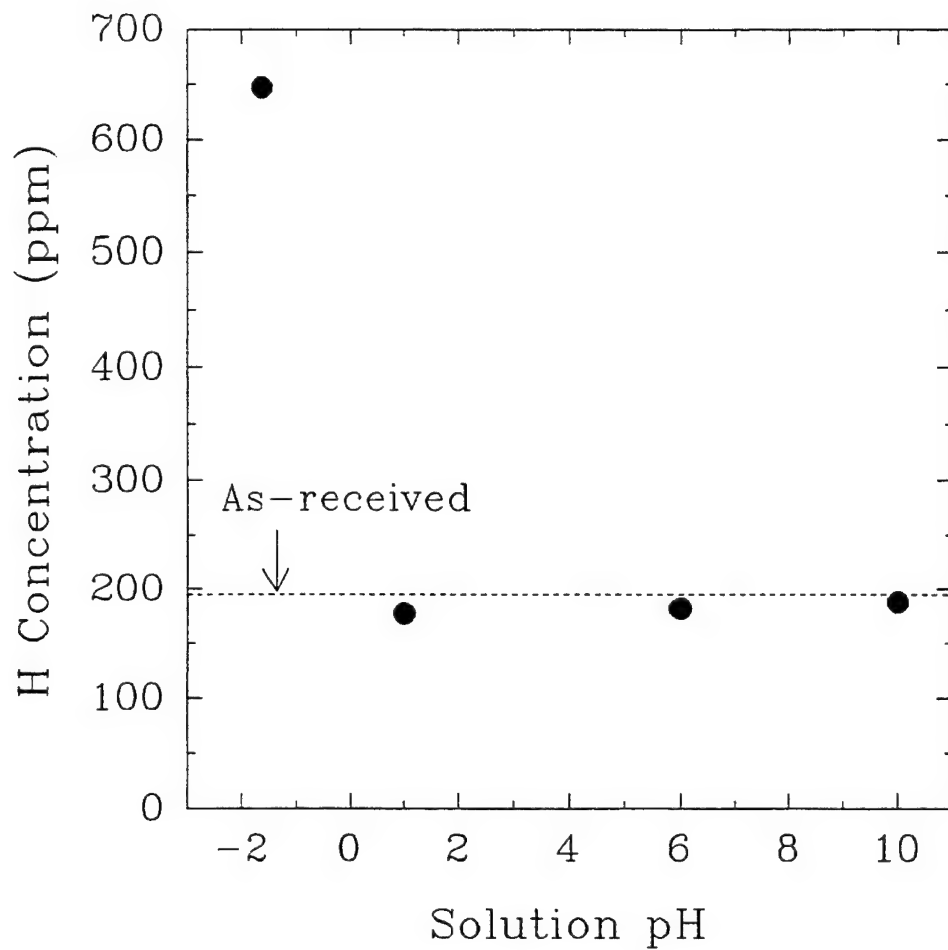


Figure 9 - Accumulated total hydrogen concentrations measured in STA Ti 15Mo-3Nb-3Al foils (thickness = 0.38 mm) following cathodic polarization to $-1V_{SCE}$ for 5 days. Solutions are 0.6 M NaCl (pH adjusted the indicated value with either HCl or NaOH), except 5 M HCl at a pH of -1.64. The results imply that oxide films are not chemically destabilized except in 5 M HCl.

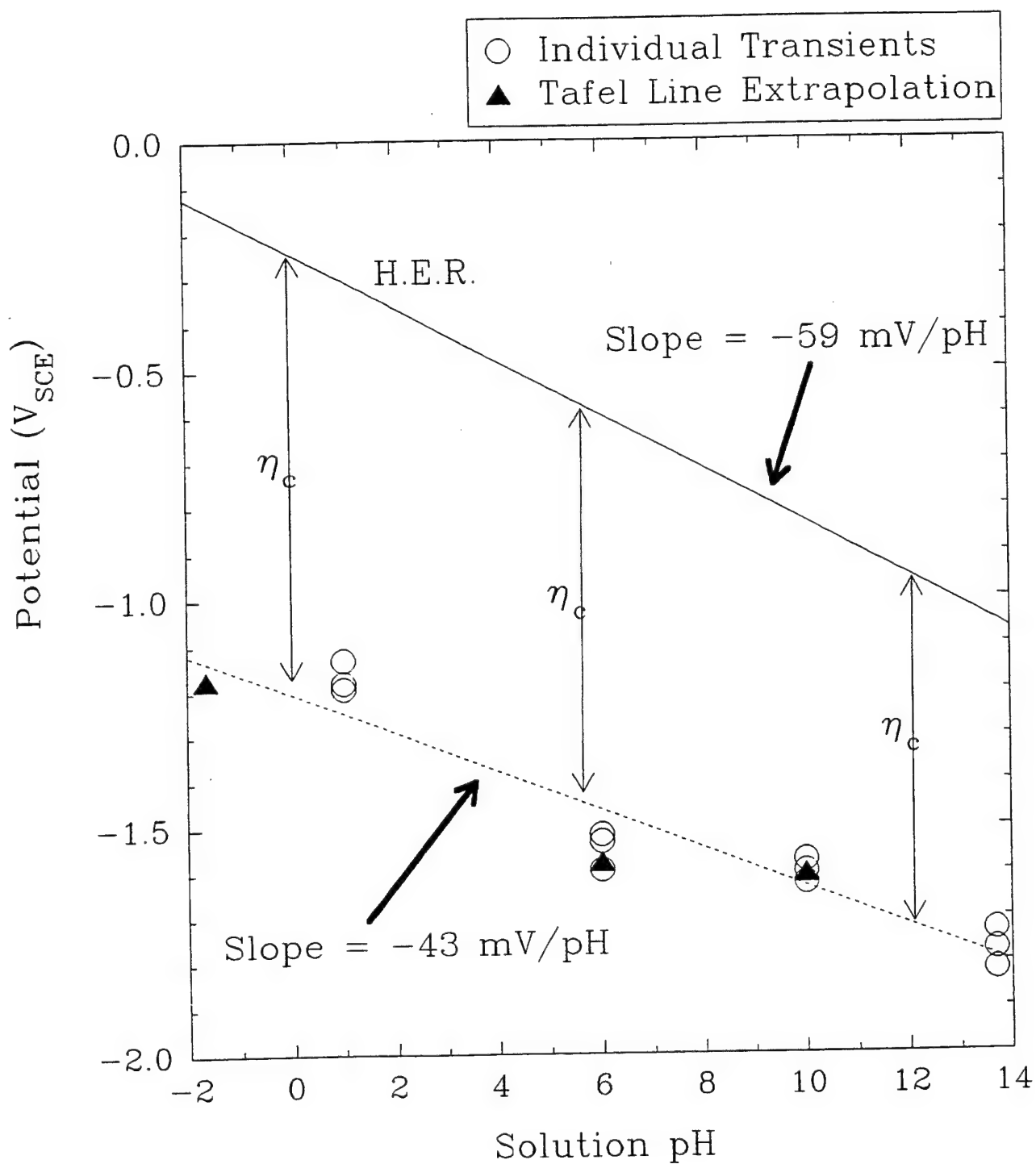


Figure 10 - Plot of bare metal open circuit potentials from fractured titanium thin film electrode tests as a function of bulk solution pH. The overpotential for hydrogen production from water discharge is the difference between the reversible potential for hydrogen production and the open circuit potential.

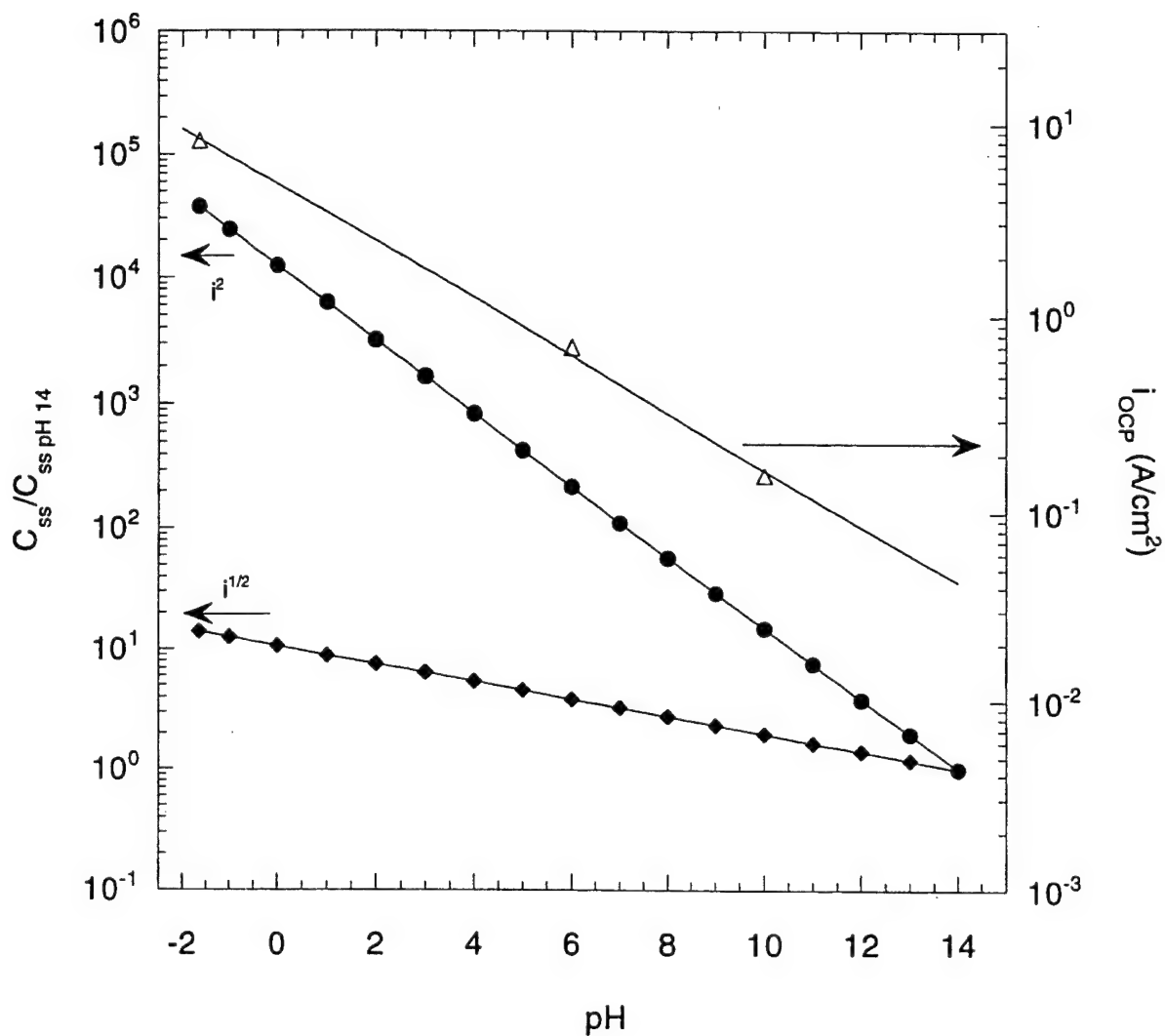


Figure 11 - Plot of cathodic reduction of water current density at the bare open circuit potential (i_{ocp}) and the normalized steady state sub-surface hydrogen concentration ($C_{ss}/C_{ss, pH 14}$) as a function of solution pH. i_{ocp} was calculated from the intersection of the anodic and cathodic Tafel lines using the bare surface polarization curves³⁴. $C_{ss}/C_{ss, pH 14}$ data are determined for the coupled-discharge recombination mechanism using the Langmuir [$C_{ss} = f(i^{1/2})$], Temkin non-activated [$C_{ss} = f(I)$], and Temkin activated [$C_{ss} = f(i^2)$] adsorption isotherms.

**On the Repassivation Behavior of High-Purity Titanium and Selected α ,
 β and $\beta + \alpha$ Titanium Alloys in Aqueous Chloride Solutions**

D. G. Kolman and J. R. Scully



On the Repassivation Behavior of High-Purity Titanium and Selected α , β , and $\beta + \alpha$ Titanium Alloys in Aqueous Chloride Solutions

D. G. Kolman^{*a} and J. R. Scully^{*}

Center for Electrochemical Science and Engineering, Department of Materials Science and Engineering,
University of Virginia, Charlottesville, Virginia 22903-2442, USA

ABSTRACT

The repassivation characteristics of a titanium thin film evaporated from a high-purity Ti source as well as selected α (commercially pure Ti, Ti-5Al-2.5Sn), β , and $\beta + \alpha$ titanium alloys (Ti-15Mo-3Nb-3Al, Ti-15V-3Cr-3Al-3Sn, and Ti-3Al-8V-6Cr-4Zr-4Mo) were examined. Both the rapid thin film fracture and scratch depassivation methods were used in aqueous chloride solutions (0.6 M NaCl, 5 M HCl, 5 M LiCl, 5 M HCl + 1 M TiCl₃). Bare surface open-circuit potentials followed the relationship $E(V_{SCE}) = -1.20$ (pH = 0) - 0.043 pH based on the mixed potential established between the anodic Ti/Ti³⁺, Ti/TiO₂, and water or H⁺ reduction reactions. Oxide formation after depassivation was of low overall current efficiency on all titanium materials; a large percentage of the anodic charge following depassivation contributed to dissolution. Consequently, an empirical expression was used to describe the anodic current density decay during repassivation; $i = i_0(t/t_0)^{-m}$. Potentiostatic current transients on rapidly fractured thin film Ti produced plateau bare-metal i_0 values greater than 100 A/cm² which were below the theoretical ohmic limit, $m = 1.0$ to 1.4 depending on solution and potential and t_0 values from 20 to 30 μ s. Two anodic Tafel regions and a single cathodic region best described IR-corrected $E - \log i$ relationships for bare Ti in all electrolytes. LiCl and TiCl₃ inhibited bare surface dissolution but slightly delayed current density decay. Minimal differences between any of the repassivation parameters utilized were observed for selected α , β , and $\beta + \alpha$ titanium alloys. The similarity was attributed to dominance of Ti³⁺ production in the total anodic charge during repassivation and predominantly TiO₂ formation in the passivating oxides of all alloys.

Introduction

Environmentally assisted cracking (EAC) of metastable β -titanium alloys has been observed in aqueous chloride environments.¹⁻³ The mechanism by which cracks initiate and propagate is unknown. Mechanical tests on hydrogen-precharged, air-tested, metastable β -titanium (bcc) alloys have suggested that some hydrogen mechanism is responsible for cracking in chloride environments.⁴ Conversely, research on many other alloys susceptible to EAC, such as aluminum alloys, has suggested that a dissolution mechanism is responsible for EAC in chloride environments.⁵ Previous research in this laboratory has shown that film rupture is required to explain EAC in β -titanium alloys, regardless of the exact mechanism.^{6,7} In order to fully evaluate cracking in titanium alloys, whether by a dissolution mechanism, a hydrogen mechanism, or any other

EAC mechanism, the bare surface electrode kinetics must be evaluated.

Other researchers have attempted to evaluate the bare surface kinetics on commercially pure titanium⁸⁻¹⁴ with limited success, due to a variety of limitations of the potentiostatic test techniques. These limitations have been thoroughly discussed by the authors elsewhere.¹⁵ Bare surface polarization curves on α -titanium (hcp) alloys have been generated by previous researchers^{8,14} utilizing Ti-8Al-1Mo-1V (Ti-8-1-1) fractured rods exposed to 12 M HCl. However, these tests were ohmically limited, and the fracture speed was relatively slow (approximately 1 ms).^{9,14} The effects of alloy composition, cation, solution pH, and TiCl₃ were also examined.¹⁴ It was generally found that alloy composition, bulk solution pH, and cation type had little effect on repassivation behavior. It is unclear, however, whether real differences would be revealed if shorter times could be accessed. The true bare surface kinetics on titanium alloys are unknown. Although previous research has examined repassivation behavior of titanium, the data

^{*} Electrochemical Society Active Member.

^a Los Alamos National Laboratories, Los Alamos, NM 87545.

are limited by relatively slow depassivation rate and ohmic drop in solution.^{12,14,16} Recently, other researchers have examined the bare surface kinetics on aluminum^{17,18} and niobium¹⁹ utilizing thin films deposited on insulating brittle substrates, which are fractured. The fracture and resulting current transient spike occur over approximately 1 to 2 μ s, reducing depassivation rate effects.¹⁵ The small amount of bared area reduces the total current and allows a much higher current density to be observed before the ohmic limit is reached. Moreover, the smaller bared area may more accurately simulate the amount of area exposed at a crack tip following film rupture. Therefore, in an effort to better understand the role of crack tip electrode kinetics in EAC of β -titanium alloys, one goal of this research is to examine the bare electrode kinetics on titanium exposed to aqueous chloride solutions through the utilization of fractured titanium thin films. The effects of applied potential on parameters such as bare surface peak current densities, repassivation charge densities, and other repassivation parameters were examined in chloride solutions of differing pH.

EAC has been observed for modern STA (solution heat-treated plus aged) β -titanium alloys exposed to chloride solutions but not for the ST (solution heat-treated) versions of these alloys.¹⁻³ Also, planar slip has been correlated with the EAC susceptibility of STA alloys.¹⁻⁴ The Ti-15Mo-3Nb-3Al alloy examined here exhibited planar slip while Ti-15V-3Cr-3Al-3Sn did not.⁴ Thus, it is important to examine the repassivation behavior of the STA ($\beta + \alpha$) and ST (β) microstructures of β -titanium alloys separately to discern any differences in their electrochemical behaviors following film rupture that may account for the observed difference in EAC susceptibility. Further, it is of interest to compare the behaviors of the distinct α and β phases in the STA variants of the β alloys to gain insight into the individual components that form the susceptible STA material.

Limited repassivation data exist for β -titanium alloys. Unfortunately, the fractured thin film method cannot readily be used with engineering alloys, due to the difficulty in producing thin films with the identical composition and structure as a bulk multiphase alloy. Thus, a different method must be used to compare the repassivation properties of β -titanium alloys. The manual scratch repassivation test was chosen to compare the repassivation behavior of the alloys of interest. The limitations of this method have been previously discussed by the authors.¹⁵ Although the scratch method is imperfect due to the relatively slow depassivation speed (1 ms) and relatively large scratch area, it may be used qualitatively to discern differences between alloys. If differences between alloys are not observed during scratch testing, it can only be stated that there are no differences between the alloys within the limitations of the test method. The scratch repassivation behaviors of six different alloys were examined: STA and ST Ti-15V-3Cr-3Al-3Sn, STA and ST Ti-15Mo-3Nb-3Al, grade 6 Ti (which simulates α precipitates in the β matrices),⁷ and grade 2 Ti (commercially pure).

Experimental

Experimental procedure for manual scratch testing was optimized to minimize shortcomings.²⁰ Manual scratch testing comprised a variety of α , β , and $\beta + \alpha$ titanium alloys imbedded in epoxy and mounted on edge so that 0.09×0.6 cm was exposed to solution. The small width of the sample (0.09 cm) helped to reduce depassivation speed effects. Electrical connection was made through the back of the sample, opposite the side exposed to solution. The sample was coated with a thin layer of vacuum grease to prevent capacitive current contributions from oxide adjacent to the scratch.²⁰ Capacitive current contributions from the surrounding oxide has been shown to alter the current response during potentiostatic testing when potentiostatic control of the surface is not maintained.²⁰ A diamond-tipped glass marker was utilized to scratch through both the vacuum grease and underlying titanium

across the 0.09 cm width. Samples were examined with an optical microscope to ensure that no vacuum grease contaminated the scratched region. A Mitutoyo SurfTest 401 surface profilometer was utilized to determine the scratch area. The amount of area bared (54.7μ m wide \times 0.09 cm scratch length) was obtained by the averaging of many separate scratch tests.¹⁵ A small scratch length was used to minimize depassivation rate effects.^{15,21}

Thin film fracture samples comprised a 500 nm thick titanium layer evaporated from a 99.999% titanium source (at 1.8×10^{-7} Torr) onto a glass substrate. A 200 nm thick layer of insulating SiO_2 was sputtered on top of the titanium to prevent capacitive charging^{18,20} of the freshly bared surface by its surrounding oxide. A supplemental layer of GLPT insulating varnish was used to ensure insulation of the Ti layer from solution for all open-circuit potential tests, the open-circuit potential being very sensitive to even the smallest of pinholes in the SiO_2 . The samples were 1 cm in width, yielding an exposed net-section area of 5×10^{-5} cm² upon fracture. Surface roughness of the film was not measured. The film appeared to maintain cohesion with the substrate after fracture, as observed in scanning electron microscopy (SEM). The samples were scored on the glass side of the sample and mounted in the thin film fracture cell.¹⁵ The samples were fractured by impressing a rotationally mounted acrylic breaker onto the bottom of the sample.¹⁵ This method was found to be more satisfactory than guillotining the sample, resulting in far less cell vibration and solution perturbation. Assuming the thin film breaks in a brittle fashion with the crack propagating perpendicular to the thickness of the film, the 500 nm thick layer should be depassivated in 1.6 ns.

Both scratch testing and thin film experiments incorporated a saturated calomel reference electrode (SCE) and a platinized niobium mesh counterelectrode. The reference electrode was placed approximately 50 mm away from the newly exposed metal to allow calculation of the solution resistance, satisfying the condition of being infinitely far from the exposed area.²¹

Samples were held potentiostatically with an EG&G Princeton Applied Research (EG&G PAR) 273 potentiostat. Surface potential and repassivation current were measured with either a Hewlett Packard 54600A or 54601B digital oscilloscope (thin film experiments, 500 ns/data pt), and/or 7090A measurement plotting system (thin film and scratch tests, 100 μ s/data pt). The potential and current signals were sampled through their respective analog outputs on the potentiostat.

Potentiostat and reference electrode response have been addressed earlier.¹⁵ In summary, it was found that the response time of the EG&G PAR 273 potentiostat was approximately 5 μ s. The deviation of the true potential from the applied potential due to finite potentiostat rise time was found to be far less than that due to ohmic loss in solution. Additionally, the reference electrode imposed no additional limitation on testing beyond that of the potentiostat. Additional tests beyond those discussed in Ref. 15 have been performed. Potentiostatic fractured thin film experiments were performed with an EG&G PAR 283 potentiostat (rise time \sim 500 ns). No difference was discernible between the current transients obtained with either the EG&G PAR 273 or 283. Thus, the potentiostat rise time does not appear to limit the peak current density as was hypothesized in Ref. 15. Moreover, additional calculations not included in Ref. 15 indicate that double-layer charging contributions are small as determined by current density ($i_{\text{max}} = 2$ A/cm² assuming complete double-layer charging in 10 μ s) or charge ($<0.1\%$ of charge).

Electrochemical impedance spectroscopy (EIS) measurements were performed with a Solartron 1286 electrochemical interface and 1255 frequency response analyzer to determine solution resistance. Solution pH was measured with a Corning 350 pH analyzer.

Solutions of 0.6 M NaCl [$\kappa = 0.0521$ (Ω -cm)⁻¹] and 5 M LiCl [$\kappa = 0.162$ (Ω -cm)⁻¹] incorporated reagent-grade NaCl and LiCl, respectively, added to distilled, deionized,

18 M Ω water. Other 0.6 M NaCl solutions [$\kappa = 0.0521$ ($\Omega\text{-cm}$)⁻¹] were adjusted to alkaline pH values with reagent-grade NaOH or to acidic pH values with reagent-grade HCl. 5 M HCl solutions [$\kappa = 0.602$ ($\Omega\text{-cm}$)⁻¹, calculated pH -1.64²²] incorporated reagent-grade HCl added to distilled, deionized, 18 M Ω water. TiCl₃ was added to the 5 M HCl in powder form in an inert, dry atmosphere. The conductivity of 5 M HCl + 1 M TiCl₃ was found to be approximately equal to that of 5 M HCl.

The physical metallurgy of the metastable β -titanium alloys, Ti-15Mo-3Nb-3Al (Ti-14.9Mo-2.64Nb-3.15Al, weight percent (w/o)), and Ti-15V-3Cr-3Al-3Sn (Ti-15.0V-2.99Cr-3.14Al-2.81Sn, w/o), have been discussed elsewhere.^{4,6,7} Ti-15Mo-3Nb-3Al was solution heat-treated (ST) for 8 h at 871°C (1600°F) followed by an air cool. Ti-15V-3Cr-3Al-3Sn was solution heat-treated for 30 min at 816°C (1500°F) followed by an air cool. Peak aging for both alloys comprised a subsequent single-step heat-treatment at 538°C (1000°F) for 8 h followed by an air cool. The presence of a $\beta + \alpha$ microstructure, and the absence of other phases, was confirmed by both x-ray diffraction (XRD) experiments, transmission electron microscopy (TEM)/selected area diffraction, and optical microscopy on the STA β alloys.¹ Limited testing was also performed on STA β -C (Ti-3.4Al-8.3V-5.9Cr-4.4Zr-4.1Mo, w/o). β -C was solutionized at 815°C for 1 h followed by an air cool. The material was aged at 500°C for 24 h followed by air cooling. Scratch tests on grade 6 Ti were performed to examine the repassivation behavior of precipitates in β -titanium alloys. The composition of grade 6 Ti (Ti-5.2Al-2.3Sn) roughly approximates that of precipitates within STA β -titanium alloys.⁷

Potential-current plots were corrected for ohmic loss in solution except for plots where "applied potential" is noted. Metal cation concentrations were assumed to be 10^{-6} M for all reversible potential calculations.

Results and Discussion

Bare Surface Open-Circuit Potential Measurements

Figure 1 shows the bare surface open-circuit potentials (OCP) obtained from fractured titanium thin films exposed to 0.6 M NaCl solutions of various pH, from pH 1 to pH 13.7. Three individual OCP measurements were obtained in each solution. The bare open-circuit potential was taken as the most negative potential in the OCP transients. Additionally, the intersections of the anodic and cathodic Tafel lines obtained by fitting of the bare surface polarization curves at various pH (discussed later) are also plotted in Fig. 1. In contrast, filmed steady-state OCP range from -0.2 to -0.7 V_{SEC} in deaerated 5 M HCl and near-neutral 0.6 M NaCl solutions.^{6,7} Linear regression of the data in Fig. 1 indicates that the bare surface OCP decreases 43 mV/pH unit [E_{OCP} (V_{SCE}) = -1.20 (pH 0) - 0.043 pH], a slope shallower than that proposed by Beck.^{14,23} The linear correlation coefficient for the regression is 0.92, and there is greater than 95% confidence that the magnitude of the slope is less than 50 mV. Good agreement is observed between the individual transients and the values obtained from fitting of the polarization curves.

Beck attempted to determine the dependence of bare surface OCP on pH.^{14,23} The depassivation time for these experiments was approximately 1 ms. However, it has been shown that a 1 ms depassivation time alters the apparent bare OCP from the true bare surface OCP.¹⁵ Further, almost all of the tests were performed over a relatively narrow band of pH in concentrated acid, complicating slope determination. Moreover, the activity coefficient of H⁺ was assumed to be 1 (i.e., the activity was assumed to be equal to the concentration), which is erroneous in concentrated acid solutions.²² Thus, the -59 mV/pH result appears to be an overestimate.

The bare surface OCP data shown in Fig. 1 are superimposed on the equilibrium potential-pH diagram using the thermodynamic data compiled by Silverman.²⁴ Oxidation of titanium to Ti³⁺ is thermodynamically possible over the

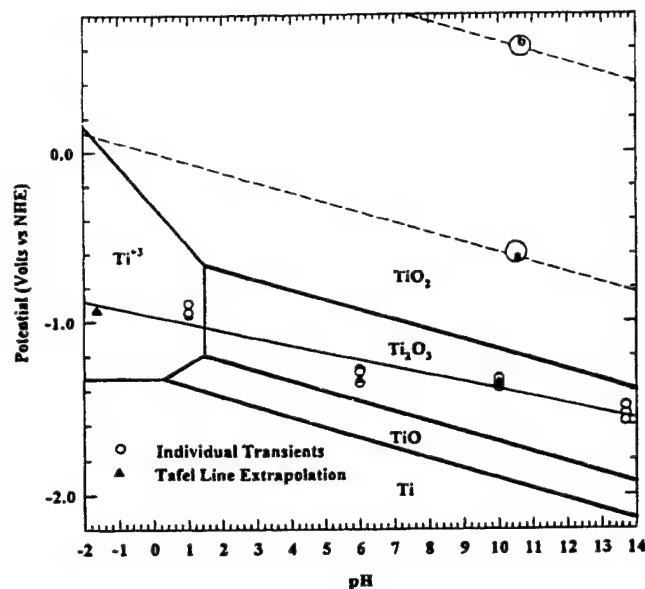


Fig. 1. Bare surface OCP as a function of pH superimposed on the equilibrium potential-pH diagram for titanium considering stability and solubility of anhydrous Ti substances.²⁴ The open circles are mixed potential minima observed from individual fractured titanium thin film experiments. The filled triangles represent the OCP as determined by extrapolation of anodic and cathodic lines from the bare surface polarization curves. Calculations of equilibrium potential-pH boundary lines assume that all metal cation concentrations equal 10^{-6} M. Lines a and b delineate the stable region for water. Limits of the domains of predominance of all dissolved Ti substances are not shown.

observed OCP-pH range. Reduction of water is also thermodynamically possible at these bare metal OCP values. Therefore, Fig. 1 illustrates that the OCP values on bare Ti are mixed potentials established between Ti oxidation and the reduction of water, or hydrogen ions. As such, the slope of -43 mV/pH obtained here is a result of several kinetic and thermodynamic factors changing with pH. If the OCP is a mixed potential that depends on all of the kinetic factors associated with both the anodic and cathodic reactions, as well as their reversible electrode potentials, then a slope of exactly 59 mV/pH unit²³ would not be expected.

Disagreement exists over the details of the electromotive force (EMF)-pH relationships for the Ti-H₂O system.²⁴⁻²⁷ Silverman found no evidence for presence of Ti²⁺ ions.²⁴ Olver and Ross^{24b} utilized kinetic and thermodynamic evidence to deduce that the Ti²⁺/Ti³⁺ equilibrium potential is approximately -2.54 V_{SEC} rather than -0.61 V_{SEC} used by Pourbaix.^{25,26} Beck argued that the standard equilibrium potential for direct Ti oxidation to Ti³⁺ is -1.451 V_{SEC} and that freshly generated bare Ti may oxidize to TiO₂ at -1.221 V_{SEC} - 0.059 pH.²⁷ It has also been argued that TiH₂ should form spontaneously upon scratching²⁷ and that bare titanium is never a thermodynamically favorable surface state at any potential.²⁶

Bare Surface Current Density Measurements

Effect of applied potential.—An individual potentiostatic current transient observed during the fracture of a titanium thin film exposed to 0.6 M NaCl ($E_{\text{applied}} = 0$ V_{SCE}) is seen in Fig. 2. A peak current of 8.75 mA was recorded. This corresponds to a current density of 175 A/cm². Comparable current densities have been observed on fractured aluminum^{17,18} and niobium¹⁹ thin films. The anodic bare surface current density is approximately eight orders of magnitude larger than that seen at similar potentials at steady state.^{6,7} Also, the measured anodic current density is approximately 100 to 1000 times larger than that observed from tests which utilized different depassivation methods.^{8,10-12} In contrast to previous repassivation meth-

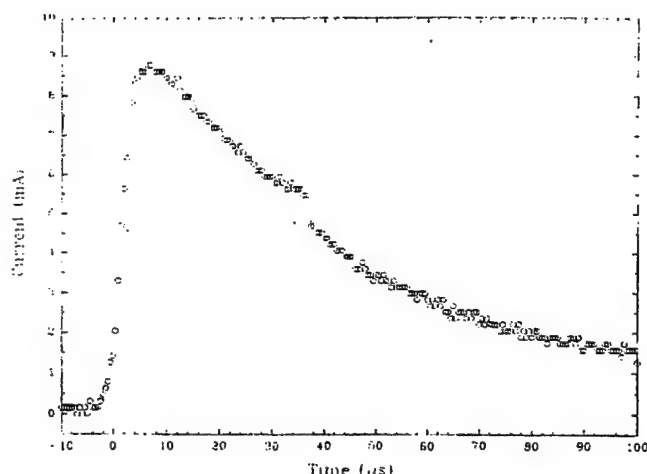


Fig. 2. Measured current repassivation transient for a fractured titanium thin film electrode exposed to 0.6 M NaCl at $E_{app} = 0 V_{SCE}$.

ods, fractured thin films yield peak current densities that are neither limited by voltage drop in solution^a nor by depassivation speed.¹⁵ (The theoretical ohmic limit for the experiment of Fig. 2 is 23 mA.) Thus, fractured thin film data appear to be a more accurate characterization of the bare surface dissolution plateau for titanium.

Current transients at selected applied potentials are plotted in Fig. 3 on a $\log i - \log t$ scale. The current transient of Fig. 2 is the 0 V_{SCE} experiment in Fig. 3. Each transient is a combination of two sets of data recorded at different sampling rates from the same test, in order to examine current decay over five time decades. Current decay is plotted from the peak current observed. The time of the peak current (2.5×10^{-7} s) is taken to be half of the sampling frequency. The peak anodic bare surface current densities decrease with decreasing potential due to decreasing overpotential for anodic dissolution. The transients at the most positive potentials in Fig. 3 (0, -0.3, and -0.9 V_{SCE}) remain net anodic over the duration of the test. Experiments at intermediate potentials (-1.1 and -1.525

^a We strictly define the term "ohmically limited" to describe the instance where the current reaches the ohmic limit. Tests that are not ohmically limited may still be ohmically affected, i.e., may experience ohmic loss in solution.

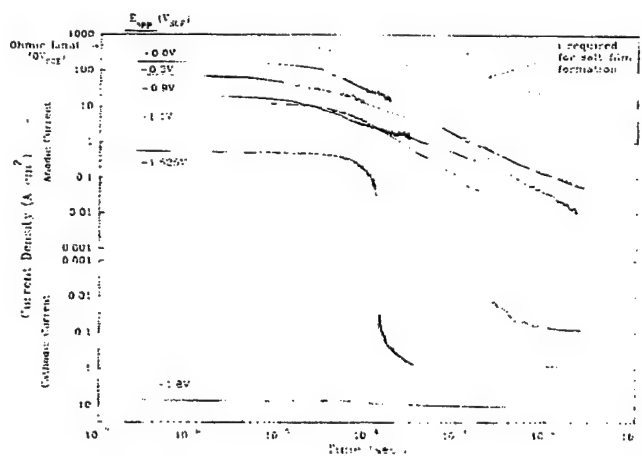


Fig. 3. Individual current transients of fractured titanium thin films at the indicated applied potentials in 0.6 M NaCl. Each current transient is a combination of two sets of data acquired from the same experiment at different acquisition rates. The theoretical ohmically limited maximum current density is indicated. The time required at constant current density for salt film formation assuming semi-infinite linear diffusion from a planar electrode is indicated.

V_{SCE}) are initially anodic but become cathodic as repassivation occurs. This is due to the fact that the applied potential is anodic to the bare surface OCP (Fig. 1) but cathodic to the OCP of the filmed surface (-0.2 to -0.7 V_{SCE}) at steady state. Tests at the most negative potentials (-1.8 V_{SCE}) remain net cathodic throughout the length of the test, also consistent with Fig. 1. In fact, little change is observed following fracture. The surface has been shown to never remain film-free at equilibrium, even at potentials below -2 V_{SCE} . Under these conditions, TiH_2 may be the equilibrium surface state instead.^{26,27}

Other investigators have attached significance to the length of the current density plateau at the earliest times following depassivation.¹⁰⁻¹² Models have been developed²⁸ and used¹⁰⁻¹² which attribute the plateau length to the time required for the formation of the initial monolayer of oxide. However, experimental artifacts have been shown to affect the length and magnitude (current) of the plateau in ohmically limited^{9,15,16} or depassivation speed limited experiments.¹⁵ In the absence of ohmic or depassivation speed limitations, as in fractured thin film tests, it may be possible that the 10 to 50 μ s plateau length may be indicative of the time required for monolayer chemisorbed oxygen or oxide formation. Further study would be required to confirm this hypothesis.

Charge density.—The charge density passed following fracture was calculated by integration of current density-time curves up to 30 ms (Table I). For all of the charge densities in Table I, the net current remained anodic for the entire 30 ms of data acquisition, thereby allowing integration over this time. At potentials below -0.6 V_{SCE} , charge densities are not reported, due to significant contribution from cathodic reactions on the repassivating surfaces at longer time periods which could not be accounted for accurately. For instance, at 0 V_{SCE} in 0.6 M NaCl, the charge density was found to be 25 mC/cm² after 30 ms. The calculated charge density, an average of multiple tests, is actually an underestimate of the true anodic charge density, because it neither incorporates unaccounted anodic current equaling the cathodic current supplied by the bare surface nor anodic current data after 30 ms. If it is assumed that the current decays with a slope of -1.09 on the $\log i - \log t$ plot until the steady-state current passive density^{1,7} is reached, the anodic charge density would be almost 50% greater than obtained after 30 ms at all applied potentials reported in Table I. The charge densities required for oxides of steady-state thicknesses formed at -0.6, -0.3, and 0 V_{SCE} in 0.6 M NaCl range from 1.2 to 3.2 mC/cm², assuming steady-state thicknesses that increase 2.3 nm/V (as determined by EIS¹⁴), a 0.52 nm monolayer thickness²⁹ assumed to exist below -0.37 V_{SCE} , and 3.4 g/cm³ oxide density.²⁹ The oxide thickness on titanium following repassivation has been found to be consistent with these.²⁹ The resulting overall current efficiencies after 30 ms are less than about 13%. The extrapolated anodic charge densities for complete repassivation, assuming the current decays with a slope of -1.09 on the $\log i - \log t$ plot at -0.6, -0.3, and 0 V_{SCE} in 0.6 M NaCl, range from 27 to 32 mC/cm². The overall current efficiency for oxide formation after decay to steady state would be less than 10% for the applied potentials reported in Table I.

Table I. Comparison of charge densities passed (mC/cm²) following fracture of titanium thin films up to 30 ms. Charge densities are obtained by integration of the current density-time transient and represent an average of at least two experiments. (Charge density to form steady-state oxide = 1.2 to 3.1 mC/cm² for steady-state oxide thicknesses at -0.6 to 0 V_{SCE} .)

Potential	5 M HCl	0.6 M NaCl	0.6 M NaCl, pH 10
0.5 V_{SCE}	36	—	—
0 V_{SCE}	30	25	23
-0.3 V_{SCE}	28	16	—
-0.6 V_{SCE}	—	17	16

Therefore, the large majority of repassivation charge goes toward dissolution of titanium for all of the conditions of Table I (probably as Ti^{3+} or TiO^{+2} , as confirmed elsewhere from scraped disk/ring experiments²⁷) and not into oxide formation ($\text{Ti} + 2\text{H}_2\text{O} \rightarrow \text{TiO}_2 + 4\text{H}^+ + 4\text{e}^-$). Therefore, the conclusion that a large portion of the charge passed following Ti film rupture in chloride solutions goes toward dissolution is well supported.^{27,30} However, the rapid fracture thin film technique gives a more accurate assessment of overall current efficiencies for oxide formation.

Previous theories have suggested that the entirety of the dissolution occurs during the plateau current density region (Fig. 3) at early time.¹⁰⁻¹² The charge passed during the subsequent current decay was attributed to oxide thickening.¹⁰⁻¹² The depth of metal penetration by dissolution in 20 μs (Fig. 3) could reach 1.6 nm, possibly undercutting islands of oxide attempting to cover the bare surface as reasoned before.⁹ However, this effect could only partially account for low efficiencies seen. The charge density passed during each subsequent time decade is roughly equal, because the current decay is nearly logarithmic.¹⁵ Therefore, significant dissolution must take place for the entire duration of the current decay transient because nearly 90% of the total charge goes toward dissolution. It is probable, therefore, that a high concentration of Ti^{3+} or TiO^{+2} , depending upon applied potential, will be present in a crack tip solution following film rupture. Since hydrolysis is probable, the hydrolysis product of Ti^{+3} (i.e., $\text{Ti}(\text{OH})^{2+}$) may be present (Appendix A).

Current decay.—The general expression where i is current density (A/cm^2), i_0 (A/cm^2) is the peak bare surface current density, t is elapsed time at $t > t_0$ or $t = t_0$ for $t < t_0$ (s), and t_0 (s) and m (unitless) are constants, was utilized for analysis of the current decay following depassivation³¹

$$i = i_0 \left(\frac{t}{t_0} \right)^{-m} \quad [1]$$

Table II shows the constants obtained by linear regression of the more positive applied potential experiments. A typical fit of $\log i$ vs. $\log t$ is seen in Fig. 4 (0.6 M NaCl, $E_{\text{app}} = 0 \text{ V}_{\text{SCE}}$, linear correlation $r^2 = 0.998$). Fitting was performed from 10^{-4} to 0.03 s. The transients fitted in Table II were chosen for fitting because they remained net anodic over the entire acquisition time. Thus, they were less influenced by cathodic reactions on the repassivating surface than those at more negative potentials and may be considered to represent the anodic repassivation behavior on titanium in 0.6 M NaCl. It is seen from Table II that both t_0 and m are similar for the various potentials. This suggests that the repassivation behavior (oxide reformation and dissolution) at the different potentials is similar at times greater than 10^{-4} s following fracture. Moreover, m , which represents the slope of the transient on the $\log i - \log t$ plot, is seen to be greater than one. It has been shown that m cannot be greater than one if the high field approximation is applicable.¹⁶ The high field approximation³² has been used to model the current decay recorded during potentiostatic repassivation tests.^{8,10-12,16} However, the high field approximation is inappropriate for modeling the repassivation of titanium exposed to chloride solutions, because the model assumes that current is entirely due to oxide thickening. Instead, the observed anodic current transient is mainly due to dissolution as shown.¹⁵ Thus, the

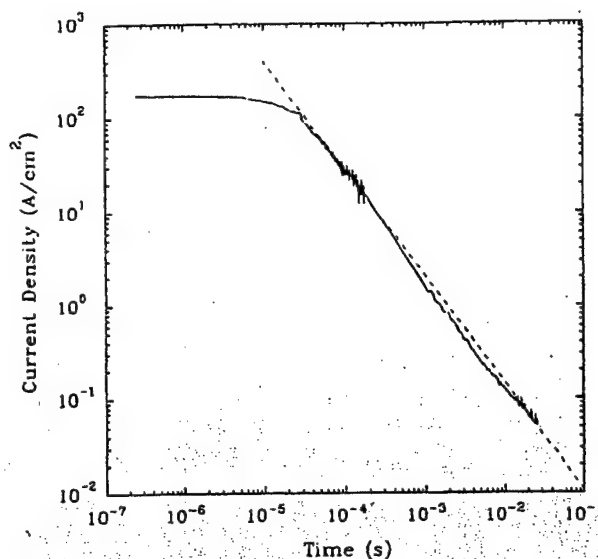


Fig. 4. Typical fit of $\log i = -m \times \log t$ from Eq. 1 to a titanium thin film repassivation transient ($E_{\text{app}} = 0 \text{ V}_{\text{SCE}}$, 0.6 M NaCl). The m parameters from such fits are seen in Table II. The linear correlation coefficient $r^2 = 0.998$.

fact that m is greater than one is not unreasonable. It has been hypothesized that when the current efficiency for oxide formation is low, increasing oxide perfection instead of oxide thickening accounts for the roughly logarithmic current decay.³³ Such a scenario may be valid for the case of titanium exposed to chloride solutions.

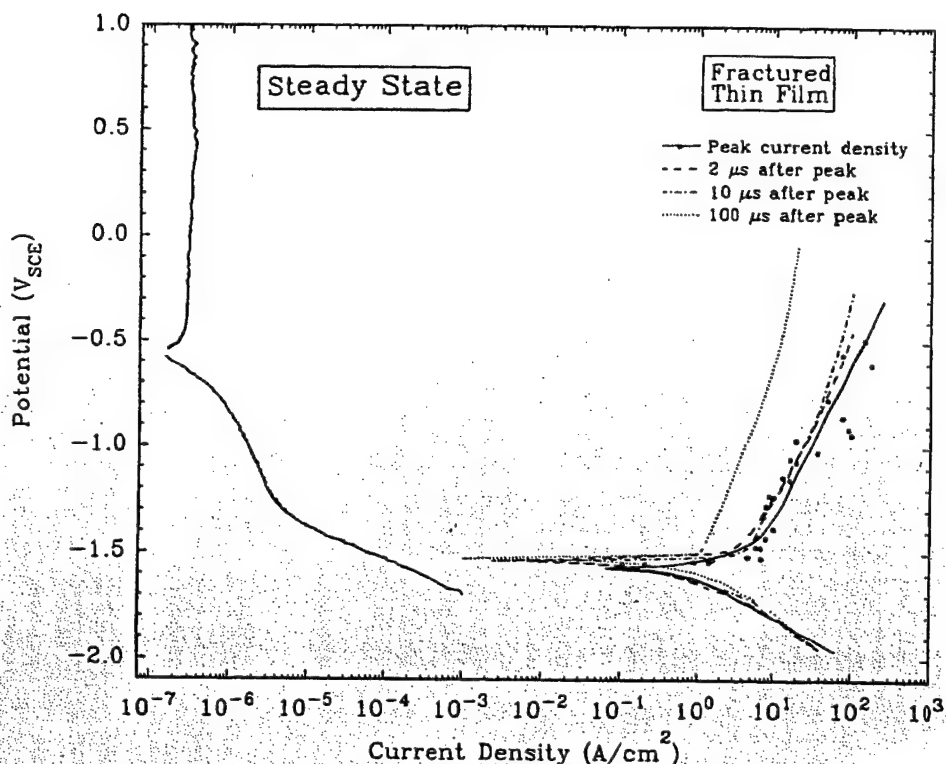
The current density required for salt film formation ($i = 2.2 \text{ t}^{-1/2}$)⁹ is plotted in Fig. 3. The current density transients are generally orders of magnitude below the current-time product required for salt film formation. Thus, the current decay is attributable to oxide perfection and not salt film formation. Beck hypothesized that the steep decay (slope ≈ -2 on $\log i - \log t$ plot) following the current density plateau observed in potentiostatic repassivation experiments might be attributable to salt film production.³⁴ However, the repassivation experiments performed by Beck were ohmically limited and Burstein and Davenport have shown that ohmic drop in solution can yield $m > 1$.¹⁶ Beck also formulated an extensive theory in the late 1960s [the mass transport kinetic (MTK) model] which argued that cracking of titanium alloys in chloride environments was due in part to the formation of a salt film near the crack tip.^{23,34,35} The salt film formation hypothesis was subsequently weakened by Beck's later calculations and by experiments incorporating anions which form salts with Ti^{+3} of widely varying solubility⁹ which yielded similar repassivation behavior. Thus, it appears that salt film formation does not take place upon repassivation of titanium at the potentials and for the electrode geometry examined here.

Polarization behavior.—The current densities at different potentials can be plotted to produce polarization curves at various times following depassivation (Fig. 5). Surface potentials have been corrected for ohmic drop in solution using the calculated solution resistance²¹ (discussed later). Individual data points are shown for the peak current density data only. It is seen that current densities on freshly exposed titanium are 4 to 9 orders of magnitude larger than that seen at steady state. Extremely large current densities are seen to occur at short times following film fracture. However, these large current densities are short-lived and rapidly decay toward that seen at steady state. This is seen from the family of polarization curves at times following the peak current density. Moreover, it is seen that the OCP increases with time, toward that seen at steady state, as expected.

Table II. Comparison of parameters obtained by fitting of current transients at different potentials (0.6 M NaCl) to Eq. 1. Values for m are ± 0.04 .

Potential	t_0 (s)	m
0 V_{SCE}	2.05×10^{-5}	1.14
0.3 V_{SCE}	1.76×10^{-5}	1.05
-0.6 V_{SCE}	2.56×10^{-5}	1.08

Fig. 5. Comparison of the bare surface (peak current density) polarization curve, polarization curves at various times following depassivation of fractured titanium thin films, and the steady-state polarization curve on grade 2 titanium (0.05 mV/s scan rate) in 0.6 M NaCl. Only individual data points for the peak current density curve are shown. Polarization curves are lines qualitatively drawn as the best fit.



The theoretical ohmically limited current density can be calculated from the formula shown. (Assuming that the oxidation charge-transfer resistance $R_{ct} \ll R_s$ for a bare metal, this calculation gives the theoretical ohmically limited current density.)

$$i = \frac{E_{app} - E_{bare OCP}}{(R_s)(Area)} \quad [2]$$

These current densities are compared to the bare surface polarization curves for 0.6 M NaCl and 5 M HCl in Fig. 6. (The data points in Fig. 6 are the averages of the current densities of multiple tests for a given applied potential.) The solution resistance is calculated from²¹

$$R_s = \left(\frac{1}{2\pi\kappa b} \right) \ln \left(\frac{4b}{a} \right) \quad [3]$$

where R_s is the solution resistance (Ω), κ is the solution conductivity ($\Omega\text{-cm}^{-1}$), a is one-half of the bared area width (cm), and b is one-half of the bared area length (cm). For 0.6 M NaCl solutions, R_s is calculated to be 69.0 Ω . This is in excellent agreement with the solution resistance determined by current interrupt measurements (68.0 Ω) and EIS (66.6 Ω). The peak current densities fall below the theoretical ohmic limit.¹⁵ It is reasonable to argue, therefore, that the fractured thin film tests are not ohmically limited. A plot of measured current vs. applied potential¹⁵ displays a nonlinear slope, thus confirming this conclusion.

Two Tafel region anodic behaviors.—For the anodic portion of the ohmically corrected bare surface polarization curve (Fig. 7), two different regions are observed, a region of relatively low slope near the bare OCP and a region of relatively high slope at more noble potentials. The current densities obtained during testing are the net current densities supplied by the potentiostat. Far above the OCP, these current densities are a good approximation of the anodic current density, because the cathodic current density supplied by the bare surface, which cannot be measured, is insignificant compared to that supplied by the potentiostat. However, near the OCP, the contribution of the cathodic current is significant compared to the anodic

current. The net current measured is substantially less than the true anodic current and yields a region near the OCP wherein the slope is shallow compared to the slope far away from the OCP. On initial inspection, it appeared that this situation might explain the distinct regions of the anodic polarization behavior. A nonlinear least squares fit of the data using one anodic Tafel slope and one cathodic Tafel slope, however, suggests that this is not the case (Fig. 7a and b).⁶ Two distinct anodic regions are observed and a fit with two Tafel slopes describes the data accurately in 5 M HCl, 0.6 M NaCl, and 0.6 M NaCl at pH 10. A single Tafel slope is seen for the cathodic data in all cases. Moreover, because the cathodic data are linear (on the $E - \log i$ plot) over the same current densities (5 to

⁶ Reversible potentials were fixed during fitting. Exchange current densities and Tafel slopes were allowed to vary.

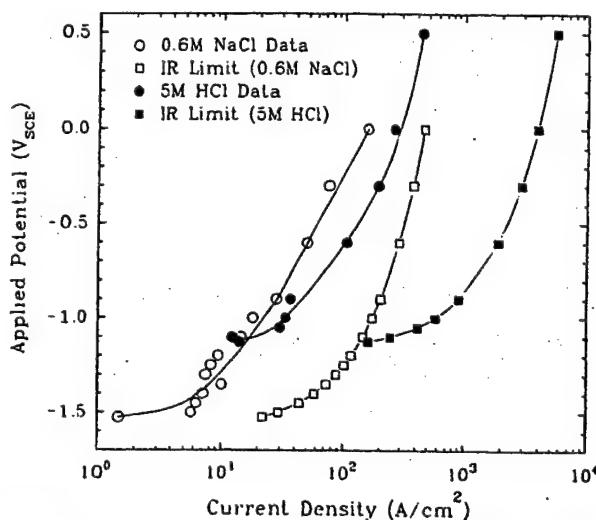


Fig. 6. Comparison of the average current densities at their respective applied potentials to the theoretical ohmically limited current density [Eq. 2] for the solutions shown.

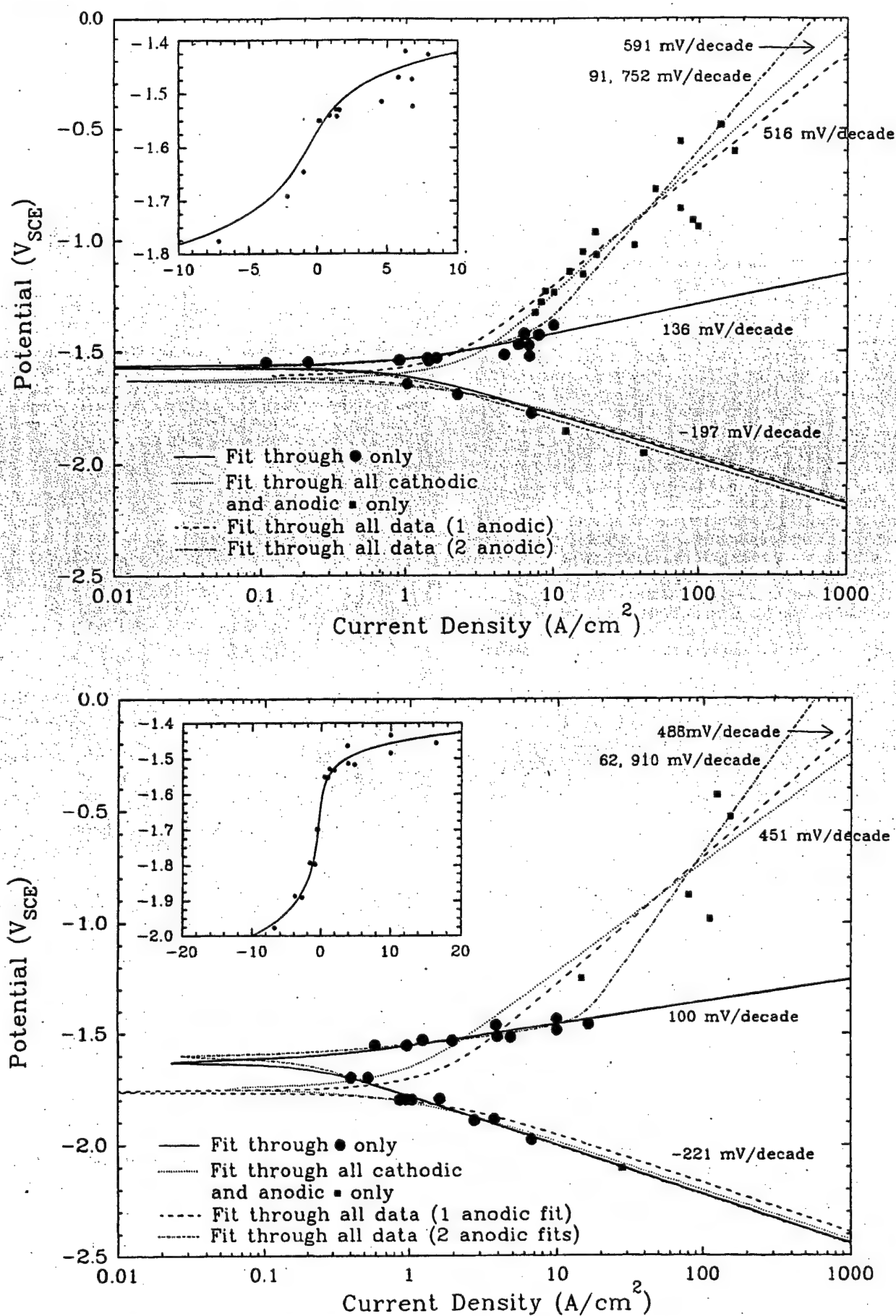


Fig. 7. Fractured titanium thin film bare surface polarization data in (a, top) 0.6 M NaCl and (b, bottom) 0.6 M NaCl at pH 10. Various nonlinear least squares fits are shown. Reversible electrode potentials were fixed during fits to Tafel slopes and exchange current densities. Inset shows $E-i$ relationships in the vicinity of the mixed potential.

100 A/cm²) where the anodic data display two different slopes, it does not appear that the anodic region of the steep slope is the result of some artifact of testing, such as potentiostat response, slow surface wetting, or ohmic shielding by the freshly broken-off thin film end.

Others have seen the double anodic slope phenomenon with scratched iron and stainless steel electrodes.^{36,37} The shallow sloped region was attributed to Tafel behavior.^{36,37} The region of steep slope has been explained as a scratch speed-limited regime.¹⁵ Other work with fractured Ti-8-1-1 rods in 12 M HCl appears to show two regions as well.⁸ The region of steep slope, however, appears to be a region of ohmic limitation. As discussed earlier, the fractured thin films are ohmically corrected and are neither limited by voltage drop in solution or by depassivation speed.¹⁵ Thus, it may be that the region of steep slope is actually indicative of the true kinetic response of the surface. In conventional electrochemistry, dual Tafel slopes are often a result of a change in kinetic rate-determining step or change in reaction intermediate surface coverage. However, the bare metal kinetic response cannot continue to be of low Tafel slope (i.e., a Tafel slope of 100 mV/dec or so) at 0 V_{SCE}, because unreasonable current densities exceeding 10¹⁰ A/cm² would be required. Thus, some limiting factor, which is not a known artifact of the test method, may play a role in limiting the current density. This limiting factor would produce a steep slope in order to maintain attainable current densities in the 0 V_{SCE} potential range. The mass transport-limiting current density for reduction of water is approximately 3000 A/cm² at 10 ms. Thus water transport can be eliminated as a possible limiting factor.

High Tafel slopes may be explained at the very high current densities measured here. If the free energy of the initial state becomes high enough (a possibility for bare titanium which is extremely unstable), the reaction becomes essentially activationless.^{38,39} Further increases in applied potential would not produce current density increases that are exponential with overpotential. It has been suggested that an activationless reaction may possibly control the apparent Tafel behavior in light of the absence of other known limiting factors.⁴⁰ The reader should recognize that many of the common assumptions utilized for steady-state electrochemical kinetics may not apply to metal dissolution at such high rates. Little experimental work is available to validate assumptions of conventional Tafel slopes.

Effect of solution chemistry.—Variation of pH.—Individual current transients arising from thin film fracture tests in chloride solutions of different pH (5 M HCl, 0.6 M NaCl, and 0.6 M NaCl adjusted to pH 10) at similar anodic overpotentials are seen in Fig. 8. 5 M HCl resulted in a slightly greater bare surface peak current density than that in neutral and pH 10 solutions at similar overpotentials when corrected for ohmic loss in solution. None of the curves shown are at the theoretical ohmic limit (Fig. 6). Repassivation is fast for all anodic transients, with approximately logarithmic current decay, even in 5 M HCl. This is not surprising as repassivation of titanium has been observed by others in 12 M HCl.¹⁴ Transient morphology is similar in neutral and pH 10 NaCl solutions. However, 5 M HCl transients appeared to have a slightly faster repassivation rate (larger *m* values). Table III, which shows repassivation parameters (at identical applied potentials, 0 V_{SCE}) fitted to Eq. 1, confirms these observations. The peak current densities from individual transients may be plotted vs. potential to generate bare surface polarization curves (see Fig. 9). Potentials are ohmically corrected. It is seen that for a given overpotential, bare surface anodic and cathodic polarization behaviors are qualitatively similar in solutions of widely differing pH, with the more acidic solutions displaying higher current densities for a given overpotential. The bare surface polar-

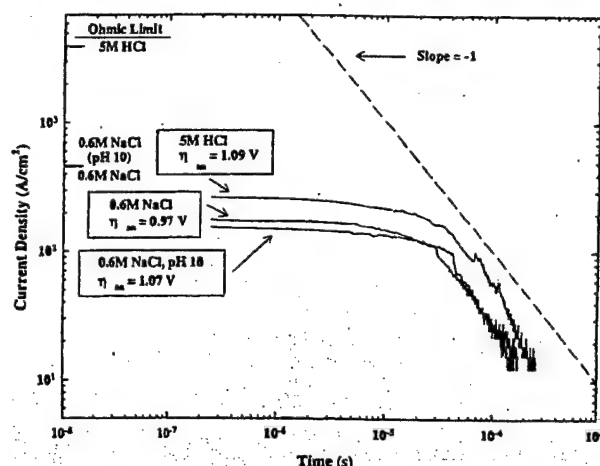


Fig. 8. Individual fractured titanium thin film current transients in different solutions. The current transients have similar anodic overpotentials (with respect to open circuit) at the peak current density when corrected for ohmic loss in solution. The applied potential for all tests was 0 V_{SCE}. Ohmically limited current densities for each test (Eq. 2) are shown on the left side of the plot.

ization curve of titanium in all of the solutions has two distinct anodic regions and one cathodic region. Additionally, the polarization curves at various times following depassivation (similar to that seen in Fig. 5) appear comparable as well, with the current densities decreasing over time at similar rates in all solutions.

Anodic charge densities passed following depassivation in different pH solutions are compared in Table I. As in the neutral solution, the average anodic charge densities passed in both 5 M HCl and 0.6 M NaCl adjusted to pH 10 far exceed that required for oxide film formation. Thus, in all these solutions, the large majority of anodic charge goes toward dissolution with only a small fraction utilized for film formation. Because the 0 V_{SCE} experiments have roughly similar anodic overpotentials (Fig. 8), the anodic charge densities may be compared. It is seen that the charge densities in the different solutions are statistically similar, as the charge density data revealed some scatter ($\pm 20\%$). In summary, anodic charge densities, as a function of overpotential, show little dependence upon solution pH. Similar behaviors in solutions of widely varying pH argue against a dissolution mechanism controlling EAC of β -titanium alloys, as cracking is observed when acidic crack tip chemistries are present, but not when alkaline chemistries exist.⁴¹

Anodic and cathodic Tafel slopes were obtained by non-linear least squares fitting of the peak current density data. As with the neutral bare surface polarization curve (Fig. 7), the polarization curves from 5 M HCl and pH 10 solutions displayed two distinct anodic regions. The two anodic and one cathodic Tafel slopes, OCPs, and corrosion current densities in the three solutions are compared in Table IV. The calculated OCPs are in good agreement with those obtained from individual thin film fractures (Fig. 1). Additionally, the corrosion current density was found to be greater in the acidic solution than in the neutral or basic solutions. The cathodic water reduction exchange current densities are orders of magnitude larger than that

Table III. Comparison of parameters obtained by fitting of current transients from fractured thin film tests in different solutions ($E_{app} = 0$ V_{SCE}) to Eq. 1. Values for *m* are ± 0.04 .

Solution	<i>t</i> ₀ (s)	<i>m</i>
5 M HCl	2.99×10^{-5}	1.36
0.6 M NaCl	2.05×10^{-5}	1.14
0.6 M NaCl, pH 10	2.04×10^{-5}	1.16

* This paper focuses on chloride solutions. It should be noted that fractured titanium thin film tests in 0.6 M and 1 M Na₂SO₄ revealed behavior indistinguishable from that in 0.6 M NaCl.

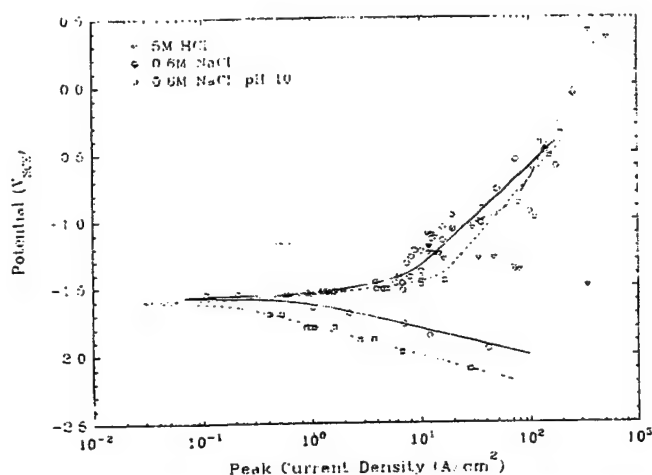


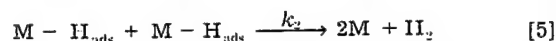
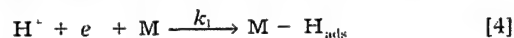
Fig. 9. Bare surface polarization curves (peak current densities) of fractured titanium thin films in various environments.

seen on TiO_2 -covered titanium.⁷ Exchange current densities are many decades of current removed from the data and are not reported due to resulting uncertainties. Also, high anodic slopes are only approximate in 5 M HCl and pH 10 solutions, because fewer data points were obtained in the steep portions of these curves.

The low anodic Tafel slope may be indicative of conventional Tafel behavior. Caprani *et al.* have proposed a general anodic reaction mechanism of $\text{Ti} \rightarrow (\text{Ti}^{3+})_{\text{ads}} \rightarrow \text{Ti}^{3+}$ in acidic chloride media for the production of trivalent titanium.⁴²⁻⁴⁶ The observed anodic Tafel slopes vary from 62 mV/dec in pH 10 to 167 mV/dec in 5 M HCl. Because the rate-determining step is unknown, especially on bare titanium, a variety of factors (rate-determining step, intermediate coverages, rate constants, etc.) may account for the observed Tafel slopes. Although it is known that the Tafel slope decreases with increasing pH, any mechanism that would account for this would be entirely speculative at this time.

The cathodic reaction is likely attributable to water reduction for the neutral and alkaline experiments, because hydrogen ion and oxygen reduction are unable to support such high current densities, even in the microsecond regime. Hydrogen ion reduction is likely charge-transfer controlled in this time frame in 5 M HCl. The cathodic Tafel slopes increase with increasing pH. The differences in Tafel slope could be accounted for by a change in the symmetry factor, β , or an entirely different reaction pathway when transitioning from hydrogen ion to water reduction with pH. A slow discharge-fast recombination mechanism has been proposed for film-covered titanium in acidic chloride solutions.⁴⁷ However, the reaction mechanism on bare titanium is likely different due to the presence

of a bare metal surface instead of a semiconducting oxide. If the difference in cathodic Tafel slope with pH is due to a changing distance along the reaction path, *i.e.*, β , the water reduction reaction mechanism on bare titanium could be attributed to a conventional mechanism, such as the coupled discharge-recombination mechanism⁴⁸



Water reduction, in place of proton reduction (Eq. 4), is likely at neutral and alkaline pH. The current density for this reaction in 5 M HCl can be written as

$$i = k_1 C_{\text{H}^+} (1 - \theta) \exp \left[\frac{-\beta \eta F}{RT} \right] = k_2 \theta^2 \quad [6]$$

where θ is the surface coverage of H_{ads} , k_1 is a constant, and C_{H^+} is the H^+ concentration in solution. Assuming $\beta = 1/2$, a Tafel slope ranging from 120 (Langmuir) to 180 mV/dec (activated Temkin isotherm) is obtained for this mechanism. Of all the conventional hydrogen evolution reaction mechanisms, 180 mV/dec is the closest to those seen in Table IV. Larger Tafel slopes would be obtained for $\beta < 1/2$. Also, possible repulsive interactions between surface-adsorbed hydrogen atoms, at very high coverage on bare Ti, could also increase apparent Tafel slopes.

Variation of chloride concentration.—Chloride ion concentration is often a critical factor in electrochemical behavior of passive metals. Experiments were performed in 5 M LiCl (pH 3) to examine the effect of high chloride concentration without the extreme acidity of 5 M HCl (pH -1.64). Chloride concentrations less than 0.6 M were not examined, because the higher resistivity solutions would result in ohmic limitation of the peak current densities. Titanium thin films were fractured at applied potentials of 0 and -0.6 V_{SCE} as well as at open circuit in 5 M LiCl (Fig. 10). The bare surface OCP of the titanium film in 5 M LiCl is approximately 200 mV more positive than that in 0.6 M NaCl, as expected from its lower pH. This OCP falls along the OCP vs. pH line of Fig. 1, within experimental error. The peak current densities are slightly lower than those in 0.6 M NaCl at the same anodic overpotential but are not at theoretical ohmic current limits using Eq. 2 and 3. These results imply that either Cl^- or Li^+ weakly affects Ti/Ti^{3+} oxidation. Individual current transients were similar to those in 0.6 M NaCl, with roughly logarithmic decay. Therefore, for a given overpotential, repassivation behavior in 5 M LiCl appears to be similar to that in 0.6 M NaCl and is weakly dependent on chloride concentration for concentrations greater than 0.6 M.

Table IV. Comparison of parameters obtained by nonlinear least squares fitting of the bare surface polarization curves of Fig. 9. Reversible potentials were fixed during fitting. Exchange current densities (not reported) and Tafel slopes were allowed to vary. Anodic Tafel slope 2 is observed at low overpotential while anodic Tafel slope 1 is observed at high overpotential.

Solution	Anodic Tafel slope 1 (mV/dec)	Anodic Tafel slope 2 (mV/dec)	Cathodic Tafel slope (mV/dec)	Corrosion current density (A/cm ²)	OCP (V _{SCE})
5 M HCl	1600	167	182	8.1	-1.17
0.6 M NaCl	750	90.6	197	0.70	-1.58
0.6 M NaCl, pH 10	910	62.1	221	0.16	-1.60
d/d(pH)	—	-9.1	3.2	-0.15 ^a	-0.039

^a $d [\log(\text{corrosion current density})]/d (\text{pH})$.

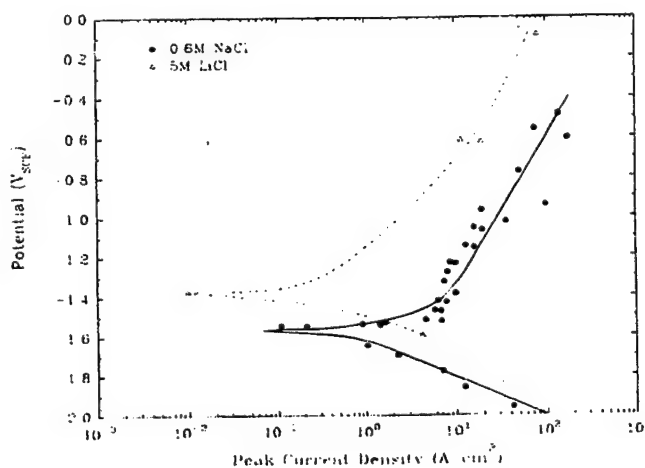


Fig. 10. Comparison of fractured titanium thin film peak current densities in 0.6 M NaCl and 5 M LiCl (pH 3).

Addition of TiCl_3 .—Separate observations suggest that TiCl_3 is likely present in a crack tip solution. First, as discussed previously, the majority of charge passed following depassivation goes toward dissolution. Also, the presence of trivalent (rather than tetravalent) ions in solution has been noted following depassivation.²⁷ Moreover, an acidified crack tip solution (pH 1.7) has been observed following crack advance of an α -titanium alloy.⁴⁹ Hydrolysis of Ti^{3+} following film rupture, Cl^- migration toward the crack tip, and an accompanying decrease in solution pH with TiCl_3 concentration is expected. Appendix A discusses the expected hydrolysis for Ti^{3+} .

Thin film fracture tests were performed in 5 M HCl + 1 M TiCl_3 to examine the effect of TiCl_3 additions. Figure 11 compares peak current densities at applied potentials of 0 and $-0.6 \text{ V}_{\text{SCE}}$ in the TiCl_3 solution to 5 M HCl only. It appears that the bare surface peak current densities are lower in the solution with the added TiCl_3 . The peak current density of the $0.6 \text{ V}_{\text{SCE}}$ test in the TiCl_3 solution appears to be significantly lower than that in 5 M HCl alone. Figure 12 displays this more clearly, wherein tests in 5 M HCl show a higher peak current density at both smaller and larger anodic overpotentials. The peak current density at 0 V_{SCE} in 5 M HCl + 1 M TiCl_3 is only slightly lower than that in the 5 M HCl, however. Further, the OCP has been found to be about 160 mV more positive in the solution with additional TiCl_3 .

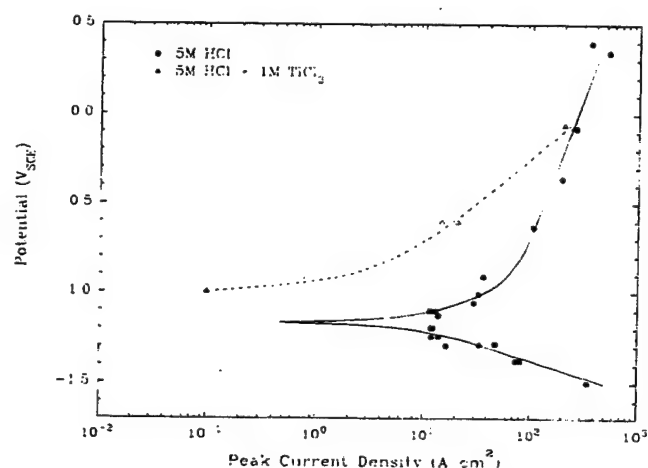


Fig. 11. Comparison of peak current densities of fractured titanium thin films exposed to 5 M HCl and 5 M HCl + 1 M TiCl_3 .

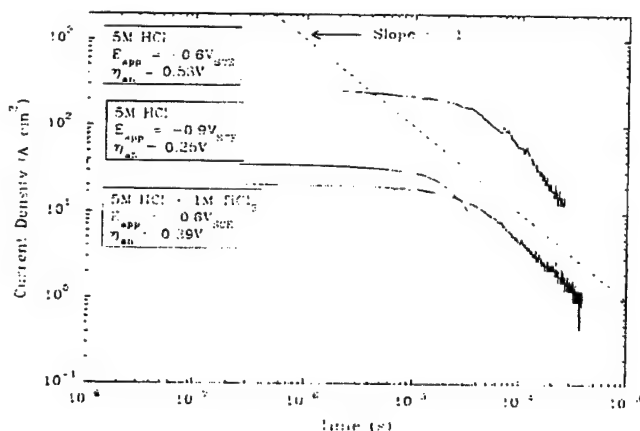


Fig. 12. Comparison of an individual current density transient in 5 M HCl + 1 M TiCl_3 to those in 5 M HCl only. The ohmically corrected overpotentials in 5 M HCl bracket the overpotential in the TiCl_3 solution. Overpotentials are with respect to the zero applied current condition at open circuit.

The effect of TiCl_3 on the repassivation behavior of fractured titanium alloy specimens has been previously examined.¹¹ Potentiostatic ($E_{\text{app}} = 0.24 \text{ V}_{\text{NHE}}$) current transients in 3 M HCl and 3 M HCl saturated with TiCl_3 were compared. Although the data were ohmically limited, it was observed that the peak current density in the TiCl_3 solution was 25% of that in the HCl solution alone, even though the solution conductivity was 70% of that of the HCl solution. Moreover, it was stated that the rate of current decay appeared lower, suggesting a slower repassivation. This result is somewhat clouded by the ohmic limitation, which can affect the observed potentiostatic repassivation decay kinetics.^{15,16} The OCP (obtained from the intersection of anodic and cathodic slopes) was found to be 300 to 400 mV more positive in the TiCl_3 solution compared to HCl.¹⁴ It was concluded from these results that the presence of saturated TiCl_3 suppressed the anodic reaction.¹⁴ The smaller positive shift in OCP seen here is likely due to differences in the concentration of TiCl_3 used.

Beck qualitatively described a change in repassivation behavior with the addition of TiCl_3 .¹⁴ This was confirmed by the present work. The slope of the current decay on the $\log i - \log t$ plot was affected by the 1 M TiCl_3 addition. In the present work, m (Eq. 1) was found to be 1.3 to 1.4 (Table III) in 5 M HCl. For the test in 5 M HCl + 1 M TiCl_3 in Fig. 12, however, m was 1.14. Thus, the anodic current density decays more slowly in the TiCl_3 solution, as proposed by Beck.¹⁴ Therefore, the present results confirm the results of earlier work,¹⁴ namely, that significant additions of TiCl_3 reduce the peak current density on bare titanium surfaces, inhibit anodic reactions, and slow repassivation. These findings appear consistent with those of Wanhill who found that TiCl_3 slowed stage II stress corrosion crack growth rates.⁵²

Comparison of Scratch Depassivation and Fractured Thin Film Data

Bare surface polarization curves for the six alloys were each generated in 5 M HCl, 0.6 M NaCl, and 0.6 M NaCl adjusted to pH 10 by scratch repassivation. Figure 13 compares the six different materials in 0.6 M NaCl, the lines being a qualitative best fit through the data. As before, potentials are ohmically corrected utilizing the solution resistance calculated from Eq. 3 (approximately 280Ω). Within the limitations of the scratch test, little difference is observed between the anodic bare surface repassivation

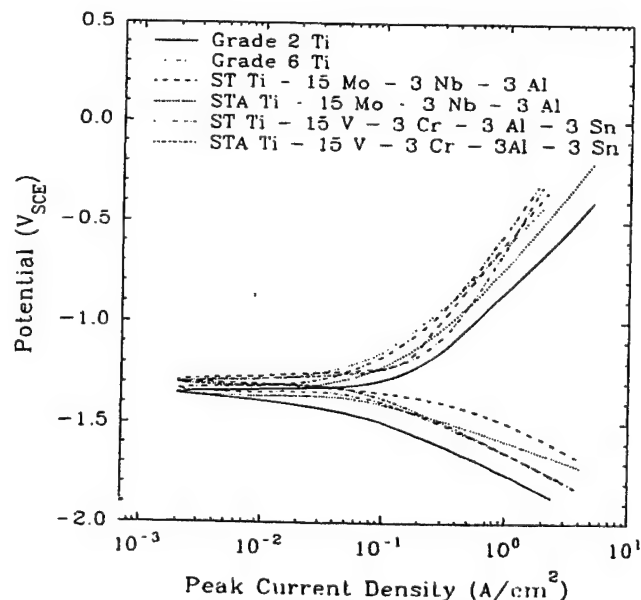


Fig. 13. Comparison of the bare surface (peak current) polarization behaviors after scratching of six different α , β , and $\beta + \alpha$ alloys exposed to 0.6 M NaCl.

behavior of all of the alloys examined, regardless of chemical composition or microstructure. Peak currents, OCP, total anodic charges, and repassivation rates were all comparable as well, except for grade 2 Ti which consistently yielded a higher charge density per repassivation event at every potential (Table V). Results were analogous in the acidic and alkaline solutions also. A single test performed with STA Ti-3Al-8V-6Cr-4Zr-4Mo (0.6 M NaCl, $E_{app} = 0.6 V_{SCE}$) yielded a similar peak current density and slightly lower anodic charge density than those seen for STA Ti-15Mo-3Nb-3Al and STA Ti-15V-3Cr-3Al-3Sn.

A bare surface polarization curve resulting from scratch testing (grade 2 titanium) is compared to fractured thin film data (evaporated from pure Ti target) in Fig. 14. Scratch depassivation testing appears to qualitatively show the same results as for fractured thin films. Quantitatively, however, there are differences between fractured thin film and scratch tests. The scratch test peak current densities are one to two orders of magnitude lower than those arising from fractured thin films, as predicted.¹⁵ The OCP is 250 mV more noble as well, because significant repassivation has occurred at the start of the scratch by the time the end of the scratch is reached.

The qualitative similarity between thin film and scratch tests was further investigated by comparing scratch test polarization curves on grade 2 titanium (peak current density) from solutions of varying pH (Fig. 15). As with thin film experiments (Fig. 9), the bare surface anodic polarization curves display two distinct regions of shallow and steep slope. The cathodic Tafel slope is also steep, relative to that seen at steady state.^{6,7} The OCPs are all approximately 250 mV more positive than those obtained from the fractured films. The differences in OCP between solutions are similar, in general, regardless of depassivation method. The OCP was found to decrease approximately 50 mV/pH (in tests from pH -1.64 to 14, not shown), a magnitude slightly larger than that seen with thin films (Fig. 1). Moreover, the corrosion current density appears to be about an order of magnitude higher in 5 M HCl than in the neutral and pH 10 solutions, as seen previously (Fig. 9 and Table IV). Therefore, it appears that scratch tests adequately predict repassivation trends on titanium, albeit in a strictly qualitative manner. With this result, comparison between repassivation behaviors of various alloys using the scratch method can be undertaken with an increased level of confidence.

Figure 16 is a plot of bare surface polarization curves on STA Ti-15Mo-3Nb-3Al exposed to 0.6 M NaCl at various times following depassivation. As with fractured thin films, the observed bare surface current density is much

Table V. Comparison of scratch test charge densities on various alloys exposed to different solutions. Charge densities were calculated by integrating the first 90 ms of the current transient from the peak current density.

Solution	Applied potential	Material	Charge density (mC/cm ²)
0.6 M NaCl	-0.6 V _{SCE}	STA Ti-15Mo-3Nb-3Al	3.4
	-0.6 V _{SCE}	Grade 2	5.0
	-0.6 V _{SCE}	ST 15V-3Cr-3Al-3Sn	3.6
	-0.6 V _{SCE}	ST Ti-15Mo-3Nb-3Al	3.4
	-0.6 V _{SCE}	STA Ti-15V-3Cr-3Al-3Sn	3.3
	-0.6 V _{SCE}	Grade 6	2.7
	-0.6 V _{SCE}	STA Ti-3Al-8V-6Cr-4Zr-4Mo	2.3
	-1 V _{SCE}	STA Ti-15Mo-3Nb-3Al	0.76
5 M HCl	-0.9 V _{SCE}	Grade 2	1.8
	-0.6 V _{SCE}	STA Ti-15Mo-3Nb-3Al	4.7
	-0.6 V _{SCE}	Grade 2	6.0
0.6 M NaCl pH 10	-0.6 V _{SCE}	STA Ti-15Mo-3Nb-3Al	5.7
	-0.6 V _{SCE}	Grade 2	6.9
	-1 V _{SCE}	STA Ti-15Mo-3Nb-3Al	0.49
	-1 V _{SCE}	Grade 2	1.4

^aNo experiment performed at -1 V_{SCE}. Charge density from $E_{app} = -0.9 V_{SCE}$ is shown instead.

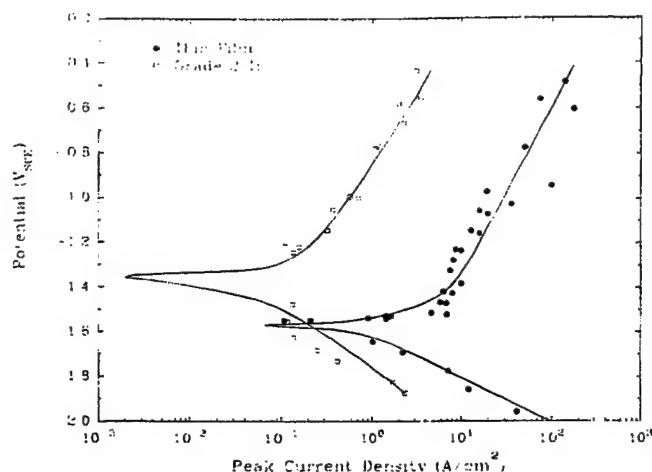


Fig. 14. Comparison of bare surface (peak current) polarization curves utilizing fractured titanium thin films and scratch testing on grade 2 titanium in 0.6 M NaCl.

larger than that seen during "steady-state" potentiodynamic tests. The OCP and current density shift over time toward those seen at steady state, similar to that observed with fractured thin films (Fig. 5). The 5 ms $E - \log i$ plots for grade 2 and STA Ti-15V-3Cr-3Al-3Sn are also shown in Fig. 16. The behavior of these alloys at 5 ms, as well as all of the other alloys examined at 5 ms, was similar. The repassivation $E - \log i$ behaviors of all of the alloys at 5 ms and other longer times (not shown) are all still similar at times beyond which depassivation speed or other experimental factors limit peak current densities.¹⁵

Others have also noted similar anodic repassivation behavior between commercially pure titanium, Ti-8-1-1, and Ti-14 Mo.¹⁴ Two factors likely account for the similar repassivation behaviors of the different titanium alloys in aqueous chloride solutions. The predominance of TiO₂ in all of the oxide films and Ti/Ti³⁺ dissolution following repassivation^{6,7} likely contributes to the similar results. At the more negative potentials examined here, oxides of the major alloying elements found in Ti-15Mo-3Nb-3Al and Ti-15V-3Cr-3Al-3Sn; Mo and V, respectively,^{6,7,24} are not thermodynamically stable (assuming metal ion concentrations of 10⁻⁶ M and pH 6). The reversible potentials for stable oxidation states of Mo and V are shown in Fig. 16. Therefore, these oxides cannot contribute to repassivation.

The charge (Table V) and peak current (Fig. 13) densities for grade 6 Ti, which approximates the composition of the α precipitates within the β matrix, were similar to those of

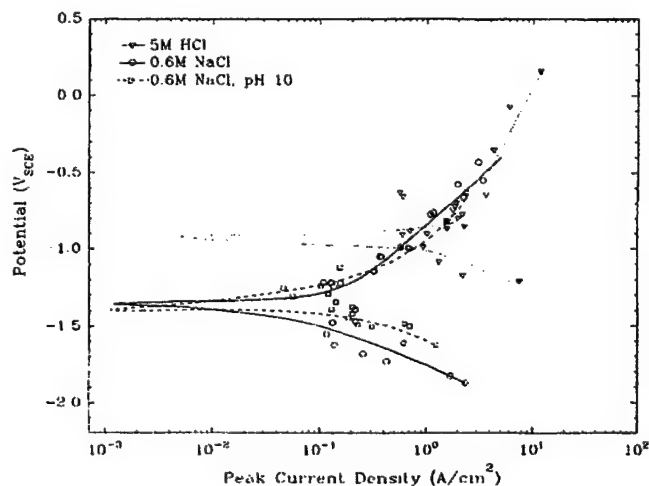


Fig. 15. Bare surface polarization curves on grade 2 titanium in different solutions obtained by scratch testing.

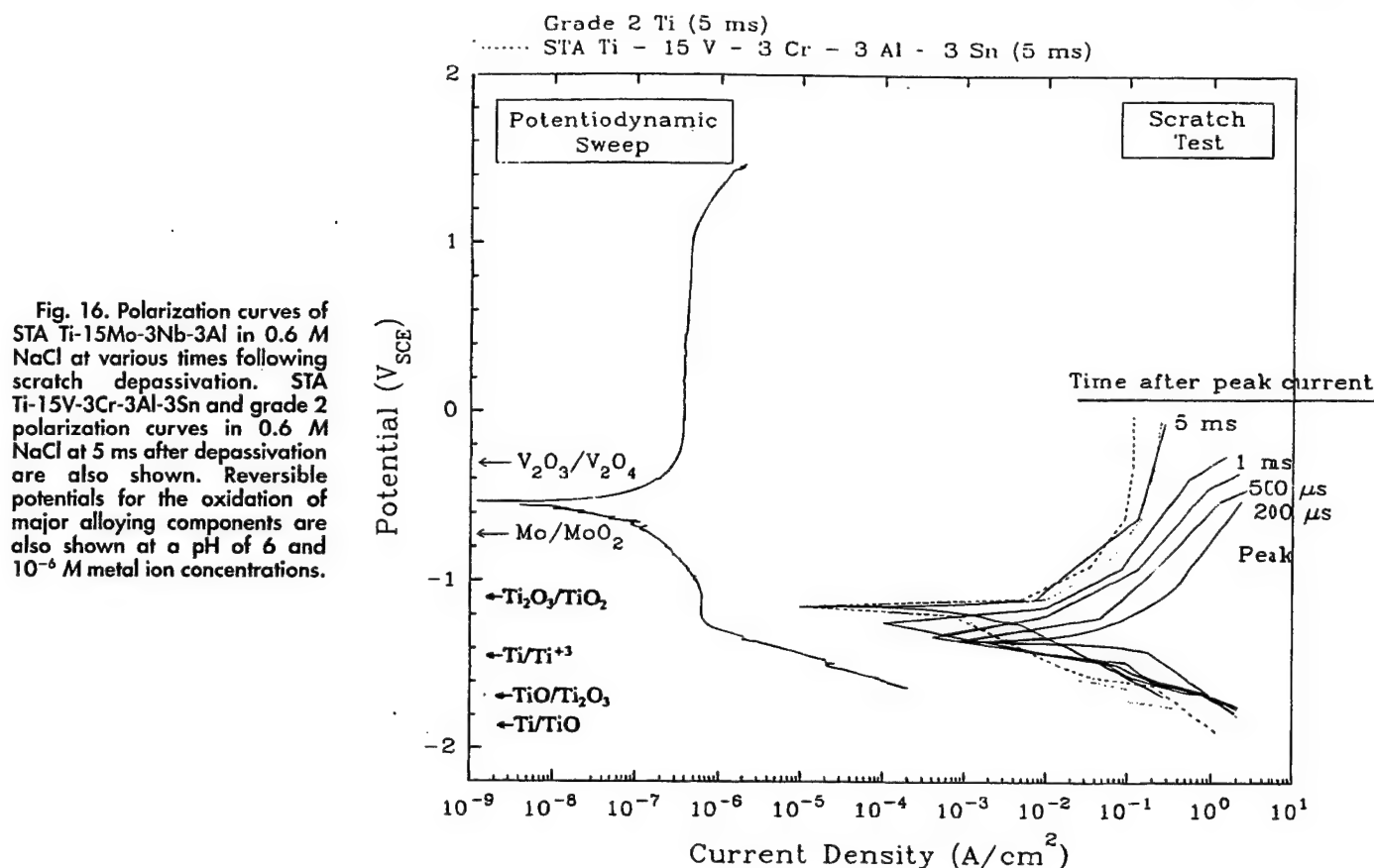


Fig. 16. Polarization curves of STA Ti-15Mo-3Nb-3Al in 0.6 M NaCl at various times following scratch depassivation. STA Ti-15V-3Cr-3Al-3Sn and grade 2 polarization curves in 0.6 M NaCl at 5 ms after depassivation are also shown. Reversible potentials for the oxidation of major alloying components are also shown at a pH of 6 and 10^{-6} M metal ion concentrations.

the ST β alloys. This indicates that α precipitates in a $\beta + \alpha$ alloy containing similar Al and V contents as grade 6 Ti may behave similarly to the β matrix when the passive film is destabilized at room temperature. In summary, it appears that less than 15 w/o differences in composition and microstructure have little effect on the repassivation behavior of a β -titanium alloy. Observed differences in EAC susceptibility between alloys do not appear to result from differences in repassivation behavior of β - vs. α -Ti. However, high segregated Al concentrations may exert a negative influence on the passivity and repassivation of Ti.³⁴

Conclusions

The repassivation behavior of titanium in aqueous chloride environments has been examined to obtain a better understanding of observed EAC behavior under dynamic strain. The bare surface OCP was found to decrease 43 mV/pH unit. Current densities greater than 100 A/cm² were observed upon fracture of titanium thin films in 0.6 M NaCl. The large majority of anodic charge during repassivation contributed to dissolution of titanium and not film formation. It was shown that significant dissolution takes place over the length of the current decay transient. Little difference was seen in the repassivation behavior of titanium in acidic, alkaline, and neutral chloride solutions. Similar behaviors in solutions of widely varying pH argues against a slip-film rupture-dissolution mechanism controlling EAC of β -titanium alloys, as crack initiation is observed when acidic crack tip chemistries are present, but not when alkaline chemistries exist. 5 M LiCl lowered peak current densities but did not affect repassivation behavior. Repassivation experiments performed in 5 M HCl + 1 M TiCl₃ found that TiCl₃ lowered peak current densities and slowed repassivation. Scratch depassivation tests indicate that little difference exists between the repassivation behaviors of selected β -titanium alloys. Tests comparing EAC-immune and susceptible alloys, e.g., ST vs. STA Ti-15Mo-3Nb-3Al or STA Ti-15Mo-3Nb-3Al vs. STA

Ti-15V-3Cr-3Al-3Sn, showed similar behavior, indicating that EAC susceptibility is not controlled by readily apparent alloy-specific differences in repassivation behavior. Grade 6 Ti yielded identical behavior to the ST β -titanium alloys, indicating little difference in repassivation behavior between the β -matrix and the α -precipitates in the STA alloys containing small concentrations of Al and V.

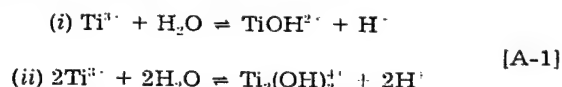
Acknowledgment

The authors acknowledge the Office of Naval Research (Grant No. N00014-91-J-4164) and the Virginia Center for Innovative Technology for their support of this work. The authors also thank TIMET and RMI for their generous donation of alloys. Further, we would like to acknowledge R.G. Kelly, E. Gileadi, and L. L. Scribner for their helpful discussions.

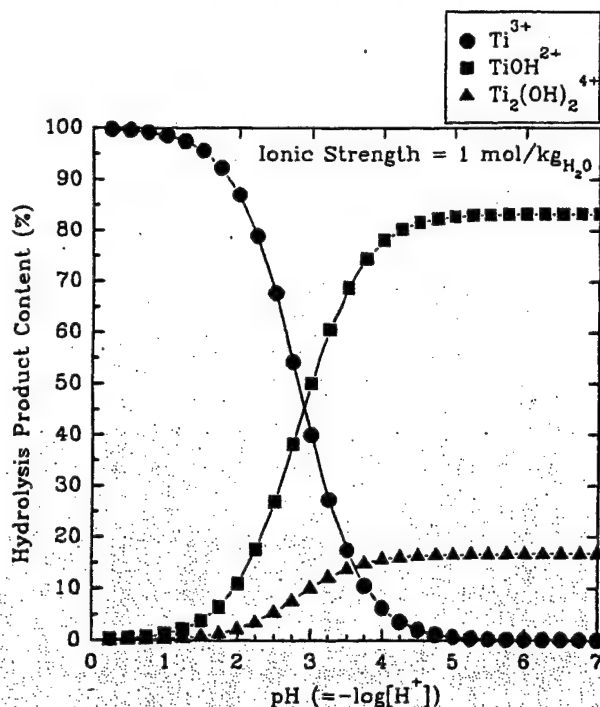
Manuscript submitted June 9, 1995; revised manuscript received March 12, 1996.

APPENDIX A

Crack tip solution acidification following cracking has been observed.⁴⁹ Solution acidification can be explained as follows. Trivalent titanium is produced following depassivation.²⁷ The trivalent titanium may then hydrolyze. Two hydrolysis reactions of Ti^{3+} are possible⁵⁰

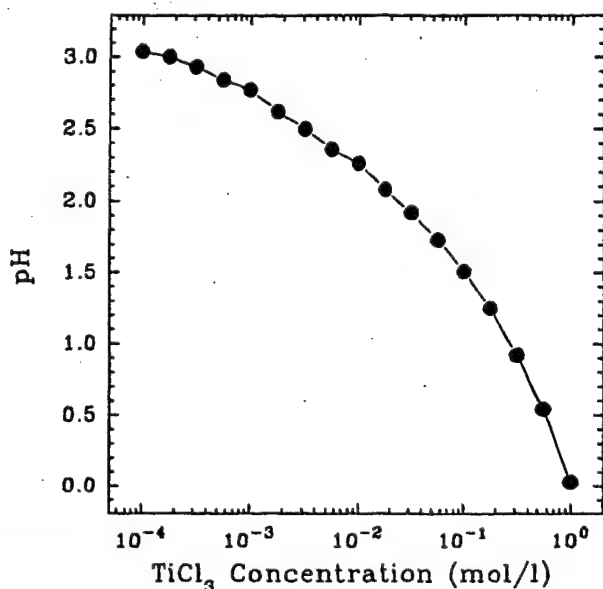


Using published hydrolysis constants,⁵⁰ a distribution diagram of hydrolysis products can be calculated for Ti^{3+} ions, similar to that for other ions.^{50,51} Figure A-1 shows the distribution diagram (assuming the activity coefficient of $H^+ = 1$ at all pH, which is not a good assumption at low pH) for trivalent titanium at ionic strength, I , of 1 mol/kg H₂O. The distribution diagram for $I = 3$ mol/kg H₂O (not shown) is nearly identical, with the curves shifted slightly to the left. The ionic strength, I , is defined as⁵⁰

Fig. A-1. Distribution diagram for Ti^{3+} and its hydrolysis products.

$$I = \frac{\sum z_i^2 [i]}{2} \quad [\text{A-2}]$$

where z and i are the charge and concentration, respectively, of each individual species. Figure A-1 assumes titanium ion additions to 0.6 M NaCl, such that 0.6 of the 1. mol/kg H_2O ionic strength is attributable to sodium and chloride ions added as NaCl. The distribution diagram indicates that Ti^{3+} additions to neutral 0.6 M NaCl solution readily hydrolyze and that TiOH^{2+} is the dominant hydrolysis product. To confirm this calculation, TiCl_3 was added to distilled, deionized water in an inert atmosphere and the pH recorded. Concentrations of 10^{-4} to 1 M TiCl_3 were examined (see Fig. A-2). The pH of the solution was

Fig. A-2. Variation of measured pH for various TiCl_3 concentrations in distilled, deionized water in an inert atmosphere.

found to decrease from neutral to about pH 3 when 10^4 M TiCl_3 was added. At 1 M TiCl_3 , the pH approached 0.

REFERENCES

1. L. M. Young, G. A. Young, Jr., J. R. Scully, and R. P. Gangloff, *Metall. Trans. A*, **26A**, 1257 (1995).
2. L. M. Young, M. S. Thesis, University of Virginia, Charlottesville, VA (1993).
3. B. P. Somerday, J. P. Grandle, and R. P. Gangloff, in *Proceedings of the Tri-Service Conference on Corrosion*, p. 375, Materials Laboratory, Wright Patterson Air Force Base, OH (1994).
4. G. A. Young, *Scr. Metall.*, **28**, 507 (1993).
5. F. P. Ford, *Met. Sci.*, 326 (1978).
6. D. G. Kolman and J. R. Scully, *This Journal*, **140**, 2771 (1993).
7. D. G. Kolman and J. R. Scully, *ibid.*, **141**, 2633 (1994).
8. T. R. Beck, *ibid.*, **115**, 890 (1968).
9. T. R. Beck, in *Passivity of Metals*, R. P. Frankenthal and J. Kruger, Editors, p. 1035, The Electrochemical Society Corrosion Monograph Series, Princeton, NJ (1978).
10. H. J. Rätzer-Scheibe, in *Passivity of Metals and Semiconductors*, M. Froment, Editor, p. 731, Elsevier Science Publishers, Amsterdam (1983).
11. H. J. Rätzer-Scheibe, in *Proceedings of the 8th International Congress on Corrosion*, p. 212, Mainz, Germany (1981).
12. H. J. Rätzer-Scheibe and H. Buhl, in *Titanium Science and Technology - Proceedings of the 5th International Conference on Titanium*, G. Lütjering, U. Zwicker, and W. Bunk Editors, Vol. 4, p. 2641, Deutsche Gesellschaft für Mettalkunde, Germany (1984).
13. I. A. Ammar and I. Kamal, *Electrochim. Acta*, **16**, 1539 (1971).
14. T. R. Beck, *ibid.*, **18**, 815 (1973).
15. D. G. Kolman and J. R. Scully, *This Journal*, **142**, 2179 (1995).
16. G. T. Burstein and A. J. Davenport, *ibid.*, **136**, 936 (1989).
17. G. S. Frankel, B. M. Rush, V. A. Brusic, S. M. Mirzamaani, and A. J. Davenport, in *Corrosion of Electronic Materials and Devices*, J. D. Sinclair, Editor, PV 91-2, p. 263, The Electrochemical Society Proceedings Series, Pennington, NJ (1991).
18. G. S. Frankel, B. M. Rush, C. V. Jahnes, C. E. Farrell, A. J. Davenport, and H. S. Isaacs, *This Journal*, **138**, 643 (1991).
19. A. J. Davenport and H. S. Isaacs, in *Transient Techniques in Corrosion Science and Engineering*, W. H. Smyrl, D. D. Macdonald, and W. J. Lorenz, Editors, PV 89-1, p. 357, The Electrochemical Society Proceedings Series, Pennington, NJ (1989).
20. P. D. Bastek, R. C. Newman, and R. G. Kelly, *This Journal*, **140**, 1884 (1993).
21. H. J. Pearson, G. T. Burstein, and R. C. Newman, *ibid.*, **128**, 2297 (1981).
22. P. O. Gartland, SINTEF Publication STF16-A88085, Trondheim, Norway (1988).
23. T. R. Beck, in *Proceeding of the Conference on Fundamental Aspects of Stress Corrosion Cracking*, R. W. Staehle, A. J. Forty, and D. VanRooyen, Editors, p. 608, NACE, Houston, TX (1969).
24. (a) D. C. Silverman, *Corrosion*, **38**, 541 (1982); (b) J. W. Olver and J. W. Ross, Jr., *J. Am. Chem. Soc.*, **85**, 2565 (1963); (c) G. B. Naumov, B. N. Ryzhenko, and I. L. Khodakawsky, *Handbook of Thermodynamic Data*, USGS Translation, USGS-WRD-74-000 (1974); (d) D. D. Wagman, NBS Technical Note 270-3, 270-5 (1971); (e) D. P. Feldman, V. M. Berdonikov, and B. P. Matseevskii, *Russ. J. Phys. Chem.*, **49**, 1858 (1975).
25. *Atlas of Electrochemical Equilibria in Aqueous Solutions*, M. Pourbaix, 2nd ed., NACE, Houston, TX (1974).
26. M. Pourbaix, in *The Theory of Stress Corrosion Cracking*, J. C. Scully, Editor, p. 17, NATO Scientific Affairs Division, Brussels, Belgium (1971).
27. T. R. Beck, *Electrochim. Acta*, **18**, 807 (1973).
28. M. Fleischmann and H. R. Thirsk, in *Advances in Electrochemistry and Electrochemical Engineering*, Vol. 3, P. Delahay and C. W. Tobias, Editors, p. 123, John Wiley & Sons, Inc., New York (1963).
29. D. Laser, M. Yaniv, and S. Gottesfeld, *This Journal*, **125**, 358 (1978).
30. J. R. Ambrose and J. Kruger, *ibid.*, **121**, 599 (1974).

31. F. P. Ford, *J. Pressure Vessel Technol.*, **110**, 113 (1988).
32. N. F. Cabrera and N. F. Mott, *Rep. Prog. Phys.*, **12**, 163 (1948/1949).
33. B. MacDougall, *This Journal*, **130**, 114 (1983).
34. T. R. Beck, *Corrosion*, **30**, 408 (1974).
35. T. R. Beck and E. A. Grens II, *This Journal*, **116**, 177 (1969).
36. G. T. Burstein and D. H. Davies, *ibid.*, **128**, 33 (1981).
37. G. T. Burstein and P. I. Marshall, *Corros. Sci.*, **23**, 125 (1983).
38. L. I. Krishtalik, in *Comprehensive Treatise of Electrochemistry, Kinetics and Mechanisms of Electrode Processes*, B. E. Conway, J. O'M. Bockris, E. Yeager, S. U. M. Khan, and R. E. White, Editors, Vol. 7, p. 87, Plenum Press, New York (1983).
39. R. Audubert, *Discuss. Faraday Soc.*, **1**, 72 (1947).
40. D. G. Kolman, Ph.D. Thesis, University of Virginia, Charlottesville, VA (1996).
41. M. J. Blackburn, J. A. Feeney, and T. R. Beck in *Advances in Corrosion Science and Technology*, M. G. Fontana, Editor, Vol. 3, p. 67, Plenum Press, New York (1972).
42. A. Caprani, J. P. Frayret, R. Pointeau, S. K. Marya, and F. Le Maitre, *Electrochim. Acta*, **28**, 141 (1983).
43. A. Caprani and J. P. Frayret, *J. Less-Common Met.*, **69**, 29 (1980).
44. A. Caprani and J. P. Frayret, *Electrochim. Acta*, **24**, 835 (1979).
45. J. P. Frayret and A. Caprani, *ibid.*, **27**, 391 (1982).
46. J. P. Frayret, A. Caprani, T. Jaszay, and F. Priem, *Corrosion*, **41**, 656 (1985).
47. E. J. Kelly and H. R. Bronstein, *This Journal*, **131**, 2232 (1984).
48. P. K. Subramanyan, in *Comprehensive Treatise of Electrochemistry*, J. O'M. Bockris, Editor, Vol. 4, p. 411, Plenum Press, New York (1981).
49. B. F. Brown, C. T. Fujii, and E. P. Dahlberg, *This Journal*, **116**, 218 (1969).
50. C. F. Baes, Jr. and R. E. Mesmer, *The Hydrolysis of Cations*, Krieger Publishing Co., Malabar, FL (1986).
51. R. G. Buchheit, J. P. Moran, and G. E. Stoner, *Corrosion/90*, Paper No. 93, NACE, Houston, TX (1990).
52. R. J. H. Wanhill, *Br. Corros. J.*, **10**, 69 (1975).
53. B. D. Lichter, R. M. Bhatkal, and W. F. Flanagan, in *Parkins Symposium on Fundamental Aspects of SCC*, S. Bruemmer, Editor, p. 270, TMS, Warrendale, PA (1992).
54. T. Yu and J. R. Scully, Submitted to *Corrosion* (March 1996).

**On the Requirements for a Sharp Notch or Precrack to Cause
Environmentally Assisted Crack Initiation of β -Titanium
Alloys Exposed to Aqueous Chloride Environments**

D. G. Kolman and J. R. Scully

David G. Kolman¹ and John R. Scully²

ON THE REQUIREMENT FOR A SHARP NOTCH OR PRECRACK TO CAUSE ENVIRONMENTALLY ASSISTED CRACK INITIATION IN β -TITANIUM ALLOYS EXPOSED TO AQUEOUS CHLORIDE ENVIRONMENTS

Kolman, D.G. and Scully, J.R., "On The Requirement For A Sharp Notch or Precrack To Cause Environmentally Assisted Crack Initiation Of β -Titanium Alloys Exposed To Aqueous Chloride Environments", Effects of the Environment on the Initiation of Crack Growth, ASTM STP 1298, W.A. Van der Sluys, R.S. Piascik, and R. Zawierucha, Eds., American Society for Testing and Materials, 1997.

ABSTRACT: The requirement of a sharp notch or precrack to cause environmental crack initiation of metastable β -titanium alloys exposed to 0.6 M NaCl has been observed. The causal relationship has not been thoroughly examined, however. This paper seeks to explain the sharp notch requirement by examining notch acuity effects on a variety of parameters that affect HEAC susceptibility. These include the effects of a sharp notch on cation accumulation - hydrolysis - acidification, potential drop in solution and resulting hydrogen production, and localization of dynamic strain. It is shown that solution resistance down a sharp crack is two orders of magnitude larger for a fatigue precracked compact tension specimen than for a smooth bar. The potential drop down a sharp crack is severe enough to enable hydrogen production even when the applied potential is more positive than the reversible potential for hydrogen production. It also shown that a fatigue precrack results in an acidified crack tip chemistry (approximately pH 1) which is deleterious to HEAC resistance. The effects of a sharp notch on the interplay of mechanics, film rupture and hydrogen uptake are also examined. It is shown that the slip behavior at a sharp crack tip promotes localized film rupture and localized hydrogen uptake. Localization of hydrogen uptake may be critical for HEAC susceptibility in light of the large hydrogen concentration required to cause crack initiation (ca. 1000 wt. ppm) and the lack of significant hydrogen uptake on filmed surfaces.

¹ Postdoctoral Research Associate, MS G755, Los Alamos National Laboratory, Los Alamos, NM, 87545.

² Associate Professor, Department of Materials Science and Engineering, University of Virginia, Charlottesville, VA 22903.

KEYWORDS: Hydrogen environmentally assisted cracking (HEAC), notch radius, β -titanium alloys, crack tip solution acidification, ohmic loss, bare surface electrode kinetics, film rupture, hydrogen uptake, fatigue precrack.

INTRODUCTION

Environmentally assisted cracking (EAC) of titanium alloys exposed to aqueous chloride environments has been observed by many researchers [1,2,3,4,5,6,7,8,9,10]. EAC has been noted on α (hcp), β (bcc), $\alpha+\beta$ and $\beta+\alpha$ alloys. In the case of both α - and β -titanium alloys, a pre-existing sharp notch is usually required for EAC with a few exceptions (e.g., Ti - 8 Mn and Ti - 13 V - 11 Cr - 3 Al) [6]. Beck examined the effect of notch root radius on the EAC behavior of Ti - 8 Al - 1 Mo - 1 V [7] and found that the alloy was immune to EAC when exposed to 0.6 M LiCl at $-0.5V_{SCE}$ for notch radii greater than 250 μm . Conversely, radii less than 250 μm produced EAC, with susceptibility increasing as the notch radius decreased. Lane and Cavallaro observed the same phenomenon on Ti - 7 Al - 2 Nb - 1 Ta [11]. Several recent studies on solution treated (ST) and solution treated and aged (STA) β -titanium alloys, such as Ti - 15 Mo - 3 Nb - 3 Al and Ti - 3 Al - 8 V - 6 Cr - 4 Mo - 4 Zr, have employed smooth or blunt notch specimens [12,13,14,15]. In contrast to the results for precracked specimens, no EAC was observed. Further, others have suggested that localized plastic deformation under crevice conditions may be required for EAC [11] and a sharp notch or precrack appears to promote both these phenomena. Although the sharp notch requirement has been widely observed and cited in titanium alloy EAC literature, there is little discussion in the literature of the underlying reasons for the necessity of a sharp notch. This paper seeks to explain this phenomenon.

It has been well documented that EAC of α -titanium alloys is controlled by hydriding of the α phase [16,17,18,19,20,21]. For the case of STA β -titanium alloys, a hydrogen environmentally assisted cracking (HEAC) mechanism has been proposed [1,2,3], in light of the link established between lattice and trapped hydrogen and intergranular cracking [22]. Interestingly, EAC has been observed for both α - and β -titanium alloys during potentiostatic tests where the applied potential was more positive than the reversible potential for hydrogen production [1,2,3,5,7]. Such results indicate that potential drop between the reference electrode and the crack tip is required to produce hydrogen and the resulting damage. It is possible that one requirement for a sharp notch arises from a need to generate a restrictive solution path, increasing the potential drop in solution. This is one focus area of this paper.

A variety of precracked $\alpha+\beta$ and $\beta+\alpha$ alloys have been shown to be susceptible to EAC in neutral pH environments [6]. It has also been shown that: 1) precracked $\alpha+\beta$ alloys are immune to cracking at $-1V_{SCE}$ in neutral solutions but are susceptible to cracking at $-1V_{SCE}$ when exposed to strongly acidic bulk environments [6,8]; 2) at potentials where cracking is observed, cracking can be slowed or eliminated in strongly alkaline bulk

environments [6]; and 3) an acidic crack tip chemistry forms in a neutral bulk environment [23]. It is likely that the pH and potential dependencies are linked. The EAC immunity of precracked specimens observed below $-1V_{SCE}$ in neutral solution appears to result from proton or water reduction in the occluded region near the crack tip which increases the crack tip pH. In strongly acidic environments, it is likely that the cathodic polarization is unable to overcome the bulk acidity, uptake occurs via process zone charging (and possibly by bulk surface ingress if oxide films are destabilized) and cracking occurs. Conversely, in strongly alkaline environments, both process zone and filmed surface uptake is limited. Crack tip acidification due to hydrolysis and / or oxide formation [24] is unable to overcome the bulk alkalinity and EAC immunity results. Since the susceptibility in acidic solutions and the immunity in alkaline solutions appears to be independent of applied potential, it is reasonable to assert that the observed potential dependency in neutral solutions originates from the alteration of the crack tip solution pH and not from the electrochemical potential per se. Since a sharp notch or crack results in an occluded region, it is possible that a sharp notch results in an acidic crack tip chemistry which is deleterious to the EAC resistance of titanium alloys. It is an object of this paper to examine this aspect of sharp notches as well.

A difference in mechanics generated by varying notch acuity likely plays a role in EAC susceptibility. Research by Young and Scully incorporating hydrogen precharged STA Ti - 15 Mo - 3 Nb - 3 Al circumferentially notched tensile bars (CNTBs) tested in air showed that the increased constraint produced by reduced notch radius promoted lower failure stress [22]. Since the CNTBs were not exposed to the embrittling environment, it is clear that some component of EAC arises from a purely mechanical interaction of stress and hydrogen. Moreover, notch acuity has been shown to alter the slip offset during film rupture events [2], which may affect EAC susceptibility. Therefore, another goal of this paper is to examine the effects of notch acuity on the interplay of stress, hydrogen concentration and film rupture, and to relate them to observed EAC behavior.

EXPERIMENTAL PROCEDURE

The physical metallurgy of Ti - 15 Mo - 3 Nb - 3 Al (Ti - 14.9 Mo - 2.64 Nb - 3.15 Al (wt%)) has been described elsewhere [3,25]. Ti - 15 Mo - 3 Nb - 3 Al was solutionized for 8 h at 871°C (1600°F) followed by an air cool. Aging of STA material comprised a subsequent single step heat treatment at 538°C (1000°F) for 8 h followed by an air cool.

0.6 M NaCl solutions ($\kappa = 0.0521 (\Omega\text{-cm})^{-1}$) incorporated reagent grade NaCl added to distilled deionized water. Other 0.6 M NaCl solutions were adjusted to alkaline pH values with reagent grade NaOH or to acidic values with reagent grade HCl. 5 M HCl solutions ($\kappa = 0.602 (\Omega\text{-cm})^{-1}$, calculated pH = -1.64 [26]) incorporated reagent grade HCl added to distilled deionized water.

Electrochemical tests incorporated a PAR 273 potentiostat and a variety of different data recording devices. Experimental procedures and sample geometries for CNTB [2] and compact tension (CT) specimen [1] tests are detailed elsewhere. The radius of the circumferential notch on each CNTB was 0.544 mm.

RESULTS

Sharp notch - fatigue precracked CT specimen tests

Threshold stress intensities (K_{th}) for precracked STA β -titanium alloys exposed to chloride environments at different potentials are shown in Figure 1. The fracture toughnesses of the alloys in air are similar to the stress intensities observed at the most negative potential shown for each alloy in Figure 1. Thus, EAC immunity is observed at the most negative potentials. Conversely, a dramatic reduction in K_{th} is observed at more positive potentials, with a minimum observed at intermediate potentials. At these potentials, precracked STA β -titanium alloys are highly susceptible to EAC.

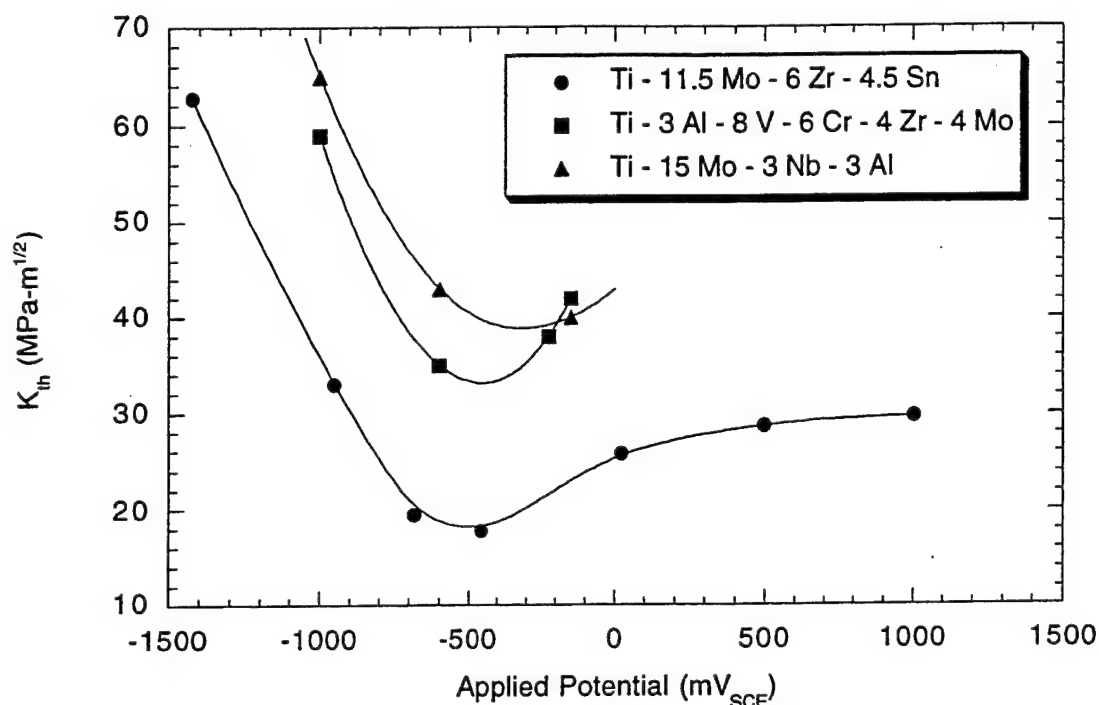


Figure 1 - Plot of threshold stress intensities for various precracked STA β -titanium alloys exposed to 0.6 M NaCl. (Ti - 11.5 Mo: reference 6; Ti - 3 Al: reference 5; Ti - 15 Mo: reference 3).

Blunt notch - circumferentially notched tensile bar tests

The ratio of the failure load in environment to the failure load in air for different blunt notched and smooth bar β -titanium specimens exposed to chloride solutions at different potentials is shown in Figure 2. It is seen that the ratio is approximately 1 for both STA Ti - 15 Mo - 3 Nb - 3 Al and STA Ti - 3 Al - 8 V - 6 Cr - 4 Mo - 4 Zr, indicative of EAC immunity. In contrast to precracked samples (Figure 1), no reductions in failure load (Figure 2) or reduction in area (not shown) are observed at any applied potential in environment. Thus, EAC susceptibility depends not only on applied potential, but the presence of a sharp notch also.

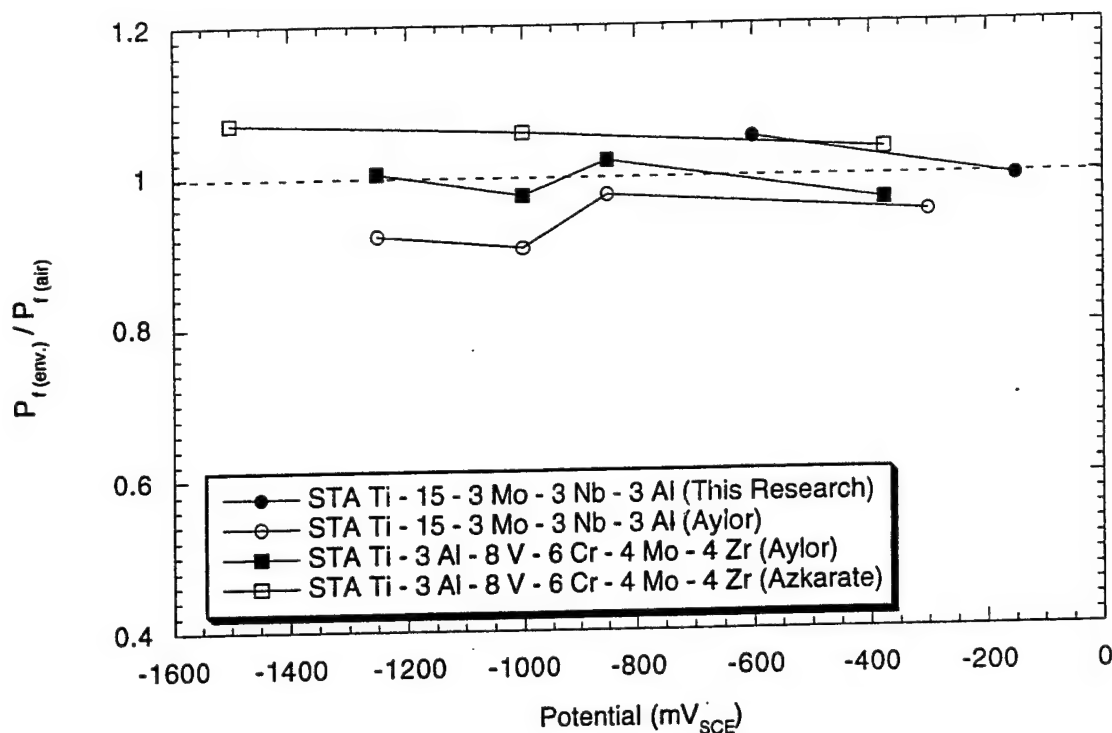


Figure 2 - Ratio of failure load in environment to that in air for blunt notch and smooth β -titanium alloys exposed to chloride environments. A ratio of 1 is indicative of EAC immunity. Data from Azkarate and Aylor are from references 12 and 15, respectively.

Hydrogen uptake as a function of pH

As shown in Figure 1, K_{th} exhibits a strong potential dependency when samples are precracked. Since the potential dependency of HEAC is believed to be related to crack or notch solution pH, hydrogen uptake experiments were conducted with chloride solutions of varying pH. STA Ti - 15 Mo - 3 Nb - 3 Al foils (0.38 mm thickness) were polarized to $-1V_{SCE}$ for 5 days. The samples were subsequently analyzed for hydrogen concentration. The results for samples exposed to 0.6 M NaCl adjusted to pH 10, 0.6 M NaCl, 0.6 M NaCl adjusted to pH 1 and 5 M HCl are seen in Figure 3. It is seen that no hydrogen uptake occurred on the foils exposed to pH 10, 6 and 1 solution. That is, the hydrogen concentrations within the foils were similar to that in the as-received material. Conversely, significant hydrogen uptake was found to occur on foils exposed to 5M HCl.

A crack tip pH of 1.8 has been measured on Ti - 8 Al - 1 Mo - 1 V following crack propagation at open circuit [23]. Assuming that this pH is similar to that which occurs with β -titanium alloys, it can be inferred that hydrogen uptake through the oxide would be precluded during EAC, even near the crack tip. In other words, there would be an almost complete lack of "bulk" hydrogen uptake away from the crack tip. Therefore, hydrogen uptake must occur at the bare crack tip following film rupture in order to explain EAC by hydrogen embrittlement. Potential drop in solution, crack tip acidification and localization of film rupture are also required. These are discussed below.

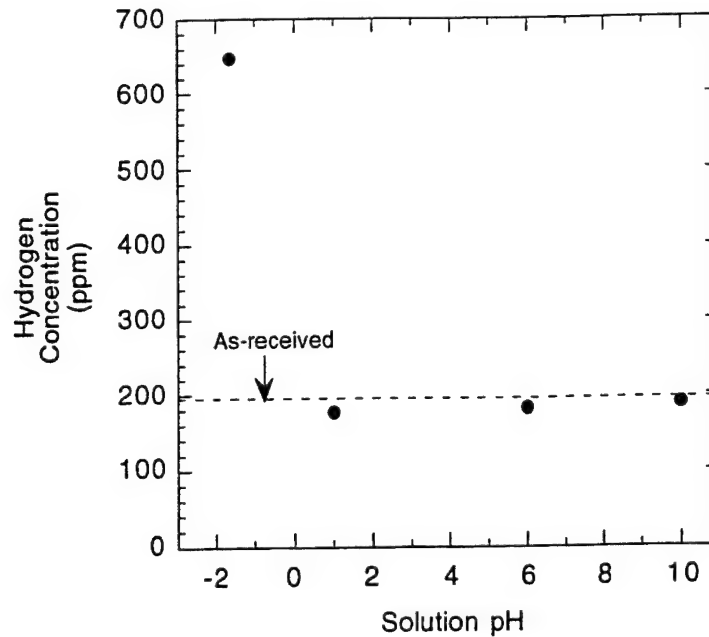


Figure 3 - Hydrogen concentration measured in 0.38 mm thick STA Ti - 15 Mo - 3 Nb - 3 Al foils following cathodic polarization to $-1 V_{SCE}$ for 5 days. All solutions are 0.6 M NaCl (pH adjusted) except pH -1.64 which is 5 M HCl.

DISCUSSION

Potential drop in solution

It is apparent that potential drop in solution is necessary for HEAC when the applied potential is more positive than the reversible potential for hydrogen production. Since HEAC is observed in conductive solutions, a restrictive solution pathway is required to generate significant potential drop. The presence of a sharp notch fulfills this requirement.

Both experiment and theory predict large ohmic loss in solution when a sharp notch or precrack is present. Experiments incorporating a model CT specimen indicated that the solution resistance between a crack tip and the bulk solution was a minimum of 2.2 k Ω in 0.6 M NaCl [1]. Additionally, the effect of crack angle on the solution resistance can be estimated using a model proposed by Newman [27] (Table 1)³. It is seen that the solution resistance is over 2 orders of magnitude larger to a CT specimen crack tip than to a smooth bar. At the solution resistance estimated for the Ti - 3 Al - 8 V - 6 Cr - 4 Zr - 4 Mo CT specimen geometry of Figure 1 (4300 Ω), calculations indicate that when an area as little as 1/500th of the crack tip ($5 \times 10^{-7} \text{ cm}^2$) is bared following film rupture, ohmic loss is so severe that the crack tip potential never exceeds the reversible potential for hydrogen

³ The values for parameters in the Newman model were obtained experimentally: $\rho = 19.2 \text{ } \Omega\text{-cm}$ (0.6 M NaCl), $w_0 = 1 \text{ CTOD} = 5 \times 10^{-4} \text{ cm}$, $i_t = 270 \text{ A/cm}^2$ ($E_{app} = -0.6 V_{SCE}$, 0.6 M NaCl), $i_w = 10^{-7} \text{ A/cm}^2$ (0.6 M NaCl), $L = 2.4 \text{ cm}$.

production regardless of the applied potential [1]. Moreover, because the model does not account for crack tortuosity, the solution resistances are likely even larger. Further, it has been estimated that solution resistances greater than 100 k Ω would be obtained when preferential dissolution occurs at grain boundaries intersecting the crack tip [1]. It is possible then to generate significant potential drop before crack initiation even when the crack tip current is on the order of microamps. Currents on the order of microamps have been measured preceding crack initiation [28]. Therefore, hydrogen production is possible in a sharp notch before crack initiation, even when the applied potential is more positive than the reversible potential for hydrogen production. This explains, in part, the HEAC susceptibility observed in Figure 1 at potentials more positive than the reversible potential for hydrogen production.

TABLE 1[†] -- Calculated crack tip parameters as a function of crack angle

Crack Angle (radians)	Solution Resistance (Ω)	Crack tip Ti^{3+} concentration (mol/l)	Crack tip (near surface) solution pH
0.0054	7400	0.47	0.6
0.011 ^{††}	4300	0.27	1.0
0.021	2500	0.16	1.3
0.11	640	0.040	1.9
1.1	84	0.0053	2.3
3.14 ^{†††}	7.6	2.3×10^{-6}	5.6

† - Solution resistance and crack tip Ti^{3+} concentration were calculated from equations 8 and 7, respectively, of reference 27 and assuming currents similar to those seen preceding crack initiation [1,24]. Solution pH values were correlated with Ti^{3+} concentrations via reference 24. The diffusivity of Ti^{3+} ($= 8.5 \times 10^{-6} \text{ cm}^2/\text{s}$) was obtained from estimates in the literature [29].

†† - Estimated crack angle of CT specimen at K_{th} in Figure 1.

††† - Smooth bar. Solution resistance calculated from ref. 30 for the smooth bar experiments of Figure 2 from this research. Ti^{3+} concentration calculated from the mass transport limited current density, assuming a diffusion layer thickness of 30 μm .

Crack tip solution acidification

An acidified crack tip solution is a prerequisite for EAC of β -titanium alloys exposed to 0.6 M NaCl. Acidification has been shown to promote hydrogen entry in two ways. First, it has been shown that an acidified solution enhances hydrogen production kinetics on bare titanium following film rupture [1,24]. Enhanced hydrogen production arises from an increased overpotential for hydrogen production following film rupture and ohmic drop in solution [1].

Hydrogen uptake also can be enhanced on a filmed titanium surface exposed to strongly acidic solutions (Figure 3). It is likely that the hydrogen uptake in low pH solution results from the presence of a nonprotective film. In-situ characterization of STA

Ti - 15 Mo - 3 Nb - 3 Al exposed to 5 M HCl indicated that the material was spontaneously active at open circuit even though a film was present [31]. This result is in agreement with other research which noted that a porous film of Ti_2O_3 was present in the active region [32]. Conversely, a passive film of TiO_2 is observed on STA Ti - 15 Mo - 3 Nb - 3 Al exposed to 0.6 M NaCl, pH 1 [31]. It appears, therefore, that there is a transition in film properties between pH 1 and pH -1.64 wherein the film becomes nonprotective.

It is apparent from the literature [33,34,35] and Figure 3 that bulk charging of titanium through the oxide is unlikely in room temperature neutral solutions above $-1V_{\text{SCE}}$ because the oxide (TiO_2) is a strong barrier to hydrogen uptake. Moreover, the very slow hydrogen diffusivity through the oxide and through the β -titanium matrix itself [22,33], makes bulk (i.e., noncrack tip) charging of the process zone unlikely for either sharp or blunt notched specimens. Therefore, hydrogen entry must occur either at the crack tip (where depassivation occurs) or in close proximity to the crack tip (where the pH results in an oxide with a reduced barrier to hydrogen entry).

The concentration of Ti^{3+} near the crack tip was estimated using equations developed by Newman [27] (Table 1). The concentration of Ti^{3+} was converted to a solution pH via reference 24. Table 1 reveals that increasing notch acuity results in a reduced crack tip solution pH, as would be expected. It is seen that the near-surface pH is much lower for a sharp notch than a smooth bar. A crack tip pH of 1.0 was calculated for the CT specimen test of Figure 2. At this pH, uptake on a filmed surface would not be expected (Figure 3). Therefore, hydrogen entry is restricted to the bare crack tip surface following mechanical depassivation.

A minimum in K_{th} at intermediate potentials has been observed for many different β -titanium alloys [3,5,6], as seen in Figure 1. Since hydrogen production and crack tip acidification are prerequisites for EAC (see Introduction), it is likely that the minimum at $-0.5V_{\text{SCE}}$ results from a maximization of the hydrogen production / crack tip acidification combination. A maximum susceptibility to EAC would be expected at some intermediate potential because crack tip acidification increases with potential⁴ while hydrogen production decreases with potential. This is shown schematically in Figure 4.

The question arises as to how hydrogen production and crack tip acidification can occur concurrently. The answer can be discerned from the repassivation behavior, as follows. It has been shown that film rupture is required for EAC of β -titanium alloys [1] and that film rupture indeed precedes [2] crack initiation. Fractured thin film tests on titanium⁵ indicate that anodic current densities greater than 100 A/cm^2 can occur during the initial period following depassivation [24]. The majority of this current was shown to go towards dissolution of titanium ($\text{Ti} \rightarrow \text{Ti}^{3+}$) rather than towards film reformation [24]. The

⁴ Tests (not shown) have confirmed that a crack tip becomes alkaline with cathodic polarization in a bulk solution of 0.6 M NaCl. Crevice pH values of 9.85 and 11.3 were measured following polarization of a creviced Ti - 15 Mo - 3 Nb - 3 Al sample to $-0.65 V_{\text{SCE}}$ and $-1V_{\text{SCE}}$, respectively.

⁵ Fractured thin film tests are indicative of the true surface response following rapid film rupture because the peak currents are less than the ohmic limit and the rapid fracture rate eliminates depassivation speed limitations.

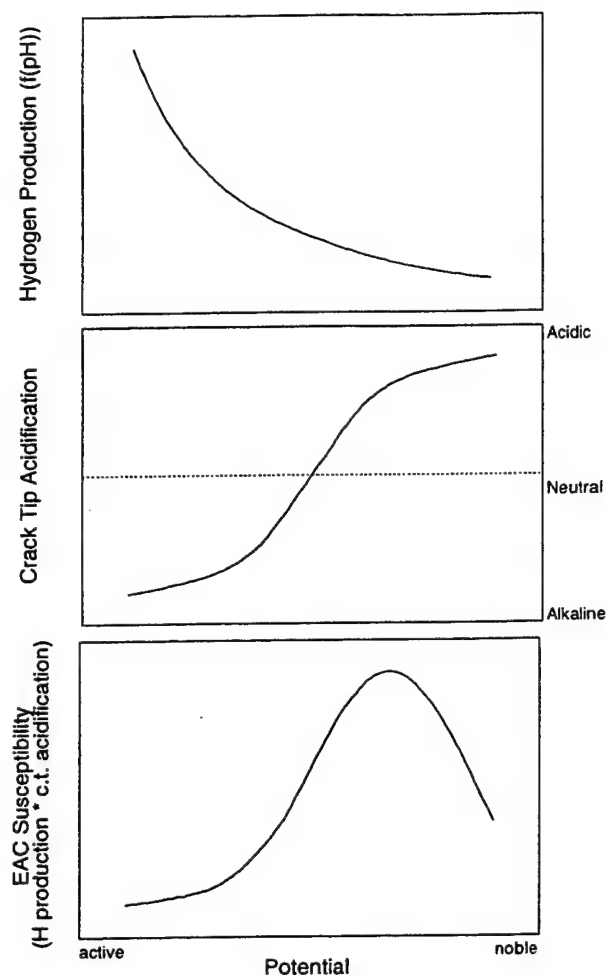


Figure 4 - Schematic representation of hydrogen production, crack tip acidification and EAC susceptibility vs. applied potential for a titanium alloy.

driving force for the large anodic reaction rates is the large anodic overpotential. The overpotential is large because the bare surface open circuit potential is very negative ($-1.58V_{SCE}$ in 0.6 M NaCl) [24]. As repassivation commences, the open circuit potential of the repassivating surface increases. When the open circuit potential becomes more positive than the actual surface potential, the net current on the repassivating surface becomes negative and cathodic reactions (almost entirely hydrogen production) dominate. These current densities may be quite significant ($> 1 A/cm^2$), depending upon potential. The overall net charge passed on the depassivated surface is positive (anodic), however, for applied potentials above approximately $-1.2V_{SCE}$ [24]. Since the majority of this charge is dissolution product (Ti^{3+}), and since hydrolysis of Ti^{3+} results in strong solution acidification [24], film rupture will result in crack tip solution acidification in the absence of strong cathodic polarization.

Film rupture (as measured by anodic current) has been shown to increase with increasing K preceding crack initiation [2]. Since the initial film rupture events are smaller in current amplitude, they are less likely to result in significant potential drop (i.e., ohmic drop severe enough to lower the potential below the reversible potential for hydrogen production). They would yield solution acidification however. As the magnitude of the

anodic current emanating from the crack tip increases, significant ohmic drop becomes increasingly likely. Thus, hydrogen production would occur in the presence of an acidified crack tip solution, which appears to be a prerequisite for cracking as discussed above. In summary, solution acidification and hydrogen production are not mutually exclusive events with both occurring following film rupture.

Mechanical effects

The resulting difference in mechanics between blunt and sharp notches may play a role in EAC susceptibility. Research by Young and Scully showed that hydrogen precharged STA Ti - 15 Mo - 3 Nb - 3 Al CNTBs tested in air were embrittled by hydrogen concentrations greater than 1000 ppm and produced intergranular fracture similar to that observed following EAC [22]. These tests showed that the increased constraint produced by reduced notch radius promoted lower failure loads. This result suggested that a critical combination of local tensile stress, hydrogen concentration and governing microstructural features may be required for HEAC of β -titanium alloys exposed to 0.6 M NaCl [22].

A second effect of notch acuity with respect to mechanics is the localization of slip. High speed current recordings indicate that quasi-continuous film rupture precedes crack initiation [2]. Moreover, it has been shown that film rupture is attributable to dislocation intersection of the surface, as opposed to exceeding the tensile failure strain of the oxide [2]. Since a bare surface is required for hydrogen entry, hydrogen entry on β -titanium alloys must occur as a result of slip. Indeed, it has been shown that dynamic straining is required for EAC of β -titanium alloys exposed to 0.6 M NaCl [3,4,5]. The relationship between notch radius and HEAC may therefore be attributable in part to slip behavior, as follows.

It is often stated that a sharp crack tip has the effect of localizing dislocation motion to a few favorably oriented slip planes [36]. Since film rupture is attributable to slip, it may be inferred that increasing notch acuity results in film rupture localization. This has been confirmed through experimentation incorporating STA Ti - 15 Mo - 3 Nb - 3 Al. Tests were performed utilizing three different geometries [2] - a smooth bar, a CNTB and a CT specimen. The net anodic charge passed preceding cracking in 0.6 M NaCl was obtained by integration of current - time data above the background current (the steady state or passive current). These charges are shown in Table 2⁶. The charge can be divided by the surface area adjacent the plastic zone for each geometry to yield a charge density. This charge density is directly proportional to the quantity of bare area generated adjacent the plastic zone and, hence, the intensity of film rupture. In other words, the charge density is a direct measure of film rupture localization. Results in Table 2 indicate that the film rupture intensity (charge density) for the smooth bar and CNTB are similar. These intensities are greater than one thousand times smaller than that of the CT specimen. Therefore, film rupture is far more localized for the EAC susceptible geometry than for the EAC immune geometries.

⁶ The charges shown in Table 2 actually underestimate the true anodic charge because of the experimental method employed [2]. The underestimate is highest for the CT specimen (as much as 50%) and lowest for the smooth bar (as much as 2%).

Slip localization has been correlated with EAC of ST [37] and STA [3] β -titanium alloys exposed to 0.6 M NaCl by different researchers. There are two possible reasons why slip localization promotes EAC. First, localization results in an increased slip offset. It has been hypothesized (but never proven) that these larger slip steps are more difficult to repassivate [38,39]. Second, slip localization results in film rupture localization, as shown in Table 2. Film rupture localization results in hydrogen uptake localization because hydrogen entry is restricted to bared surfaces as discussed above. Hydrogen uptake localization may be critical for HEAC in light of the large hydrogen concentrations required to embrittle β -titanium (> 1000 wt. ppm) and the lack of "bulk" hydrogen charging. A secondary effect may be to enhance dislocation transport of hydrogen to grain boundaries, which may be important in light of the intergranular nature of the HEAC of β -titanium alloys. Since HEAC appears to result from the attainment of a critical combination of hydrogen concentration and stress, and since a sharp crack tip increases both stress and local hydrogen concentration, a sharp crack tip appears to promote EAC of β -titanium alloys.

TABLE 2[†] -- Charges and plastic zone sizes for different geometries [2]

Geometry	Charge (C)	Plastic Zone Surface Area (mm ²)	Charge Density (C/mm ²)
Smooth	4×10^{-4}	130	3×10^{-6}
CNTB	2×10^{-5}	14	2×10^{-6}
Compact Tension	2×10^{-4}	0.022	8×10^{-3}

[†] - Charges were determined via integrations of the anodic currents above background during potentiostatic mechanical testing in 0.6 M NaCl. Plastic zone sizes are calculated at the onset of quasi-continuous film rupture [2]. The plastic zone for the smooth bar was assumed to comprise the entire smooth section of the bar. The CNTB plastic zone surface area / volume was obtained from finite element analysis. The CT specimen plastic zone surface area / volume was obtained from standard fracture mechanics calculations [40,41,42].

CONCLUSIONS

The causal relationship between notch acuity and HEAC of β -titanium alloys exposed to 0.6 M NaCl was examined. It was shown that the presence of a sharp notch produces a restricted pathway capable of generating ohmic loss in solution. This ohmic loss can be severe enough to result in a crack tip potential below the reversible potential for hydrogen production even when the applied potential exceeds this reversible potential. This is a requirement for HEAC. It was also shown that a sharp notch produces an occluded corrosion site. The solution pH at this site was shown to be lower than that achieved in the absence of a notch. Since an acidified solution has been correlated with EAC, a sharp crack tip may yield HEAC by forming an acidified crack tip solution. The effect of a sharp crack tip on HEAC was examined from a mechanics standpoint also. It

was shown that a sharp crack tip enhances HEAC by a slip localization phenomenon. Slip localization may be deleterious to the HEAC resistance of β -titanium alloys because of larger slip step production and localization of hydrogen uptake. In summary, a sharp notch enhances the HEAC susceptibility in a variety of disparate ways. The enhancement of ohmic loss in solution, crack tip acidification and localized hydrogen uptake (in the absence of "bulk" uptake) explains the widely observed requirement of a sharp notch for HEAC. In contrast, smooth or blunt notched samples lack sufficient potential drop, solution acidification and strain localization to enable hydrogen uptake, resulting in EAC immunity.

ACKNOWLEDGMENTS

The authors would like to acknowledge the Office of Naval Research (Grant No. N00014-91-J-4164) for their support of this work and TIMET for their generous donation of alloys. The authors gratefully acknowledge R.P. Gangloff, R.G. Kelly, and F.P. Ford for their helpful discussions and B.P. Somerday, M.A. Gaudett and D.G. Enos for their aid with various tests.

REFERENCES

- 1) D.G. Kolman and J.R. Scully, Metallurgical Transactions A, in review.
- 2) D.G. Kolman, Ph.D. Dissertation, University of Virginia, Charlottesville, VA, 1996.
- 3) L.M. Young, G.A. Young, Jr., J.R. Scully and R.P. Gangloff, Metallurgical Transactions A, Vol. 26A, 1995, p. 1257.
- 4) L.M. Young, M.S. Thesis, University of Virginia, Charlottesville, VA, 1993.
- 5) B.P. Somerday, J.P. Grandle and R.P. Gangloff in Proceedings of the Tri-Service Conference on Corrosion, Materials Laboratory, Wright Patterson Air Force Base, OH, 1994, p. 375.
- 6) M.J. Blackburn, J.A. Feeney, and T.R. Beck in Advances in Corrosion Science and Technology, Vol. 3, M.G. Fontana and R.W. Staehle eds., Plenum Press, New York, 1972 p. 67.
- 7) T.R. Beck, J. Electrochem. Soc., Vol. 114, 1967, p. 551.
- 8) D.T. Powell and J.C. Scully, Corrosion, Vol. 24, 1968, p. 151.
- 9) R.J.H. Wanhill, Br. Corr. J., Vol. 10, 1975, p. 69.
- 10) H. Buhl in Stress Corrosion Cracking - The Slow Strain Rate Technique. ASTM STP 665, G.M. Ugiansky and J.H. Payer eds., ASTM, Philadelphia, PA, 1979, p. 333.
- 11) I.R. Lane and J.L. Cavallaro, Applications Related Phenomena in Titanium Alloys. ASTM STP 432, ASTM, Philadelphia, PA, 1968, p. 147.
- 12) I. Azkarate and A. Pelayo, presented at the INASMET conference, San Sebastain Spain, 1992.
- 13) B. Bavarian, V. Wahi, G. Canzona and M. Zemanzedah in Beta Titanium Alloys in the 1990's, D. Eylon, R.R. Boyer and D.A. Koss eds., TMS, Warrendale, PA, 1993, p. 105.
- 14) D.E. Thomas and S.R. Seagle in Titanium '80. Science and Technology. Proceedings of the Fourth World Conference on Titanium, H. Kimura and O. Izumi eds., TMS, Warrendale, PA, 1980, p. 2533.
- 15) D.M. Aylor, "An environmental cracking evaluation of fastener materials for seawater applications", paper # 94484, NACE - Corrosion '94, Baltimore, MD, 1994.
- 16) G. Sanderson and J.C. Scully, Corrosion Science, Vol. 6, 1966, p. 541.
- 17) D.N. Williams, J. Inst. of Metals, Vol. 91, 1962-63, p. 147.
- 18) H.G. Nelson, in First Thermal Structures Conference, E. Thornton ed., University of Virginia, Charlottesville, VA, 1990, p. 301.

- 19) B.G. Pound, Corrosion, Vol. 47, 1991, p. 99.
- 20) D. Hardie in Environment-Induced Cracking of Metals, R.P. Gangloff and M.B. Ives eds., NACE, Houston, TX, 1990, p. 347.
- 21) I.I. Phillips, P. Poole and L.L. Shrier, Corrosion Science, Vol. 12, 1972, p. 855.
- 22) G.A. Young, Jr. and J.R. Scully, Corrosion, Vol. 50, 1994, p. 919.
- 23) B.F. Brown, C.T. Fujii, and E.P. Dahlberg, J. Electrochem. Soc., Vol. 116, 1969, p. 218.
- 24) D.G. Kolman and J.R. Scully, J. Electrochem. Soc., Vol. 143, 1996, p. 1847.
- 25) D.G. Kolman and J.R. Scully, J. Electrochem. Soc., Vol. 141, 1994, p. 2633.
- 26) P.O. Gartland, SINTEF publication STF16-A88085, Trondheim, Norway, 1988.
- 27) R.C. Newman, Corrosion, Vol. 50, 1994, p. 682.
- 28) D.G. Kolman and J.R. Scully, unpublished research.
- 29) T.R. Beck in Passivity of Metals, R.P. Frankenthal and J. Kruger eds., The Electrochemical Society, Pennington, NJ, 1978, p. 1035.
- 30) R.C. Newman in Corrosion Chemistry within Pits, Crevices and Cracks, A. Turnbull ed., Her Majesty's Stationery Office, London, 1987, p. 317.
- 31) D.G. Kolman and J.R. Scully, J. Electrochem. Soc., Vol. 140, 1993, p. 2771.
- 32) H. Kaesche, Metallic Corrosion, NACE, Houston, TX, 1985, p. 265.
- 33) J.E. Costa, D. Banerjee and J.C. Williams in Beta Titanium Alloys in the 80's, R.R. Boyer and H.W. Rosenberg eds., TMS, Warrendale, PA, 1984, p. 69.
- 34) R.W. Schutz and D.E. Thomas in ASM Handbook, Vol. 13, Corrosion, ASM International, Metals Park, OH, 1992, p. 669.
- 35) R.W. Schutz and L.C. Covington, Corrosion, Vol. 37, 1981, p. 585.
- 36) A.J. Forty in Proceedings of Conference, Fundamentals of Stress Corrosion Cracking, R.W. Staehle, A.J. Forty and D. VanRooyen eds., NACE, Houston, TX, 1969, p. 64.
- 37) R.E. Adams and E. von Tiesenhausen in Proceedings of Conference, Fundamentals of Stress Corrosion Cracking, R.W. Staehle, A.J. Forty and D. VanRooyen eds., NACE, Houston, TX, 1969, p. 691.
- 38) J.C. Scully, Corrosion Science, Vol. 7, 1967, p. 197.
- 39) J.C. Scully, Corrosion Science, Vol. 8, 1968, p. 513.
- 40) C.F. Shih, J. Mech. Phys. Solids, Vol. 29, 1981, p. 305.
- 41) R.M. McMeeking, J. Mechanical and Physical Solids, Vol. 25, 1977, p. 357.
- 42) D. Broek, Elementary Engineering Fracture Mechanics, 4th edition, Kluwer Academic Publishers, Dordrecht, The Netherlands, 1986.

DISTRIBUTION LIST

- 1 - 3 Dr. A. John Sedriks
Materials Division, Code 1131M
Office of Naval Research
800 N. Quincy Street
Arlington, VA 22217-5660
- 4 Mr. Michael Karp
Administrative Contracting Officer
Office of Naval Research
Resident Representative
101 Marietta Tower, Suite 2805
101 Marietta Street
Atlanta, GA 30303
- 5 - 6 M. Rodeffer, Clark Hall
- 7 Director, Naval Research Laboratory
Code 2627
Washington, DC 20375
- 8 Naval Research Laboratory
Code 6000
Washington, DC 20375
- 9 Naval Research Laboratory
Code 6300
Washington, DC 20375
- 10 Naval Research Laboratory
Code 5227
Washington, DC 20375
- 11 - 12 Defense Technical Information Center, S47031
Building 5, Cameron Station
Alexandria, VA 22314
- 13 - 14 Naval Air Warfare Center
White Oak Detachment
Attention: Library, Code R33
Silver Spring, MD 20903-5000
- 15 Naval Postgraduate School
Mechanical Engineering Department
Monterey, CA 93940

- 16 Naval Air Systems Command
 Code 5304
 Washington, DC 20361
- 17 Naval Sea Systems Command
 Code 05M
 Washington, DC 20362
- 18 Naval Sea Systems Command
 Code 05R
 Washington, DC 20362
- 19 Naval Air Warfare Center
 Library
 Aircraft Division, Trenton
 Trenton, NJ 08628
- 20 Naval Facilities
 Materials Division
 Engineering Service Center
 Port Hueneme, CA 94043
- 21 Naval Surface Warfare Center
 Library
 Carderock Division
 Bethesda, MD 20084
- 22 Naval Underwater Warfare Center
 Library
 Newport, RI 02840
- 23 Naval Air Warfare Center
 Library
 Weapons Division
 China Lake, CA 93555-6001
- 24 National Aeronautics and Space Administration
 Library
 Lewis Research Center
 21000 Brook Park Road
 Cleveland, OH 44135
- 25 National Institute of Standards and Technology
 Metallurgy Division
 Gaithersburg, MD 20899
- 26 National Institute of Standards and Technology
 Ceramics Division
 Gaithersburg, MD 20899

- 27 National Institute of Standards and Technology
Fracture and Deformation Division
Gaithersburg, MD 20899

- 28 Naval Command, Control and Ocean Surveillance Center
Attention: Library
R & D Division
San Diego, CA 92152-5000

- 29 Office of the Assistant Commander HQ Marine Corps
Attention: Scientific Advisor
2 Navy Annex
Washington, DC 20380-1775

- 30 Army Research Office
Metallurgy and Ceramics Program
P. O. Box 12211
Research Triangle Park, NC 27709

- 31 Army Materials Technology Laboratory
SLCMT-TMM
Watertown, MA 02172-0001

- 32 Air Force Office of Scientific Research
Electronics and Materials Science Directorate
Building 410
Bolling Air Force Base
Washington, DC 20332

- 33 National Aeronautics and Space Administration
Headquarters
Code RN
Washington, DC 20546

- 34 Naval Surface Warfare Center
Port Hueneme Division
Attention: Library
4363 Missile Way
Port Hueneme, CA 93043-4307

- 35 Metals Information Analysis Center
Purdue University
2595 Yeager Road
West Lafayette, IN 47906

- 36 Naval Facilities Engineering Command
Code 03
Alexandria, VA 22331

- 37 Oak Ridge National Laboratory
 Metals and Ceramics Division
 P. O. Box X
 Oak Ridge, TN 37380
- 38 Los Alamos Scientific Laboratory
 Attention: Report Librarian
 P. O. Box 1663
 Los Alamos, NM 87544
- 39 Argonne National Laboratory
 Metallurgy Division
 P. O. Box 229
 Lemont, IL 60439
- 40 Brookhaven National Laboratory
 Research Laboratory
 Upton, Long Island, NY 11973
- 41 Lawrence Berkeley Laboratory
 Attention: Library
 1 Cyclotron Road
 Berkeley, CA 94720
- 42 Naval Surface Warfare Center
 Code 61
 Annapolis Detachment
 Annapolis, MD 21402-5067
- 43 Naval Surface Warfare Center
 Code 613
 Annapolis Detachment
 Annapolis, MD 21402-5067
- 44 Naval Surface Warfare Center
 Code 0115
 Annapolis Detachment
 Annapolis, MD 21402-5067
- 45 Professors G. H. Meier and F. S. Pettit
 Department of Materials Science and Engineering
 848 Benedum Hall
 University of Pittsburgh
 Pittsburgh, PA 15261
- 46 Professor Gordon P. Bierwagen
 North Dakota State University
 Department of Polymers and Coatings
 Box 5227
 Fargo, ND 58105

- 47 Professor H. W. Pickering
The Pennsylvania State University
209 Steidle Building
University Park, PA 16802
- 48 Professor D. J. Duquette
Department of Metallurgical Engineering
Rensselaer Polytechnic Institute
Troy, NY 12181
- 49 Professor D. Tomanek
Michigan State University
Department of Physics and Astronomy
East Lansing, MI 48824-1116
- 50 Dr. M. W. Kendig
Rockwell International Science Center
1049 Camino Dos Rios
P. O. Box 1085
Thousand Oaks, CA 91360
- 51 Professor R. A. Rapp
Department of Metallurgical Engineering
The Ohio State University
116 West 19th Avenue
Columbus, OH 43210-1179
- 52 Dr. R. D. Granata
Sinclair Laboratory #7
Lehigh University
Bethlehem, PA 18015
- 53 Dr. G. D. Davis
Martin Marietta Laboratories 848
1450 South Rolling Road
Baltimore, MD 21227-3898
- 54 Dr. S. M. Lipka
Department of Ocean Engineering
Florida Atlantic University
Boca Raton, FL 33431-0991
- 55 Professor D. D. Macdonald
The Pennsylvania State University
517 Deike Building
University Park, PA 16802

- 56 Dr. B. G. Pound
SRI International
333 Ravenswood Ave.
Menlo Park, CA 94025
- 57 Professor C. R. Clayton
Department of Materials Science and Engineering
State University of New York - Stoner Brook
Stoney Brook, NY 11794
- 58 Dr. J. W. Oldfield
Cortest Laboratories Ltd.
23 Shepherd Street
Sheffield, S3 7BA U.K.
- 59 Ms. D. M. Aylor
Code 613
Naval Surface Warfare Center
Annapolis, MD 21402-5067
- 60 Professor K. Sieradzki
Department of Mechanical and Aerospace Engineering
Arizona State University
Tempe, AZ 85287-6106
- 61 Dr. P. S. Pao
Code 6326
Naval Research Laboratory
Washington, DC 20375-5343
- 62 Dr. W. P. Allen
United Technologies Research Center
East Hartford, CT 06108
- 63 Dr. B. A. Shaw
Department of Engineering Science and Mechanics
207 Hallowell Building
The Pennsylvania State University
University Park, PA 16802-1484
- 64 Dr. P. Cox
SRI International
333 Ravenswood Ave.
Menlo Park, CA 94025-3493
- 65 Dr. R. E. Ricker
National Institute of Standards and Technology
Building 223, Room B-266
Gaithersburg, MD 20899

- 66 Dr. F. B. Mansfeld
Department of Materials Science
University of Southern California
University Park
Los Angeles, CA 90089-0241
- 67 Professor R. E. White
Department of Chemical Engineering
University of South Carolina
Columbia, SC 29208
- 68 Professor R. A. Buchanan
Department of Materials Science and Engineering
University of Tennessee
Knoxville, TN 37996-2200
- 69 Dr. B. J. Little
NRL Detachment
Building 1105, Room D415
Stennis Space Center, MS 39529-5004
- 70 Professor M. E. Orazem
Department of Chemical Engineering
University of Florida
Gainesville, FL 32611
- 71 Professor J. O'M. Bockris
Department of Chemistry
Texas A & M University
College Station, TX 77843
- 72 Dr. V. S. Agarwala
Code 6062
Naval Air Warfare Center
Warminster, PA 18974-0591
- 73 Professor R. C. Newman
UMIST
Corrosion and Protection Center
P. O. Box 88
Manchester M60 1QD, U.K.
- 74 Professor S. C. Dexter
College of Marine Studies
University of Delaware
700 Pilottown Road
Lewes, DE 19958

- 75 Dr. R. Brown
Department of Chemical Engineering
University of Rhode Island
Kingston, RI 02881-0805
- 76 Dr. J. Jones-Meehan
Code R301
Naval Surface Warfare Center
10901 New Hampshire Avenue
Silver Spring, MD 20903
- 77 Dr. P. Natishan
Code 6322
Naval Research Laboratory
Washington, DC 20375-5343
- 78 Dr. R. L. Jones
Code 6170
Naval Research Laboratory
Washington, DC 20375-5342
- 79 - 81 Office of Naval Research
Code 3310
800 North Quincy Street
Arlington, VA 22217-5660
- 82 - 85 R. P. Gangloff
- 86 - 89 J. R. Scully
- 90 R. G. Kelly
- 91 W. A. Jesser
- * Postaward Research Administration
- 92 SEAS Preaward Administration Files
- * Cover Letter Only